



ALICE

ALICE-TDR-016



CERN-LHCC-2013-020

February 19, 2014

Technical Design Report

for the

Upgrade of the

ALICE Time Projection Chamber

The ALICE Collaboration*

Copyright CERN, for the benefit of the ALICE Collaboration.
This article is distributed under the terms of Creative Commons Attribution License (CC-BY-3.0), which permits any use provided the original author(s) and source are credited.

*See Appendix C for the list of collaboration members

Executive summary

This Technical Design Report describes the upgrade of the ALICE Time Projection Chamber (TPC), which is an integral part of the ALICE upgrade strategy after LHC Long Shutdown 2 (LS2). The main design considerations and technical specifications are summarized in the following.

In Chap. 1 the main scientific goals of the future ALICE physics program are briefly reviewed and the resulting requirements for the TPC upgrade are presented. The expected increase of the LHC luminosity after LS2 to about 50 kHz in Pb–Pb implies that TPC operation with a gating grid is no longer possible. This motivates the choice of GEMs for the new readout chambers, since they feature intrinsic ion blocking capabilities that avoid massive charge accumulation in the drift volume from back-drifting ions, and prevent excessive space-charge distortions. However, GEMs do not feature the same opacity for ions as a gating grid. The requirement to limit the space-charge distortions to less than 10 cm in most of the TPC drift volume defines an upper limit of 1 % for the fractional ion backflow (IBF). The achievement of this goal is the result of a major R&D effort presented in this document. The replacement of the existing MWPC-based readout chambers by GEMs implies also the necessity for new readout electronics that accommodate the negative signal polarity and enable continuous data readout. Moreover, the high data rate requires data compression by a factor of about 20 in order to match the anticipated bandwidth to permanent storage. This implies that significant pattern recognition and data format optimization must be performed online. The present particle identification (PID) capability via the measurement of the specific ionization dE/dx and the combined momentum resolution of the central barrel tracking system must remain unaffected by the TPC upgrade.

Most of the main components of the existing TPC, including the field cage, the endplates, the gas system and services will be reused after the upgrade. A short overview of those components is given in Chap. 2.

The choice of the detector gas is presented in Chap. 3. The requirements in terms of drift velocity, diffusion, gas gain, and ion mobility lead to Ne-CO₂-N₂ (90-10-5) as a baseline gas mixture for the TPC, however, other gas mixtures, e.g. those containing argon, are not excluded.

The technical solution that was chosen for the new readout chambers is presented in Chap. 4. Their design is such that the segmentation in azimuth and the division into inner and outer readout chambers (IROCs and OROCs) is identical to those of the existing detector. The new readout chambers will employ stacks of four GEM foils for gas amplification and anode pad readout. Quadruple GEM stacks have proven to provide sufficient ion blocking capabilities at the required gas gain of 2000 in Ne-CO₂-N₂ (90-10-5), in particular when GEM foils with large hole pitch are used. The size of the readout chambers, in particular of the OROCs, favors the use of large-size GEM foils manufactured with the single-mask technology. Such foils were recently implemented successfully in the new KLOE-2 tracking system. Application of this technique allows production of the readout chambers such that a single large GEM foil per layer can be used in the IROCs, and three large GEM foils per layer in the OROCs. The anode readout pad structure of the existing TPC, with three different pad sizes that increase from small to large radii, will only be slightly modified for the new readout chambers. The local position resolution of the

GEM detectors is slightly worse than that of the present system due to the lack of a pad response function. Additionally, the occurrence of single-pad clusters leads to a deterioration of the position resolution at short drift lengths. However, this has no observable effect on the combined momentum resolution of the ALICE central barrel system, as shown in Chap. 7. At the same time, the difference in coupling to the readout plane will reduce the detector occupancy in GEMs compared to that in the existing MWPC. To ensure safe operation and long-term reliability, a careful quality assurance procedure for GEM foils and readout chambers at the various assembly stages is being developed and described in Chap. 4.

The main results from R&D with small and full-sized prototypes are discussed in Chap. 5. In a quadruple GEM system including foils with large hole pitch, ion backflow values below 1 % at a gas gain of 2000 and an energy resolution $\sigma(^{55}\text{Fe}) = 12\%$ are observed. These operational conditions match safely the requirements of the detector and leave room for further optimizations. The ion backflow results are well described by a microscopic detector simulation based on the Garfield++ framework. Test beam results from a full-size IROC prototype equipped with a triple GEM stack show that the same dE/dx resolution as in MWPC-based readout chambers can be achieved. Some of the possible further R&D directions, including COBRA GEMs and MicoMegs, are described in Chap. 9.

The new TPC front-end electronics and readout system is discussed in Chap. 6. The main specifications remain unchanged with respect to the existing detector. However, new characteristics have to be incorporated: The front-end ASIC has to amplify and process signals with opposite polarity as compared to those of an MWPC. The detector signals have to be sampled continuously while concurrently the acquired data is transferred off-detector. Finally, the data throughput will be strongly increased with respect to the current system. The SAMPA project aims at delivering an ASIC fulfilling these requirements. The SAMPA ASICs connect to the common read-out unit (CRU), which provides the interface to the online computing system, the trigger system and the DCS, through optical fibers via the GBT link. Both, SAMPA and CRU, are common solutions for different ALICE subsystems and are described in the separate Technical Design Report on the upgrade of the readout and trigger system.

In Chap. 7 an evaluation of the performance of the upgraded TPC is presented. Using a microscopic simulation of the TPC with GEM readout, the intrinsic momentum and dE/dx resolutions are found to be the same as with the existing TPC, if the local energy resolution does not exceed $\sigma(^{55}\text{Fe}) = 12\%$. No significant deterioration of the tracking efficiency nor the momentum resolution is observed when event pileup, corresponding to collision rates of 50 kHz, is introduced. The dE/dx resolution slightly worsens with increasing occupancy from 5.5 % in isolated pp events without pileup to about 7.5 % in central Pb–Pb at 50 kHz. This behaviour is similar when using MWPC or GEM and is understood in terms of an increasing overlap of clusters.

Detailed calculations of the ion space-charge density in the TPC caused by back-drifting ions from the amplification region are presented. The time it takes the ions to drift to the central electrode is close to 160 ms, leading on average to pileup of ions from about 8000 collisions in the TPC drift volume at an interaction rate of 50 kHz. At a gas gain of 2000 in Ne-CO₂-N₂ (90-10-5) and an ion backflow of 1 %, this results in space-charge distortions that stay below 10 cm in most of the TPC volume, with the exception of the innermost region (small r) and at the largest drift length, where radial distortions up to 20 cm are observed. In order to reach the intrinsic track resolution of the TPC of a few hundred μm , distortion corrections with a precision on the level of 10^{-3} need to be performed. Furthermore, it is demonstrated that statistical fluctuations of the collision rate and of the charged-particle multiplicity lead to temporal variations of the space-charge density that are of the order of a few percent, i.e. significantly larger than the required precision of the correction. This implies that the space-charge density and thus the space-charge distortion corrections must be determined as a function of time during the data acquisition. Detailed studies demonstrate that a given space-charge configuration can be considered as static over time intervals of ~ 5 ms.

The strategy for online reconstruction and calibration is discussed in Chap. 8. Online reconstruction is necessary in order to achieve data compression by a factor of 20 as compared to the raw data size, and to allow for permanent storage of the data. Such compression factors can be achieved if the association of clusters to tracks can be performed online, which implies also the necessity for sufficient online correction of the space-charge distortions. We argue that the standard TPC tracking scheme including the use of a coarse distortion correction map that can be determined online provides high tracking and cluster association efficiency. Moreover, it provides sufficient spatial accuracy to allow efficient matching of the TPC tracks to the Inner Tracking System (ITS), which is necessary to conduct the subsequent calibration steps. The final space-point calibration is based on a residual distortion correction employing external reference track information from the ITS and the Transition Radiation Detector (TRD). In this step, the space-charge density fluctuations, which require an updated residual correction map every 5 ms, are addressed. We demonstrate that the available track statistics accumulated over such time intervals is adequate to determine the residual distortions in a grid of sufficient spatial granularity, and with a precision that is consistent with the intrinsic resolution of the TPC.

Chapters 10 and 11 discuss the detector control system and installation, commissioning and services. Most of the aspects presented here build on the existing system and profit from the experience gained with it.

The project organization and considerations concerning budget and time schedule for two different installation scenarios are discussed in Chap. 12. The ALICE TPC collaboration has gained a significant number of new collaborators with considerable experience and manpower to carry out the upgrade project. The overall CORE cost of the project of 9.1 MCHF is consistent with the ongoing funding requests in different countries. The overall time line of the project matches the current LHC schedule and foresees that the upgraded TPC will be ready for operation after LS2 in 2020.

Contents

1	Physics objectives and design considerations	1
1.1	Physics Objectives	1
1.2	Upgrade concept	2
1.3	Design considerations	4
1.4	Detector overview	4
2	Mechanical structure, field cage, and gas system	7
2.1	Introduction	7
2.2	Field cage	7
2.3	Endplates	7
2.4	Last resistor and skirt	10
2.5	Service Support Wheel	10
2.6	Gliders and I-bars	11
2.7	Gas system	11
3	Gas choice	13
4	Readout chambers	17
4.1	Introduction	17
4.2	Mechanical structure	20
4.3	GEM planes	23
4.3.1	General structure	23
4.3.2	Inner readout chambers	25
4.3.3	Outer readout chambers	26
4.4	High voltage supply	29
4.4.1	System overview	29
4.4.2	Typical HV settings	31

4.5	Readout pad plane	31
4.6	Interface to front-end electronics	34
4.7	Quality assurance of GEM foils	34
4.7.1	Electrical characterization	36
4.7.2	Optical scanning characterization	37
4.7.3	GEM gain mapping	40
4.8	Quality assurance of chambers	41
5	R&D with prototypes	43
5.1	R&D with small prototypes	43
5.1.1	Experimental setup	43
5.1.2	Gain stability measurements	45
5.1.3	Results of ion backflow measurements	46
5.1.4	Comparison with simulations	50
5.2	Full-size IROC prototype	52
5.2.1	Detector design	52
5.2.2	Quality assurance (QA)	54
5.2.3	Detector assembly	55
5.2.4	HV supply	57
5.2.5	Prototype commissioning	59
5.2.6	Test campaign at the CERN PS	59
6	Front-end electronics and readout	65
6.1	System overview	65
6.2	Pileup and occupancies	66
6.3	Data rates and bandwidth considerations	67
6.4	Common front-end ASIC	67
6.4.1	Overview	69
6.4.2	General requirements for the analog part	69
6.4.3	Signal shaping	70
6.4.4	Noise	71
6.4.5	Further requirements for the analog part	74
6.4.6	Electrostatic discharge protection	75
6.4.7	Analog-to-digital conversion	75

6.4.8	Digital signal processor	76
6.4.9	Testing	78
6.5	Front-end card	79
6.5.1	Partitioning	79
6.5.2	PCB design and layout	80
6.5.3	System level input protection	81
6.5.4	Testing	81
6.5.5	Irradiation campaign	81
6.6	Common Readout Unit	81
7	Simulation and detector performance	83
7.1	Current performance	83
7.1.1	Tracking performance	83
7.1.2	Particle identification performance	84
7.2	Intrinsic performance of the upgraded TPC	85
7.2.1	Microscopic GEM simulations	85
7.2.2	Tracking performance	86
7.2.3	Particle identification performance	86
7.3	Performance with event pileup	88
7.4	Space-charge distortions and corrections	90
7.4.1	Space-charge sources	90
7.4.2	Magnitude of the distortions	91
7.4.3	Simulation of the space-charge distortions	91
7.4.4	Space-charge density fluctuations	94
7.4.5	Impact of the fluctuations on the distortion corrections	96
7.5	Performance with space-charge distortions	97
8	Online reconstruction, calibration, and monitoring	101
8.1	Continuous TPC operation at high luminosities	101
8.1.1	LHC conditions in RUN 3	101
8.1.2	TPC reconstruction, calibration, and data compression in RUN 3	103
8.2	Space-charge distortion corrections	106
8.2.1	TPC coordinate transformation	106
8.2.2	Space point corrections	107

8.2.3	Space-charge density maps	107
8.3	First reconstruction stage	108
8.3.1	Standard tracking approach	108
8.3.2	Performance using corrections from the scaled average map	109
8.4	Second reconstruction stage	110
8.4.1	ITS-TRD track interpolation approach	110
8.4.2	Momentum resolution after residual correction	113
8.5	Further optimizations	114
8.5.1	TPC standalone tracking approach	114
8.5.2	Space-charge calibration by current measurements	117
8.6	Additional calibration requirements, monitoring, and quality control	118
8.6.1	Futher calibration requirements	119
8.6.2	Monitoring and quality control	120
9	Alternative R&D options	123
9.1	R&D with COBRA GEMs	123
9.1.1	Characterization of single COBRA GEMs	125
9.1.2	Triple structures with COBRA and standard GEMs	127
9.1.3	Energy resolution	129
9.1.4	Conclusion and outlook	129
9.2	R&D with hybrid gain structures: 2GEMs + MicroMegas	129
9.3	Studies with fast gas mixtures	132
10	Detector control system	135
10.1	Overview	135
10.1.1	Hardware architecture	135
10.1.2	Software architecture	135
10.1.3	System implementation	136
10.1.4	Interfaces to devices	136
10.1.5	Interlocks	136
10.2	Front-end electronics control	137
10.2.1	Overview	137
10.2.2	Monitoring	137
10.2.3	Configuration and control	138

10.3	Parameter export for online calibration and reconstruction	138
11	Installation, commissioning and services	139
11.1	General	139
11.2	Installation	139
11.3	Commissioning	139
11.4	Services	140
11.4.1	High voltage	141
11.4.2	Low voltage	142
11.4.3	Cooling	143
11.4.4	Calibration	143
12	Project organization, cost estimate and time line	145
12.1	Participating institutions	145
12.2	Cost estimate	145
12.3	Schedule	147
12.4	TPC upgrade TDR editorial committee	150
12.5	TPC upgrade TDR task force	150
Appendices		
A	Coordinate systems	153
A.1	Global coordinate system	153
A.2	Local coordinate system	153
B	TPC upgrade collaboration	155
C	The ALICE Collaboration	159
References		
167		
List of Figures		
175		
List of Tables		
181		

Chapter 1

Physics objectives and design considerations

Studies of heavy-ion collisions at the Large Hadron Collider (LHC) are ideally suited to probe fundamental properties of QCD, including its non-perturbative aspects related to color charge deconfinement, and the restoration of chiral symmetry. In particular, heavy-ion collisions allow the detailed characterization of the Quark-Gluon Plasma (QGP), and the nature of the phase transition between QGP and normal hadronic matter.

ALICE¹ at the LHC is dedicated to these studies [1]. Operation of the ALICE detector in collisions of ²⁰⁸Pb-ions at $\sqrt{s_{NN}} = 2.76$ TeV in 2010 and 2011 (integrated luminosity $\mathcal{L}_{int} = 0.16 \text{ nb}^{-1}$) has demonstrated its excellent tracking and particle identification (PID) capabilities in an environment of large charged-particle densities. The lead ion campaigns in RUN 2 after the LHC Long Shutdown 1 (LS1), starting in 2015, will conclude the initial LHC heavy-ion programme with 1 nb^{-1} .

A significant increase of the LHC luminosity for heavy ions is expected in RUN 3 after Long Shutdown 2 (LS2), leading to collision rates of about 50 kHz and $\mathcal{L}_{int} = 10 \text{ nb}^{-1}$. This implies a substantial enhancement of the sensitivity to a number of rare probes that are key observables for the characterization of strongly interacting matter at high temperature.

In order to fully exploit the scientific potential of the LHC in RUN 3, ALICE plans to extend its physics programme by improving its detector performance. As an integral part of the ALICE upgrade strategy, this Technical Design Report describes the concept of a novel readout scheme, based on GEM² technology, that will be implemented in the Time Projection Chamber (TPC) upgrade. The present MWPC³-based readout chambers will be replaced by a GEM system to match the TPC readout rate with the increased Pb–Pb collision rate of the LHC in RUN 3. At the same time, the front-end electronics and readout system will be replaced in order to match the new readout chamber technology and increased data rates. After these upgrades, the data collection rate of the TPC will be increased by about a factor 100 in the high-luminosity environment of the LHC in RUN 3, while the tracking and PID capabilities of the present TPC will be retained.

1.1 Physics Objectives

The scientific goals of the upgraded ALICE detector are described in a comprehensive Letter of Intent [2]. They are aimed at improving measurements for understanding heavy-quark production at low transverse

¹A Large Ion Collider Experiment (ALICE)

²Gas Electron Multiplier (GEM)

³Multi-Wire Proportional Chamber (MWPC)

31 momentum (p_T), mechanisms of quarkonium production and interaction in the QGP, initial tempera-
 32 ture and partonic equation of state, possible effects of chiral symmetry restoration, parton energy loss,
 33 medium modification and its dependence on properties of the parton and the QGP, and exotic hadronic
 34 states. To accomplish these, the following measurements will be undertaken in the central barrel of the
 35 ALICE detector:

- 36 – Yields and azimuthal distributions of hadrons containing heavy quarks (c, b) to study the mecha-
 37 nism of heavy-quark thermalization in the QGP.
- 38 – Production of quarkonia at low p_T , in particular the study of their possible dissociation and regen-
 39 eration mechanisms in the QGP.
- 40 – Low-mass dielectron production to extract information on early temperature and the partonic equa-
 41 tion of state, and to characterize the chiral phase transition.
- 42 – Jets and jet correlations, in particular their structure and particle composition, to study the mech-
 43 anism of partonic energy loss in medium and its dependence on parton color-charge, mass and
 44 energy.
- 45 – The production of nuclei, anti-nuclei and hyper-nuclei as well as exotic hadronic states such as the
 46 H-dibaryon.

47 These measurements require excellent charged-particle tracking capabilities as well as a variety of PID
 48 techniques in the central barrel, down to the lowest possible p_T . Measurements at low transverse mo-
 49 menta typically imply small signal-to-background ratios, which limits the applicability of standard low-
 50 level triggering schemes. As a consequence, the detectors and readout systems must allow to operate at
 51 very high readout and data acquisition rates in order to collect sufficient statistics.

52 1.2 Upgrade concept

53 A significant increase in the sensitivity of ALICE to these observables is achieved by major upgrades of
 54 its detectors and readout systems in the central barrel of the experiment. A new Inner Tracking System
 55 (ITS) improves by a factor 3 the resolution for secondary vertices and extends its tracking capabilities to
 56 lower transverse momentum. Moreover, the material budget of the ITS is reduced from 1.1 % to 0.3 %
 57 of X_0 per detector layer. The performance of the new ITS will significantly expand the physics reach of
 58 the ALICE central barrel, in particular in the heavy-flavor and low-mass dielectron sector.

59 On the other hand, precision measurements of the key observables outlined above require tracking and
 60 PID information from the TPC. In order to conduct the envisaged physics programme with optimum
 61 precision, exploiting the full LHC luminosity, the TPC will be upgraded. This upgrade is intended
 62 primarily to overcome the rate limitation of the present system, which arises from the gated operation of
 63 the MWPC-based readout chambers.

64 The ALICE TPC is the largest detector of its type, with an overall active volume of about 90 m^3 [3, 4].
 65 The TPC employs a cylindrical field cage with a central high voltage electrode at $z = 0$ (for a definition
 66 of the ALICE coordinate system see Apx. A.1) and a readout plane on each endplate. It covers full
 67 azimuth in $|\eta| < 0.9$ and provides charged-particle tracking over a wide transverse momentum range.
 68 The readout planes consist of 72 MWPC-based readout chambers, with a total of about 550,000 readout
 69 cathode pads.

70 Charged-particle tracking and PID via ionization energy loss (dE/dx) in the TPC is accomplished by the
 71 measurement of the ionization of up to 158 samples along a trajectory of $\sim 160 \text{ cm}$. In pp and central

72 Pb–Pb collisions a resolution $\sigma(dE/dx)/(dE/dx)$ of about 5.5 % and 7 % is achieved, respectively. Fur-
 73 ther PID capabilities arise from topological reconstruction of the weak decays of strange hadrons and
 74 gamma conversions.

75 The readout chambers are operated with an active dipolar Gating Grid (GG) which, in the presence of
 76 a trigger, switches to transparent mode to allow the ionization electrons to pass into the amplification
 77 region. After the maximum drift time of $\sim 100 \mu\text{s}$ the GG wires are biased with an alternating voltage
 78 $\Delta V = \pm 90 \text{ V}$ that renders the grid opaque to electrons and ions. This protects the amplification region
 79 against unwanted ionization from the drift region, and prevents back-drifting ions from the amplification
 80 region to enter the drift volume. In particular, the latter would lead to significant space-charge accumu-
 81 lation and drift-field distortions. Due to the low mobility of ions ($\mu_{\text{ion}} = \mathcal{O}(10^{-3}) \cdot \mu_{\text{electron}}$), efficient ion
 82 blocking requires the GG to remain closed for $\sim 180 \mu\text{s}$ after the end of the event readout, corresponding
 83 to the typical time it takes the ions in a Ne-based gas mixture to drift from the anode wires to the GG.
 84 This gating scheme leads to an intrinsic dead time of the TPC system of $\sim 280 \mu\text{s}$, implying a principal
 85 rate limitation of the present TPC to about 3.5 kHz. It should be noted that due to the present TPC readout
 86 system the data rate is limited to $\sim 300 \text{ Hz}$ for central Pb–Pb collisions.

87 Operation of the TPC at 50 kHz cannot be accomplished with an active ion gating scheme. On the other
 88 hand, back-drifting ions from the amplification region of a MWPC without gate will lead to excessive
 89 ion charge densities and drift distortions that render precise space-point measurements impossible. The
 90 proposed scheme therefore entails replacement of the existing MWPC-based readout chambers by a
 91 multiple-stage GEM system. GEMs have proven to operate reliably in high-rate applications and provide
 92 intrinsic ion blocking capabilities, therefore enabling the TPC to operate in a continuous, ungated readout
 93 mode at collision rates of 50 kHz. The TPC upgrade increases the readout rate by about two orders of
 94 magnitude as compared to the present system, thus giving access to previously inaccessible physics
 95 observables. As an example, the low-mass dielectron invariant mass spectrum is shown in Fig. 1.1,
 96 accumulated in a typical yearly heavy-ion run ($\sim 3 \text{ nb}^{-1}$) with the current (left) and upgraded (right)
 97 TPC.

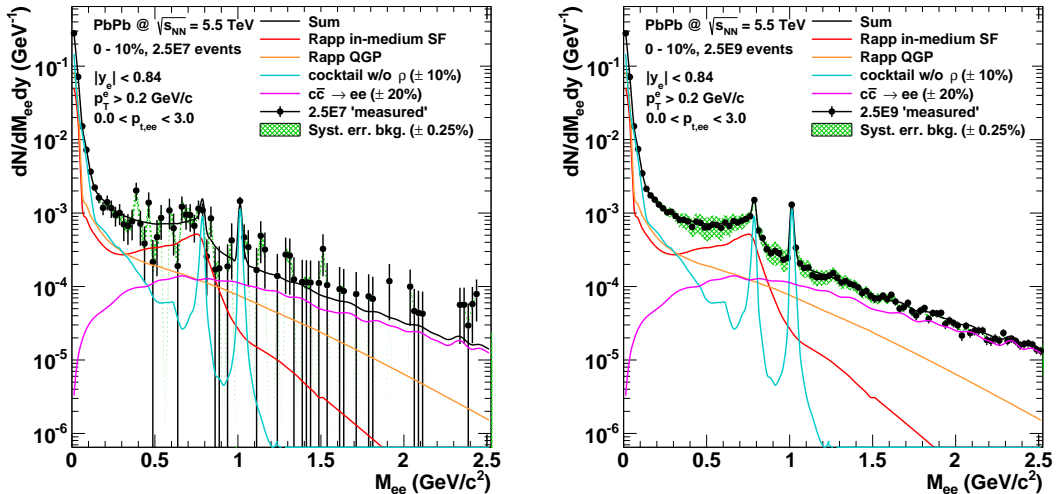


Figure 1.1: Inclusive e^+e^- invariant mass spectrum for 0–10% most central Pb–Pb collisions at $\sqrt{s_{\text{NN}}} = 5.5 \text{ TeV}$, assuming $2.5 \cdot 10^7$ events (left panel) and $2.5 \cdot 10^9$ events (right panel). The spectra include a set of tight primary track cuts based on the new ITS system to suppress leptons from charm decays. Also shown are curves that represent the contributions from light hadrons (blue), charm (magenta) and thermal radiation from a hadronic gas (red) and a QGP (orange). The figures are from [2].

1.3 Design considerations

The present document describes a proposal for a new readout scheme of the ALICE TPC, based on GEM technology. The main considerations for the design of the system and choices of technologies are summarized in the following.

- The new GEM-based readout chambers must provide sufficient ion blocking to limit the resulting drift field distortions in Pb–Pb collisions to less than 10 cm in most of the active volume of the TPC. Distortions of this magnitude must be correctable without deterioration of the online reconstruction efficiency and the final momentum resolution of the detector.
- The new readout scheme requires a complete redesign of the TPC front-end and readout electronics system. The new electronics must accommodate the negative signal polarity of the GEM detectors and the continuous readout scheme. Additionally, the minimization of the ion space-charge density requires the operation of the readout chambers at the lowest possible gas gain, leading to a front-end noise requirement of $ENC^4 < 600 e$.
- The limited bandwidth of the data acquisition system requires significant online data reduction. The present scheme foresees that cluster finding and association to tracks is performed in an online computing system to achieve the required data compression factor of ~ 20 .
- The upgraded TPC must preserve the performance of the existing system in terms of momentum and dE/dx resolution. This requires that the space-charge distortions must be corrected to the level of the intrinsic spatial track resolution of the TPC, i.e. to a few hundred μm . The present dE/dx performance of the TPC requires a precise equilibration and normalization of the ionization energy loss throughout the entire TPC volume. Moreover, the local energy resolution of the readout chambers must not exceed 12 % at 5.9 keV. The latter is affected by the transparency of the GEM system and demands a careful optimization of the operational point with respect to electron collection efficiency and ion blocking.
- The upgrade of the TPC readout chambers and electronics must allow the re-use of the existing hardware to the greatest possible extent. This applies in particular to the existing field cage, gas system, cooling, and services.

1.4 Detector overview

The requirements for the TPC upgrade listed above have led to the technical design presented in this document. In the following section we summarize briefly the main aspects of the proposed solution.

The overall dimensions of the TPC will remain unchanged. Also the segmentation of the readout planes into Inner and Outer Readout Chambers (IROCs and OROCs), 18 each on either endplate, will be preserved. This permits to re-use most of the components of the existing field cage and endplate structures.

The upgraded TPC will be operated with a Ne-CO₂-N₂ (90-10-5) gas mixture. This choice is mainly driven by the higher ion mobility in neon as compared to argon, which leads to less space-charge accumulation in the drift field.

The new TPC readout chambers will be equipped with quadruple GEM stacks for gas amplification. Comprehensive R&D studies have shown that conventional triple GEM stacks using standard geometry GEM foils will not lead to sufficient ion blocking. In prototype measurements with quadruple GEM systems, ion backflow fractions $< 1\%$ have been reached at a gas gain of 2000 and an energy resolution

⁴Equivalent Noise Charge (ENC)

138 of 12 % at 5.9 keV. These operational conditions will preserve the intrinsic dE/dx resolution and keep
139 the space-charge distortions at a tolerable level.

140 A new front-end electronics and readout system is being developed. The design of the new electronics is
141 driven by the requirement of low-noise operation and the challenges of continuous readout and high data
142 rate.

143 The upgraded TPC will provide similar momentum resolution as the present system. However, the
144 operation in continuous readout at high luminosity demands for innovative calibration and correction
145 schemes, in particular with respect to space-charge distortions. Moreover, significant data reconstruction
146 will have to be performed online to allow efficient data compression. With the design presented in this
147 document, these requirements can be fulfilled.

148 A summary of the TPC parameters is given in Table 1.1.

Detector gas	Ne-CO ₂ -N ₂ (90-10-5)
Gas volume	90 m ³
Drift voltage	100 kV
Drift field	400 V/cm
Maximal drift length	250 cm
Electron drift velocity	2.58 cm/ μ s
Maximum electron drift time	97 μ s
$\omega\tau$ ($B = 0.5$ T)	0.32
Electron diffusion coefficients	$D_T = 209 \mu\text{m}/\sqrt{\text{cm}}, D_L = 221 \mu\text{m}/\sqrt{\text{cm}}$
Ne ⁺ drift velocity	1.632 cm/ms
Maximum Ne ⁺ drift time	153 ms
Readout chambers	
Total number	$2 \times 2 \times 18 = 72$
Readout technology	4-GEM stack, single mask, standard (140 μ m) and large (280 μ m) hole pitch
Gas gain	2000
Ion back flow	< 1 %
Resolution at 5.9 keV	12 %
Inner (IROC)	
Total number	$2 \times 18 = 36$
Active range	$848 < r < 1321$ mm
Pad size	$4 \times 7.5 \text{ mm}^2$ ($r\phi \times r$)
Pad rows	63
Total pads (IROC)	5504
$S:N$	20:1
Outer (OROC)	
Total number	$2 \times 18 = 36$
Active range	$1346 < r < 2461$ mm
Pad size (inner)	$6 \times 10 \text{ mm}^2$ ($r\phi \times r$) ($1346 < r < 2066$ mm)
Pad rows (inner)	70
Total pads (inner)	6656
Pad size (outer)	$6 \times 15 \text{ mm}^2$ ($r\phi \times r$) ($2086 < r < 2461$ mm)
Pad rows (outer)	25
Total pads (outer)	3200
Total pads (OROC)	9856
$S:N$	30:1
Readout electronics	
Number of channels	552,960
Signal polarity	negative
Dynamic range	$30 \times \text{MIP}$
System noise	$600 e$
PASA conversion gain	20 (30) mV/fC
PASA peaking time	160 (80) ns
ADC number of bits	10
ADC sampling rate	10 (20) MHz
Power consumption	< 35 mW/ch
Operating conditions and data rate	
Collision rate in Pb-Pb	50 kHz
Raw event size (Pb-Pb min bias)	20 MByte
Online data compression factor	20

Table 1.1: Synopsis of parameters of the upgraded TPC.

149 Chapter 2

150 Mechanical structure, field cage, and gas 151 system

152 2.1 Introduction

153 The upgraded TPC consists of the current structures of the detector, where the new readout chambers
154 and electronics will replace the existing ones. Thus, the field cage, the endplates, the insulating volumes,
155 the service support wheels, the I-bars, and the gas system will remain the same. These structures and
156 systems are described elsewhere [1]. In this chapter a brief overview of the mechanical structure of the
157 TPC is given, with emphasis on aspects relevant for the integration of the new readout chambers.

158 2.2 Field cage

159 The field cage is composed of four concentric cylinders which define the drift volume and the inner
160 and outer insulating volumes. These cylinders, the field cage vessels and the containment vessels, are
161 held together by the endplates. A schematic view of this assembly is shown in Fig. 2.1. They are made
162 of composite material, namely a Nomex honeycomb structure sandwiched between layers of prepreg
163 composite and Tedlar. The Tedlar foils provide gas tightness. Field-defining strips are employed to
164 degrade the potential from the central electrode, an aluminized mylar foil at the center, to nearly ground
165 potential close to the readout chambers.

166 The inner and outer voltage-degrading strips are suspended on 18 Macrolon rods each. These rods are
167 also used to circulate the gas through tiny holes along their length, such that the gas flows radially
168 outwards and does not exert any force on the central electrode. In addition, some of these rods are used
169 to house services such as optical elements for the laser system, the high voltage cable to the central
170 electrode, and the four removable and water-cooled resistor rods for the voltage degrading (see Fig. 2.2).

171 2.3 Endplates

172 The endplates keep together the field cage and containment vessels, and also hold the readout chambers.
173 These are arranged in 18 sectors, each one covering 20° in azimuth. The cutouts of the endplates define
174 the dimensions of the part of the chamber bodies which form the exterior surface of the endplates. The
175 gas tightness is ensured by one O-ring on the endplate, one on the chamber body and a sealing foil in
176 between. The chambers are mounted such that the whole body is inserted into the field cage and then
177 moved back into the endplate, where it is fixed from the inside. This allows to maximize the active
178 area of the detectors, but requires that the whole chamber is brought into the drift volume for insertion.
179 The full dimensions of the chambers bodies are determined by the geometry of the endplates, and in

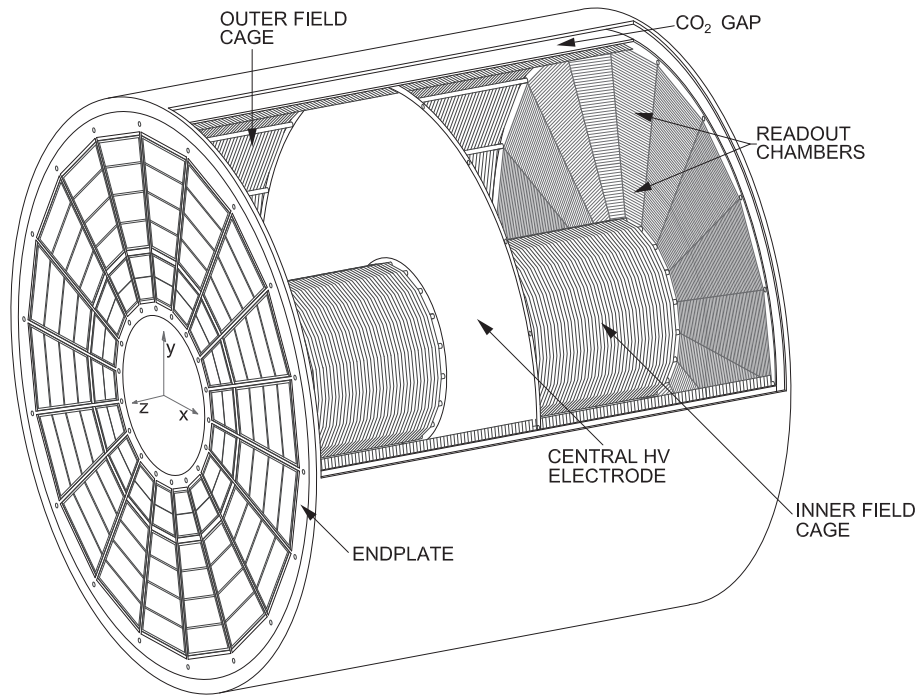


Figure 2.1: Schematic view of the ALICE TPC.

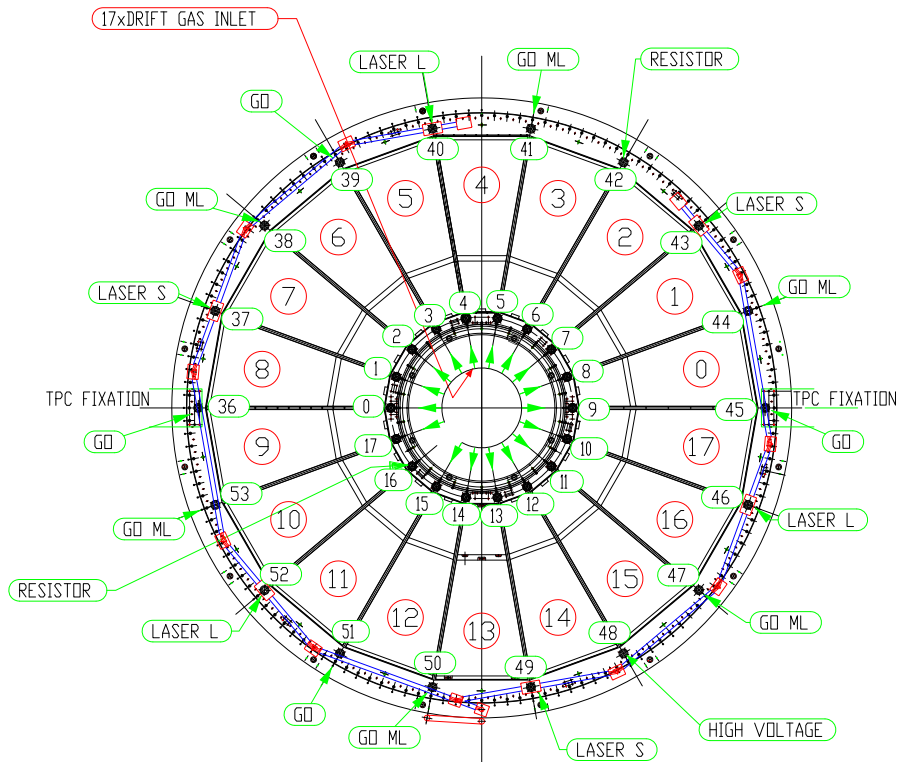


Figure 2.2: View of one of the endplates of the TPC; the different types of rods are indicated.

180 particular by the fixations on the endplate. A specialized mounting tool is used to install the chambers in
 181 place. Special care has to be taken of the small clearances that occur during this operation, as shown in
 182 the detailed views in Fig. 2.3 for the IROC and Figs. 2.4 and 2.5 for the OROC.

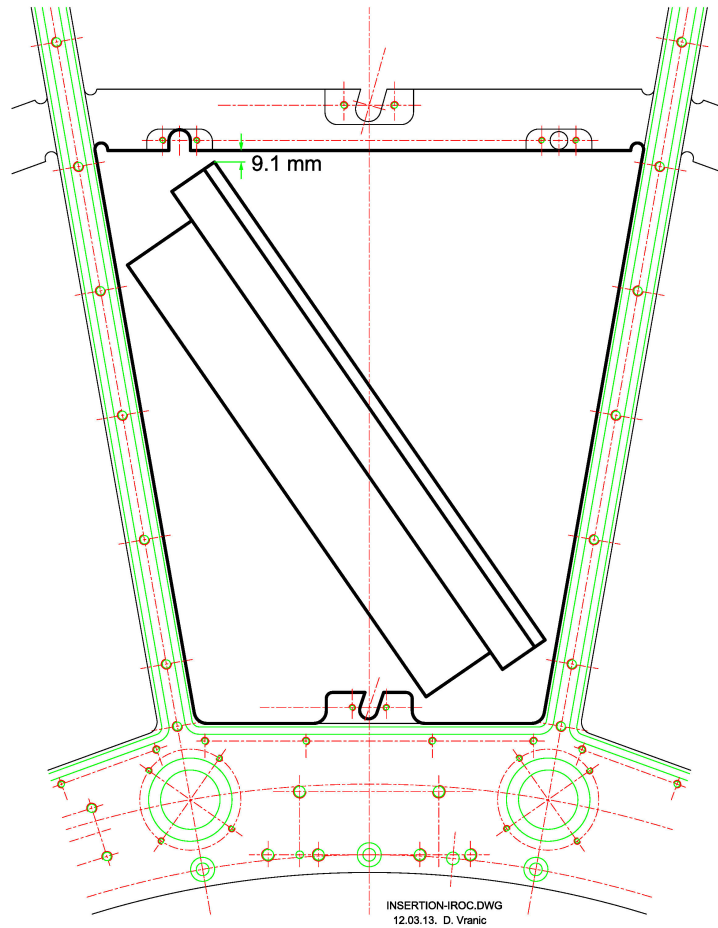


Figure 2.3: During the insertion of an IROC through the endplate the minimum clearance is 9 mm.

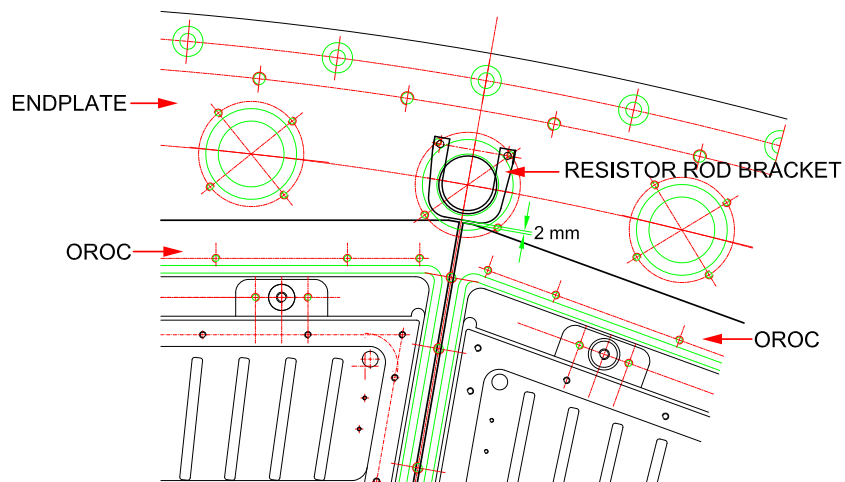


Figure 2.4: Insertion detail of an OROC. In the last stage, while moving the OROC back into its final position on the endplate, the clearance between the chamber and the bracket that holds the rod is only 2 mm.

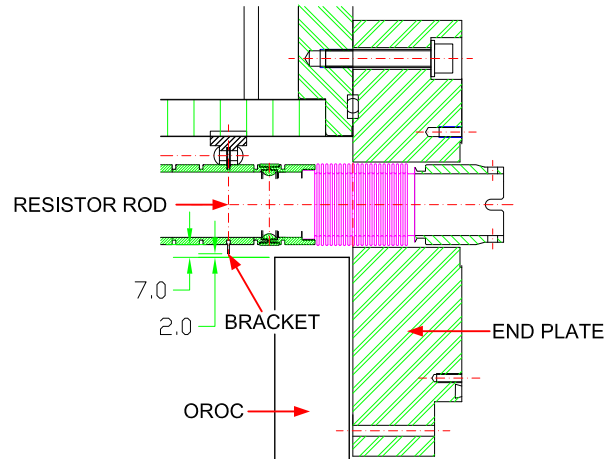


Figure 2.5: Side view of the clearance between the OROC and the rod bracket.

183 2.4 Last resistor and skirt

184 The field cage has provisions for matching the drift field at the interface between the drift volume and the
 185 readout chambers. On one hand, the resistor chain in the voltage dividers are terminated on the ground
 186 side by a last, external resistor. The value of this resistor is tuned such that the drift field matches the
 187 ground equipotential plane defined at the wire chambers. The potential of the gating grid is then fine-
 188 tuned to minimise field distortions in this region, resulting in a potential of some -70 V . On the other
 189 hand, there is a gap of a few cm between the outer side of the OROCs and the outer field cage, where
 190 the ground defined by the endplates would produce sizeable field distortions. In order to avoid this, a
 191 so-called skirt electrode is placed in this gap, as illustrated in Fig. 2.6.

192 In the case of the upgraded TPC, the potential on the GEM electrode facing the drift volume will amount
 193 to $3 - 4\text{ kV}$, i.e. 50 times higher than with wire chambers. This means that the skirt electrode will be set
 194 to a comparable potential. For the tuning of the potential of the last strip via the last resistor, though, an
 195 extra power supply to provide the necessary voltage while allowing to sink the current across the voltage
 196 dividers will be necessary.

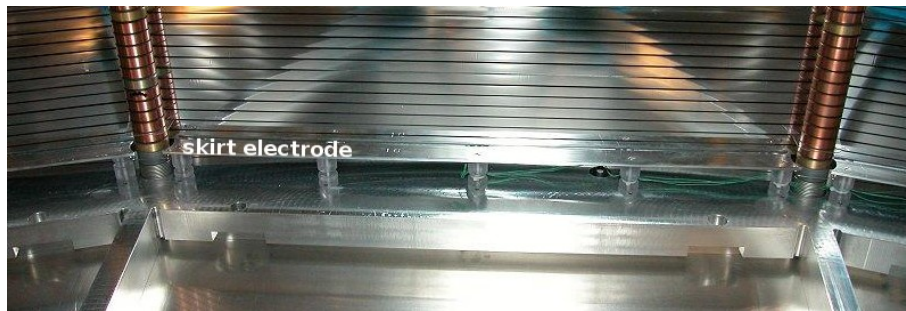


Figure 2.6: Detail of the ground side of the outer field cage showing the skirt electrodes elevated from the endplate in order to homogenize the electric field in the gap between OROCs and field cage.

197 2.5 Service Support Wheel

198 The Service Support Wheels (SSWs) are installed in front of, and mechanically decoupled from, the
 199 endplates. Their function is to hold the Front-End Cards (FECs) and their cooling panels and associated
 200 services. Currently, each SSW supports $2,800\text{ kg}$ of weight. The FECs are connected to the pad connec-
 201 tors at the chambers via flexible cables. The low voltage to the FECs is supplied via bus bars installed in
 202 the spokes of the SSW. The wheels themselves can be reused for the upgraded detector, but the frames
 203 that hold the FECs may have to be replaced if new pad planes or FECs result in a different configuration

204 of the readout partitions. The 18 cutouts of the SSW are finally covered by flat cooling panels in order
205 to thermally isolate the endplates from the surrounding environment.

206 **2.6 Gliders and I-bars**

207 The TPC is inserted into and extracted from its position in the space-frame of the experiment by gliding
208 it on two rails with four pairs of teflon gliders installed on opposite sides, front and rear, on the endplate
209 and on the SSW. The relative position of these gliders is monitored at all times during gliding operations.
210 Finally, in order to keep the two field cage vessels well aligned, a set of so-called I-bars are used to push
211 or pull the set of inner cylinders against the outer set. A view of the TPC with SSW, I-bars and gliders
212 on the rails is shown in Fig. 2.7.

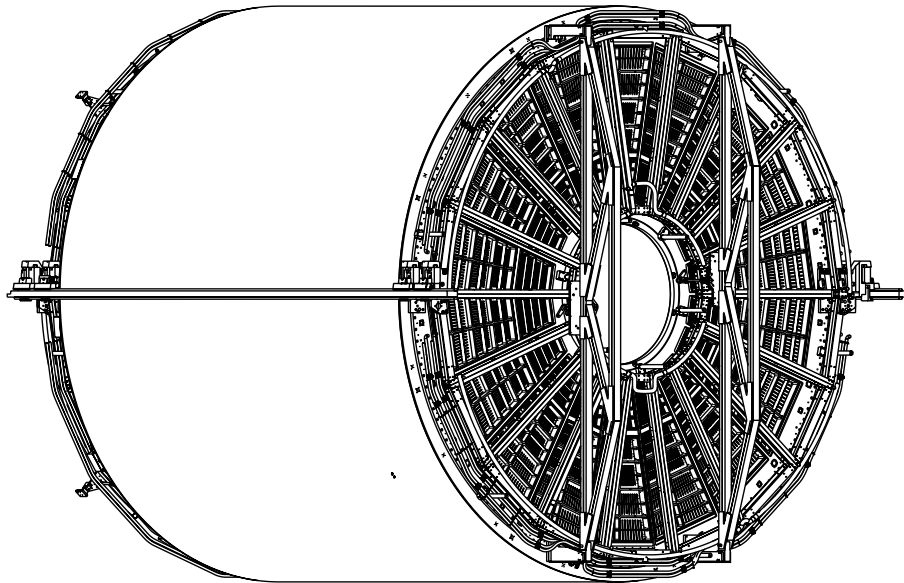


Figure 2.7: Overall view of the full TPC with SSW, I-bars and rails.

213 **2.7 Gas system**

214 The gas system is a closed-loop system where most of the gas is recirculated through the detector at
215 about $15\text{ m}^3/\text{h}$ with a regulated compressor module. The pressure in the TPC relative to atmospheric
216 is kept constant with better than 0.1 mbar precision. Oxygen and water are removed from the gas with
217 cartridges filled with a copper catalyzer. Some 50 l/h of mixed gas is continuously added to the system.
218 A small amount of gas is exhausted through an analysis line which provides a measurement of the O_2
219 and H_2O contents, as well as the gas composition. Periodic samples are taken to analyze the gas with
220 a gas chromatograph. The excess gas is exhausted through a regulated flowmeter. A high-pressure gas
221 storage is used as a buffer to accumulate or release gas such that the system can absorb atmospheric
222 fluctuations without interruptions. The system, schematically shown in Fig. 2.8, is arranged in functional
223 modules distributed on the surface, in the shaft, and in the cavern. A PLC¹ controls the system and a
224 SCADA² system provides a suitable user interface. The mixer unit is designed to mix up to three gases.
225 Default gases are Ne, CO_2 , and N_2 , but the mixer could inject Ar and CF_4 in the desired proportions
226 by simply recalibrating the mass flow controllers for these gases. In the case of neon as noble gas, a

¹Programmable Logic Controller (PLC)

²Supervisory Control and Data Acquisition (SCADA)

227 filling procedure where CO₂ is trapped in molecular sieve cartridges minimizes wasting of neon during
228 this operation. The technique does not work for argon, which is however a low cost gas. In summary, no
229 significant hardware nor software modifications are needed in the gas system for any foreseen scenario
230 for the upgraded TPC.

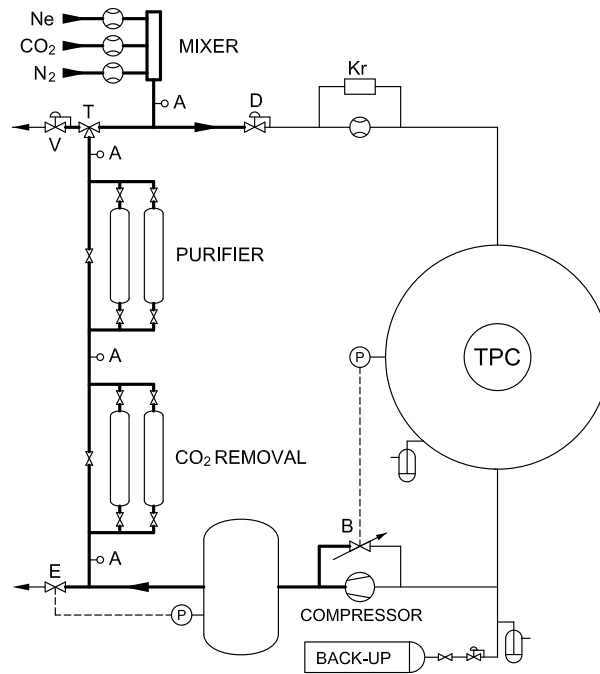


Figure 2.8: Schematic diagram of the TPC gas system.

231 **Chapter 3**

232 **Gas choice**

233 The current TPC, which employs MWPCs as readout chambers, uses Ne-CO₂ (90-10) as operating gas
 234 mixture. The addition of 5% N₂ has also been successfully tried out. The transport properties of these
 235 two mixtures, shown in Fig. 3.1, are very similar, while the stability against glow discharge is improved
 236 in the case of the mixture containing N₂. At the high rates foreseen for RUN 2, 10 kHz Pb-Pb, sustained
 237 glow discharges may originate at the cathode wires, which lead to instabilities of the current chambers
 238 in Ne-CO₂ (90-10). Adding the N₂ back into the mixture would be beneficial to this end; however the
 239 replacement of the Ne by Ar is a more drastic solution to glow discharge problems in MWPCs. Detailed
 240 simulations have shown that, with Ar-CO₂ (90-10), similar resolutions in momentum and dE/dx can be
 241 achieved as in Ne mixtures. With a triggered gating grid, space charge distortions remain at the level
 242 of 1 cm with this gas, at a slight reduction of the event rate to tape. An Ar-CO₂ (90-10) mixture will
 243 therefore be used in RUN 2.

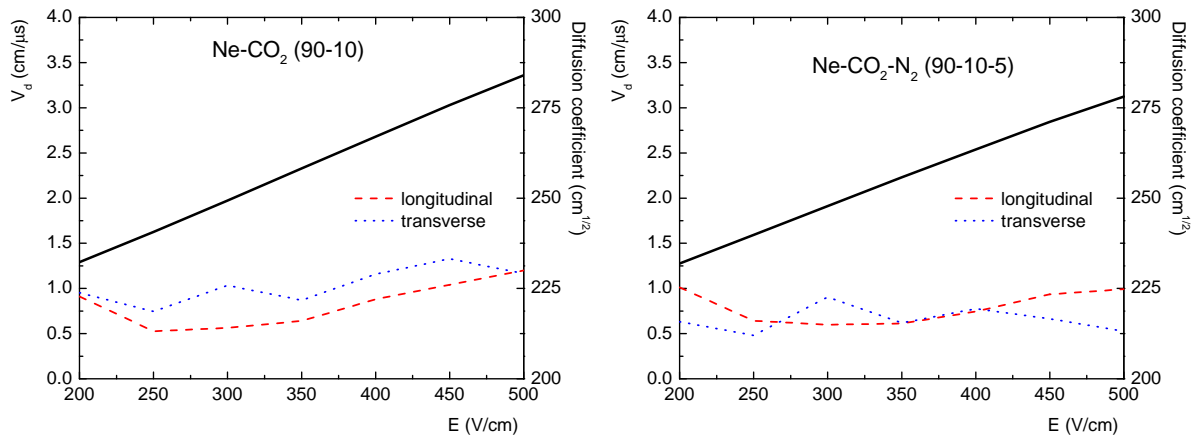


Figure 3.1: Drift velocity and diffusion at moderate electric fields. (Left) Ne-CO₂ (90-10). (Right) Ne-CO₂-N₂ (90-10-5).

244 The space charge distortions expected in the upgrade scenario are an important criterium in the gas
 245 choice for RUN 3. An example of the distortions calculated for a few candidate gas mixtures is shown in
 246 Fig. 3.2. The mobility of Ar⁺ ions in Ar is 1.52 cm²V⁻¹s⁻¹, about three times lower than that of Ne⁺
 247 ions in Ne (4.08 cm²V⁻¹s⁻¹). We disregard here the effect of drifting CO₂⁺ ions in these mixtures. Since
 248 the ion backflow is similar for these two noble gases (see Sec. 5.1.3), the different mobilities result in
 249 larger space-charge distortions in argon, even at a factor of 2 lower gain gain.

250 Admixtures of CO₂ or CF₄ to neon are attractive for the upgraded TPC. Both perform similarly in terms
 251 of space-point distortions. Due to the differences in the $\omega\tau$ factor, CO₂ performs better in $r\phi$, but CF₄
 252 does better in r . Of course CF₄, which provides a very high drift velocity and thus results in a reduced

253 event pileup, is still to be thoroughly validated for compatibility with all materials of the detector and the
 254 gas system, before it could be regarded as a suitable operating gas.

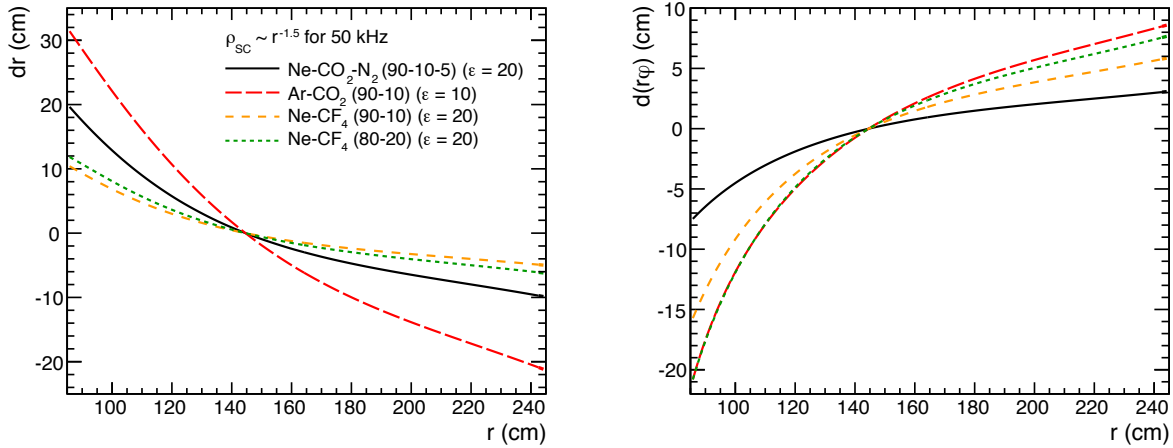


Figure 3.2: Radial and azimuthal distortions as a function of r calculated for four gas mixtures in the upgrade scenario at $z = 0$. ε is defined in Eq. (4.2).

255 In the anticipated configuration of our GEM system rather large transfer fields are used. However, at
 256 fields around 4 kV/cm amplification starts in Ne-CO₂, as shown in Fig. 3.3, and this in turn negatively
 257 affects the ion backflow performance. This disadvantage adds to the instability issue of the Ne-CO₂
 258 mixture discussed above. An increased concentration of CO₂ rapidly decreases the drift velocity unless
 259 the field cage voltage is increased beyond its certified limits. The addition of N₂ alleviates both issues
 260 as shown in the figure and explained in [1]. The base gas mixture is therefore Ne-CO₂-N₂ (90-10-5),
 261 although Ar mixtures are not excluded.

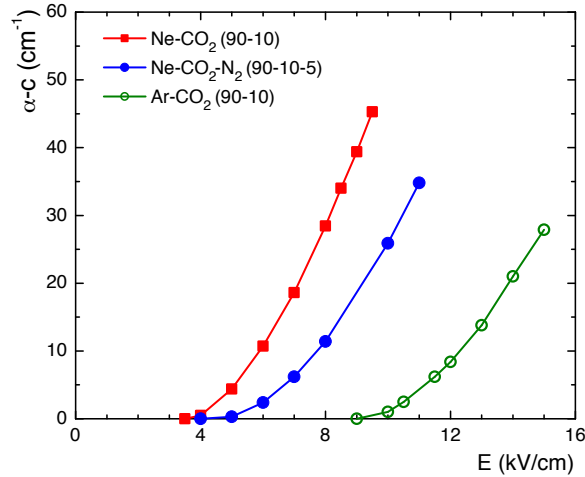


Figure 3.3: Calculation of the difference between the Townsend and the attachment coefficients in Ne-CO₂ (90-10), Ne-CO₂-N₂ (90-10-5) and Ar-CO₂ (90-10) mixtures as a function of the electric field. The onset of gain is shifted upwards by 1 kV/cm with the admixture of N₂ to the neon mixture. The onset for argon is substantially further away.

262 Fast mixtures, like Ne-CF₄ (90-10) or (80-20), as shown in Fig. 3.4, are to be considered if a compre-
 263 hensive material validation program is completed successfully. A set of basic properties of relevant gas
 264 mixtures is summarized in Tab. 3.1.

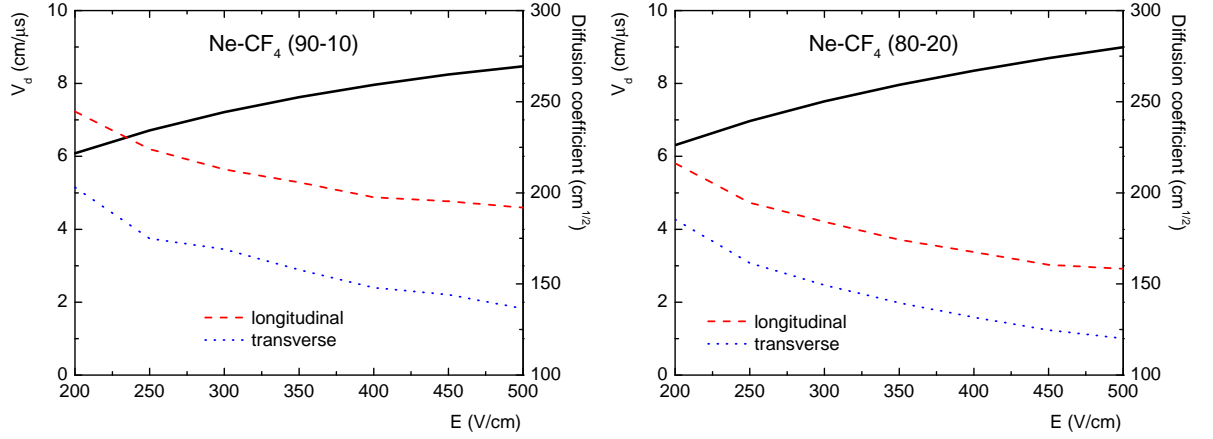


Figure 3.4: Drift velocity and diffusion at moderate electric fields. (Left) Ne-CF₄ (90-10). (Right) Ne-CF₄ (80-20).

Gas	v_d (cm/ μ s)	D_L ($\sqrt{\text{cm}}$)	D_T ($\sqrt{\text{cm}}$)	$\omega\tau$	W_i (eV)	N_p (cm ⁻¹)	N_t (cm ⁻¹)
Ne-CO ₂ -N ₂ (90-10-5)	2.58	0.0221	0.0209	0.32	37.3	14.0	36.1
Ne-CO ₂ (90-10)	2.73	0.0231	0.0208	0.34	38.1	13.3	36.8
Ne-CF ₄ (90-10)	8.02	0.0152	0.0131	1.77	37.7	15.7	42.7
Ne-CF ₄ (80-20)	8.41	0.0131	0.0111	1.84	37.3	20.5	54.1
Ar-CO ₂ (90-10)	3.31	0.0262	0.0221	0.43	28.8	26.4	74.8
Ar-CF ₄ (90-10)	10.77	0.0144	0.0123	2.07	28.8	28.9	83.1

Table 3.1: Some properties of various gas mixtures which could be used in modern TPCs: drift velocity v_d and longitudinal and transverse diffusion coefficients D_L and D_T , evaluated at 400 V/cm; $\omega\tau$ factor, effective ionization energy W_i , number of primary electrons per MIP N_p , and total number of electrons per MIP N_t .

Chapter 4

Readout chambers

4.1 Introduction

An interaction rate of $R_{\text{int}} = 50 \text{ kHz}$ for minimum bias Pb-Pb interactions is expected after the luminosity upgrade of the LHC during LS2 [1]. At these rates particle tracks from $N_{\text{pileup}} = 5$ events on average will be superimposed in the drift volume of the TPC at any given time: $N_{\text{pileup}} = R_{\text{int}} \times t_d \approx 50 \text{ kHz} \times 100 \mu\text{s} = 5$, where t_d is the maximum electron drift time in the TPC¹. A continuous, untriggered readout of the TPC is the obvious mode of operation in such a scenario with overlapping events, precluding the use of a gating grid. In the absence of the gating grid, however, ions created in the multiplication region must be prevented from drifting back into the drift volume by other means.

This will be achieved by using Gas Electron Multiplier (GEM) [2] foils as charge amplifier instead of conventional MWPCs. The GEM consists of a $50 \mu\text{m}$ thin insulating Polyimide foil with Cu-coated surfaces, typically $2 - 5 \mu\text{m}$ thick. The foil is perforated by photo-lithographic processing, forming a dense, regular pattern of (double-conical) holes. In the standard geometry the holes have an inner diameter of $\sim 50 \mu\text{m}$, an outer diameter of $\sim 70 \mu\text{m}$, and a pitch of $140 \mu\text{m}$. Other geometries, e.g. with a larger pitch and thus a smaller optical transparency, are considered for the ALICE TPC readout chambers. Figure 4.1 shows an electron microscope photograph of a standard GEM foil, Fig. 4.2 displays an optical microscope photograph of a foil with a larger pitch of $280 \mu\text{m}$.

The small dimensions of the amplification structures lead to very large electric field strengths $\mathcal{O}(50 \text{ kV/cm})$, sufficient for avalanche creation, inside the holes of the GEM foil when a moderate voltage difference of typically $200 - 400 \text{ V}$ (depending on the gas) is applied between the metal layers.

The dynamics of charge movement and avalanche creation inside the GEM holes is complicated. Figure 4.3 shows a simulation performed with the Garfield / Magboltz [3] packages, illustrating the suppression of ion backflow from the amplification region. In this simulation the avalanche is started by two electrons, that are guided into the GEM hole by the drift field. The ions created in the avalanches closely follow the electric field lines because of their much smaller diffusion. Most of the ions are collected on the top side of the GEM foil, because the field inside the GEM hole is much higher than the field above the hole. Only a few ions drift back into the drift volume. The extraction of avalanche electrons from the hole proceeds more efficiently by applying a higher transfer field below the GEM.

The electrons can then be transferred to another amplification stage or collected at the anode. Typically 3 or 4 GEM foils are combined in a stack, leading to effective gains (see Eq. (4.1)) of the order of $10^3 - 10^4$ and at the same time guaranteeing a stable operation without the occurrence of discharges [5].

The effective gain of a GEM detector is determined by measuring the current at the readout anode I_{anode}

¹A discussion of pileup and occupancies is given in Sec. 6.2.

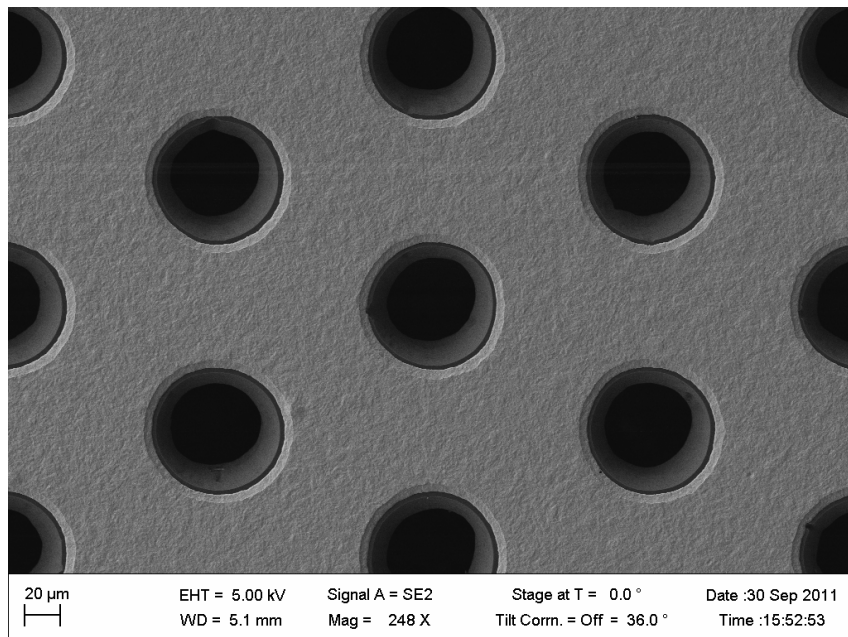


Figure 4.1: Electron microscope photograph of standard GEM foil with hole pitch $140\ \mu\text{m}$.

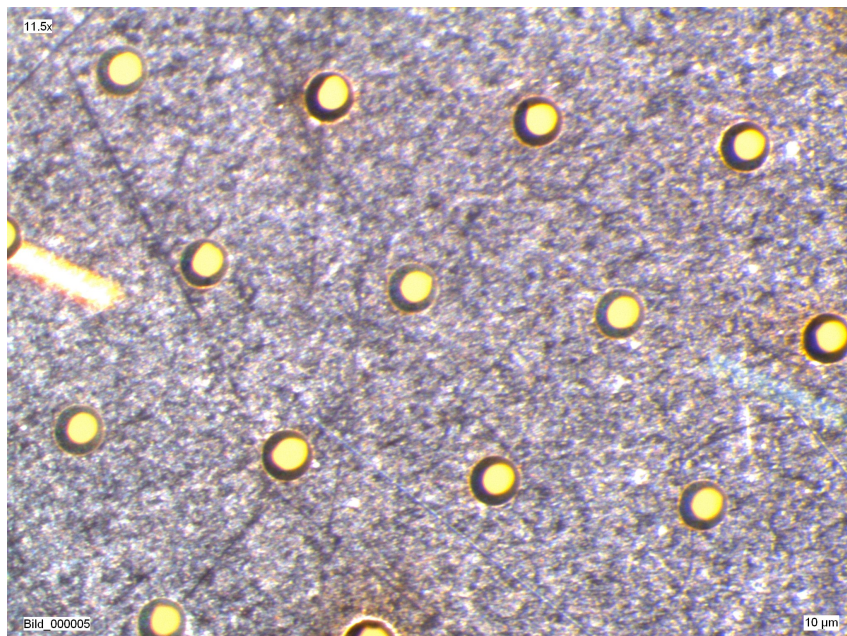


Figure 4.2: Optical microscope photograph of large pitch GEM foil with hole pitch $280\ \mu\text{m}$. Note that the length scale is different from Fig. 4.1.

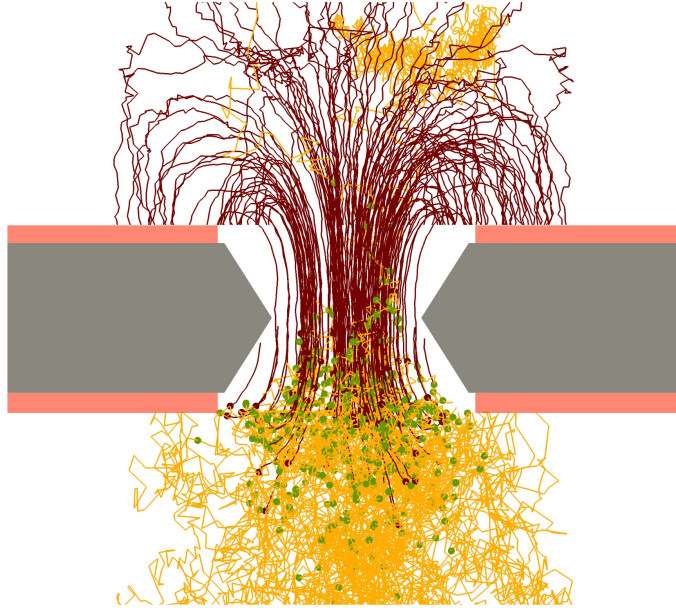


Figure 4.3: Garfield / Magboltz simulation of charge dynamics for electrons (two in this simulation) entering into a GEM hole [4]. Electron drift paths are shown as light lines, ion drift paths as dark lines. Dots mark places where ionization (multiplication) processes have occurred. The paths have been projected onto the cross section plane.

298 for a given rate R of incident X-rays, each X-ray conversion producing N_{ion} ionization electrons:

$$G_{\text{eff}} = \frac{I_{\text{anode}}}{eN_{\text{ion}}R} \quad (4.1)$$

299 Defined in this way, Eq. (4.1) corresponds to the gain seen by the readout, and takes into account charge
300 losses in the GEM structures.

301 We define the ion backflow as² the ratio of cathode to anode current,

$$IB = \frac{I_{\text{cathode}}}{I_{\text{anode}}} = \frac{1 + \varepsilon}{G_{\text{eff}}} \quad (4.2)$$

302 with ε being the number of ions drifting back into the drift region from the amplification region per
303 incoming electron. Note that IB also includes a contribution from ions created during the ionization
304 process. Ion backflow values of $IB = 0.25\%$ have been reached experimentally in conditions which were
305 rather different from the ones in ALICE, i.e. in a high magnetic field of 4T in an Ar-CH₄-CO₂ (93-5-2)
306 mixture with a drift field of 200 V/cm [6].

307 Detectors based on GEM amplification were pioneered by the COMPASS experiment at CERN [7–10],
308 and are now routinely used in several high-rate particle physics experiments like LHCb [11], PHENIX [12],
309 and TOTEM [13]. New applications include the use of GEM-based detectors in KLOE-2 [14] and
310 CMS [15].

311 The usage of GEM detectors as readout chambers in the ALICE TPC, however, is a new domain of
312 application of these detectors with regard to several aspects:

- 313 – The ion backflow from the detector must be carefully optimized. A value of 1% is necessary in
314 order to achieve the goal of limiting drift field distortions due to space charge to well below 10 cm

²There appear different definitions of the term *ion backflow* in the literature. We choose this definition since it can be easily measured.

in most of the drift volume. This value has been established in the default gas mixture Ne-CO₂-N₂ (90-10-5). At a gain of 2000, which is needed for a signal-to-noise-ratio of 20, this corresponds to $\epsilon = 20$, i.e. 20 ions flowing back into the drift region per incoming electron. As is shown in Sec. 5.1.3, a further reduction of the ion backflow by a factor of 2–3 is likely to be achieved in the near future. This will immediately ease the task of distortion corrections. Thus, R&D on further optimizing the ion backflow is presently underway and will continue even after the completion of this TDR.

- Special attention must be given to a high electron collection efficiency of the GEM system, in particular when the operational conditions are optimized for small ion backflow (see Sec. 5.1.3). Finite electron transparency, in particular in the first layer, leads to a degradation of the local energy resolution due to a loss of primary electrons, that will eventually compromise the dE/dx performance of the detector. Simulations have shown that a local energy resolution equivalent to 12 % at 5.9 keV is sufficient to preserve the present dE/dx resolution of the TPC (see Sec. 7.2.3).
- For a Ne-based gas mixture the dependence of the Townsend coefficient on the electric field is steeper compared to the standard Ar-based mixtures, with which most GEM detectors have been operated until now. In order to be able to apply the very asymmetric fields above and below the GEM, required for maximum ion backflow suppression, without entering a regime of avalanche multiplication in the gaps between GEM foils, a small admixture of N₂ is added to the detector gas (see Chap. 3).
- At a rate of primary ionization clusters of 100kHz/cm² for an IROC at a radius of $r = 85$ cm (for $dN_{\text{ch}}/d\eta = 500$) the current density at the readout anode at a gain of 2000 is ~ 1 nC/(cm²s), assuming that all primary particles are MIPs. With a safety factor of 10, which takes into account the contribution of highly ionizing particles, background, secondaries, etc., the upper limit for the rate and the current density is 10kHz/mm² and 0.1 nC/(mm²s), respectively. Both values are far below experimentally verified limits of rate capability (> 100 kHz/mm²) for GEM detectors [9, 16]. Nevertheless, the long-term operation in ALICE requires careful testing of all materials used in the detector construction concerning their aging properties.

In the following we describe the concept of the GEM-based readout chambers and show the design choices that are consistent with the above considerations.

4.2 Mechanical structure

The readout chambers are installed at both end plates of the cylindrical gas vessel of the TPC. The two readout planes are azimuthally segmented into 18 sectors of trapezoidal shape, each sector covering 20°, as shown in Fig. A.2. Each sector is further divided into two different chambers, called Inner Readout Chambers (IROCs) and Outer Readout Chambers (OROCs). The dimensions of the ALICE readout chambers are shown in Fig. 4.4. These dimensions, as well as the segmentation, are taken over from the original ALICE TPC design and will remain unchanged after the upgrade.

Figure 4.5 shows an exploded view of a GEM IROC. It consists of the following components:

- a trapezoidal aluminum frame (*alubody*),
- a support plate made of fiberglass (*strong back*),
- the pad plane (multilayer PCB) and
- the GEM stack including a cover electrode.

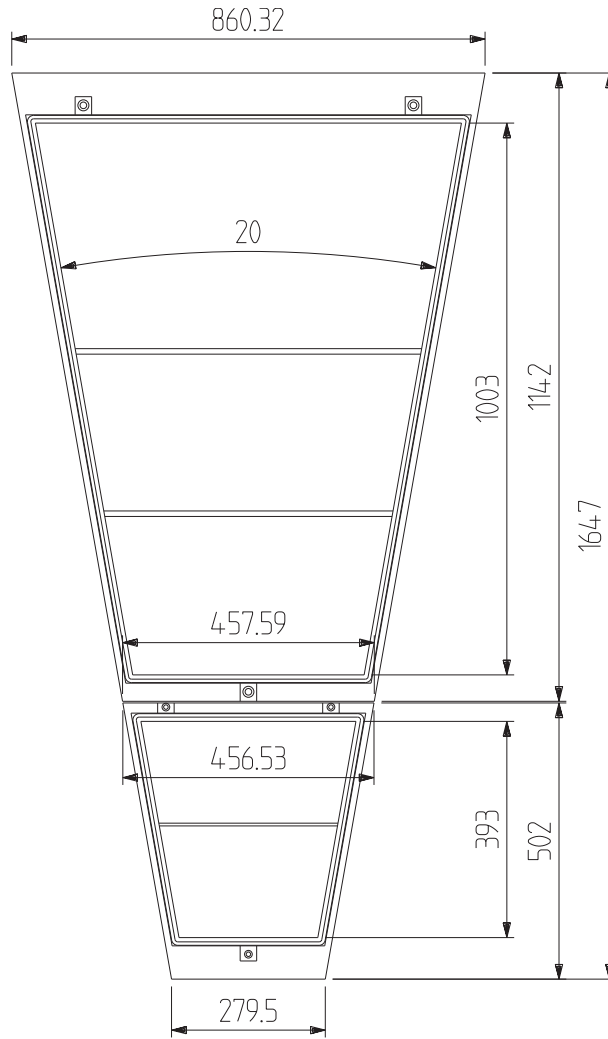


Figure 4.4: Dimensions (mm) of the ALICE TPC readout chambers.

356 The corresponding view of a GEM OROC is depicted in Fig. 4.6.

357 We intend to rebuild the complete readout chambers including the alubodies. This allows (i) to fully
 358 adapt the mechanics to the GEM amplification scheme, (ii) to rearrange the connector layout to the new
 359 front-end electronics and to optimize the accessibility of the front-end cards, and (iii) to start production
 360 and testing of the chambers well in advance of the end of LHC RUN 2.

361 The overall design of the alubodies will be taken over from the MWPC-based chambers. The mechanical
 362 stability of the chambers will be more than sufficient to prevent deformations due to gravitational forces
 363 and the tension on the GEM foils. Minor modifications will be introduced for the feedthroughs of the
 364 high-voltage (HV) supplies, the mounting of the boxes with the resistor chains for the HV, the cut-outs
 365 for connectors of the front-end cards, and the mounting of the GEM planes.

366 The pad plane consists of a single multi-layer PCB for the IROCs, and, for production reasons, between
 367 two and four PCBs for the OROCs. The final segmentation depends on the choice of number of readout
 368 channels per FEC. The size of the readout pads of the present TPC matches the expected occupancy
 369 during RUN 3 and will therefore be kept. Some reshuffling of pads and traces to connectors is needed
 370 in order to accommodate the GEM stacks and the new front-end cards. For improved stiffness and gas
 371 tightness, the pad plane with a thickness of 2 mm will be glued to a strong back plate of 3 mm thickness
 372 made of fiber-glass reinforced epoxy. This design has proven to provide extremely good gas tightness
 373 and stability in the original version of the readout chambers.

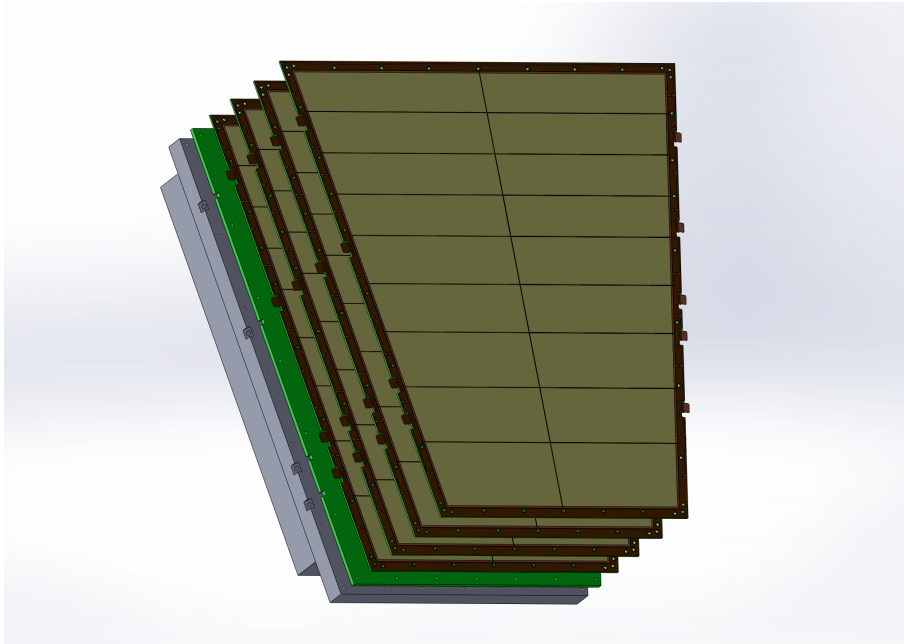


Figure 4.5: Exploded view of a GEM IROC.

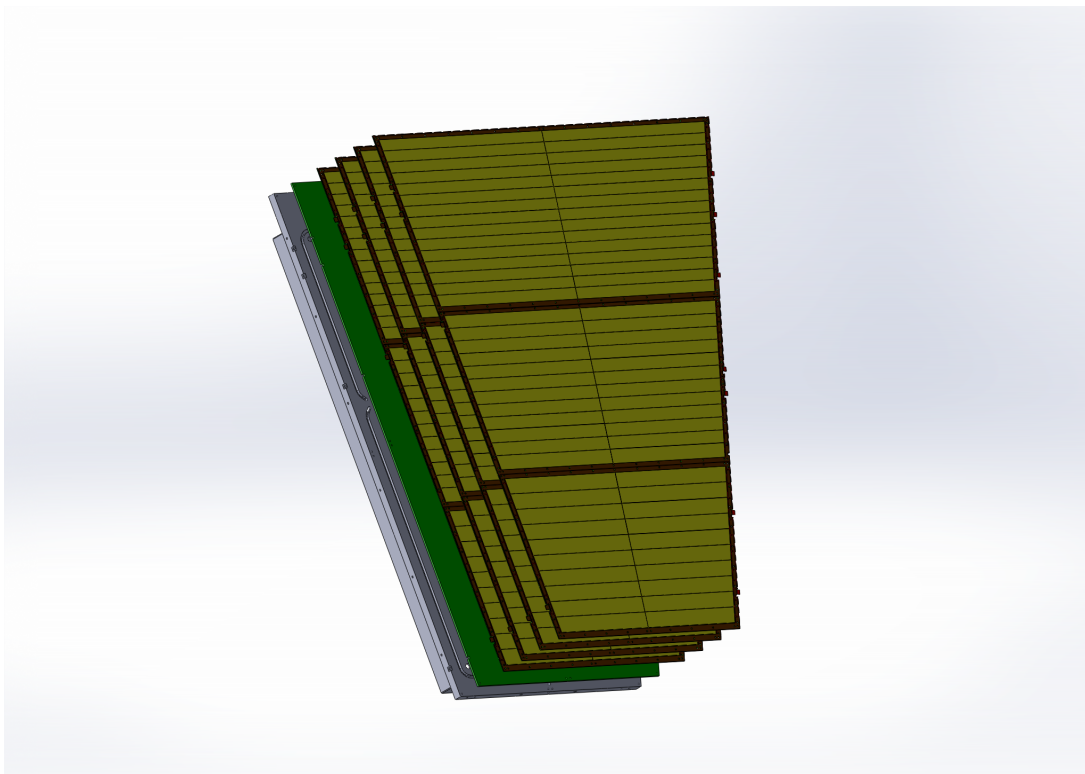


Figure 4.6: Exploded view of a GEM OROC.

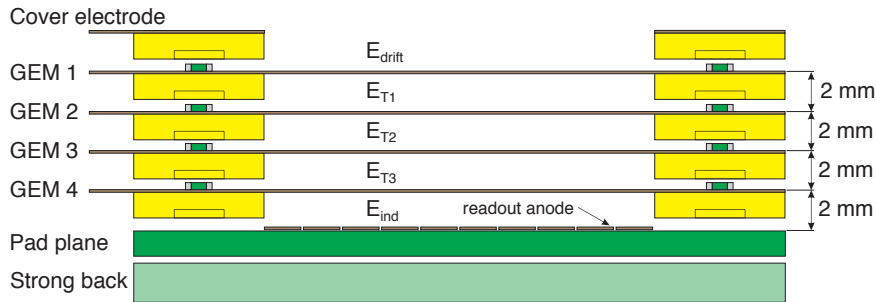


Figure 4.7: Schematic exploded cross section of the GEM stack. Each GEM foil is glued onto a 2 mm thick support frame defining the gap. The designations of the GEM foils and electric fields used in this TDR are also given. E_{drift} corresponds to the drift field, E_{T_i} denote the transfer fields between GEM foils, and E_{ind} the induction field between the fourth GEM and the pad plane. The readout anode (see Eq. (4.2)) is indicated as well. The drift cathode is defined by the drift electrode not shown on this schematic.

374 The technique for insertion and mounting the chambers into the TPC will be taken over from the original
 375 ALICE TPC (see Sec. 11). Special care has to be taken in order not to expose the GEM foils to dust
 376 during the mounting procedure.

377 4.3 GEM planes

378 4.3.1 General structure

379 The electrons created by ionizing particles traversing the active volume of the TPC drift towards the end
 380 plates, where they are amplified in order to induce a detectable signal in the readout pads. In the new
 381 readout chambers, the amplification will be provided by avalanche creation inside the GEM holes. In
 382 order to achieve the required gain and at the same time provide a sufficiently high suppression of back
 383 flowing ions, a stack of four GEM foils will be used for all chambers. A schematic drawing of a GEM
 384 stack is shown in Fig. 4.7.

385 The mechanical layout of the GEM stage follows a modular design wherever possible to allow pre-
 386 assembly and testing of individual components at every stage. The introduction of dead zones is kept at
 387 a minimum, so as not to deteriorate the resolution of the chambers.

388 The size of GEM foils needed for the ALICE IROC and OROC exceeds that of most of the currently
 389 operating GEM detectors. The conventional method of GEM foil patterning requires photo-lithographic
 390 processes based on two masks with identical hole patterns, placed on the two sides of the copper-coated
 391 base foil, and aligned with a precision of $1 \mu\text{m}$ with respect to each other in order for the holes to be
 392 perpendicular to the surface. These alignment requirements limit the maximum size for GEMs produced
 393 with this technique. Another important constraint is the size of the industrially available base material
 394 and of the machinery required for the processing, both being presently limited to a width of 600 mm.

395 The first limitation can be bypassed by employing a single-mask technique [17]. This technique has
 396 proven to deliver comparable results with respect to homogeneity and gain performance of the GEM-
 397 foils as the standard technique. A small decrease in gain by 25 % has been observed in comparison with
 398 a standard GEM at the same conditions, which can easily be compensated for by a slight increase of the
 399 operating voltage.

400 Large-size foils with single-mask GEM technique have been pioneered in the framework of R&D for the
 401 cylindrical GEM tracker of the KLOE-2 detector by the RD51 collaboration [18]. For the construction
 402 of the full-size KLOE-2 tracker, which has been completed recently [19], a total of 50 large-size single-
 403 mask foils with active areas of up to $430 \times 700 \text{ mm}^2$ have been produced at CERN. After thorough testing
 404 with QA criteria similar to the ones to be adapted for ALICE (see Sec. 4.7), only eight bad foils were

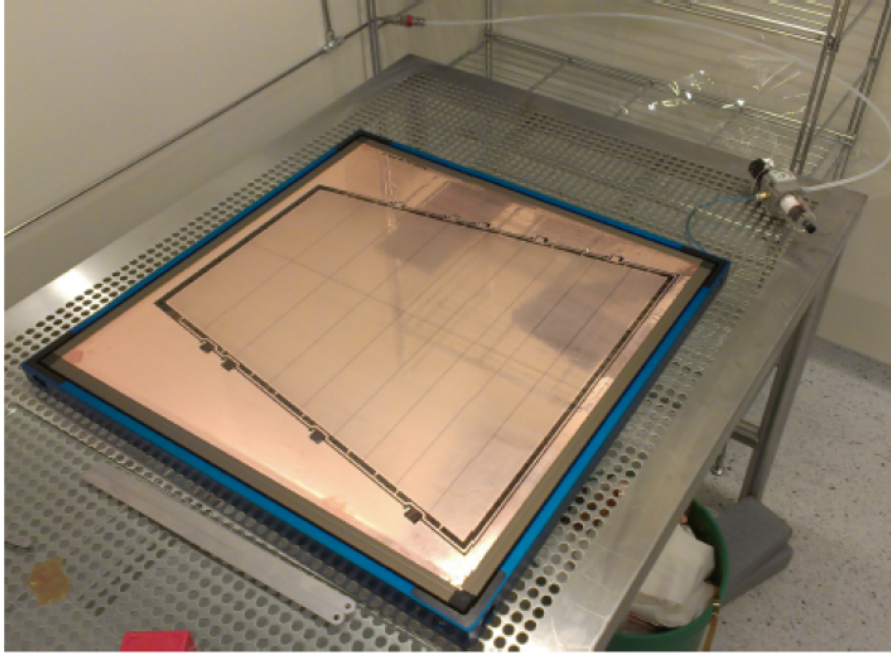


Figure 4.8: Photograph of an IROC GEM foil in the stretching frame.

405 identified. Most of the problems were related to an over-etching of the polyimide, a problem which,
 406 according to the CERN workshop, has been solved in the meantime. GEM foils with even larger active
 407 areas ($990 \times (220 - 455) \text{ mm}^2$) are now routinely being produced in the framework of developments for
 408 the CMS muon system [15, 20]. At the time of writing this TDR, six full-size triple-GEM detectors
 409 with single-mask GEM foils have been built by the CMS GEM collaboration. This collaboration also
 410 measured the uniformity of the gain of a final detector to be within 12–15 % (RMS). The GEM foils
 411 needed for the ALICE TPC³ are of a similar size. Hence the single-mask technique can be considered
 412 mature enough for application to the ALICE TPC.

413 In order to reduce the total charge stored in the GEM foil, one side of the foil is segmented into HV
 414 sectors with a surface area of approximately 100 cm^2 , as shown in Figs. 4.9 and 4.13. The inter-sector
 415 distances are reduced to $200 \mu\text{m}$. Each HV sector is powered separately through high-ohmic SMD⁴
 416 loading resistors soldered directly onto the foil and connected to a HV distribution line implemented on
 417 the boundary of the foil. This scheme has proven to reduce the probability of discharges propagating
 418 between GEM foils and from the last GEM foil to the readout circuit [5]. Figure 4.12 shows a detailed
 419 view of the segmented side of an IROC GEM foil with the loading resistors in place and the frame of the
 420 next GEM layer on top of it. The voltages to each GEM foil are supplied by two external HV sources,
 421 one for each side of the foil (see Sec. 4.4).

422 The GEM foils will be pre-stretched with a force of 10 N/cm on all four sides using a stretching technique
 423 developed at GSI and TUM, making use of a pneumatical method. A frame originally designed for the
 424 stretching of stencils for PCB assembly was modified to meet the stretching force needed for GEM foils.
 425 The system is shown in Fig. 4.8. The stretching force is applied by springs integrated in the frame. For
 426 mounting, the spring tension is released by the pneumatic system. When the pressure is taken away, the
 427 foils are tensioned.

428 The foils in the stretching frames are then positioned on a custom-made alignment plate for gluing of the
 429 support frames made of glass-fiber reinforced plastics. The width of the frames is chosen to be 10 mm
 430 to match the outer edges of the pad plane and for sufficient stability. The total thickness of the frames

³See Tab. 4.1

⁴Surface Mount Device (SMD)

431 is constrained by the distance between the layers in the stack of 2 mm. The frames also include a grid
 432 of very thin bridges of $\sim 400 \mu\text{m}$ thickness intersecting the active area of the detector, which serves as
 433 spacer in order to guarantee sufficiently small sagging of the foils due to electrostatic forces. The spacer
 434 grid is aligned with the HV sector boundaries of the GEM foils in order to minimize the dead area.

435 Four framed GEM foils are stacked on top of each other above the pad plane and fixed to it by non-
 436 metallic screws. Our prototype studies have shown that this can be achieved without wrinkles even for
 437 the trapezoidal shape of foils needed for ALICE (see Sec. 5.2.3). The top side of GEM 1 facing the drift
 438 electrode of the TPC is covered by one extra frame which is metallized on the top side (see Fig. 4.7). The
 439 potential applied to this cover electrode is adjusted to homogenize the electric field in the drift region
 440 above the first GEM.

441 4.3.2 Inner readout chambers

442 The first batches of large-area GEM foils for the ALICE IROC prototype (see Sec. 5.2) with a size of
 443 $500 \times 470 \text{ mm}^2$ were produced at CERN during the last year. The results are encouraging, although some
 444 problems have been identified related to the etching process and the storage of foils during transport.
 445 Measures have been taken to improve the hole uniformity across the active area. Quality assurance tests
 446 have been implemented and are being studied in order to identify GEM defects both at macroscopic
 447 and microscopic levels as early during the assembly stage as possible, and to avoid potential problems
 448 during the operation with Ne-based gas mixtures in advance (see Sec. 4.7 for a detailed discussion of QA
 449 procedures).

450 Figure 4.9 shows the top view of the design of an IROC GEM foil, including the segmentation into 18
 451 HV sectors, powered from both sides of the foil. Figure 4.10 shows a photograph of a prototype foil
 452 used in the first beam tests (see Sec. 5.2). Slight wrinkles observed at the edges of foils for the initial
 453 prototypes have been removed by adding more fixation screws around the edges.

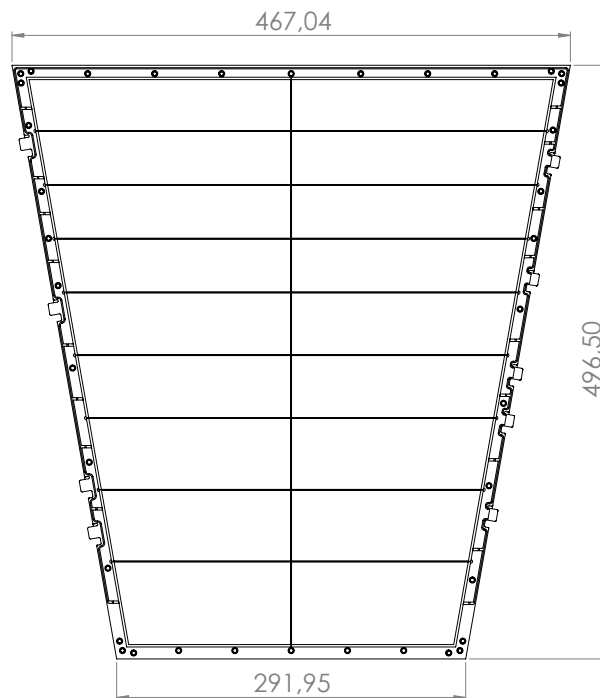


Figure 4.9: Dimensions of an IROC GEM foil.

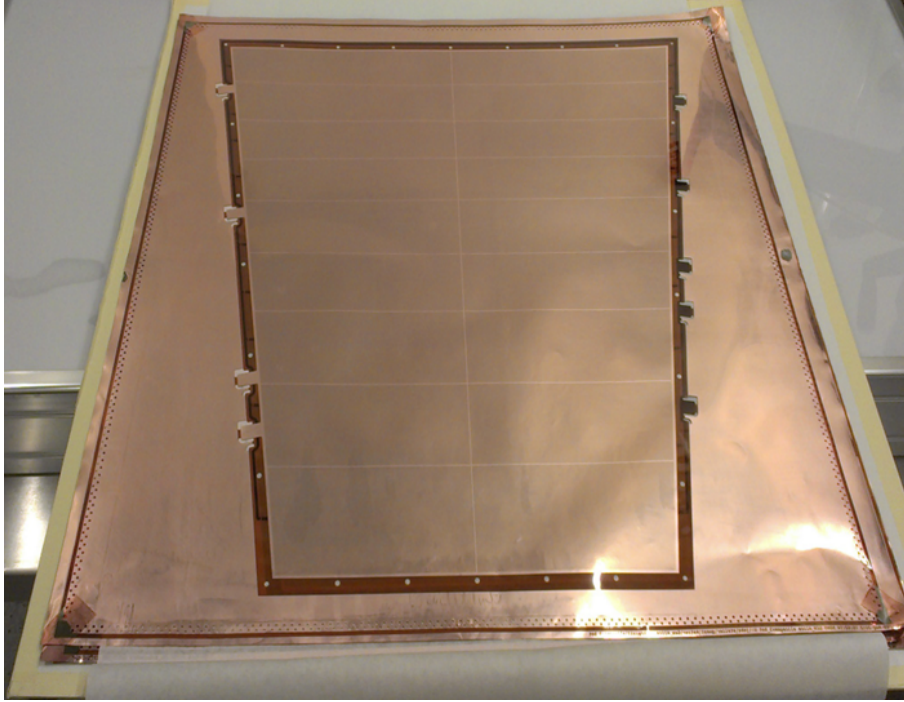


Figure 4.10: Photograph of an IROC GEM foil. The outer part is required for stretching and alignment and is cut away after the frame has been glued onto the foil.

4.3.3 Outer readout chambers

The size of an OROC as given in Fig. 4.4 would require GEM foils with a size of more than 1000mm length and 900mm width, which is beyond the limits of today's technology. The obvious solution is to segment the active area into three independent detector modules, tiled in radial direction. With this scenario we end up with foil sizes of $900 \times 400 \text{mm}^2$ or smaller. This is well in accordance with what has already been achieved at the CERN production site in recent developments for ALICE prototypes and other experiments [14, 15, 21]. Figure 4.13 shows the dimensions of the three modules for one ALICE OROC, each having a width of $\sim 360 \text{mm}$. The division in separate smaller detector modules is also expected to increase the yield of foils and facilitate their handling. For stability of the frames, however, a minimum width of 10mm is required. This will create two insensitive zones of 20mm width in radial direction in each OROC. Corresponding gaps are also foreseen in the pad layout, making room for fixation holes for the frames. The design of the foils allows to distribute the power to all HV sectors from two sides of the detector, without the need for HV lines between sectors. Thus, the gaps between HV sectors will also be as small as $200 \mu\text{m}$ as for the IROC case. The number of HV sectors is 20, 24, and 30 for the three detector modules.

Table 4.1 summarizes the parameters of the four different types of GEM foils needed for the upgraded TPC:

Detector	Size (cm^2)	Active area (cm^2)	No. of HV sectors	No. of foils
IROC	$54 \times 54 \text{cm}^2$	1678.0cm^2	18	144
OROC 1	$70 \times 54 \text{cm}^2$	1997.3cm^2	20	144
OROC 2	$77 \times 54 \text{cm}^2$	2240.5cm^2	24	144
OROC 3	$91 \times 54 \text{cm}^2$	2949.0cm^2	30	144

Table 4.1: Parameters of GEM foils for the ALICE TPC.

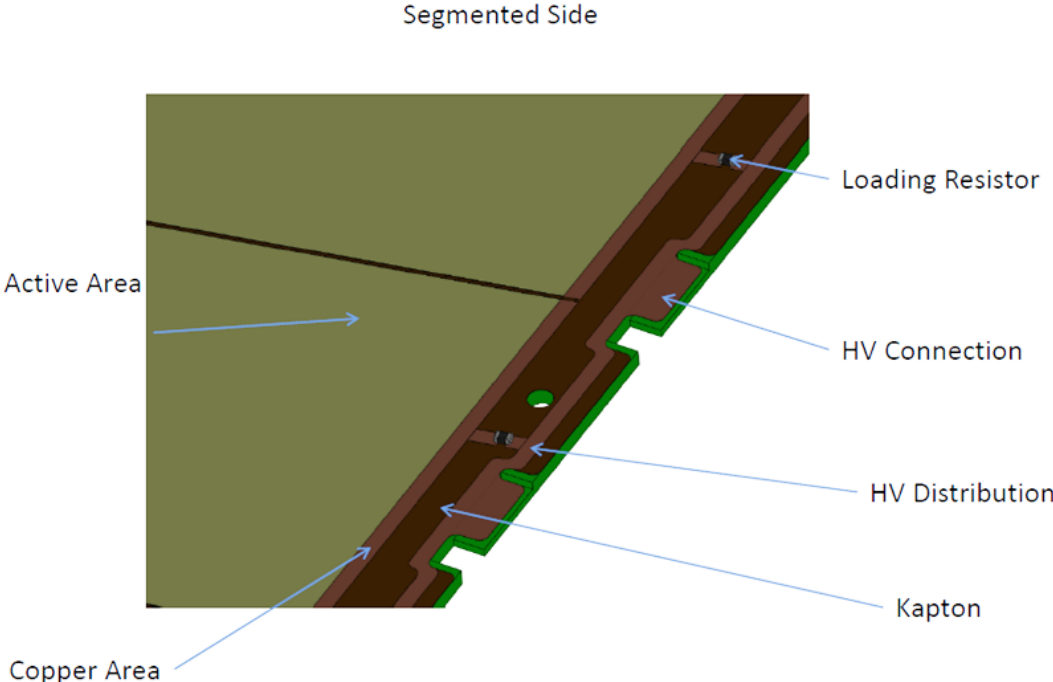


Figure 4.11: Detailed view of the HV distribution on the segmented side of an IROC GEM foil.

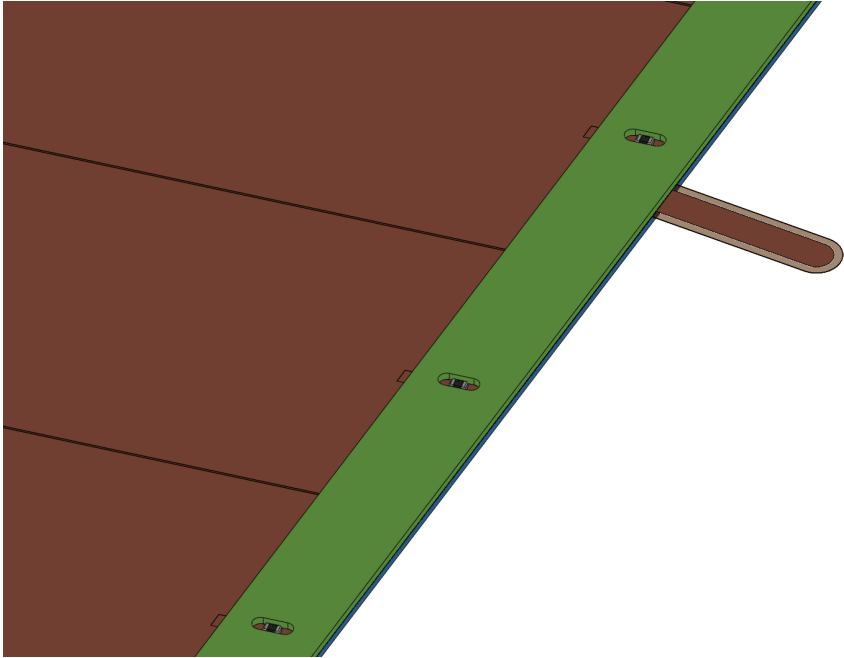


Figure 4.12: Bias resistors and HV supply of an IROC GEM foil.

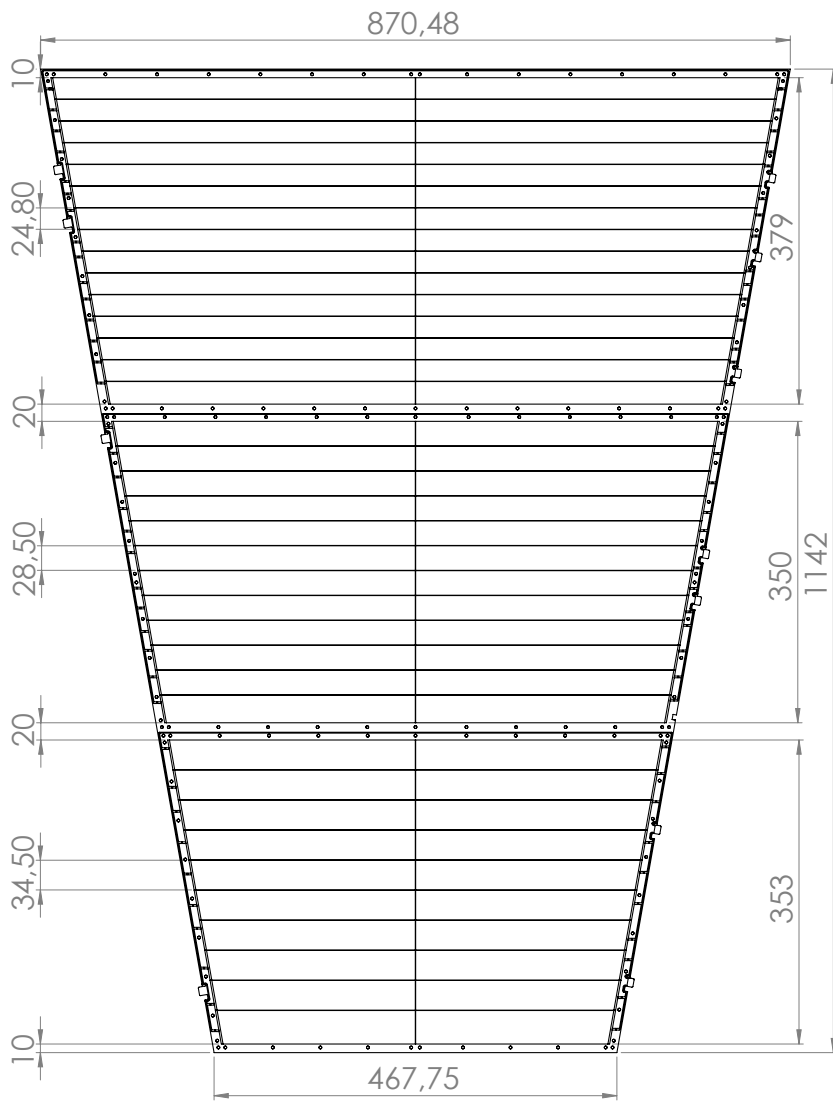


Figure 4.13: Dimensions (mm) of OROC GEM foils. The active area of the OROC is divided into three individual GEM stacks of different sizes.

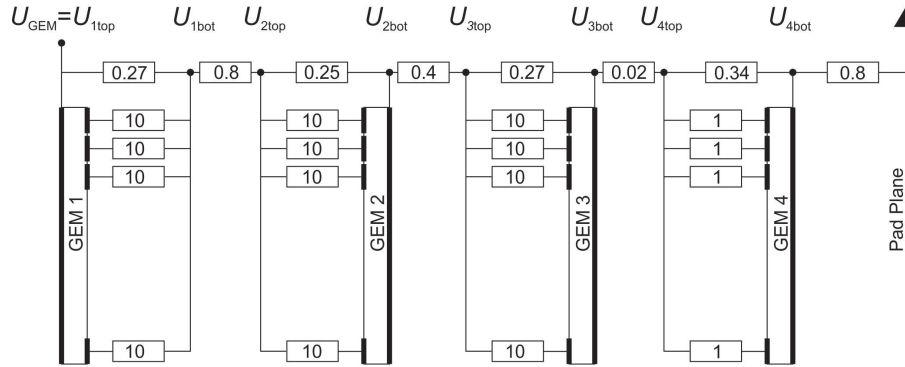


Figure 4.14: Schematics of the HV distribution scheme for a GEM detector module. The resistor values are given in units of $M\Omega$ and correspond to the field settings of Tab. 4.2.

471 4.4 High voltage supply

472 4.4.1 System overview

473 Extensive studies have shown that by reducing the capacitance between the two metal surfaces of a GEM
 474 foil the probability of discharges in a GEM detector can be significantly reduced [5]. To this end, one
 475 side of the GEM foil is segmented into individually powered HV sectors with a surface of $\sim 100 \text{ cm}^2$,
 476 limiting the amount of charge which is involved in case of occasional sparks.

477 The potential at the segmented side of the GEM foil is defined through large $\mathcal{O}(M\Omega)$ bias resistors. The
 478 potential at the unsegmented side is supplied directly, i.e. without bias resistor. This scheme has the
 479 advantage that in case of a temporary or permanent short circuit across a GEM foil in one or several HV
 480 sectors a voltage drop over the bias resistor occurs only for the affected sectors, while the rest of the foil
 481 remains fully operational without change of potential.

482 In a standard GEM detector, e.g. as used for the COMPASS experiment [7], the GEM foils are oriented
 483 such that the segmented sides face the drift electrode. In case of a discharge between the two sides of a
 484 GEM foil a voltage drop then occurs only on the segmented side, whereas the unsegmented side remains
 485 at its nominal potential. This prevents the propagation of the discharge to the next GEM foil or to the
 486 readout circuit.

487 In the case of the ALICE TPC, however, this scheme cannot be applied to the first GEM foil in the stack,
 488 because its potential on the side facing the drift electrode defines the drift field, which has to remain
 489 constant under all circumstances. Therefore, GEM 1 will be mounted with the unsegmented side facing
 490 the drift electrode, as shown in Fig. 4.14. In this way, its potential will be defined by the voltage U_{GEM}
 491 applied to the GEM stack. Considering the moderate voltage drop across GEM 1, this scheme is expected
 492 to be safe in terms of discharge propagation despite the inverted orientation of the foil.

493 The potentials at the GEM electrodes are defined by an external voltage divider network, which is housed
 494 in a box mounted to the backside of the alubodies. Therefore, nine HV-feedthroughs are needed for the
 495 four GEM foils and the cover electrode of each detector module. The values of the resistors in the
 496 network are chosen such that an effective gain of 2000 and a minimum ion backflow of around 0.5–1 %
 497 is provided. The voltage necessary to achieve a given gain will vary between modules due to variations
 498 of GEM foil parameters like e.g. hole diameters. In order to have a homogeneous drift field in the drift
 499 volume of the TPC, the potential at the top electrode of GEM 1 has to be the same for all modules. Thus,
 500 the potential difference across GEM 4 will be adjusted with the use of a remote controlled regulation
 501 circuit in parallel to the resistor defining the coarse potential drop.

502 Figure 4.15 (top panel) shows the absolute potentials at all four GEM foils of a stack during an event
 503 where a temporary short circuit (due to a discharge) occurs between the two electrodes of GEM 1 (upper

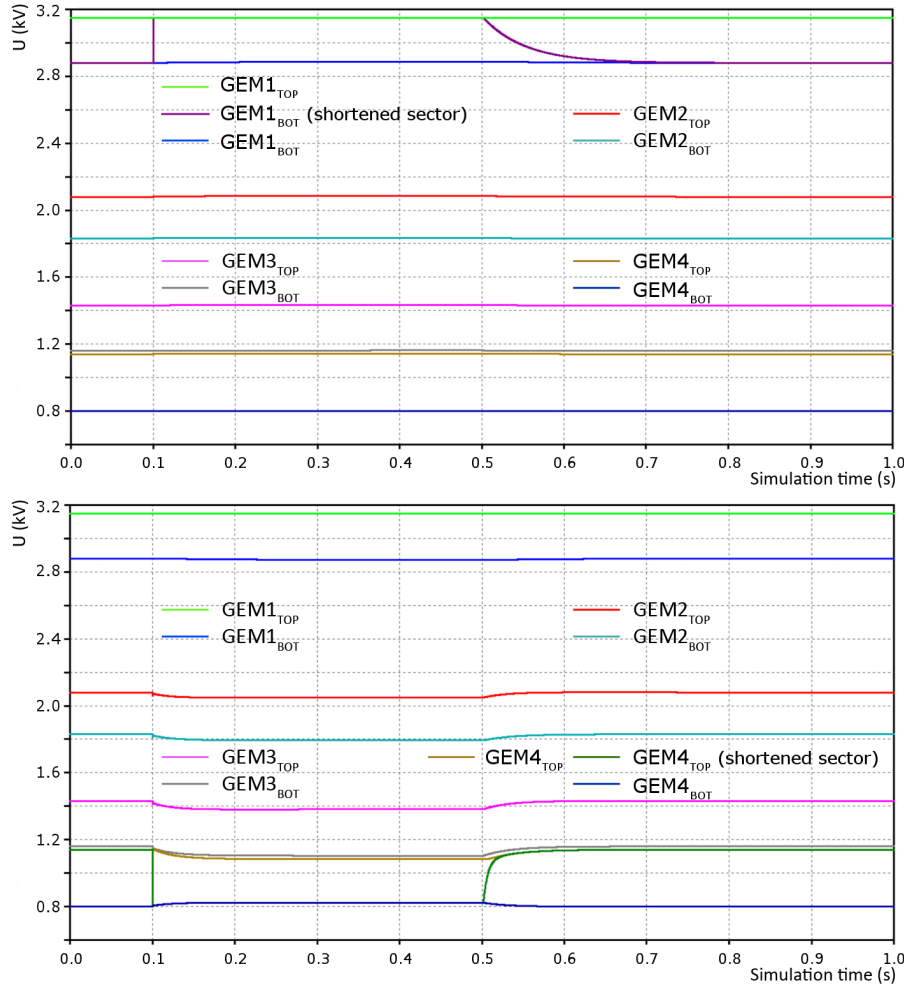


Figure 4.15: Potentials at all GEM electrodes of a quadruple GEM stack in case of a temporary short circuit between the two electrodes of GEM 1 (top panel) and GEM 4 (bottom panel), occurring at time 0.1 s and lasting until 0.5 s.

504 panel). Due to the bias resistors at the bottom side in case of GEM 1, the potential at the bottom side
 505 increases to the value of the top side (blue curve). The potential at the top side of GEM 1 does not
 506 change, as required for a constant drift field. Figure 4.15 (bottom panel) displays the analogous situation
 507 for GEM 4, which has the bias resistors on the top side. Here, the potential at the bottom side remains
 508 approximately constant in order to minimize the probability of the discharge propagating to the readout
 509 pads. The short circuits result in an increase of the overall current through the resistive divider of $1.4 \mu\text{A}$
 510 for the case of GEM 1, and of $25.4 \mu\text{A}$ for the case of GEM 4.

511 For online monitoring of space-charge effects it is essential to measure the currents on all GEM sectors
 512 with a high frequency of the order of ms and a precision of ~ 100 pA. The current measurement will be
 513 implemented in the HV divider box, and the data will be included in the TPC data stream (see Sec. 10.3).
 514 In this way, the data are readily available for online calibration. We also intend to include in the HV
 515 distribution boxes the possibility to send a pulse to the lowest GEM electrode, which then induces sig-
 516 nals on all electronic channels of a given module for calibration purposes. This will be accomplished
 517 by a coupling capacitor, which will however be disconnected during normal operation for reasons of
 518 operational safety. The voltage divider boxes have to be accessible from the outside in order to allow for
 519 access during a shutdown period of the experiment.

520 The high voltage system for the GEM stacks requires good voltage stability (ripple and noise ≤ 50 mV),
 521 high precision current measurement (resolution 1 nA), a fast trip mechanism, adjustable ramp speeds,
 522 full remote controllability and output voltages up to 6 kV at a maximum current of 1 A. While a single

523 HV channel is required for each IROC, the three OROC modules will be powered separately but syn-
 524 chronously for reasons of flexibility and stability. In total, therefore, 144 HV channels are needed for the
 525 GEM stacks, plus the same number for the cover electrodes.

526 4.4.2 Typical HV settings

527 In order to minimize the backflow of ions produced in the amplification region, the electric field con-
 528 figuration of the GEM stack as well as the sharing of the gain among the four amplification stages is
 529 optimized, thus bringing the ALICE TPC to a novel mode of operation of a GEM detector. Our measure-
 530 ments on small test detectors, reported in Sec. 5.1.3, show that an ion backflow of less than 1 % can be
 531 achieved with a quadruple GEM system at typical voltage settings shown in Tab. 4.2. At an effective gain
 532 of $2 \cdot 10^3$ in the GEM stack this corresponds to $\varepsilon < 20$ back-drifting ions per electron reaching the GEM
 533 stack. In order to achieve this result, a configuration was used, where the second and the third GEM foils
 534 have a pitch of $280 \mu\text{m}$ in contrast to the standard $70 \mu\text{m}$. Such large-pitch foils have a smaller optical
 535 transparency and therefore block ions more effectively. Strategies for an even further reduction of the
 536 ion backflow will be discussed in Sec. 9.

Drift Field		= 0.4 kV/cm
ΔU_{GEM1}	= $U_{1\text{top}} - U_{1\text{bot}}$	= 270 V
Transfer Field 1 (E_{T1})	= $(U_{1\text{bot}} - U_{2\text{top}})/0.2 \text{ cm}$	= 4.0 kV/cm
ΔU_{GEM2}	= $U_{2\text{top}} - U_{2\text{bot}}$	= 250 V
Transfer Field 2 (E_{T2})	= $(U_{2\text{bot}} - U_{3\text{top}})/0.2 \text{ cm}$	= 2.0 kV/cm
ΔU_{GEM3}	= $U_{3\text{top}} - U_{3\text{bot}}$	= 270 V
Transfer Field 3 (E_{T3})	= $(U_{3\text{bot}} - U_{4\text{top}})/0.2 \text{ cm}$	= 0.1 kV/cm
ΔU_{GEM4}	= $U_{4\text{top}} - U_{4\text{bot}}$	= 340 V
Collection/Induction Field	= $U_{4\text{bot}}/0.2 \text{ cm}$	= 4.0 kV/cm

Table 4.2: Typical high voltage settings for $IB < 1\%$ in a quadruple GEM in Ne-CO₂-N₂ (90-10-5) at an effective gain of $2 \cdot 10^3$.
 Note the high transfer field in the 1st and 2nd gap, whereas E_{T3} is very low.

537 4.5 Readout pad plane

538 The electrons emerging from the last GEM stage induce a fast signal on the readout pads. A very precise
 539 determination of the position in two-dimensional space of an arriving electron cluster can be achieved if
 540 the signal is distributed over several adjacent pads. In this case a suitable weighting of these signals will
 541 yield a resolution much better than the typical pad size. Charge sharing is achieved by the combination
 542 of several effects: spread of the drifting charge clouds due to diffusion and track inclination, intrinsic
 543 response width of the amplification stage due to diffusion in the GEM stack, finite hole distance, and
 544 signal induction in the induction gap. The fraction of the total charge in the avalanche which is induced
 545 on a given pad as a function of the distance between the center of the pad and the arrival point of the
 546 electron initiating the avalanche is described by the Pad Response Function (PRF). Amplification in a
 547 multi-GEM detector results in a narrower PRF compared to that of an MWPC, approximately equal to
 548 the width of the charge cloud emerging from the last GEM.

549 In a microscopic simulation of the TPC it was studied whether diffusion in the drift gas is sufficient
 550 to provide adequate charge sharing despite the smaller PRF, when GEM detectors are combined with
 551 the present readout pad geometry. For the following studies, single tracks with minimum energy loss,
 552 a flat distribution in polar angle θ and zero azimuthal inclination (i.e. very high momentum) have been
 553 used. It should be noted that a finite azimuthal inclination of tracks gives a dominant contribution to the
 554 point resolution, so that the differences between MWPC and GEM amplification shown in the following
 555 would be washed out. In this sense, the simulation results correspond to a worst-case scenario. A purely
 556 projective PRF was assumed for the GEM case, i.e. no broadening of the charge cloud in the GEM

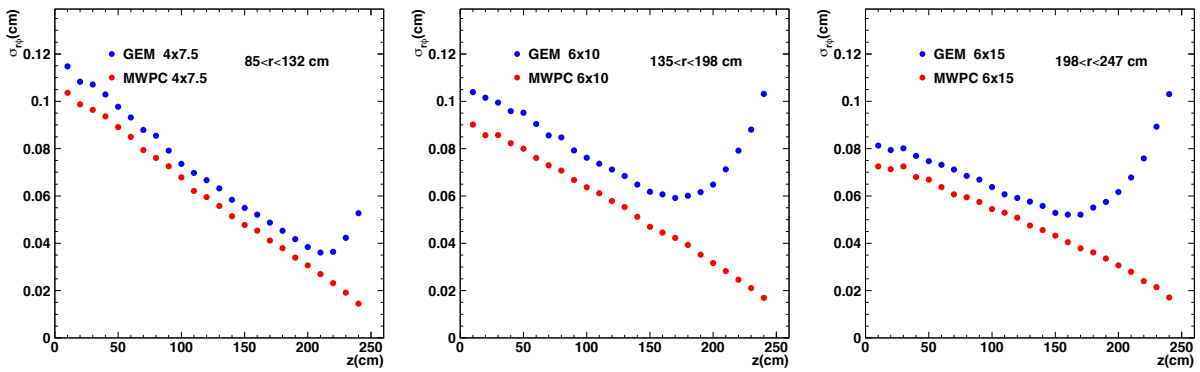


Figure 4.16: Point resolution in the magnetic bending plane $r\phi$ as a function of z for (blue) GEM and (red) MWPC amplification, with (left panel) $4 \times 7.5 \text{ mm}^2$, (middle panel) $6 \times 10 \text{ mm}^2$, and (right panel) $6 \times 15 \text{ mm}^2$ pads, respectively.

557 stack was taken into account. Exponential gain fluctuations for single electrons in the GEM stack were
 558 included. The average gain was adjusted such that a signal-to-noise ratio of 20 for the most probable
 559 value was reached. A Gaussian shaping with $\sigma = 100 \text{ ns}$ was applied and the resulting signal was sampled
 560 at 10 MHz.

561 Figure 4.16 shows the position resolution in the azimuthal $r\phi$ coordinate as a function of the z -coordinate
 562 of the cluster (the drift distance increases towards smaller values of z) for the three different pad sizes
 563 used in the current pad planes (see Tab. 4.3). For drift distances larger than about 30 cm for the small
 564 pads and 80 cm for the larger pads, the resolution achieved with GEM readout is only about 10% worse
 565 than for the MWPC-based readout, despite the large pad size compared to the GEM PRF. In this region,
 566 diffusion provides sufficient broadening of the charge cloud, such that clusters with more than a single
 567 pad dominate, as shown in Fig. 4.17.

568 For shorter drift distances, however, the resolution gradually deteriorates due to the appearance of single-
 569 pad clusters. As expected, the effect is strongest for the OROCs with large pads and $z > 180 \text{ cm}$. It should
 570 be noted, however, that short drift distances correspond partially to regions outside the nominal accep-
 571 tance of the ALICE central barrel ($|\eta| < 0.9$). This implies that, even with the present pad granular-
 572 ity, the position resolution with GEM detectors will decrease by no more than 20% for tracks in $|\eta| < 0.75$.

573 The effect of the different PRF for GEMs and MWPCs is also visible in Fig. 4.18, where the average size
 574 of clusters for the different pad sizes as a function of radius r is presented. Since clustering is performed
 575 in pad rows, i.e. a cluster extends over several pads within a given pad row and over several time bins,
 576 the cluster size is given in units of its area in $r\phi$ - z coordinate space, i.e.

$$A_{\text{cl}} = N_{\text{bins}} \times (\text{pad width}) \times (\text{time bin width}) . \quad (4.3)$$

577 Here, N_{bins} is the number of bins above threshold in pad and time units, pad width is 0.4 or 0.6 cm,
 578 and time bin width is given by the drift velocity divided by the sampling frequency. For all radii, the
 579 GEM readout gives an approximately 20% smaller cluster size than the MWPC readout, mainly in $r\phi$ -
 580 direction, due to the smaller PRF. Within a given pad size the cluster size increases with decreasing r
 581 because of the increasing average polar inclination of tracks, which extends the clusters in time direction.
 582 The steps in cluster size at $r \approx 140 \text{ cm}$ and 200 cm appear because of the increasing pad size, which,
 583 combined with the polar inclination of tracks, mostly affects the extension of a cluster in time.

584 On the one hand, the smaller cluster size with GEM readout reduces the occupancy of the detector.
 585 However, the larger number of single-pad clusters will make it more difficult to disentangle overlapping
 586 clusters. The number of single-pad clusters can be reduced using Chevron-shaped pads, which could
 587 restore the spatial resolution of the MWPC-based readout, at the expense, however, of a larger occupancy.

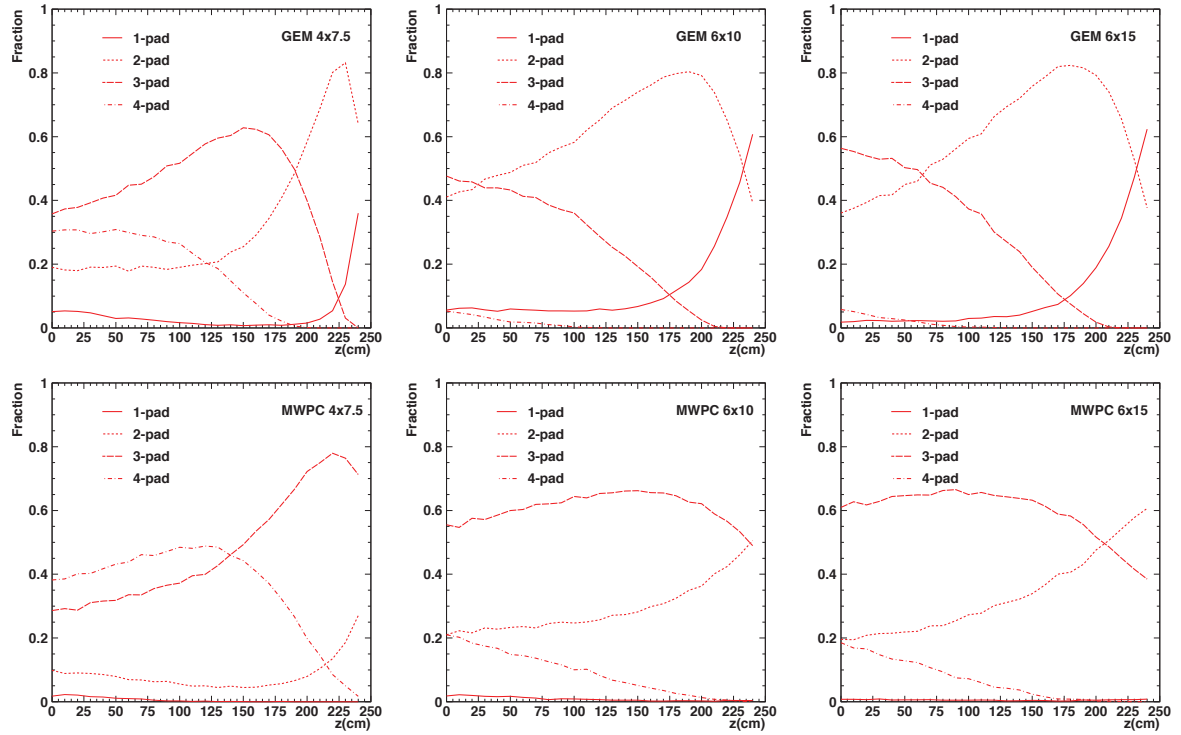


Figure 4.17: Fraction of one-, two-, three- and four-pad clusters for a (top row) GEM-based readout and (bottom row) an MWPC-based readout, with (left) $4 \times 7.5 \text{ mm}^2$, (middle) $6 \times 10 \text{ mm}^2$, and (right) $6 \times 15 \text{ mm}^2$ pads, respectively.

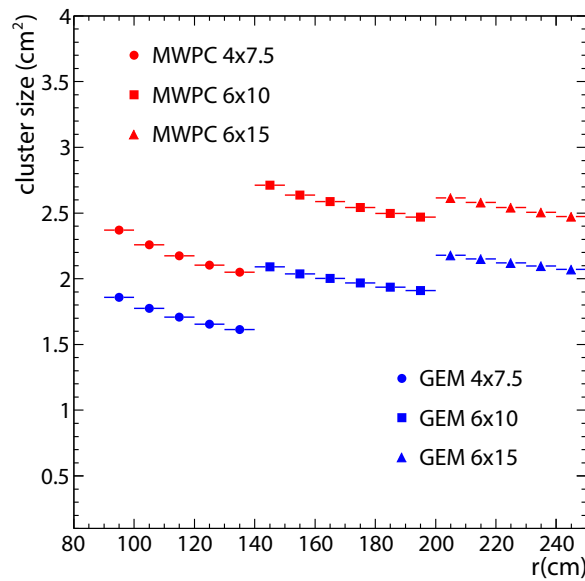


Figure 4.18: Cluster size as defined in Eq. (4.3), as a function of radius r and the corresponding pad sizes, for (blue) GEM and (red) MWPC readout.

		Pad size (mm ²)	Number of rows	Number of pads
IROC	(841 < r < 1321 mm)	4 × 7.5	63	5504
OROC	(1346 < r < 1696 mm)	6 × 10	35	2944
OROC	(1716 < r < 2066 mm)	6 × 10	35	3712
OROC	(2086 < r < 2461 mm)	6 × 15	25	3200
TPC total (2 × 18 sectors)			158	552,960

Table 4.3: Dimensions and parameters of readout planes and pads.

588 It should be noted that occupancy prohibits a larger pad size in radial direction, at least for the IROCs,
 589 which would allow to operate the TPC at a lower gain while maintaining a given signal-to-noise ratio.
 590 This in turn would decrease the distortions due to ion backflow, as can be seen from Eq. (4.2). The use
 591 of a faster gas, like the CF₄ option discussed in Chap. 3 and Sec. 9.3, would reduce the occupancy and
 592 therefore allow larger pad sizes in radial direction, or Chevron-shaped pads.

593 In conclusion, the current choice of pad sizes, optimized for occupancy and resolution with an MWPC-
 594 based readout, provides sufficient space-point resolution even for the case of GEM amplification without
 595 decreasing the pad size. The good momentum resolution in the acceptance of the barrel detectors of
 596 ALICE will be maintained after the upgrade, as shown in Chap. 7. It should be noted that the smaller
 597 PRF for GEM detectors reduces the occupancy of the detector. Thus, it allows to operate the TPC with a
 598 Ne-CO₂-N₂ (90-10-5) gas mixture also at the luminosity foreseen after the upgrade of the LHC.

599 Figure 4.19 shows the design of the pad plane for the OROC, where the division of the GEM detectors
 600 in three separate modules has been taken into account. There are two dead areas under the frames of the
 601 foils. Moreover, the transition between medium and large pads has been moved up by 8 cm with respect
 602 to the current pad plane. This results in 1 pad row less in the new pad plane, i.e. 1.3 % less pads as
 603 compared to the current system.

604 Table 4.3 summarizes the pad sizes for the different regions of the readout chambers. In total, the pad
 605 re-arrangement in the OROCs results in 0.8 % less pads in the TPC as compared to the current system.

606 4.6 Interface to front-end electronics

607 The front-end electronics is described in Chap. 6. The signals induced on the readout pads are routed
 608 to connectors on the backside of the pad plane. As in the present system, short flexible flat cables will
 609 be used to decouple the weight of the FEE⁵, which is supported by the service support wheel, from the
 610 readout chambers and the field cage. The signal routing must be optimized in order to minimize the trace
 611 length. The exact configuration of the connectors, flat cables and cards is still a matter of optimization
 612 and has thus not been decided upon yet.

613 4.7 Quality assurance of GEM foils

614 The proper selection of the GEM foils to be assembled into the readout chambers is of major importance.
 615 COMPASS was the first large-scale experiment to use GEM-based detectors. Quality assurance pro-
 616 cedures for all detector components have been established in order to guarantee a uniform and stable
 617 operation of the COMPASS readout chambers [7]. These procedures have successfully been applied and
 618 extended to other projects like LHCb [22], PHENIX [12], TOTEM [13] and the SuperFRS [23, 24], and
 619 will be adopted to a large extent for the ALICE TPC.

620 In this section we will go through the transportation requirements and the characterization process, in

⁵Front-End Electronics (FEE)

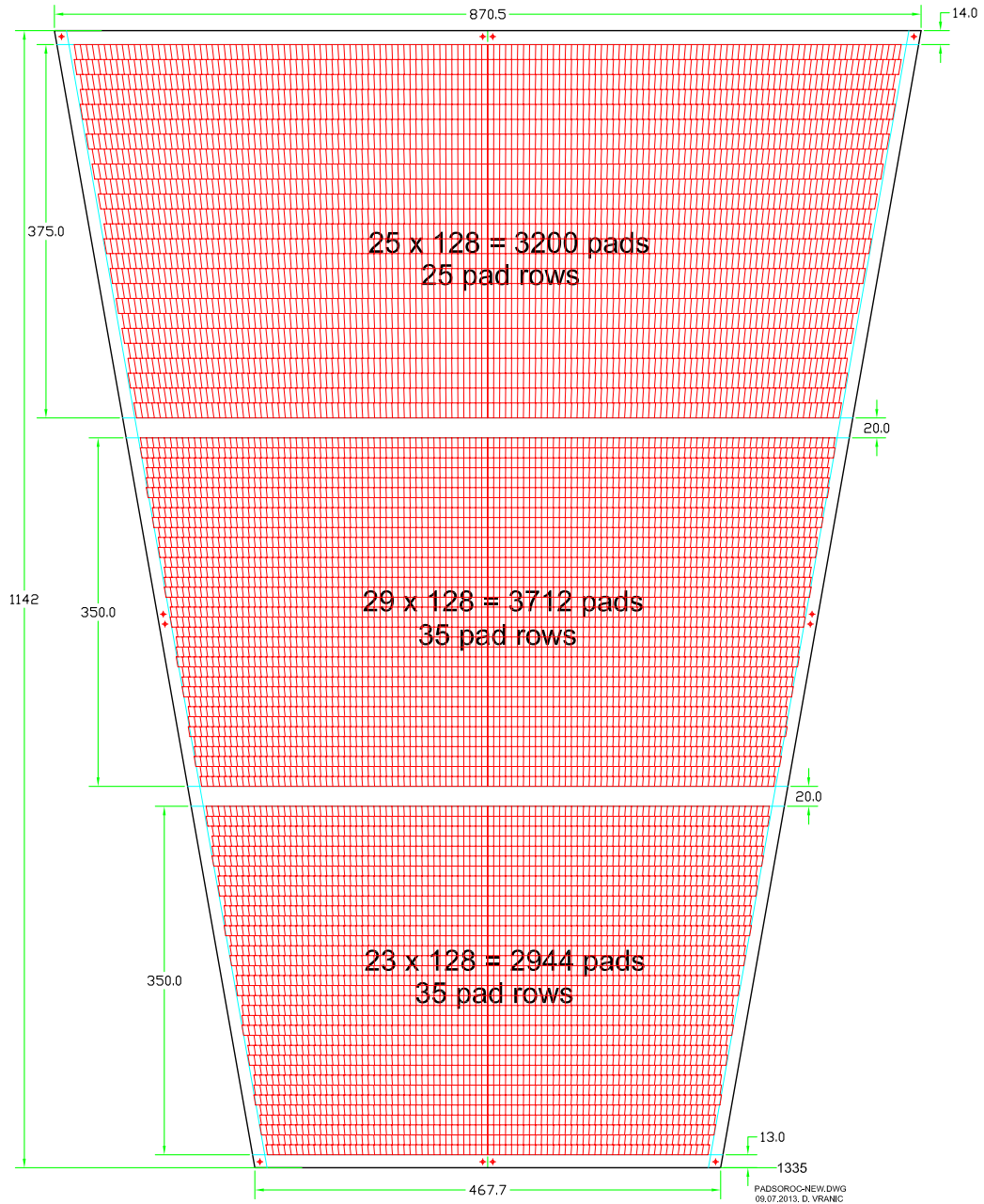


Figure 4.19: Pad layout of an ALICE OROC. The gaps have been introduced to allow fixation of the GEM detector modules. Units are in mm.

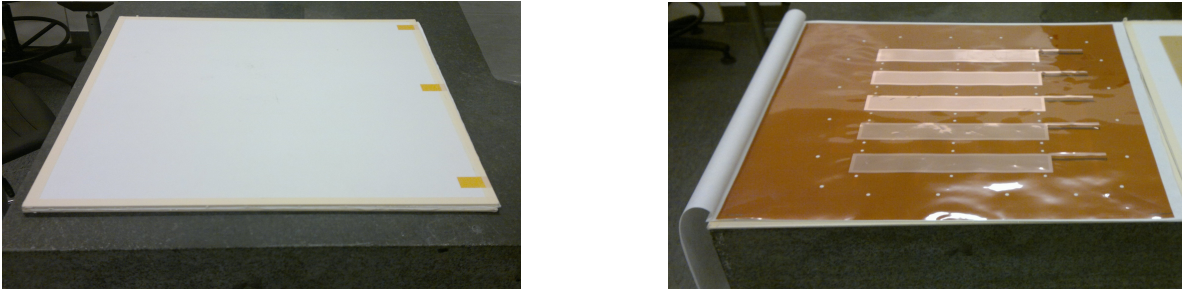


Figure 4.20: (Left) GEM foil transportation package. (Right) GEM foil for the SuperFRS GEM-TPC.

621 particular optical and electrical uniformity checks, that are essential in order to minimize the risk of
 622 initial failure and in order to ensure the long-term stable operation of the modules. A methodology has
 623 been developed for some of the characterization steps. These will be treated separately in the following.

624 Once a GEM foil has been prepared to leave the production site, care must first be taken in packing
 625 the foil to ensure that it will not suffer any damage. Until recently, the transportation procedures used
 626 by the Electronics Department at CERN, where the GEM foils were wrapped in paper, placed between
 627 cardboard plates and finally sealed with tape (see Fig. 4.20), seemed reliable. However, careful visual
 628 inspection of foils has suggested that small particles from the wrapping paper could enter the holes of
 629 the GEM foils and therefore contribute to a degradation of its performance, possibly resulting in the need
 630 for re-cleaning. During the preparation of the detectors of the above-mentioned experiments, cellophane
 631 paper had been used to cover the foil metallic surfaces when the foils were being manipulated in air. The
 632 current understanding is that this procedure helps in effectively detaching particles of dust from the foil
 633 surface by electrostatic forces, suggesting that it will prove advantageous to use cellophane paper for
 634 wrapping newly produced foils before shipping.

635 After the foils arrive at the characterization site, the first step is visual inspection. Here, the foils are
 636 placed on a light table inside a clean room⁶ to control the quality of the metallic surface on both sides.
 637 This method is most effective for discovering large defects, e.g. large areas without metallization or
 638 under-etching of the Kapton layer, and metallization problems at the HV sector boundaries, e.g. missing
 639 insulation. Large defects typically disqualify a foil for further consideration. Gross visual inspection
 640 can also locate scratches on the metallic surface. Deep scratches into the copper may in some cases
 641 reach the Kapton foil increasing the risk of failure during stretching or locally changing the electrical
 642 characteristics. Finally, this method can reveal wrinkles or residuals left during the production such as
 643 spots of oxidation that may affect the stability of the foils by charging up. Such foils should be rejected.

644 4.7.1 Electrical characterization

645 The first electrical quality assurance test consists of measuring the leakage current in each GEM HV sec-
 646 tor in response to an applied voltage across the foil. The test is performed in a dry nitrogen environment
 647 to avoid instabilities related to water or dust. In order to measure the leakage current, a setup as shown
 648 in Fig. 4.21 is used.

649 The components of this setup are: a desiccator with a gas flowmeter, an electrometer, a high voltage
 650 source and a computer to control the ramping of voltages and to read and store the current measurements.
 651 A voltage is applied between the unsegmented side and one of the HV sectors on the other side of the foil,
 652 with all the other sectors grounded. The voltage is ramped in steps up to a final potential difference of
 653 550 V between the two sides of the GEM foil, which is slightly below the breakdown limit of GEM foils
 654 in N₂ gas. Once the GEM is fully charged, the current drops and saturates at the leakage current through
 655 the GEM HV sector under study, which should normally be $\lesssim 0.1$ nA. Foils with leakage currents larger
 656 than ~ 0.5 nA are rejected and returned for re-cleaning. The foil is kept at maximum voltage for up to

⁶A class 10000 is required for the preparation work and class 1000 for the final assembly.



Figure 4.21: Leakage current measurement setup.

657 30 min. If the foil is stable during this time with a leakage current smaller than 0.5 nA, it is accepted and
658 given to the next characterization setup (optical scanning).

659 A typical leakage current evolution during the electrical characterization is shown in Fig. 4.22. Fig-
660 ure 4.23 shows a second example of a leakage current test, where a HV sector experienced several
661 discharges, but could be fully recovered after flushing with N₂. In cases where continuous discharges are
662 observed, the foil is rejected and returned for re-cleaning.

663 4.7.2 Optical scanning characterization

664 After a foil has passed the coarse visual inspection and the static electrical quality assurance testing, it
665 is subjected to precision optical inspection using a high resolution camera. In this way the geometrical
666 characteristics of the GEM foil can be studied. In particular, the distributions of inner and outer hole
667 diameters and the hole pitch for both surfaces of the foil are measured. It is well known that a variation
668 of the inner hole diameter causes a variation of the intrinsic gain of the foil. The dispersion of the
669 distributions can be taken as a quantitative indicator of the general foil uniformity. Foils not meeting
670 the specifications over the full surface (i.e. copper hole diameter typically $70\ \mu\text{m} \pm 5\ \mu\text{m}$, polyimide hole
671 diameter typically $55\ \mu\text{m} \pm 5\ \mu\text{m}$) are rejected.

672 In addition, the method is suited to identify smaller defects which were not detected in the first visual
673 inspection step. Defects in the form of under- or over-etched areas in the foils can occur during the
674 manufacturing process. Other defects may come in the form of chemical residues from the production
675 process, droplets of glue or dust attached to the foil, very large holes, missing holes, etc. All of them
676 may cause operational instabilities; such foils are rejected and possibly re-cleaned.

677 The setup used for this purpose is based on a back-illuminated light table with area $100 \times 100\text{cm}^2$. It
678 accommodates a full foil used for an IROC or OROC. In Fig. 4.24 the scanner used for this optical
679 characterization is shown [25]. A 9 Megapixel camera with a single pixel size of $1.75\ \mu\text{m}^2$ is mounted on

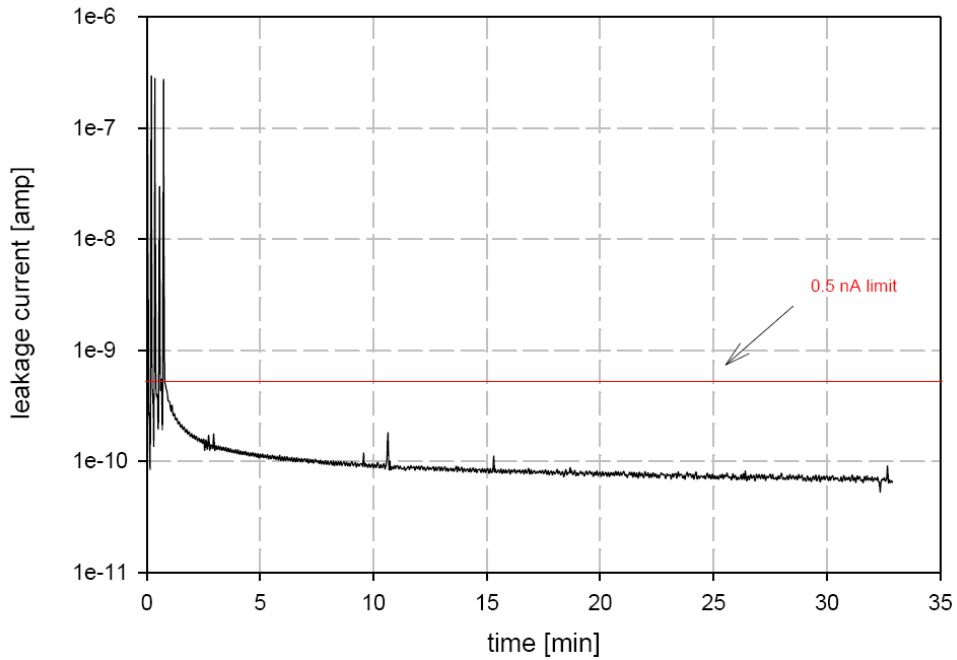


Figure 4.22: Leakage current evolution during electrical characterization of an accepted GEM foil. The spikes at early times correspond to the five voltage steps scanned through during ramping up at the beginning of the test. After the target voltage has been reached, the current quickly drops below 1 nA. It is then measured for as long as 30 min.

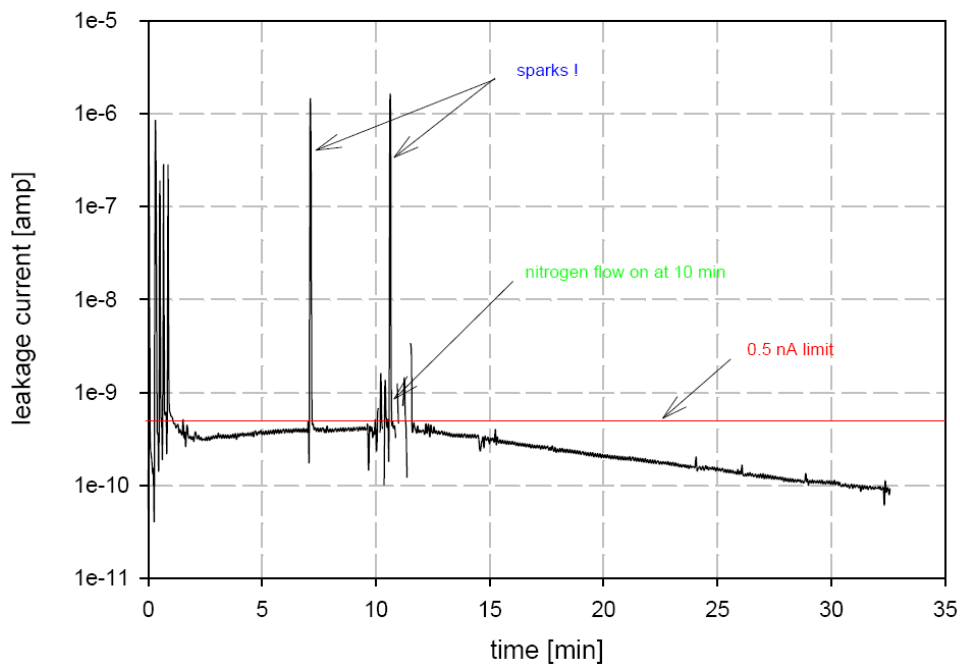


Figure 4.23: Leakage current results from a recovered GEM foil.

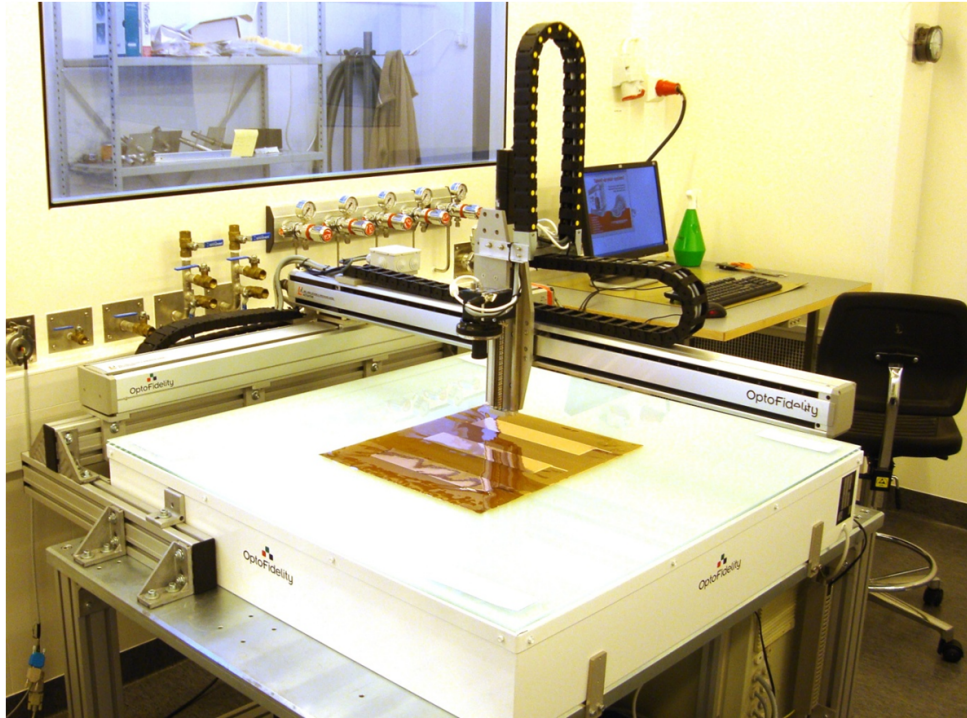


Figure 4.24: Setup of the high resolution scanning system.

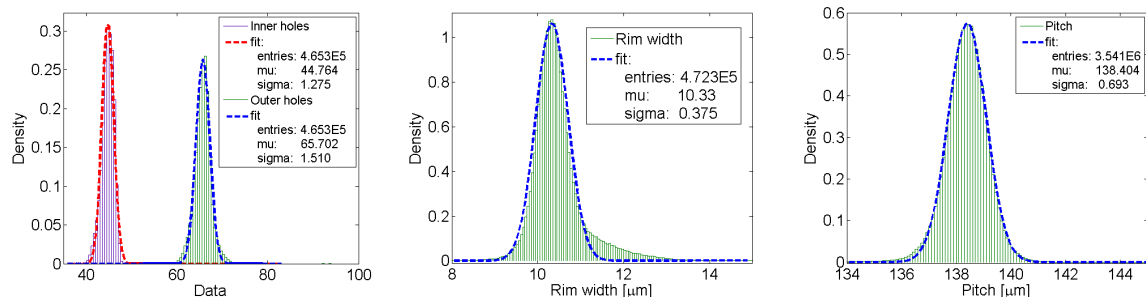


Figure 4.25: Distributions of inner and outer hole diameters (left panel), the rim width (middle panel), and the pitch between holes (right panel).

680 an x - y positioning system above the light table. The optical system has a resolution of 144 light points
 681 per mm and a field of view (single image) of $6.1 \times 4.6 \text{ mm}^2$. After compression, the total image size is
 682 about 20 MByte. Up to 32,000 individual images are required to cover the full active area.

683 During the scanning procedure the diameters of inner and outer holes, the pitch between holes and their
 684 shape are recorded. Distributions of the diameter, the width of the polyimide rim (the distance between
 685 the border of the outer and inner holes), and the pitch are shown in Fig. 4.25. Parameters describing the
 686 shape of the hole are obtained from an ellipse interpolation with a sigma of $0.52 \mu\text{m}$.

687 A two-dimensional map of the GEM foil characteristics is used to visualize the uniformity of measured
 688 parameters as a function of position on the foil. Figure 4.26 shows an example of the spatial variation
 689 of the diameters of the inner and the outer holes. Here, the diameters of holes are averaged over an area
 690 of 1 mm^2 . Maps such as these can be used during assembly of the GEM stack to avoid accumulation of
 691 unwanted features in similar positions over the stack area.

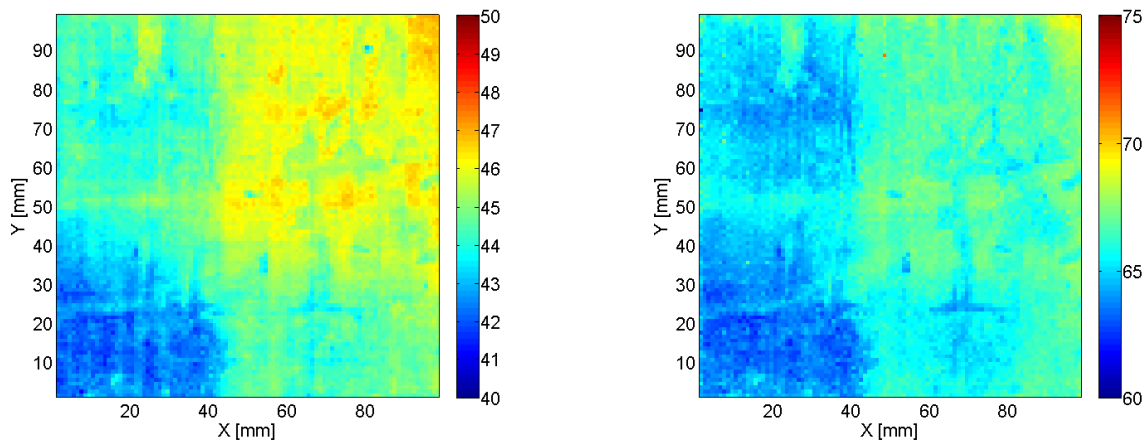


Figure 4.26: Map of hole diameters of a $10 \times 10 \text{ cm}^2$ GEM foil. (Left) inner hole diameter, (right) outer hole diameter.

692 4.7.3 GEM gain mapping

693 To evaluate the uniformity of the gain distribution, a mapping of the gain of each GEM foil is performed.
 694 An acceptance criterion can be specified for the gain variation across the surface of the foil, e.g. 10% (RMS). In order to determine the gain map of a GEM foil, a setup as shown schematically in Fig. 4.27

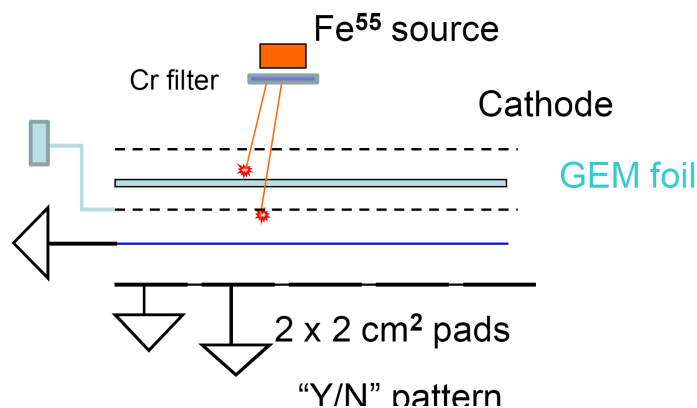


Figure 4.27: Schematics of the setup for the gain mapping measurement.

695 is used. It includes the GEM foil under test and a reference detector, typically a multiwire proportional
 696 chamber or alternatively a Micromegas detector. The reference detector detects the primary ionization
 697 that takes place either above or below the GEM foil. In addition, a pad readout geometry is used to
 698 record a 2D map of the foil under test. The source on top of the detector is used to illuminate the entire
 699 GEM foil, making it possible to measure the gain and its evolution in time without having to scan over
 700 the detector surface. A prototype of this setup, shown in Fig. 4.28, has been built at Yale University.
 701

702 By illuminating the whole active area with a source, a double spectrum is measured for each pad, as
 703 shown in Fig. 4.29. The low-amplitude spectrum corresponds to X-rays absorbed below the GEM,
 704 whereas the high-amplitude one corresponds to X-rays absorbed above the foil. The ratio between the
 705 position of the two main peaks is therefore proportional to the gain of the GEM foil for this particular
 706 pad area. The uniformity of the gain is then obtained from the variations of the gain of each pad with
 707 respect to the mean gain value. For the particular example shown in Fig. 4.30, the pad dimensions were
 708 $2 \times 2 \text{ cm}^2$, and the total area of the GEM foil was $10 \times 10 \text{ cm}^2$, resulting in the 5×5 bin gain map shown.

709 For the GEM foil test illustrated in this figure, the mean gain obtained was 23 with a dispersion of 4.8%
 710 (RMS). At the same time this setup also permits mapping of the energy resolution of a single GEM foil,

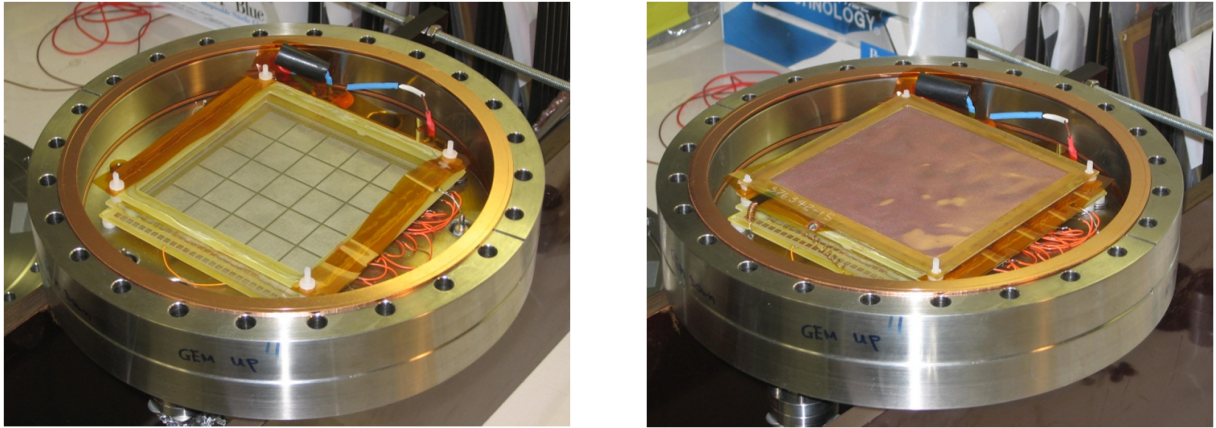


Figure 4.28: (Left) Gain map setup. (Right) Flange together with the multiwire proportional chamber and the GEM foil under test.

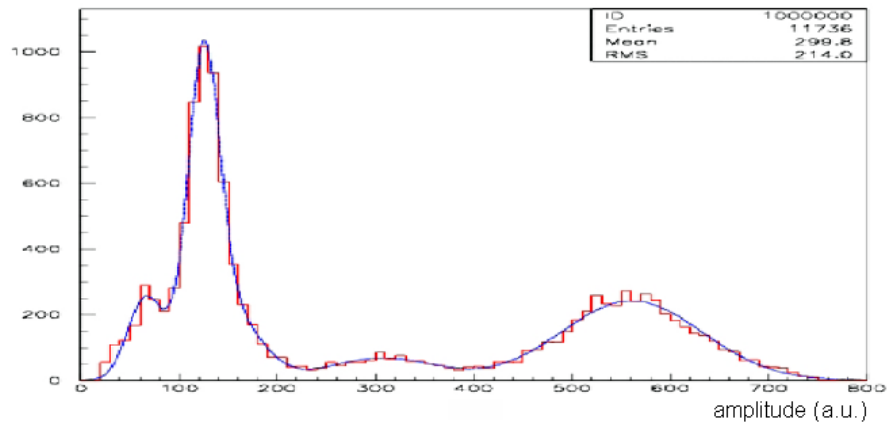


Figure 4.29: Pulse height distribution for a single pad.

711 and thus a measurement of the uniformity of the expected energy resolution.

712 4.8 Quality assurance of chambers

713 Once the GEM stacks are mounted on the IROCs or OROCs, the completed chambers need to pass
 714 further tests. They are installed in test boxes which provide a gas volume and a small field cage with a
 715 drift electrode and a voltage divider. The box is flushed with the nominal gas at a reasonable flow.

716 The first test is the gas tightness test. The pad plane structure may exhibit leakage if not properly as-
 717 sembled. For testing this, the oxygen contamination in the gas outlet of the test box is measured with
 718 an appropriate oxygen sensor. In order to provide final oxygen levels compared to the current ones in
 719 the TPC, levels of 1 – 2 ppm in the test box at flows of 20 l/h should be achievable. However, viscous
 720 leaks, e.g. through tortuous paths between the pad plane and the alubody, can be difficult to detect by
 721 this method, unless the gas pressure in the test box is kept lower, by a few mbar, than the ambient pres-
 722 sure. Therefore, the gas system utilized for these tests will contain provisions for producing a controlled
 723 underpressure in the test box.

724 The next test is to produce the gain curve as a function of the applied voltages in order to characterize
 725 each chamber. All chambers should deliver similar gains at similar voltages, and should hold at least a
 726 factor of 2 higher gain than the anticipated operational gain.

727 The measurement of the uniformity of the gain across the active area follows next, with a coarser gran-

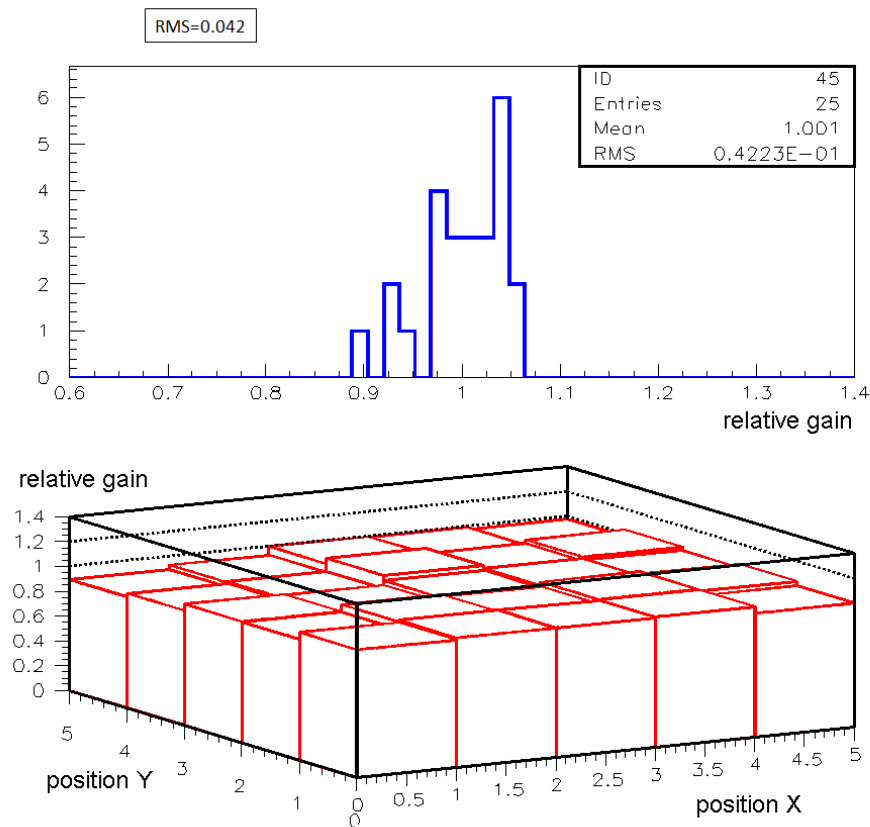


Figure 4.30: Relative gain distribution (top panel) and map (bottom panel) of a single GEM foil.

728 ularity than in the previous QA of the foils. This test assures that the stack is properly mounted and
 729 clean.

730 Finally, a long-term test is carried out. The chamber is operated at a gain higher than the nominal
 731 value for one or two days, while being irradiated with e.g. an Fe^{55} source. During this test the relevant
 732 parameters are periodically recorded: currents, main peak position for the Fe^{55} spectrum, FWHM of
 733 the main peak, ambient conditions, oxygen and water concentrations. The chamber must hold this test
 734 without any trips or current excursions.

735 Once a chamber passed all these tests (timescale ~ 1 week per chamber) it is validated and properly
 736 stored in a sealed environment under controlled temperature and pressure until its installation in the TPC
 737 field cage. About 80 chambers will be built and tested this way.

738 Chapter 5

739 R&D with prototypes

740 In this chapter the R&D carried out with small and large prototype chambers is described. The obtained
741 ion backflow performance and the comparison with detailed simulation studies is presented in Sec. 5.1.
742 The construction and in-beam operation of a full-size prototype of an IROC, assembled with three GEM
743 foils, is described in Sec. 5.2.

744 5.1 R&D with small prototypes

745 In this section the question of the minimization of the ion backflow of a GEM structure is addressed.
746 To this end, scans of field configurations are performed, and various GEM structures are investigated,
747 in particular triple and quadruple stacks assembled with standard and double-pitch foils. The resulting
748 performances are compared with simulations. The energy resolution and the stability of the emerging
749 solutions are also investigated or in the process of being demonstrated. Although various gas mixtures
750 have been tried out, we focus here on results obtained with the baseline mixture Ne-CO₂-N₂ (90-10-5).

751 In the course of these studies, we discovered that the build-up of positive space charge has a strong impact
752 on the ion transport. This effect can severely bias the measurements of the ion backflow. Detailed results
753 will be reported in a separate publication. Here we note only that all reported measurements are carried
754 out with sufficiently low X-ray rates.

755 5.1.1 Experimental setup

756 Several small detector systems were built and set up in various labs within the scope of this R&D effort.

757 *Setup for gain stability measurements*

758 Measurements are performed to monitor the gain stability of a GEM stack over time, including the
759 response to changes in high voltage and radiation levels. For this purpose, a GEM chamber under test is
760 continuously irradiated while its current is periodically measured. The ambient temperature and pressure
761 are also recorded, together with the water content of the gas, which plays an important role in charging-
762 up processes of GEM foils. A single-wire proportional counter is operated in the same gas stream and
763 its gain monitored via the position of the ⁵⁵Fe line for correction purposes. Both the GEM detector and
764 the wire counter are installed in a box which may be flushed with N₂ for further moisture reduction.

765 *CERN ion backflow setup*

766 The detector housing used for ion backflow measurement at CERN comprises a GEM holder and a field
767 cage. The GEM box is equipped with HV feedthroughs for up to four 10 × 10 cm² foils and a pad plane
768 subdivided into 16 × 16 pads. All pads are connected together to a DC voltmeter for measurement of the

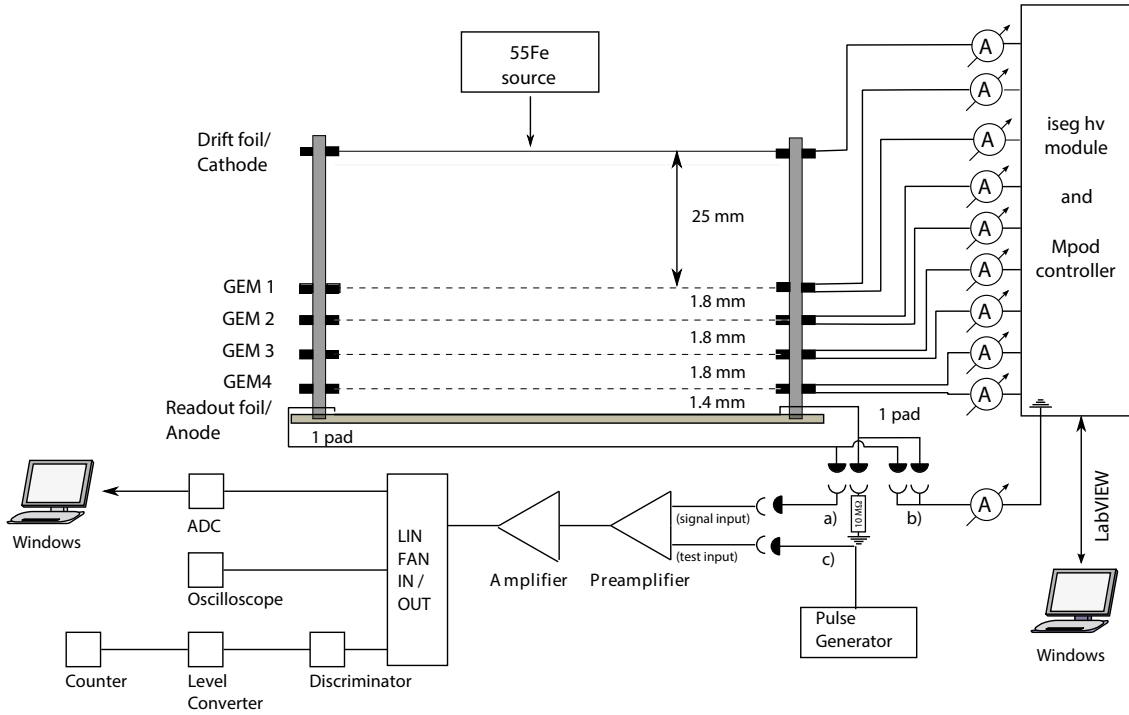


Figure 5.1: Sketch of the Munich quadruple GEM setup.

769 current. The field cage, constructed from Rohacell to permit irradiation with X-rays, is 8 cm deep and
 770 has a drift electrode and 10 strips made of copper. The drift electrode is powered with one channel of a
 771 HV power supply and its current is measured with a floating picoammeter with 100pA resolution. The
 772 field cage is powered with a second HV channel so that the current through its $10 \times 10 \text{ M}\Omega$ resistors does
 773 not add to the small current on the drift electrode. A last, external resistor ensures reasonable matching
 774 of potentials of the last strip and the top GEM electrode. The gas is supplied from a premixed bottle for
 775 the reference measurements with Ar-CO₂ (70-30) (many GEMs in the world are operated with this gas)
 776 and from a mixer for the other gas mixtures. The HV is supplied with programmable power supplies for
 777 convenient scanning of gains and fields. A small, silver-anode X-ray tube is used as source of radiation.

778 *Munich ion backflow setup*

779 The Munich detector has been specifically built to measure ion backflow. The geometrical configuration
 780 is summarized in Tab. 5.1. It features a short drift length, individual control of each HV electrode, and
 781 the possibility to irradiate the detector from the top and a side wall. Standard $10 \times 10 \text{ cm}^2$ GEM stacks
 782 are used.

783

Drift gap	25 mm
Transfer gap 1	1.8 mm
Transfer gap 2	1.8 mm
Transfer gap 3	1.8 mm
Induction gap	1.5 mm
Thickness top window	150 μm
Thickness side window	50 μm

Table 5.1: Properties of the Munich test detector in the quadruple GEM configuration.

784 The readout consists of 512 strips, that can be either read out individually or connected via analog sum-
 785 mation cards to a total of 16 channels. By setting the appropriate jumper one can select the corresponding

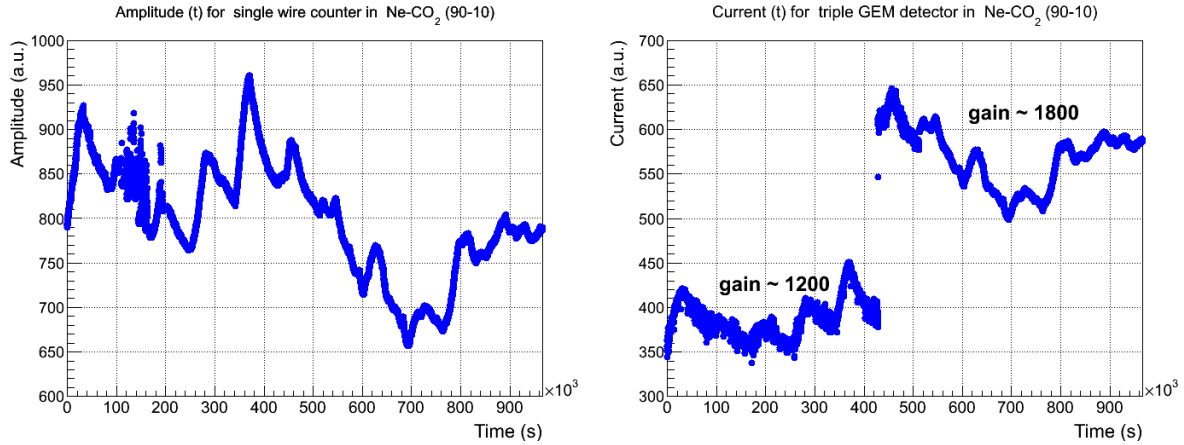


Figure 5.2: Signal amplitude in the single wire counter (left panel) and current in the triple GEM (right panel) as a function of time with a Ne-CO₂ (90-10) gas mixture and 180 ppm of water.

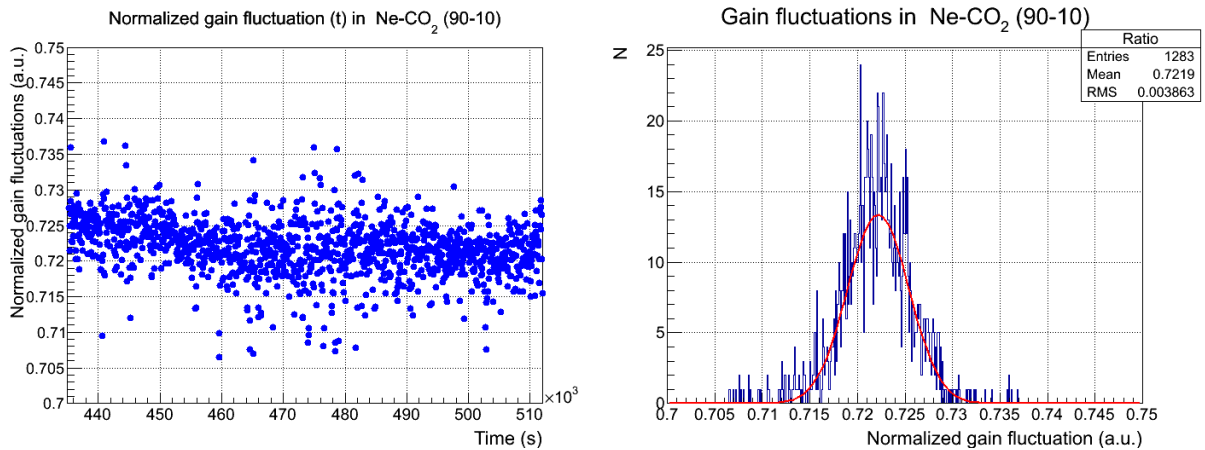


Figure 5.3: (Left) GEM current corrected by the gain of the single wire counter as a function of time. (Right) Projected distribution fitted with a Gaussian. The relative variation is 0.45 %

786 size of the readout area, while all other strips remain grounded.

787

788 The picoammeters used to measure all currents contain a wireless transmission unit which allows them
 789 to be kept at a floating potential. They are able to measure currents down to 0.1 nA at up to ~5 kV.
 790 These picoammeters are connected to each electrode as shown in Fig. 5.1. All currents are measured
 791 simultaneously and therefore should sum up to zero. The readout of the pads is realized with conventional
 792 spectroscopy amplifiers and a multichannel analyzer for recording pulse height spectra. Two small X-ray
 793 tubes, with gold and silver targets, are used to irradiate the detector.

794 The ion backflow and ϵ used in the following are defined according to Eq. (4.2). The gain is determined
 795 by the usual method of recording the current at the pad plane and the rate of absorbed X-rays of known
 796 energy.

797 5.1.2 Gain stability measurements

798 Figure 5.2 shows the long term behavior of the amplitude as a function of time for a reference wire
 799 counter and a triple GEM setup. The measurements were performed in Ne-CO₂ (90-10). The right-hand
 800 panel shows the long term behavior of the current of the triple GEM stack for two gain settings. A
 801 humidity level of about 180 ppm of water was maintained for the entire period. The wire counter data is
 802 used to correct the gain variations of the GEM detector due to ambient fluctuations such as pressure and

803 temperature. In Fig. 5.3 the corrected GEM gain is shown for a period of about 21 hours. Within this
 804 time the corrected gain remains very stable, within 0.45 %, as indicated by the fit of the right panel of the
 805 figure.

806 5.1.3 Results of ion backflow measurements

807 *Ion backflow results for a triple GEM setup*

808 Extensive studies were performed with triple GEM detectors aimed at minimizing the ion backflow of the
 809 structure. In order to find the optimal settings, the transfer fields E_{T1} and E_{T2} were varied systematically
 810 while the voltage across GEM 3 was used to keep the gain at the desired value. The effective gain was
 811 kept at ~ 2000 and the drift field at 400 V/cm, while the X-ray rate was always lower than a few tens of
 812 nA/cm². Several gas mixtures have been studied, although results are shown only for the baseline gas
 813 mixture Ne-CO₂-N₂ (90-10-5).

814 As described in Sec. 4.1, ion backflow suppression in a GEM system is based on an asymmetric field
 815 configuration within the stack. This field configuration was developed by the International Linear Col-
 816 lider (ILC) community and described in [1]. Following this principle, the values of E_{T1} and E_{ind} are
 817 maximized, whereas E_{T2} is set at a minimum value to achieve maximum blocking of the ions produced
 818 at GEM 3. In addition, the potential differences across the three GEMs follow an increasing order, such
 819 that $\Delta U_{GEM1} < \Delta U_{GEM2} \ll \Delta U_{GEM3}$. In this manner, the number of ions forced to enter the trapping
 820 region is maximized.

ΔU_{GEM1}	263 V
ΔU_{GEM2}	305 V
ΔU_{GEM3}	300–370 V
E_{drift}	0.4 kV/cm
E_{T1}	3.0–5.5 kV/cm
E_{T2}	0.1–0.8 kV/cm
E_{ind}	4.0 kV/cm

Table 5.2: Electric field configuration for the scans performed on a triple GEM and the baseline gas mixture. For each field setting, the gain is tuned to 2000 by adjusting ΔU_{GEM3} .

821 As an illustrative result, in Fig. 5.4 the ion backflow is shown as a function of E_{T1} for several E_{T2} values
 822 in Ne-CO₂-N₂ (90-10-5). A clear decrease of the ion backflow as a function of E_{T1} is visible due to
 823 the higher extraction efficiency of GEM 1. The best performance is reached at the lowest applied E_{T2}
 824 (0.1 kV/cm). The HV settings used in this scan are summarized in Tab. 5.2.

825 The ion backflow observed in triple GEM systems can be reduced to 2–3 % after careful optimization
 826 of the voltage and field settings. These numbers exceed the requirements by more than a factor of two.
 827 No strong dependence on the gas mixture has been observed in any measurement (not shown here).
 828 Therefore, structures with four GEMs, with the inclusion of large pitch foils, are considered next.

829 *Ion backflow results with quadruple GEMs*

830 As a next step towards a minimization of ion backflow, the study of systems with four GEMs is discussed.
 831 In addition, the performance of foils with large hole pitch (LP) [2], 280 μ m, instead of the standard (S)
 832 value of 140 μ m, in various combinations with standard foils is explored. Simultaneous measurement of
 833 ion backflow and energy resolution with an ⁵⁵Fe X-ray source are carried out. This is important because
 834 the lower optical transparency of the LP foils may affect the electron transmission efficiency. In this
 835 section results are shown for ion backflow and energy resolution, obtained in various setups for different
 836 variations of quadruple GEM stacks for the baseline gas mixture Ne-CO₂-N₂ (90-10-5). The gain was
 837 systematically adjusted to 2000, usually by tuning ΔU_{GEM3} and ΔU_{GEM4} while maintaining a fixed ratio
 838 between the two. The strategy is to focus the ions with a strong field as they come out of the holes of a

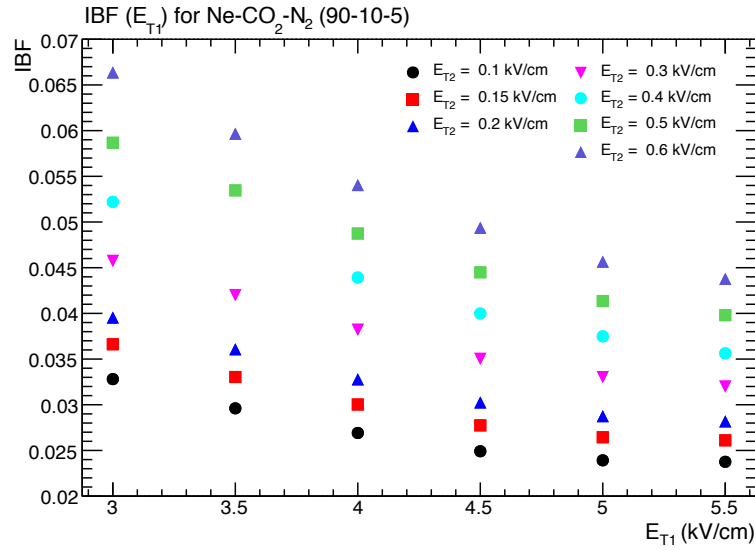


Figure 5.4: Ion backflow in a triple GEM detector as a function of E_{T1} for several values of E_{T2} .

839 foil, and to absorb them in the next, large pitch GEM with the help of a low field above it. As observed
 840 with a triple stack, low ion backflow is also favoured if the gain between the GEMs follows an increasing
 841 sequence.

842 Several HV scans have been carried out with a first structure composed of four standard foils (S-S-S-S).
 843 As an example a two-dimensional scan as a function of E_{T2} and E_{T3} is shown in Fig. 5.5, where the ion
 844 backflow reaches values of 1 % for low values of E_{T2} . The energy resolution (expressed as the sigma of
 845 a gaussian fit to the 5.9 keV peak divided by the mean value, in percent) remains near a reasonable value
 846 of 11 %.

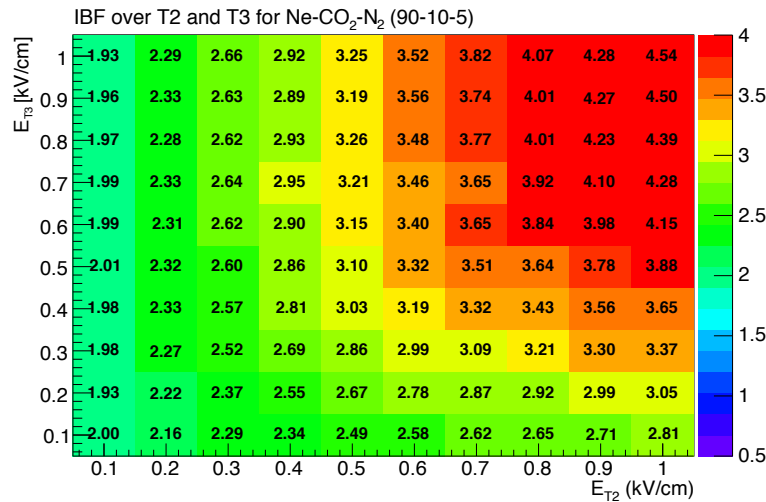


Figure 5.5: Two-dimensional scan of the ion backflow in a quadruple stack of standard GEMs (S-S-S-S) as a function of E_{T2} and E_{T3} . E_{T1} and E_{ind} are both 4 kV/cm, and the voltages across the GEMs are tuned, in an increasing sequence, to achieve an effective gain of 2000.

847 Next, a large pitch foil is introduced in a configuration of the type S-S-LP-S, aiming at improving the
 848 ion backflow by, again, establishing a low transfer field just above the large pitch GEM (E_{T2}). The
 849 two-dimensional scan shown in Fig. 5.6 illustrates how the ion backflow for this configuration indeed
 850 improves as E_{T2} decreases and, to a lesser extent, as E_{T3} increases. It should be noted that the use of
 851 large pitch foils increases the probability for large misalignments between the holes of consecutive foils.

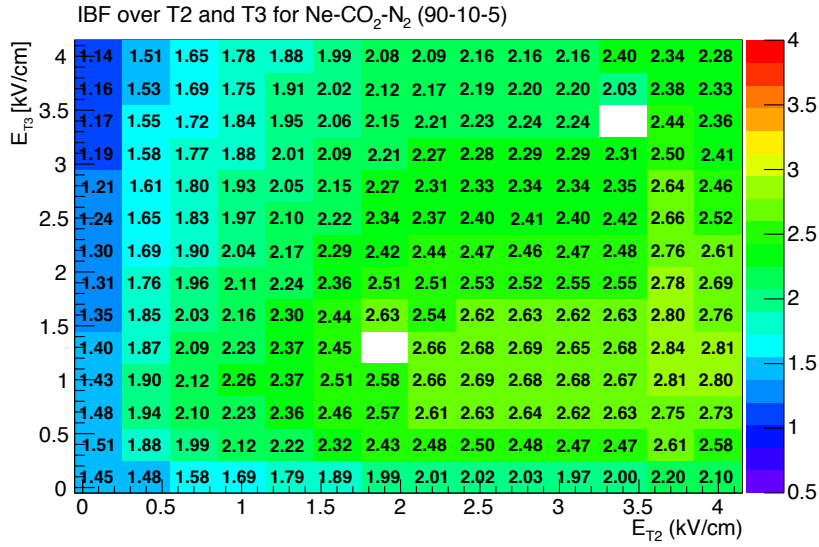


Figure 5.6: Two-dimensional ion backflow scan as a function of E_{T3} and E_{T2} for a quadruple GEM of the type S-S-LP-S (large pitch GEM in 3rd position). E_{T1} and E_{ind} are both 4 kV/cm, $\Delta U_{GEM1} = 233$ V, $\Delta U_{GEM2} = 250$ V, and ΔU_{GEM3} and ΔU_{GEM4} are adjusted to achieve the nominal gain of 2000.

852 This mechanism of ion blocking can be further extended by introducing a second large pitch foil in the
 853 quadruple structure. Intuitively, since the drift field provides by definition a low field above GEM 1, the
 854 position for the second LP GEM is initially chosen to be GEM 1, such that an optimised ion backflow can
 855 be achieved with large E_{T1} and E_{T3} but low E_{T2} . The ion backflow under such conditions, for a LP-S-
 856 LP-S stack, is shown in Fig. 5.7. As shown in the left panel, the ion backflow decreases as E_{T1} increases,
 857 to a value as low as 0.5 %. At these settings, in particular in combination with low E_{T2} , ions are absorbed
 858 at the bottom of both LP foils. However, a poor energy resolution is observed in this arrangement, which
 859 is illustrated in Fig. 5.7 (right panel). Irrespectively of the field configuration, in this case at low E_{T3} ,
 860 values of the energy resolution better than 17 % are not reached.

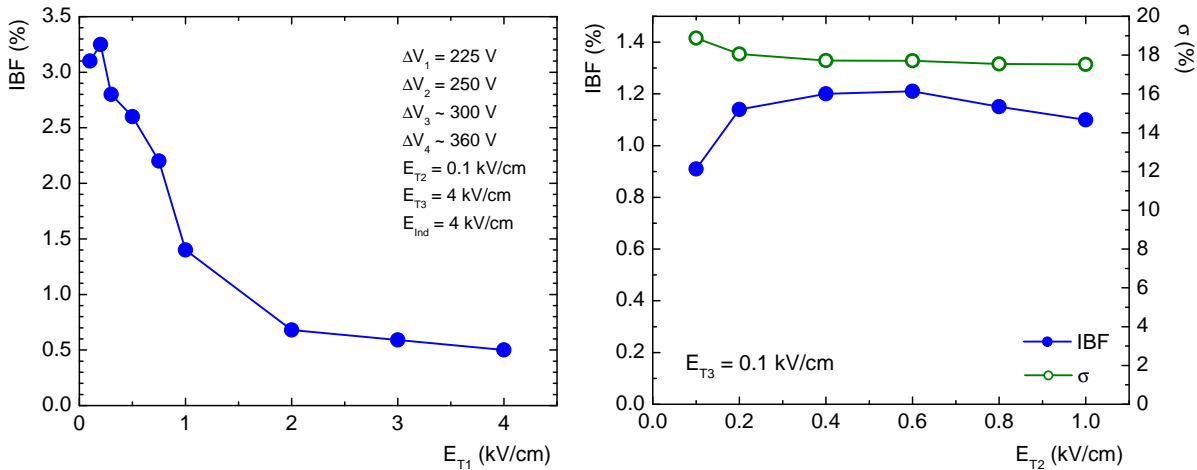


Figure 5.7: (Left) Ion backflow in a quadrupole LP-S-LP-S GEM as a function of E_{T1} . The voltage and field settings are shown in the figure. (Right) Ion backflow and energy resolution for the same GEM configuration as a function of E_{T2} for $E_{T3} = 0.1$ kV/cm. E_{T1} and E_{ind} are both 4 kV/cm, and the voltages across the GEMs are in increasing sequence to achieve the nominal gain of 2000.

861 The energy resolution in this configuration is perhaps excessively penalized by the choice of a weakly
 862 transparent first GEM, which leads to loss of primary electrons from the drift volume. Therefore, we
 863 swap the first two foils to construct an S-LP-LP-S structure, where the two large pitch GEMs are mounted
 864 in the core of the stack. A scan of the E_{T2} field for such a configuration is shown in Fig. 5.8 (left panel).

865 Although the swap did not result in an improvement of the energy resolution at all, ion backflow values
 866 of as low as 0.34 % are obtained for high E_{T2} and low E_{T3} . In this configuration ions are absorbed at the
 867 top of GEM 4 due to the low field above, and the remaining ones are focussed between two misaligned
 868 large pitch foils and partially absorbed at the bottom of GEM 2.

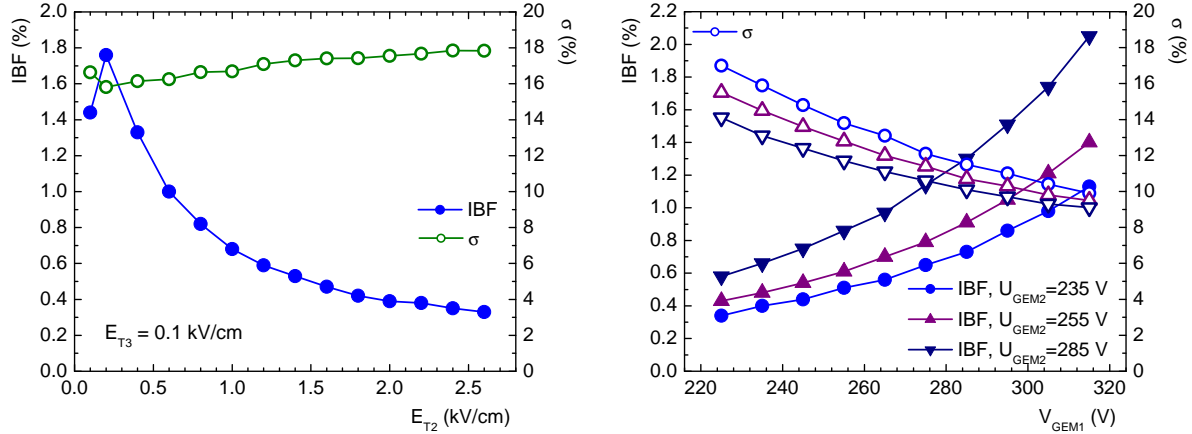


Figure 5.8: (Left) Ion backflow and energy resolution in a quadruple S-LP-LP-S GEM as a function of E_{T2} for $E_{T3} = 0.1$ kV/cm. E_{T1} and E_{ind} are both 4 kV/cm, and the voltages across the GEMs are in increasing sequence to achieve an effective gain of 2000. (Right) Ion backflow and energy resolution for the same GEM configuration as a function of ΔU_{GEM1} for various settings of ΔU_{GEM2} . The transfer and induction fields are 4, 2, 0.1 and 4 kV/cm, respectively, and the voltages on GEM 3 and GEM 4 are such that their ratio is 0.8 and the gain is 2000.

869 The low ion backflow values achieved so far allow the optimization of the energy resolution by tuning
 870 other settings, such as the voltages across the foils. As an example, Fig. 5.8 (right panel) shows the ion
 871 backflow and energy resolution for the same S-LP-LP-S arrangement as a function of ΔU_{GEM1} for three
 872 settings of ΔU_{GEM2} . A significant improvement of the energy resolution is achieved, albeit at the expense
 873 of a slight increase of the ion backflow. Nevertheless, values of ion backflow around 0.6–0.8 % and
 874 energy resolutions of 11–12 % are reached for example for $\Delta U_{GEM1} = 275$ V and $\Delta U_{GEM2} = 235–255$ V.

875 Clearly, a compromise between electron transmission through the first foils and ions produced in these
 876 foils is to be found. That the energy resolution is correlated with the efficiency of transmitting the primary
 877 electrons is demonstrated in Fig. 5.9, where the energy resolution of various ΔU_{GEM} scans is represented
 878 as a function of the inverse of the square root of the ion backflow. The correlations indicate that lower
 879 values of ΔU_{GEM2} and lower ratios of voltages between the 3rd and 4th GEMs are favoured.

880 More systematic studies remain to be performed, where further voltage settings and stack arrangements
 881 will be tried out. Given the performance and the flexibility in the choice of operational parameters
 882 demonstrated in this section, we have confidence that a working solution for the ALICE TPC upgrade
 883 will be reached with an ion backflow ≤ 1 %, based on a quadruple GEM system.

884 The question of the discharge probability is now being addressed. First measurements confirm earlier re-
 885 sults obtained by irradiating a standard triple GEM with heavily ionising radiation at very high gains [3].
 886 While evidence exists that the addition of N₂ to the Ne-CO₂ mixture reduces the discharge probability,
 887 the operation of a triple stack in a configuration typical for minimising the ion backflow (increasing gain
 888 sequence and low E_{T2}) does increase the discharge rate. The addition of a 4th foil should improve the
 889 situation. In order to assess the robustness of quadruple stacks with the inclusion of large-pitch foils and
 890 ion backflow settings several discharge measurements are being carried out in various laboratories. The
 891 studies will be focussed on operation at nominal or slightly higher than nominal gains with various types
 892 of radiation, including alpha, beta and X-ray radioactive sources, and minimum ionizing and heavy-ion
 893 beams.

894 The experience of the GEM-based muon trigger detector of LHCb can serve as a reference to judge the

895 required discharge performance of the detectors [4]. In this case a discharge probability of 10^{-12} , as
 896 measured with a close-to-MIP beam, was considered satisfactory since the detectors had survived during
 897 this beam test the equivalent of 10 years of operation in the LHC [5]. The determination of a reasonable
 898 discharge probability limit with heavily ionising radiation can be done by scaling the energy deposition
 899 to MIPs. The ultimate test, nevertheless, shall be the performance of a well-certified detector under LHC
 900 conditions.

901 5.1.4 Comparison with simulations

902 *Simulation studies with Garfield*

903 The ion backflow is studied with the Garfield++ simulation package [6] and compared with experimental
 904 measurements presented in the previous section. The geometry of the detector, the material properties
 905 of the GEM, the voltage configurations, and the boundary conditions are defined in ANSYS [7]. This
 906 program calculates the electric field in the detector with a finite elements analysis method. For the cal-
 907 culation of the properties of gas mixtures and transport properties of electrons in a given electric field,
 908 the simulation packages Heed [8] and Magboltz [9] are used. In the simulation studies, the gas mix-
 909 tures Ar-CO₂ (90-10), Ar-CO₂ (70-30), Ne-CO₂ (90-10), and Ne-CO₂-N₂ (90-10-5) are used, although
 910 results shown here are for the latter mixture only. The drift of electrons and the avalanche inside a hole
 911 are studied with a microscopic transport and avalanche method. In Garfield++, this method tracks the
 912 electron path at the molecular level using the drift velocity and the diffusion, Townsend and attachment
 913 coefficients as calculated by Magboltz from the various electron-gas cross sections. Penning effects are
 914 introduced in the calculation of the gas gain. Because a microscopic transport calculation for ions is not
 915 available in this package, transport parameters such as the ion mobility as a function of the field over the
 916 gas density (E/N) are set by hand according to [10–12]. The diffusion of ions is given by the thermal
 917 diffusion of $D_L = D_T = \sqrt{2k_B T/qE}$, where k_B is the Boltzmann constant, T the temperature, E the elec-
 918 tric field and q the electrical charge. A Monte Carlo integration technique is utilized for tracking of ions.
 919 In these simulations, the Munich detector configuration, as described in Sec. 5.1.3, is used.

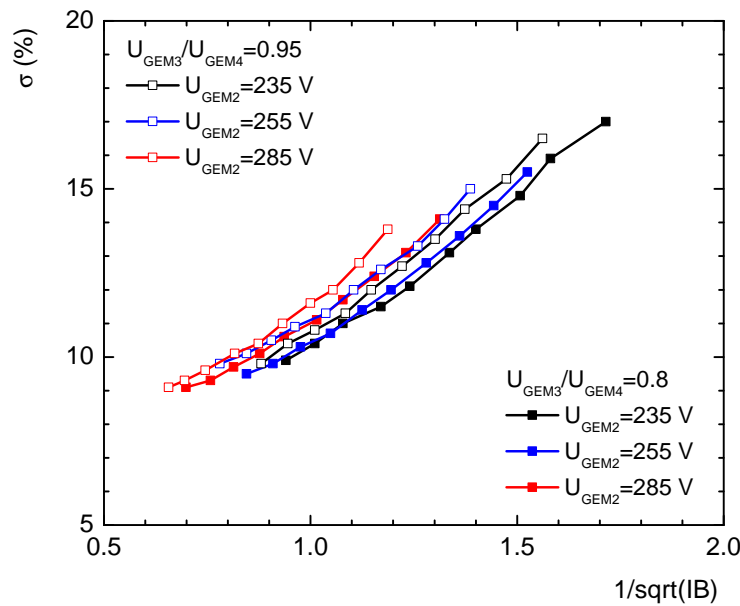


Figure 5.9: Energy resolution in a quadruple S-LP-LP-S GEM as a function of the inverse of the square root of the ion backflow for various scans of ΔU_{GEM1} and various settings of ΔU_{GEM2} . The transfer and induction fields are 4, 2, 0.1 and 4 kV/cm, respectively, and the voltages on GEM 3 and GEM 4 are such that their ratio ranges from 0.8 to 0.95 at an effective gain of 2000.

920 It has been found in the course of these studies that the alignment of the holes of GEM 1 and GEM 2
 921 crucially affect the resulting ion backflow in a triple GEM system. Since the hole alignment between
 922 standard GEMs cannot be controlled in the measurements, misalignments between GEM 1 and GEM 2
 923 are introduced as a free parameter in the simulations in order to describe the experimental results.

924 Figure 5.10 shows the probability distribution of the minimum distance between holes for two randomly
 925 positioned GEM layers of $140\ \mu\text{m}$ pitch. The mean and most probable values of the distribution are
 926 $50\ \mu\text{m}$ and $70\ \mu\text{m}$, respectively; therefore, a misalignment of $50\ \mu\text{m}$ is a reasonable value.

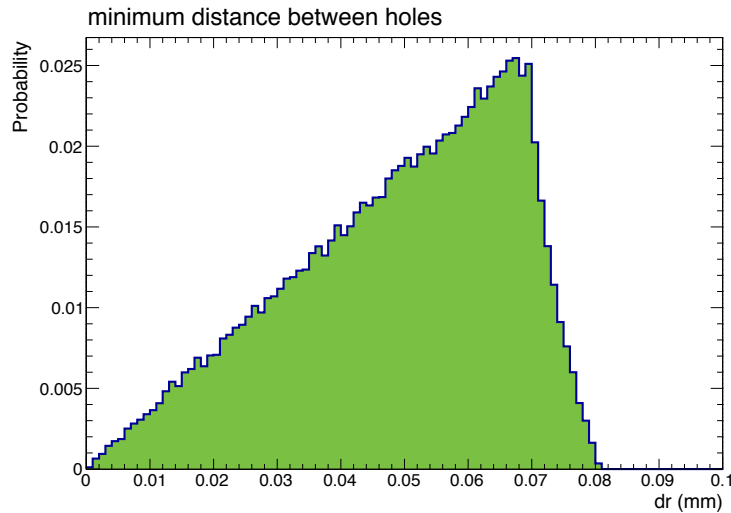


Figure 5.10: Probability distribution of the distance between closest holes in two randomly aligned GEM layers with pitch $140\ \mu\text{m}$.

927 Figure 5.11 shows ion backflow in a 3-GEM stack as functions of E_{T1} and E_{T2} in Ne-CO₂-N₂ (90-10-5)
 928 for a misalignment of $45.9\ \mu\text{m}$. Although some difference in IB is observed for $E_{T2} \geq 0.7\ \text{kV/cm}$ and
 929 $E_{T1} \leq 3.5\ \text{kV/cm}$, the measured ion backflow for $E_{T2} \leq 0.6\ \text{kV/cm}$ is well described by the simulations.

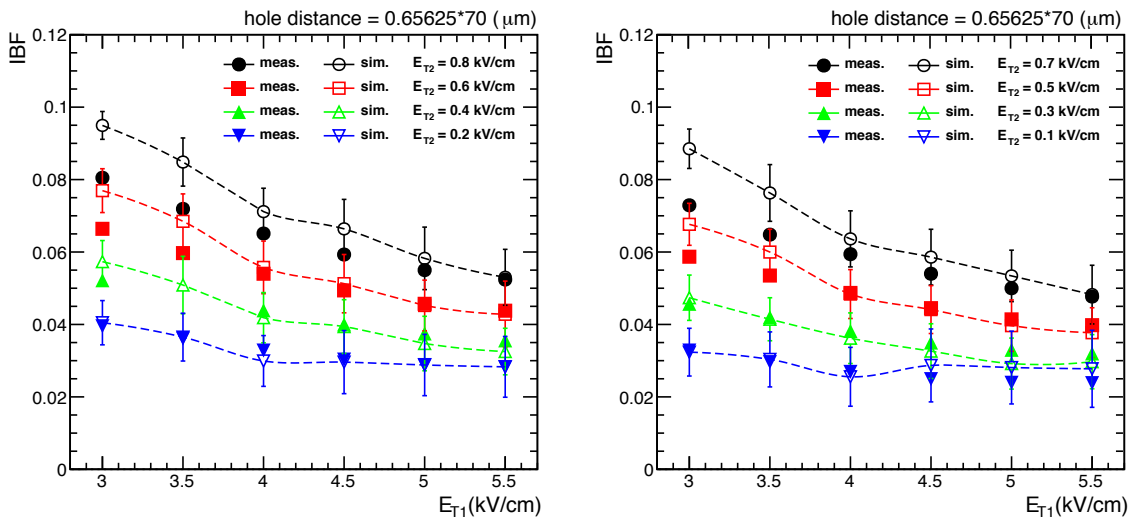


Figure 5.11: Ion backflow in Ne-CO₂-N₂ (90-10-5) as function of E_{T1} for different settings of E_{T2} for a triple GEM configuration. The data from measurements (closed symbols) and simulations (open symbols) with a misalignment of $45.9\ \mu\text{m}$ is distributed on the two panels for better visibility.

930 As E_{T2} decreases and E_{T1} increases, the number of ions drifting back into the drift region from GEM 3
 931 is reduced and the contribution of ions from GEM 2 becomes relatively large. The consistency of the
 932 misalignment values used in the simulations has been checked by comparing measurements of the ion

backflow performed with the same detector setup but with different gas mixtures: Ar-CO₂, Ne-CO₂, and Ne-CF₄. The measurements are always reproduced best in the simulations when using misalignment values between 40 and 50 μm . The uncertainties in the mobility, longitudinal and transverse diffusion of ions at low electric field, where no measurements exist, might add an additional systematic uncertainty to the comparison between simulations and measurements.

The measured ion backflow in Ne-CO₂-N₂ (90-10-5) with two different quadruple GEM configurations (with one and two large pitch foils) has been compared with the corresponding simulations. The results are shown in Fig. 5.12. In the simulations various combinations of misalignment for GEM 2 and GEM 3 were considered, otherwise the voltage settings are identical. In general, good agreement is achieved between simulations and measurements. In particular, the observed improvement from S-S-LP-S to S-LP-LP-S is well described by the simulations. This indicates that the qualitative behavior of multi-GEM stacks in terms of ion backflow is well understood, in spite of an incomplete knowledge of ion transport parameters and the uncertainty expected from alignment.

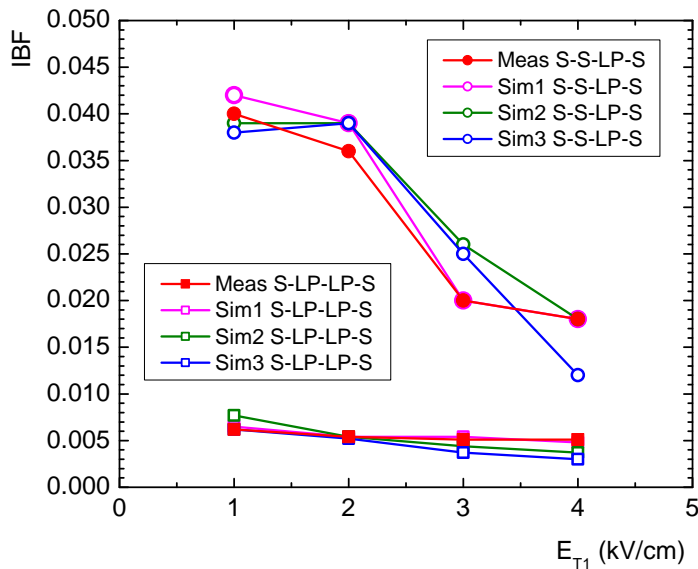


Figure 5.12: Comparison of ion backflow simulations (open symbols) with measurements (closed symbols) as a function of E_{T1} in Ne-CO₂-N₂ (90-10-5) for two quadruple GEM configurations. The circles represent an S-S-LP-S arrangement, where the voltages across the GEMs are 220, 270, ~ 275 and ~ 280 V, respectively. The squares represent an S-LP-LP-S arrangement, where the voltages across the GEMs are 230, 280, ~ 290 and ~ 320 V, respectively. For both arrangements the comparison has been done for $E_{T2} = 3.7$ kV/cm, $E_{T3} = 0.2$ kV/cm and $E_{\text{ind}} = 4$ kV/cm. In the measurements the gain is adjusted to 2000, and the simulations follow the same settings. The different simulation setups labeled Sim 1 to Sim 3 were performed with three different sets of foil misalignment.

946 5.2 Full-size IROC prototype

947 A full-size prototype of a TPC Inner Readout Chamber (IROC) equipped with a triple GEM readout stage
 948 was built. The goal was to study aspects of GEM integration on a large-size chamber and to validate the
 949 dE/dx capabilities of a GEM-based TPC. Moreover, issues of operational stability are studied under
 950 LHC running conditions.

951 5.2.1 Detector design

952 The prototype is assembled on a spare MWPC IROC of the TPC [13]. It is a trapezoidal chamber with
 953 dimensions $497 \times (292 - 467)$ mm². The chamber, after removing the wires, was equipped with three
 954 GEM foils. The mechanical structure of the chamber is described in Sec. 4.2.

955 ***GEM foils***

956 Four large area GEM foils were produced at CERN using the single-mask technique. The top side of the
 957 trapezoidal foil is segmented into 18 individually powered sectors with an area of $\sim 100\text{cm}^2$ each (see
 958 Fig. 5.13). The inter-sector gap is $400\mu\text{m}$, the same as the thickness of the spacer grid of the mounting
 959 frames (see next paragraph). An additional $100\mu\text{m}$ of copper between the edges of the sector and its
 960 active area (GEM holes) is added to account for possible misalignment during the production of the foil.
 961 The diameter of the biconical holes is $\sim 50\mu\text{m}$ (inner) and $\sim 80\mu\text{m}$ (outer). The hole pitch is $140\mu\text{m}$.

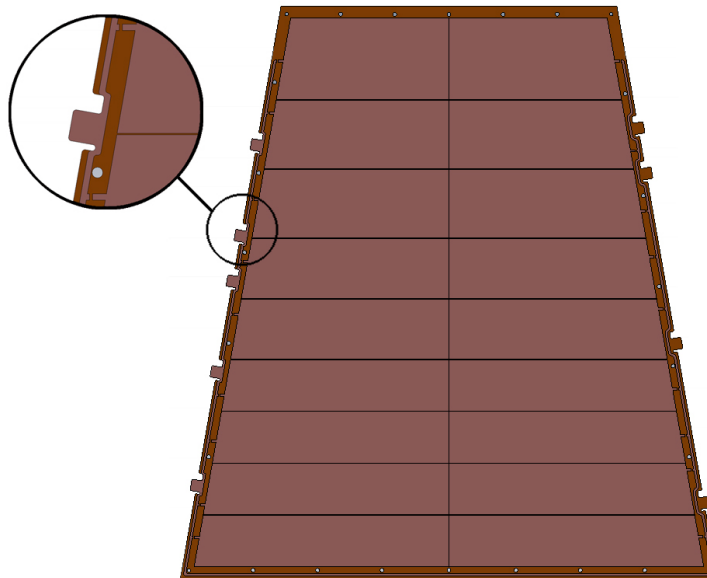


Figure 5.13: Layout of a prototype GEM foil; the top side is segmented into 18 sectors.

962 The HV distribution traces run along three sides of the foil. It consists of 2 mm copper paths and con-
 963 nection flaps (5 for the top side, 4 for the bottom). Sectors are powered in parallel loading resistors
 964 soldered directly on the foil in the designed place between the distribution path and a sector (more on
 965 HV supply in Sec. 5.2.4). The bottom (not segmented) side of the foil is connected directly to the HV,
 966 therefore no distribution path is needed.

967 ***Support frames***

968 The foils are glued on 2 mm fiberglass (G10) frames (see Fig. 5.14a) and then mounted in a stack. The
 969 frames contain a $400\mu\text{m}$ thick spacer grid whose role is to prevent the foils to approach each other due
 970 to electrostatic forces. Each grid is aligned with the sector boundaries, so no additional dead area is
 971 introduced.

972 When the stack is mounted, the loading resistors fit into grooves milled in the bottom side of the frame
 973 placed above. Framed foils, therefore, lie flat on top of each other with 2 mm distance between them.

974 The sides of the frames include grooves for the HV flaps and wires. They are aligned with feed-throughs
 975 machined in the alubody of the chamber (see Fig. 5.14b). The HV wire runs through this groove to the
 976 flap where it is soldered, as shown in Fig. 5.14c so that all material is contained within the dimensions
 977 of the alubody; this is necessary for mounting the readout chambers on the TPC endplates [13].

978 The frames, after production in the CERN workshop, were polished, cleaned in an ultrasonic bath and
 979 dried in an oven, in order to remove remaining pieces of fiber and dust of e.g. G10 material, which may
 980 spoil the electrostatic integrity of the foils.

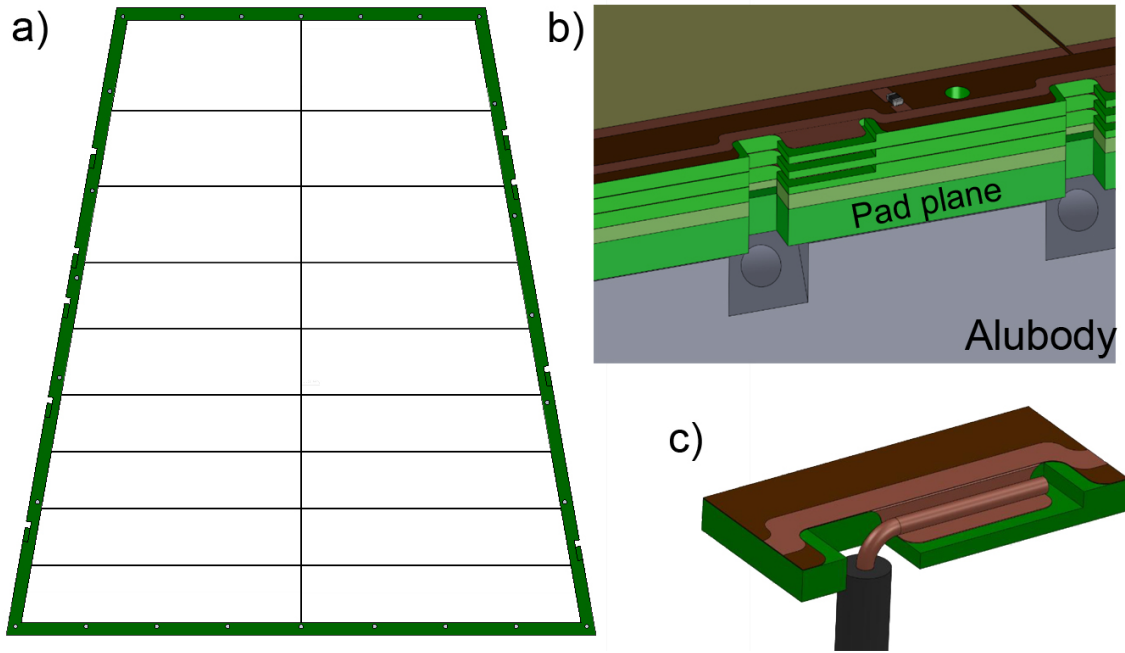


Figure 5.14: (a) Layout of the support frame. (b) Detail of the provisions for connecting each sector to its HV wire. (c) HV wire connected to the flap.

981 5.2.2 Quality assurance (QA)

982 All four foils are tested before and after framing to validate them for the final assembly. These tests
 983 include optical and high voltage tests, as foreseen for the large-scale production of the TPC chambers
 984 (see Sec. 4.7 for more details). In the following subsection, we will focus on the main results of the QA
 985 tests and its implications for the operation of the prototype.

986 *Optical check*

987 The main tasks of this QA step are to check the hole size uniformity across the GEM active area and
 988 to record the mechanical features of the foils. Large-size defects on the copper or Kapton layers may
 989 increase the probability of electrical breakdown. Big mechanical defects, like cuts, may result in short
 990 circuits between the top and bottom side of a foil.

991 The measured diameter of the inner (Kapton) holes varies between 40 and 50 μm . The outer (copper)
 992 holes have a diameter of 70 – 80 μm . The variations of the hole sizes may come from the etching process
 993 and are within reasonable limits. The pitch of $\sim 140 \mu\text{m}$ is constant over the foils, since it is defined by
 994 the printed mask. On the other hand, several local defects were indentified in all the foils, which made
 995 them not suitable for ideal operation. However, due to lack of spares, the foils were assembled in the
 996 prototype chamber for tests in the beam.

997 *HV tests*

998 A HV test is performed at each step of the detector assembly. The testing procedure is similar to the one
 999 which will be applied for QA of the final foils (see Sec. 4.7), therefore only a few particular aspects of
 1000 the procedure and the results are described in this subsection.

1001 During the HV test each sector of the foil is ramped up twice to 550 V while the surrounding sectors
 1002 are kept at ground potential. During the first ramp, the leakage current (I_{leak}) and the discharge rate are
 1003 measured at five voltage steps during the ramp. Sectors are connected via protection resistor with value
 1004 100 M Ω . Typical leakage currents vary between 0 and 0.3 nA. Sectors drawing currents higher than 5 nA
 1005 do not pass the test. Also, if the number of discharges at each ramping step exceeds 2 in about a minute,

1006 the procedure is stopped and the sector fails the test. For the second test, the sectors are ramped up to
 1007 550 V directly. To pass the test, a sector should stand at this potential without sparking for a few minutes.

1008 All foils (72 sectors) are tested before and after framing the foils. The results are summarized in Tab. 5.3.
 1009 Altogether, in the first HV check, 7 sectors failed the test; one sector featured a suspiciously increased
 1010 leakage current. After the framing procedure, however, 6 of these faulty sectors improved ($I_{\text{leak}} = 0.1 -$
 1011 0.3 nA , < 2 sparks per minute). Experience shows that while heating the foil for curing the epoxy (60°C
 1012 - see Sec. 5.2.3 for more details) often improves the HV stability of the foil (perhaps because the water
 1013 absorbed by the hygroscopic Kapton is evaporated). Two other sectors with relatively high leakage
 1014 currents were successfully recovered by conditioning them at high current limits (up to $1 \mu\text{A}$).

	before framing	after framing
high spark rate	6	0
$I_{\text{leak}} > 5 \text{ nA}$	1	2
$0.5 \text{ nA} < I_{\text{leak}} < 5 \text{ nA}$	1	0

Table 5.3: Results of the HV test of a total of 72 HV sectors on 4 GEM foils.

1015 Before assembling the detector, all sectors in all four foils were stable and had low and acceptable
 1016 leakage currents. During the HV tests the approximate positions of the observed sparks were noted but
 1017 no significant correlation was found between these spots and large defects observed in the first QA step.

1018 **5.2.3 Detector assembly**

1019 *Gluing the foils*

1020 All foils were glued onto the fiberglass (G10) frames. Before gluing, the foils are stretched on a pneu-
 1021 matic stretching tool with a tension of 10 N/cm . Once the foil is stretched, it is positioned on its frame
 1022 and aligned with metal pins. A heavy aluminum plate (milled in a way to prevent it from touching the
 1023 active area of the foil) is used to press the foil onto the frame. The epoxy used is ARALDITE 2011 [14].
 1024 The full assembly is kept for 24 hours under a hood heated to 60°C . Subsequent steps of the gluing
 1025 procedure are shown on Fig. 5.15.

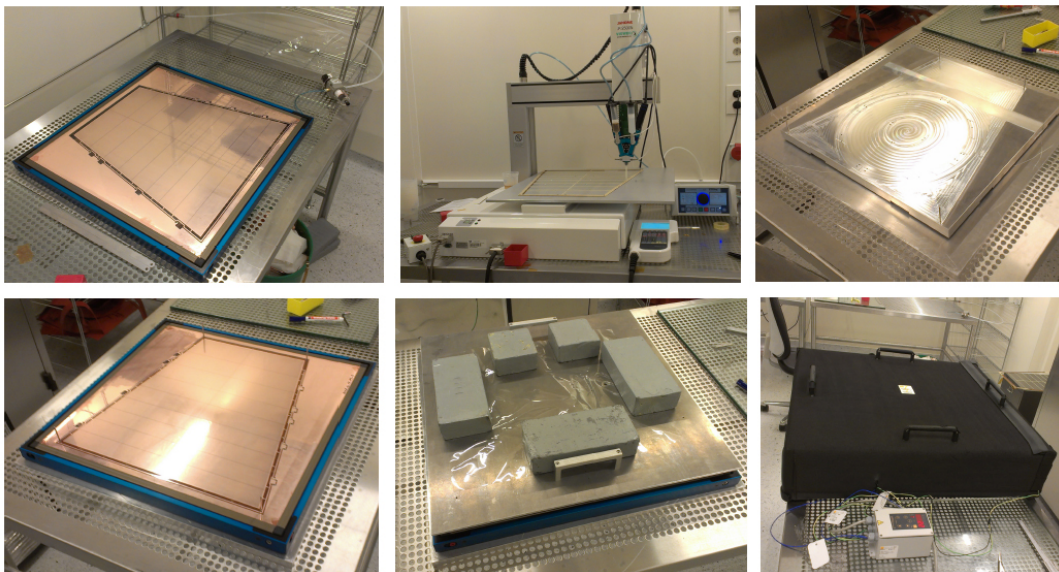


Figure 5.15: Foil gluing procedure. The different mounting steps are described in the text.

1026 **GEM stack**

1027 After gluing, the remaining material surrounding the frames is cut off, and the framed foil (see Fig. 5.16a)
 1028 is ready for a new HV test. After the test, the loading resistors (1 and 10M Ω SMD)
 1029 are soldered as shown in Fig. 5.16b. Next, the three foils are mounted in a stack on the alubody of the chamber,
 1030 with the unsectorized side facing the pad plane. Exceptionally, for this prototype an additional frame was
 1031 mounted between the last (bottom) GEM foil and a pad plane in order to increase the induction gap from
 1032 2 to 4 mm.

1033 Six HV wires are soldered to the HV flaps on each foil. High voltage is applied to the wires via SHV
 1034 connectors on the other side of the alubody. The wires run through feed-throughs drilled in the aluminum
 1035 frame of the chamber, which are then sealed with epoxy. The GEM stack is finally screwed to the alubody
 1036 with nylon screws.

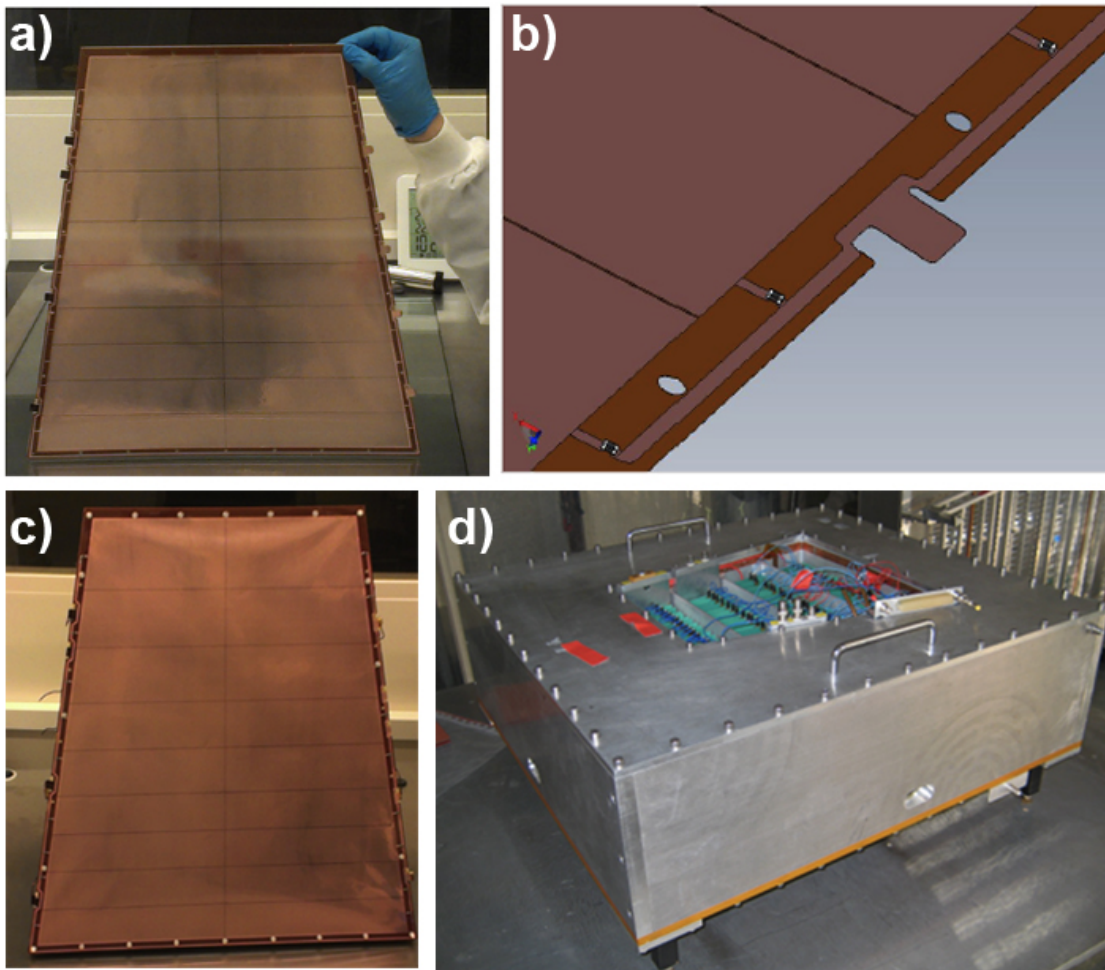


Figure 5.16: (a) Framed GEM foil (b) HV connection to a GEM sector through the loading resistors. (c) GEM stack mounted on the alubody. (d) chamber mounted in the test box.

1037 **Test box with field cage**

1038 The chamber is mounted in a test box (see Fig. 5.16d), which contains a drift cathode and a rectangular
 1039 field cage with dimensions of $57 \times 61 \text{ cm}^2$. The drift electrode is made of $50 \mu\text{m}$ aluminized Kapton
 1040 foil. The field cage has 8 field-defining strips (see Fig. 5.17) with a pitch of 15 mm. The strips are
 1041 interconnected with 1 M Ω resistors.

1042 The maximum drift distance to GEM 1 is 10.6 cm. The last strip of the field cage is located 1 mm below

1043 the position of that foil (see Fig. 5.17). Therefore, the potential of the last strip, which is grounded via a
 1044 $3.33\text{ M}\Omega$ resistor, is adjusted by applying a voltage in order to match the drift field at the top electrode of
 1045 GEM 1.

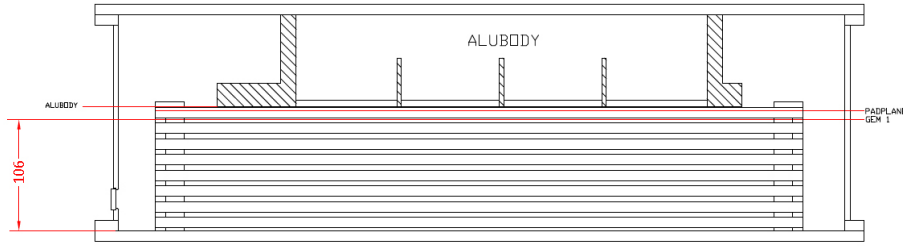


Figure 5.17: Cross section of test box with field cage and mounted IROC. The position of the first foil in the GEM stack is marked by a red line and labeled.

1046 Two walls of the test box, closest to the parallel sides of the chamber, were machined to install mylar
 1047 windows for measurements with beam and radioactive source.

1048 **5.2.4 HV supply**

1049 The detector is powered using an ISEG EHS 8060n 8-channel 6 kV high voltage module for the three
 1050 GEM foils and the last strip voltage of the field cage, and by an ISEG HPn300 30 kV module for the
 1051 drift electrode. The system features high precision current measurements (resolution 1 nA) on each HV
 1052 channel, adjustable ramp speeds and full remote control, which allows a global shutdown in case any
 1053 channel trips. The powering scheme of the GEM-stack is displayed in Fig. 5.18.

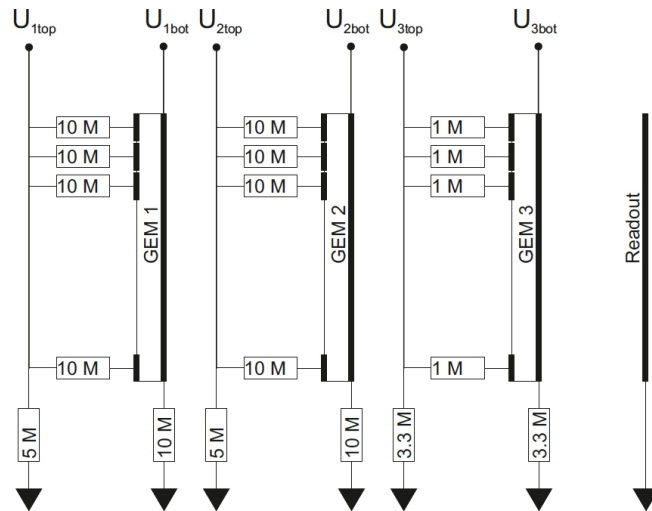


Figure 5.18: Schematics of the HV distribution of the prototype, showing the loading and grounding resistors.

1054 Loading resistors (R_L) are installed for each sector on the top side of each foil. In addition, each channel
 1055 is grounded through grounding resistors (R_G). Placing loading resistors on the top side of the foil assures
 1056 that in case of a discharge across a foil, the voltage drop occurs only on the top side, whereas the bottom
 1057 side stays at its nominal potential. This helps prevent the propagation of the discharge to the next foil or
 1058 to the pad plane and readout electronics. Moreover, in case of occasional sparks, the loading resistors
 1059 limit the current supplied by the power supply before it trips. Loading resistors also decrease the current
 1060 flowing through the sector in case of a short circuit between top and bottom sides of the foil.

1061 The values of R_L were chosen keeping in mind the current densities expected in the future Pb–Pb collisions
 1062 at 50 kHz at a gain of 2000, which is roughly $5\text{ nA}/\text{cm}^2$ (500 nA per GEM sector). Such a current

1063 may result in a significant potential drop across a large loading resistor, thus reducing the gain. Therefore
 1064 $10\text{M}\Omega$ resistors were chosen for GEM 1 and GEM 2, whereas for GEM 3 $R_L = 1\text{M}\Omega$.

1065 Large resistors to ground for each channel are chosen to assure safe discharge of the GEM foils after
 1066 a HV trip. Such connection will result in a constant DC current to ground which must not exceed the
 1067 current limit of each channel. On the other hand, in case of a short across a foil in one or several sectors,
 1068 the rest of the sectors should remain fully operational. Therefore, the value of R_G on the top side should
 1069 be high enough to allow sufficient current supply through the shortened sectors, whereas the resistor to
 1070 ground for the bottom side should be as low as possible in order to avoid reverse currents into the HV
 1071 supply. The HV powering scheme with the chosen loading and grounding resistors is shown in Fig. 5.18.

1072 Each sector can be treated as an individual capacitor in parallel with the other sectors on the foil. A time
 1073 constant RC for (dis-)charging the foil is given by the full capacitance to the foil and the sum of loading
 1074 and grounding resistances. In case the time constant is higher for the top side of the foil than for the
 1075 bottom one, the potential of the top electrode may decrease to zero slower than the bottom one. This
 1076 would result in a sudden increase of the potential difference between the electrodes which may lead to
 1077 breakdown or even damage of the foil.

1078 The example described above is simplified and does not take into account other parasitic elements or the
 1079 influence of different elements in the HV circuit on each other. Nevertheless, it shows the importance
 1080 of a proper choice of all electronic elements in the HV circuit used for powering the GEM stack. The
 1081 final choice of the grounding resistors was done after performing a set of transient SPICE simulations
 1082 and measurements of the discharge decay times. For the measurements a model of a GEM foil was made
 1083 with equivalent capacitors and resistors corresponding to the GEM assembly. The voltage difference
 1084 across both sides of the equivalent GEM was recorded on an oscilloscope. The values of the grounding
 1085 resistors were $5\text{M}\Omega$, $5\text{M}\Omega$ and $3.33\text{M}\Omega$ for the top side of GEM 1, GEM 2, GEM 3, and $10\text{M}\Omega$, $10\text{M}\Omega$
 1086 and $3.33\text{M}\Omega$ for the bottom sides, respectively. This configuration allows to run the detector with several
 1087 shortened sectors in GEM 1 or GEM 2 and up to 2 shortened sectors in GEM 3, using the HV settings
 1088 described in the next paragraph.

1089 *HV settings for the prototype*

1090 We work with two groups of HV settings: the so-called "standard" settings, typically used for triple GEM
 1091 structures, and the so-called "ion backflow (IBF) settings", where the field configurations are aimed at
 1092 minimizing the ion backflow. Each setting can be scaled in order to vary the total gain. Both are defined
 1093 in Tab. 5.4.

	Standard	IBF
Drift Field	0.4kV/cm	0.4kV/cm
ΔU_{GEM1}	276 V	225 V
Transfer Field 1	2.57kV/cm	3.8kV/cm
ΔU_{GEM2}	252 V	235 V
Transfer Field 2	2.57kV/cm	0.60kV/cm
ΔU_{GEM3}	221 V	285 V
Induction Field	2.57kV/cm	3.8kV/cm

Table 5.4: Standard and ion backflow high voltage settings for a gain of ~ 2000 in Ne-CO₂ (90-10).

1094 The standard settings are inherited from the COMPASS experiment [15] where GEM detectors are op-
 1095 erated in Ar-CO₂ (70-30). In Ne-CO₂ (90-10) however, since the amplification in this mixture starts at
 1096 lower electric fields, a scaling factor (SF) between 69 – 73 %, resulting in gains between 2000 and 6000,
 1097 is applied. The standard settings are optimized for maximum stability according to the principles of
 1098 stable operation described in [16]. The highest amplification takes place in the first GEM and decreases
 1099 in subsequent stages. These settings however are not optimized for minimum ion backflow. In the case

1100 of the ion backflow configuration, where the voltages were optimised in the lab, only the GEM voltages
 1101 ($\Delta U_{\text{GEM}i}$) were scaled with factors of 100, 103, 105 and 107 %. In addition four different values of E_{T2}
 1102 were used: 200, 400, 600 and 800 V/cm. Combining different values of SF and E_{T2} together 16 ion back-
 1103 flow settings were tested. The value of the ion backflow for these settings, in Ne-CO₂ (90-10), varies
 1104 between 3 % and 6.5 %. The approximate gains for all 16 combinations of ion backflow settings vary
 1105 between 1000 and 6000. The highest amplification in this configuration occurs in GEM 3.

1106 The nominal drift field of the ALICE TPC, $E_{\text{drift}} = 400 \text{ V/cm}$, is also applied to the prototype. The
 1107 potential on the last strip of the field cage is equal to the potential on GEM 1 top.

1108 5.2.5 Prototype commissioning

1109 The prototype in the test box was tested in the lab with Ar-CO₂ (90-10) and Ne-CO₂ (90-10) gas mixtures,
 1110 with standard HV settings, and irradiated with a ⁵⁵Fe X-ray source.

1111 For the commissioning of the detector, ~ 250 pads ($\sim 75 \text{ cm}^2$) were connected to a charge sensitive pream-
 1112 plifier and the signal was digitized with a multi-channel analyzer for measuring the X-ray spectrum. A
 1113 picoammeter is used to measure the gain by counting the rate of absorbed X-rays in the gas and measur-
 1114 ing the current in the pad plane. Figure 5.19 shows the measured effective gain of the chamber for both
 1115 gas mixtures.

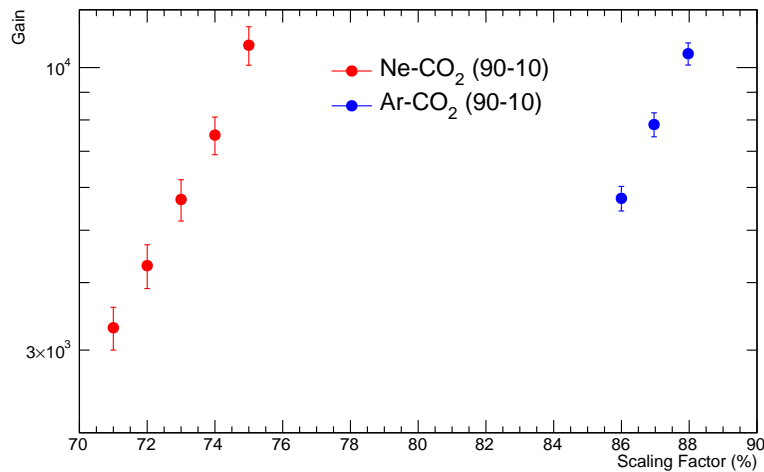


Figure 5.19: Effective gain of the chamber as a function of HV, expressed in terms of the scaling factor of the standard settings.

1116 Figure 5.20a shows the energy spectrum of ⁵⁵Fe obtained in Ar-CO₂ (90-10) at 86 % of the standard
 1117 settings, which corresponds to a gain of around 6000 (see next paragraph for more details). Figure 5.20b
 1118 shows the spectrum obtained in Ne-CO₂ (90-10) at 75 % of the standard settings, which corresponds to a
 1119 gain of around 11000. The energy resolution of the main peak for both measurements is $\text{FWHM} \approx 25 \%$.

1120 5.2.6 Test campaign at the CERN PS

1121 *Experimental setup*

1122 The dE/dx resolution of the GEM IROC prototype was evaluated in a test beam at the CERN PS with
 1123 beams of either e^+ and π^+ or e^- and π^- with momentum ranging from 1 to 6 GeV/c.

1124 For each type of beam both standard and ion backflow high voltage settings are used (see Sec. 5.2.4).
 1125 The drift field is 400 V/cm and the gas mixture Ne-CO₂ (90-10) as in the current TPC. Two scintillators
 1126 are used for beam definition, and a Cherenkov counter and a Pb-Glass calorimeter are used for online
 1127 particle identification.

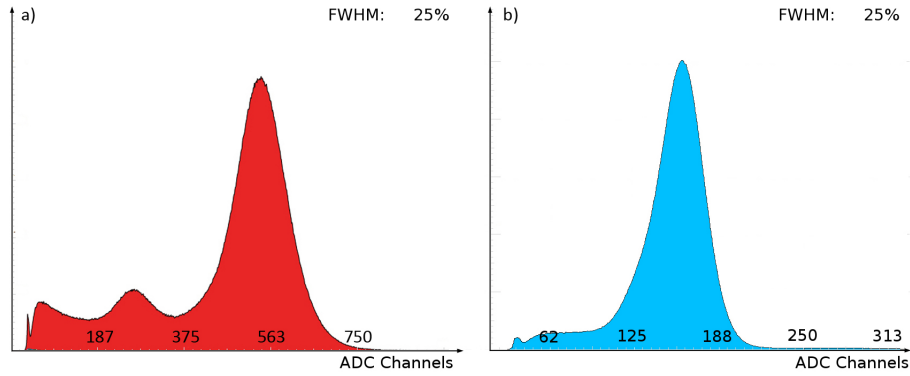


Figure 5.20: ^{55}Fe spectra obtained in Ar-CO₂ (90-10) (left panel) and Ne-CO₂ (90-10) (right panel).

1128 The prototype is equipped with 10 front-end cards, covering about 1200 pads (see Fig. 5.21a). The
 1129 readout electronics have been borrowed from the LCTPC (Linear Collider TPC) collaboration. The
 1130 width of the readout region is 6–7 cm (see Fig. 5.21b).

1131 The system has an RMS noise of about 600 electrons. The zero suppression threshold is 2 ADC counts,
 1132 corresponding to about 2000 electrons (120 ns peaking time and 12 mV/fC conversion gain). The sam-
 1133 pling frequency is 20 MHz.

1134 The FECs are read out using the current TPC readout system [13]: Two Readout Control Units (RCU)
 1135 send the data to a Local Data Concentrator PC, which contains the receiving ReadOut Receiver Card
 1136 (RORC) and runs the ALICE data acquisition system DATE. The corresponding trigger logic is handled
 1137 by a Local Trigger Unit (LTU) and a Busy Box [13]. Data transfer and trigger communication are based
 1138 on optical links. The beam detectors, scintillators, Cherenkov counter and Pb-Glass calorimeter, are
 1139 read out through a classic CAMAC system into a PC running a LabView acquisition system. In order
 1140 to synchronize the events from both systems, a busy logic is implemented in the CAMAC system which
 1141 incorporates the busy status of both systems. Thus, the CAMAC leads the acquisition. The two data
 1142 streams are subsequently merged into a single data file based on the proper synchronization of the trigger
 1143 and an event tag. This allows the online visualization of the detector response to different particle species,
 1144 as selected by the beam detectors.

1145 The average DAQ rate was 500 events/spill (where the spill length was 0.5 s) for a beam intensity of

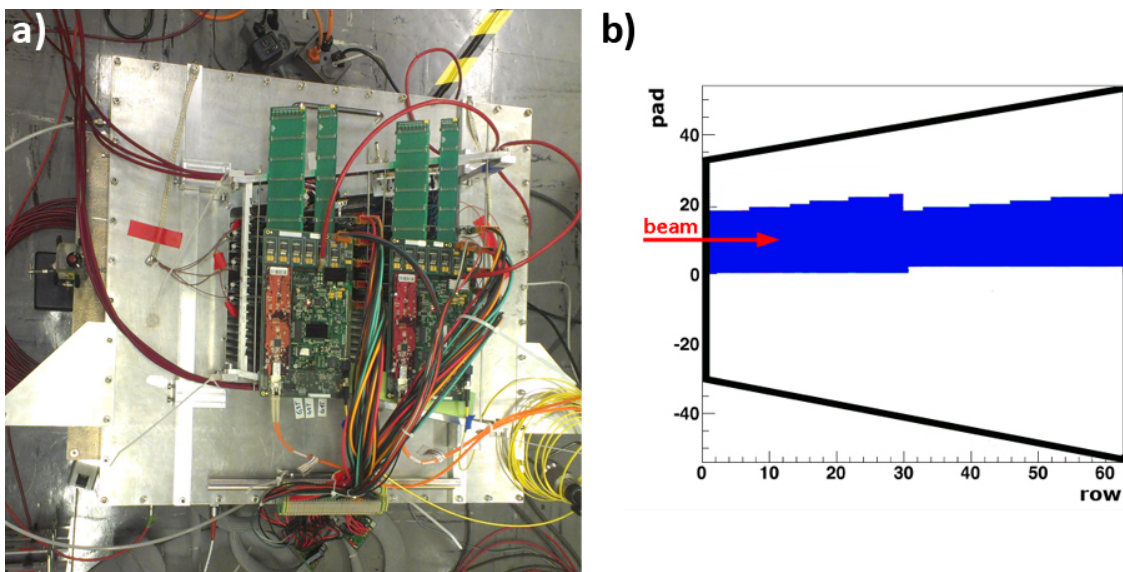


Figure 5.21: (a) Detector equipped with the front-end electronics. (b) Schematic view of the read out region of the chamber.

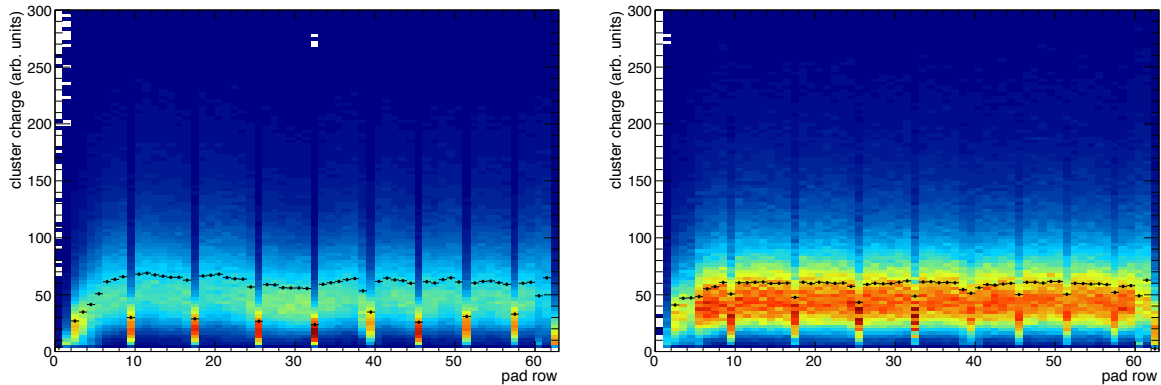


Figure 5.22: Gain profile before (left panel) and after (right panel) the gain equalization for the 63 pad rows. The structure of the spacer grid can be clearly seen in both panels.

1146 about 2000 particles/spill.

1147 *dE/dx measurements*

1148 For the measurement of the dE/dx resolution, only events with isolated tracks are selected. Additional
1149 cuts are applied on the number of clusters per track and the cluster drift time.

1150 Figure 5.22 (left) shows the distribution of cluster maxima as a function of the pad row number. The first
1151 rows show low amplitudes due to a mapping error in the readout electronics. Moreover, a few pad rows
1152 with low gain are observed. These are related to the HV sector boundaries and the position of the spacer
1153 grid. After gain equilibration, the overall spread is reduced (right) but the lower gain in the first pad
1154 rows and at the positions of the spacer is still visible. The calibration of these pad rows requires a more
1155 sophisticated procedure. For the present analysis, 17 low-gain pad rows out of 63 are excluded. It should
1156 be pointed out that the distance between the GEM sectors, $400\ \mu\text{m}$ in this prototype, (see Sec. 5.2.1) will
1157 be reduced by a factor of 2 in the final design (see Sec. 4.3.1). In addition, the number of spacer grid
1158 bridges in the support frames will also be reduced. No correction for pressure and temperature variations
1159 are applied because the runs are rather short.

1160 The dE/dx of each track is defined as the truncated mean of the 5–75 % highest of up to 46 cluster
1161 charges. An example dE/dx spectrum of $1\ \text{GeV}/c$ electrons and pions recorded at a gain of about 5000 is
1162 shown in Fig. 5.23. The dE/dx distributions are fitted with a Gaussian function to obtain the mean value
1163 $\langle dE/dx \rangle$ and the width of the distribution $\sigma(dE/dx)$. The relative resolution, defined as

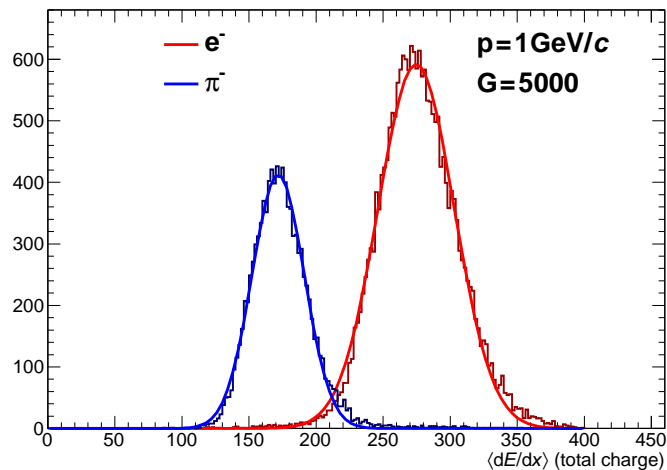


Figure 5.23: dE/dx spectrum of $1\ \text{GeV}/c$ electrons and pions at a gain of 5000.

$$\frac{\sigma(dE/dx)}{\langle dE/dx \rangle}, \quad (5.1)$$

1164 is derived for pions and electrons, for different momenta and HV settings. Figure 5.24 shows the results
 1165 obtained within this analysis. All ion backflow settings yield similar dE/dx resolution at a given beam
 1166 momentum and particle type. No significant dependence on the gas gain is observed within the range
 1167 under study. The results for the standard settings are slightly lower than those for the ion backflow
 1168 settings.

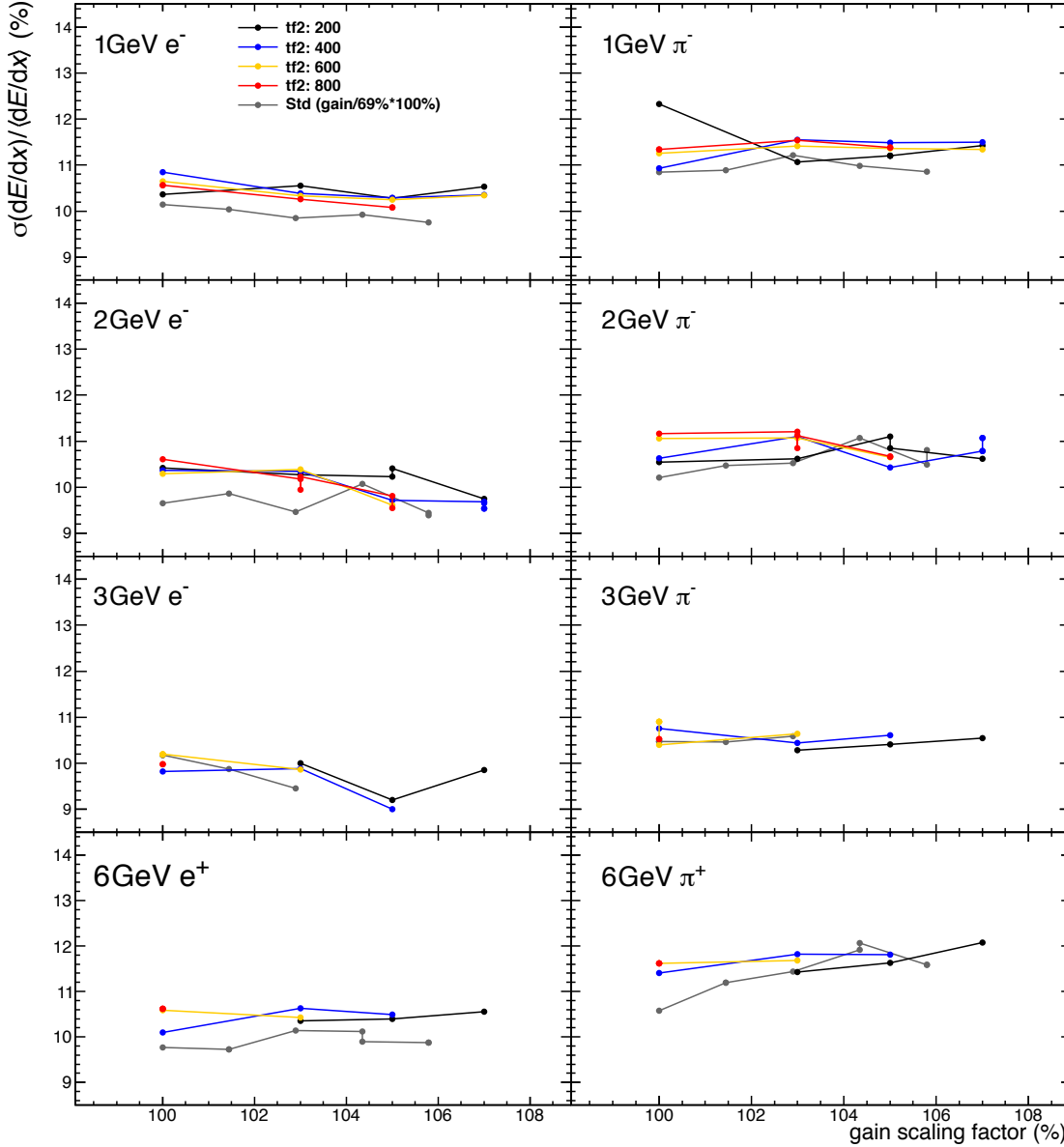


Figure 5.24: The relative dE/dx resolution measured for different HV settings for electrons and pions with momenta ranging from 1 to 6 GeV/c. Only 46 pad rows are used for the analysis. In the standard settings (grey curve) the gain ranges from 2000 to 6000; in the ion backflow settings (colourful curves) the gain spans between 1000 and 6000.

1169 The corresponding separation power, defined as

$$S_{AB} = \frac{2|\langle dE/dx \rangle^A - \langle dE/dx \rangle^B|}{\sigma(dE/dx)^A + \sigma(dE/dx)^B} \quad (5.2)$$

1170 for two particle types A and B, is shown in Fig. 5.25, for electrons and pions at all measured particle
 1171 momenta and HV settings. At a given beam momentum, asymptotic separation powers are reached for
 1172 gains above ~ 1500 .

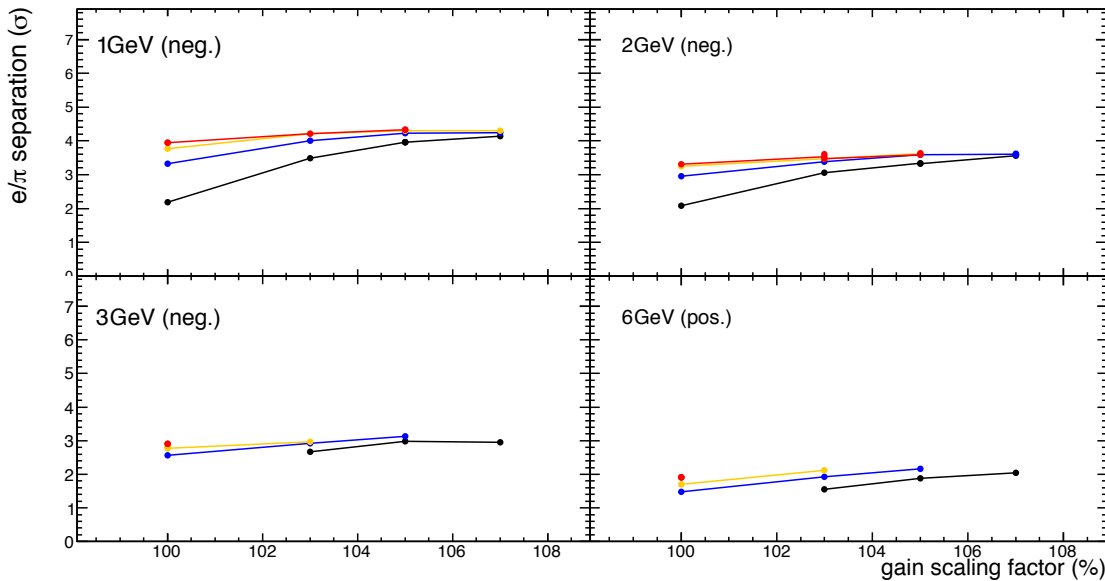


Figure 5.25: Separation power between pions and electrons with 1 – 6 GeV/c momentum measured for different HV settings. In the standard settings (grey curve) the gain ranges from 2000 to 6000; in the ion backflow settings (colourful curves) the gain spans between 1000 and 6000 (see Sec. 5.2.4 for more details).

1173 This dE/dx performance can be compared with results of a MC simulation shown in Fig. 5.26. The
 1174 simulated dE/dx spectrum for 1 GeV/c pions obtained with 46 pad rows in a GEM stack yields a relative
 1175 energy resolution of $\sim 10.5\%$. This is slightly better than our test beam results. It should be noted
 1176 that a slightly better resolution is expected for GEMs as compared to MWPCs. This is related to a
 1177 characteristic correlation of amplitude measurements in adjacent pad rows in MWPCs caused by the pad
 1178 response function. In GEMs, this correlation is much less pronounced. The dE/dx resolution observed
 1179 in the GEM IROC is compatible with that of the MWPC IROCs. These findings corroborate that the
 1180 dE/dx resolution of the upgraded TPC will be preserved.

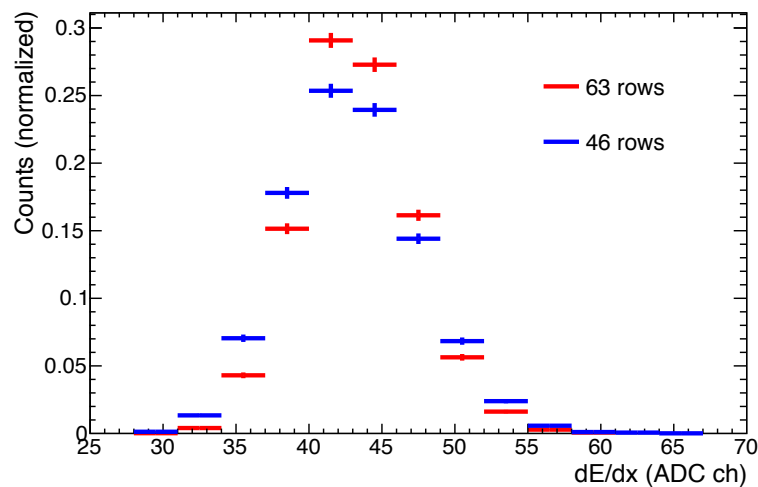


Figure 5.26: Simulated dE/dx spectrum for 1 GeV/c pions using information from all 63 rows (red) and for 46 rows (blue) as in the data from test beam. The resulting relative resolution is 10.5 % (9.0 %) for 46 (63) rows.

1181 Chapter 6

1182 Front-end electronics and readout

1183 This section reviews the requirements for the front-end electronics (FEE) and describes the general ar-
1184 chitecture and the basic building blocks of the readout chain.

1185 6.1 System overview

1186 The requirements for the front-end and readout electronics are derived from the detector performance
1187 requirements. The argumentation for many items is based on the successful implementation of the current
1188 TPC readout system (as described in [1, 2]). The three main changes for the front-end electronics with
1189 respect to the existing system are related to the new concept of continuously reading data from an ungated
1190 GEM TPC:

- 1191 1. The GEM readout provides signals with opposite polarity as compared to those generated in an
1192 MWPC.
- 1193 2. The continuous readout scheme necessitates the development of electronics that can concurrently
1194 sample the detector signals and transfer the acquired data off-detector.
- 1195 3. The continuous readout in conjunction with the step-up in interaction rate (and thus detector occu-
1196 pancy) leads to a strongly increased data throughput.

1197 The readout system for the GEM TPC is shown schematically in Fig. 6.1. The current signals are passed
1198 from the pads on the detectors readout plane to the front-end cards (FEC), located a few cm away, via
1199 flexible Kapton cables. In the FEC, a custom-made FE¹ ASIC², the SAMPA chip, processes the data
1200 from 32 individual front-end channels concurrently. The SAMPA is common among different ALICE
1201 subsystems (see Sec. 6.4). The first stage of the SAMPA is a charge-sensitive preamplifier and shap-
1202 ing amplifier, which transforms the currents induced in the pads into differential semi-Gaussian voltage
1203 signals. These signals are continuously digitized and processed by a DSP³. Concurrently, the acquired
1204 data are transferred to the GBTx ASIC [3], which multiplexes them and transmits them via the versatile
1205 optical link components [4] to a Common Readout Unit (CRU). Also the CRU is a common ALICE
1206 development. It serves as interface to the online farm, trigger and detector control system, and is situ-
1207 ated off-detector in a control room close to the online farm. The common ALICE electronics projects,
1208 SAMPA and CRU, are described in more detail in a separate Technical Design Report [5].

¹Front-End (FE)

²Application-Specific Integrated Circuit (ASIC)

³Digital Signal Processor (DSP)

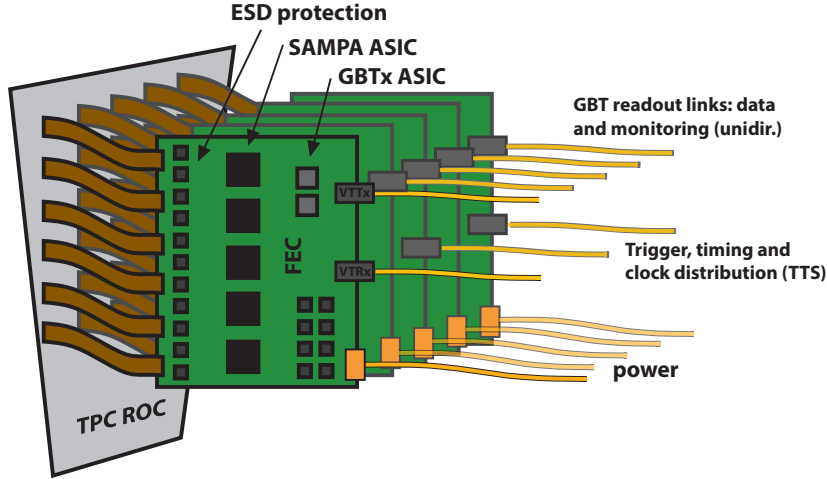


Figure 6.1: Schematic of the readout system of the GEM TPC. The two main building blocks of the FEE are shown: The front-end ASIC SAMPA on the front-end cards (FECs). The FECs connect to a Common Readout Unit (CRU), located off-detector in the control room, through radiation hard GBT links.

1209 In addition to the continuous readout mode, also a triggered mode has to be supported for calibration
 1210 purposes and for running at lower interaction and/or trigger rates. Here, the processing of the continu-
 1211 ously sampled data stream starts upon arrival of a first-level trigger; only the data corresponding to the
 1212 detector drift time ($t_d \approx 100 \mu\text{s}$) is frozen in the data memory and read out.

1213 6.2 Pileup and occupancies

1214 At Pb–Pb collisions with $\sqrt{s_{NN}} = 2.76 \text{ TeV}$ densities of primary tracks of $\langle dN_{ch}/d\eta \rangle_{cent} \approx 1600$ and
 1215 $\langle dN_{ch}/d\eta \rangle_{mb} \approx 400$ were measured for the most central collisions (0–5%) and for minimum bias colli-
 1216 sions, respectively [6]. By scaling with $s_{NN}^{0.15}$ [7] to the full LHC energy of $\sqrt{s_{NN}} = 5.5 \text{ TeV}$ this translates
 1217 to $\langle dN_{ch}/d\eta \rangle_{cent} \approx 2000$ and $\langle dN_{ch}/d\eta \rangle_{mb} \approx 500$ for central and minimum bias Pb–Pb collisions, re-
 1218 spectively.

1219 At 50 kHz interaction rate, the average number of interactions within a time window of $t_d \approx 100 \mu\text{s}$ is
 1220 $N_{pileup} = 5$. The expected primary track densities can be expressed conveniently by introducing an equiv-
 1221 alent charged-particle pseudo-rapidity density $dN_{ch}/d\eta$, which has the mean value $\langle dN_{ch}/d\eta \rangle_{equiv} =$
 1222 2500 for $N_{pileup} = 5$. For central events (embedded in 4 minimum bias events) the value is $dN_{ch}/d\eta|_{equiv} =$
 1223 4000 . This is still well below the primary charged particle multiplicity for central Pb–Pb collisions origi-
 1224 nally anticipated when the current TPC was designed ($dN_{ch}/d\eta \approx 8000$).

1225 The relative fluctuation of the number of charged tracks inside the TPC drift volume $\sigma_{N_{ch}}/\langle dN_{ch}/d\eta \rangle_{equiv}$
 1226 can be written as

$$\frac{\sigma_{N_{ch}}}{\langle dN_{ch}/d\eta \rangle_{equiv}} = \frac{1}{\sqrt{N_{pileup}}} \sqrt{1 + \left(\frac{\sigma_{N_{MB}}}{\mu_{N_{MB}}} \right)^2}. \quad (6.1)$$

1227 With $N_{pileup} = 5$ and the relative fluctuation of the number of minimum bias events $\sigma_{N_{MB}}/\mu_{N_{MB}} \approx 1.15$ this
 1228 leads to $\sigma_{N_{ch}}/\langle dN_{ch}/d\eta \rangle_{equiv} \approx 0.68$. The relative fluctuations of the equivalent multiplicity as a function
 1229 of N_{pileup} are depicted in Fig. 6.2. For $N_{pileup} = 5$ the equivalent multiplicity will stay below $(1 + 3 \times$
 1230 $0.68) \langle dN_{ch}/d\eta \rangle_{equiv} \approx 7500$ for 99.7% (corresponding to $3\sigma_{N_{ch}}$) of the time intervals ($\sim 100 \mu\text{s}$).

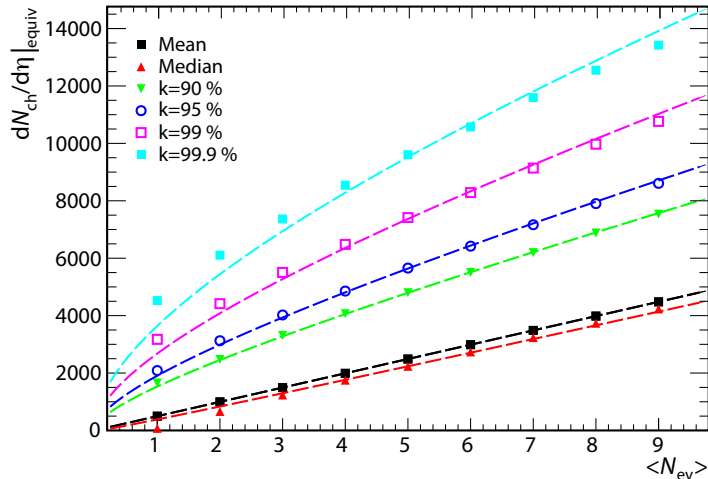


Figure 6.2: Equivalent multiplicity as function of mean number of events including k th order statistics (the k th-smallest value). E.g. at 50 kHz collision rate (for $N_{pileup} = 5$) there is a $< 1\%$ probability that the equivalent multiplicity is larger than 7500.

1231 6.3 Data rates and bandwidth considerations

1232 The following estimates of data rates are based on measured sizes of isolated events (no pileup). We
 1233 assume unchanged shaping, sampling and zero suppression parameters of the FE ASIC. In RUN 1 the
 1234 size of minimum bias TPC events for $\sqrt{s_{NN}} = 2.76$ TeV Pb–Pb collisions is 13.6 MByte. Several factors
 1235 have to be considered when extrapolating the data volume to RUN 3. An increase of the pad occupancies⁵
 1236 by a factor 1.25 must be expected due to the larger charged particle multiplicities at $\sqrt{s_{NN}} = 5$ TeV.
 1237 Moreover, an additional factor of 1.25 accounting for the deterioration of the compression ratio of the
 1238 zero suppression and run-length encoding must be incorporated at these larger occupancies⁶. On the other
 1239 hand, the cluster sizes are reduced by a factor 0.8 due to the new readout technology (see Fig. 4.18), and
 1240 overlap of clusters reduces the data volume by a small factor. With these considerations in mind we
 1241 conservatively assume an average event size of 20 MByte for an isolated event in the TPC.

1242 An average data rate from the TPC of $50\text{kHz} \times 20\text{MB} = 1\text{TByte/s}$ is expected for RUN 3. The average
 1243 pad occupancies will be around 15 %, increasing to up to 27 % for the innermost pad row, as can be seen
 1244 in Fig. 6.3. For a central event at $R_{int} = 50\text{kHz}$ we find occupancies of up to 42 % for the innermost pad
 1245 row, but even more extreme variations should be considered: for $dN_{ch}/d\eta|_{equiv} = 7500$ occupancies of
 1246 up to 80 % may be occasionally reached.

1247 Table 6.1 summarizes the number of front-end channels, the bandwidth requirements (based on the aver-
 1248 age expected occupancies) and the resulting distribution of FECs, SAMPAs, optical components (VTTx⁷
 1249 and VTRx⁸) and readout and TTS⁹ fibers. Here a segmentation of each TPC sector into 5 readout parti-
 1250 tions is used: 2 for the IROC and 3 for the OROC (following the GEM segmentation, Sec. 4.5).

1251 6.4 Common front-end ASIC

1252 The readout of the detector signals is done by a 32 channel FE ASIC that is developed as a common
 1253 solution for different ALICE sub-detectors. The concept assumes the integration of low-noise analog
 1254 components and continuously operating, digital functionality on the same silicon die.

⁵Pad occupancy is the fraction of samples within a given time window exceeding the zero suppression threshold.

⁶This is the worst case scenario. Overlap of the clusters will actually reduce the impact of this effect.

⁷Versatile Twin Transmitter (VTTx)

⁸Versatile Transceiver (VTRx)

⁹Trigger and Timing distribution System (TTS)

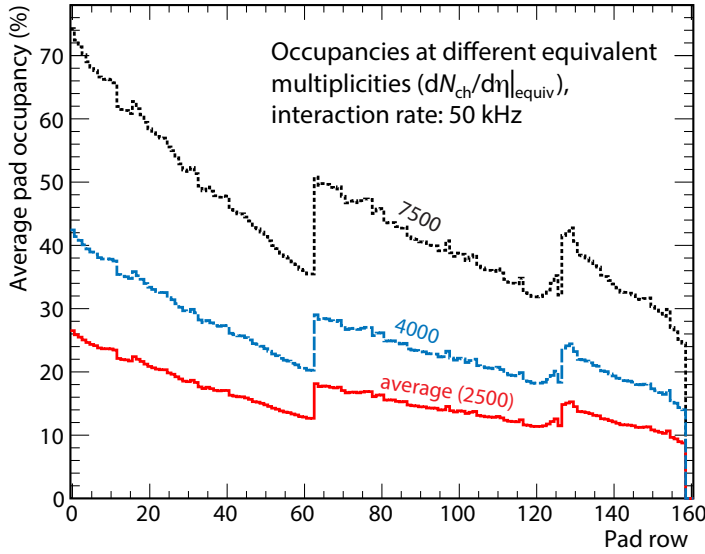


Figure 6.3: Expected average occupancies within a given time window for equivalent multiplicities of $dN_{ch}/d\eta|_{equiv} = 2500$, 4000 and 7500. The data is extrapolated using measured occupancies in isolated (no pileup) events recorded in 2010.

		IROC 1	IROC 2	OROC 1	OROC 2	OROC 3	TPC
Avg. data rate / chan.	(Mbit/s)	22	16	15	13	11	
Req. bandwidth / chan.	(Mbit/s)	40	30	30	25	20	
Front-end channels		2304	3200	2944	3712	3200	552,960
Total data rate	(Gbit/s)	50	50	45	50	35	8280
Total bandwidth	(Gbit/s)	100	100	90	100	70	
FECs (5 SAMPAs each)		15	20	19	24	20	3528
SAMPAs		75	100	95	120	100	17,640
GBTx ASICs		30	40	38	48	20	6336
Versatile link twin transmitter (VTTx)		15	20	19	24	0	2808
Versatile link transceiver (VTRx)		8	10	10	12	20	2160
GBT uni-directional data links (3.2 Gbit/s)		30	40	38	48	20	6336
GBT uni-directional TTS links		8	10	10	12	10	1800

Table 6.1: Data rates and bandwidth requirement and partitioning of SAMPAs, FECs, optical components, readout and TTS fibers with 5 readout partitions per TPC sector. The acronyms are explained in the text. The bandwidth need is calculated by using a safety factor of ~ 2 on the expected data rates. This factor depends on the occupancy distribution on the given readout partition and on the buffer size in the SAMPA. It is possible that the factor changes based on optimizations of the buffer size. The numbers in the last column show the sum over the 2×18 TPC sectors. The uni-directional versatile links [4] for the data to be sent to the CRU and online farm are driven by bi-directional optical transceivers (VTRx) or uni-directional twin transmitters (VTTx). Since the bandwidth needs in the up- and downstream directions are asymmetric, less VTRx are needed to receive trigger and timing information via the ALICE TTS⁴ system. We aim at installing one TTS link on every second FEC.

1255 The SAMPA project at the University of São Paulo in Brasil targets the design, simulation, fabrication,
 1256 experimental testing and validation of a signal acquisition and digital processing ASIC based on TSMC
 1257 0.13 μm mixed signal technology [5]. This ASIC will comply with the requirements defined by the
 1258 upgrade of the TPC, as well as the ALICE Muon tracking detector.

1259 **6.4.1 Overview**

1260 A schematic of the SAMPA is shown in Fig. 6.4. The data fed into each of the 32 channels is processed
 1261 by a PreAmplifier/ShAper circuit (we reuse the name PASA from the current system for this block), a
 1262 SAR¹⁰ ADC¹¹ and a DSP. Before being read out, the data are temporarily buffered in an event memory
 1263 and multiplexed. The PASA and DSP have configurable parameters that can be accessed via a common
 1264 logic and interface unit.

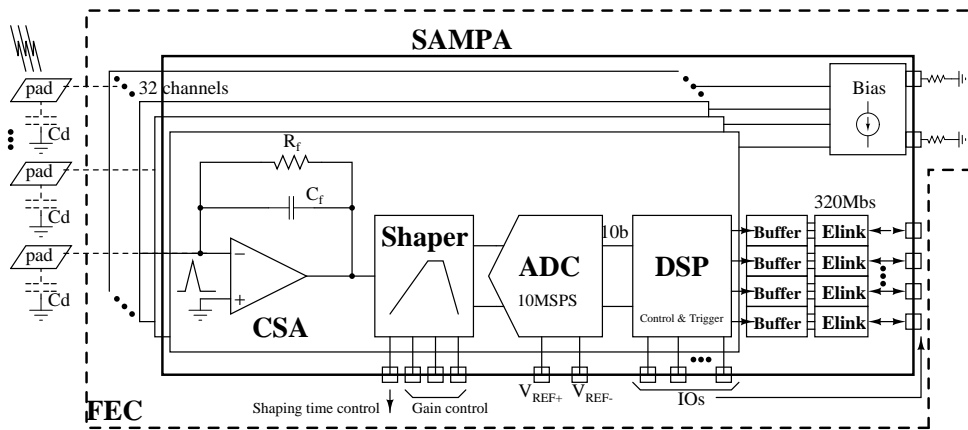


Figure 6.4: Schematic of the SAMPA ASIC for the GEM TPC readout, showing the main building blocks.

1265 **6.4.2 General requirements for the analog part**

1266 The requirements for the SAMPA are summarized in Tab. 6.2 and discussed in the following:

- 1267 – The requirement on the signal-to-noise ratio ($S:N$) is taken over from the current system [1, 2].
 1268 In order to reach the required detector resolution, a $S:N$ ratio¹² of 20:1 and 30:1 is required for
 1269 MIPs¹³ for the IROCs and OROCs, respectively. This can be achieved by applying an effective
 1270 gain of around 2000 in the GEM stack.
- 1271 – For a MIP, Q_{max} corresponds typically to a charge of 2 to 3 fC (1.25 to 1.875×10^4 electrons),
 1272 leading to an acceptable system noise level of 600 electrons (RMS). This value includes the con-
 1273 tributions from amplifier, ADC, ESD protection and the average detector capacitance.
- 1274 – A dynamic range of the electronics of 100 fC, allows the measurement of the ionization signals of
 1275 low momentum particles, which may produce signals 30 times larger than those of a MIP.
- 1276 – To minimize the quantization error¹⁴, the conversion to digital values should take place with a
 1277 precision of at least 10 bits.

¹⁰Successive Approximation Register (SAR)

¹¹Analog-to-Digital Converter (ADC)

¹²The $S:N$ ratio is calculated using the maximum pad and time bin for each charge cluster (Q_{max}).

¹³Minimum-Ionizing Particle (MIP)

¹⁴The RMS value of the quantization error is $1/\sqrt{12} \approx 0.29$ LSB. It becomes smaller with larger bit depth.

		RUN 1 (measured)	RUN 3 (requirement)
Signal polarity		Pos	Neg
Detector capacitance (range)	(pF)	12 – 33.5	12 – 33.5
MIP $S:N$ ratio (IROC)		14:1	20:1
	(OROC $6 \times 10 \text{ mm}^2$ pads)	20:1	30:1
	(OROC $6 \times 15 \text{ mm}^2$ pads)	28:1	30:1
MIP signal	(fC)	1.5–3	2–3
System noise (at 18.5 pF, incl. ADC)		670 e	600 e
PASA conversion gain (at 18 pF)	(mV/fC)	12.74	20 (30)
PASA return to baseline	(ns)	< 550	< 500
PASA average baseline value	(mV)	100	100
PASA channel-to-channel baseline variation (σ)	(mV)	18	18
PASA shaping order		4	4
PASA peaking time	(ns)	160	160 (80)
PASA crosstalk		< 0.1 %	< 0.2 %
PASA integrated non-linearity		0.2 %	< 1 %
ENC (PASA only, at 12 pF)		385 e	< 385 e
ADC voltage range (differential)	(V)	2	2
ADC linear range (differential)	(fC)	160	100 (67)
ADC number of bits		10	10
ADC sampling rate	(MHz)	10 (2.5, 5, 20)	10 (20)
Power consumption (analog & digital)	(mW/ch)	35	< 35

Table 6.2: SAMPA parameters for the current system (RUN 1) and the requirements for the upgraded front-end electronics (RUN 3).

- 1278 – The amplifier conversion gain has to be chosen such that the maximum expected output signal
1279 matches the PASA voltage swing and the input dynamic range of the ADC. The differential ADC
1280 input range of 2 V (peak-to-peak) requires a conversion gain of 20 mV/fC. In order to approxi-
1281 mately match the signal amplitudes in IROCs and OROCs a second conversion gain setting of
1282 30 mV/fC could be used in the IROCs. In this case the linear range is decreased from 100 fC to
1283 67 fC.
- 1284 – The large number of front-end electronics channels and a requirement for an overall power con-
1285 sumption < 20 kW gives a limit of 35 mW per channel. The heat is removed from the readout
1286 modules with the existing water cooling system (see Sec. 11.4.3).
- 1287 – Special care has to be taken to protect the system against potential corruption of data and control
1288 registers caused by radiation (Single Event Effects).
- 1289 – The electronics will be located in an area with limited access. High reliability is thus a requirement.

1290 6.4.3 Signal shaping

1291 The shaping parameters determine the size and shape of the individual charge clusters. The signal from
1292 an ionizing particle on an individual readout pad spreads in time due to the longitudinal diffusion D_L and
1293 due to the track inclination angle λ . The mean width in time of the charge clusters is given by:

$$\sigma_{\text{time}}^2 = \frac{1}{v_d^2} \left(D_L^2 z_d + \frac{\tan^2 \lambda L_{\text{pad}}^2}{12} \right) + \sigma_{\text{PASA}}^2, \quad (6.2)$$

1294 where z_d is the drift length for the given cluster and σ_{PASA} is the approximate sigma of the semi-gaussian
1295 signal output of the PASA. It is related to the shaping time t_{FWHM} like $\sigma_{\text{PASA}} \approx t_{\text{FWHM}}/2.4$. For Ne-CO₂-

1296 N_2 (90-10-5), the first term of Eq. (6.2) varies between 135 ns for tracks at mid-rapidity ($\eta = 0$, long drift
 1297 length) and 175 ns for tracks at $\eta \approx 0.9$ (see Fig. 6.5). A value of $\sigma_{\text{PASA}} = 80$ ns (160 ns peaking time,
 1298 190 ns FWHM), slightly shorter than the signal width, had been chosen for the current TPC readout [1]
 1299 in order to ensure that the cluster shape in time direction is not dominated by the PASA response. For
 1300 the upgraded system these considerations remain the same. Therefore, the same shaping parameters as
 1301 found in the current readout system can again be chosen.

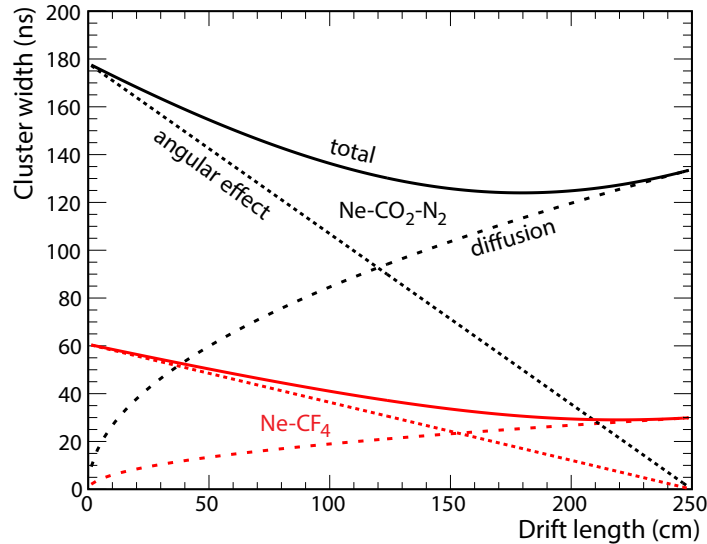


Figure 6.5: Length of clusters in time units for Ne- CO_2 - N_2 (90-10-5) and Ne- CF_4 (90-10), calculated using Eq. (6.2) at a radius in the center of the OROC medium pad region and without the contribution of σ_{PASA} .

1302 For a fast gas mixture (Ne- CF_4 (90-10)) the first term of Eq. (6.2) varies between 30 ns for tracks at mid-
 1303 rapidity and 60 ns for tracks at $\eta \approx 0.9$. Here a shorter peaking time of 80 ns represents the optimum,
 1304 keeping in mind that a shorter peaking time will have a negative effect on the noise.

1305 In summary, a peaking time programmable to at least two values (80 and 160 ns) satisfies the require-
 1306 ments for both gas mixtures.

1307 6.4.4 Noise

1308 The Equivalent Noise Charge (ENC) requirement of 600 e (mean system noise) is discussed in this sec-
 1309 tion. Such a low noise seems possible, judging from studies of the noise distributions on the current TPC
 1310 system and test data taken with the S-ALTRO demonstrator ASIC, as will be discussed in the following.

1311 *Noise on the current system*

1312 For the current TPC the ENC specification was < 1000 e at a total capacitance of 25 pF. The measured
 1313 noise distributions for all readout chambers and separately for the three different pad sizes (small pads on
 1314 IROC and medium and long pads on OROC) are shown in Fig. 6.6 (left panel). On the installed system a
 1315 noise of 0.71 LSB¹⁵ was achieved. At an average PASA gain of 12.74 mV/fC (at 18.5 pF average detector
 1316 capacitance), with 2 V linear range and with a 10 bit ADC this corresponds to an ENC value of 670 e.

1317 *Noise dependence on capacitance*

1318 The right panel in Fig. 6.6 shows how the noise correlates with the additional capacitances given by the
 1319 varying trace lengths on the padplane PCB¹⁶. A straight-line fit describes the data well and suggests a

¹⁵Least Significant Bit (LSB)

¹⁶Printed Circuit Board (PCB)

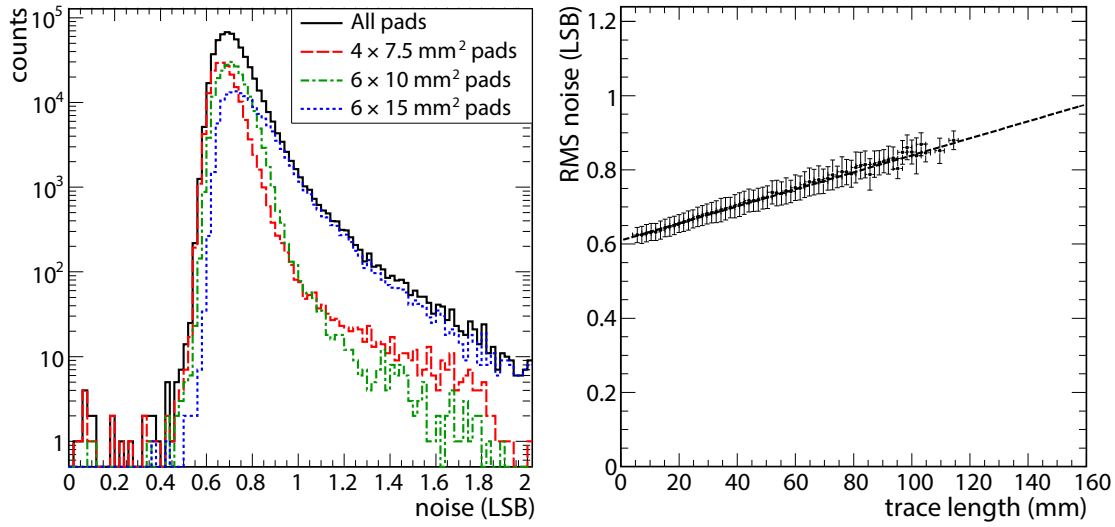


Figure 6.6: (Left) Noise distribution for all FEE channels on all readout chambers and separately for the different pad sizes for the current TPC [8]. (Right) Correlation of noise and the trace length on the padplane PCB for the medium-sized pads ($6 \times 10 \text{ mm}^2$). A straight-line fit describes the data well (compare to Tab. 6.3).

1320 capacitance of about 1.3 pF per cm of trace length. This correlation can be done for the different pad size
 1321 regions on the IROC ($4 \times 7.5 \text{ mm}^2$) and OROC ($6 \times 10 \text{ mm}^2$ and $6 \times 15 \text{ mm}^2$). The extracted noise features
 1322 are given in Tab. 6.3.

			IROC			OROC			System
Pad size		(mm^2)	4×7.5	6×10	6×15				
Trace length	(range)	(mm)	4.6–114.7	5.6–113.9	5.4–146.8				
	(mean)		39.2	45.5	60.2	47.1			
System noise	(mean)	(LSB)	0.67	0.7	0.78	0.71			
	(at zero tr. length)		0.589	0.603	0.624				
	(vs trace length)	(LSB/mm)	$2.1 \cdot 10^{-3}$	$2.2 \cdot 10^{-3}$	$2.3 \cdot 10^{-3}$	$2.2 \cdot 10^{-3}$			
PASA noise slope (simulated)		(e/pF)	17			17			
ENC	(most probable)	(e)	634	653	672	650			
	(PASA)		475	500	525	500			
	(ADC)			420		420			
Mean capacitance (extracted)		(pF)	17.4	18.8	20.2	18.5			

Table 6.3: System parameters and ENC values for the current TPC readout system (MWPCs and PASA) for the three different pad size regions [9, 10].

1323 Table 6.4 shows a breakdown of the capacitance contributions from individual elements for the current
 1324 system. The values range from 12 to 33.5 pF. For the upgraded system, a reduction of these values will
 1325 be very challenging, but could be possible by using wider flexible cables with larger distances between
 1326 the traces, a thicker pad plane PCB, a larger distance between the pad plane PCB and the metallic ROC
 1327 body (thicker *strong back*), as well as by possibly further minimizing the trace lengths.

	Capacitance (pF)			Mean
	IROC	OROC 6×10	OROC 6×15	
Chip packaging		2		2
Traces on FEC		1–3		2
Connector on FEC		0.5		0.5
Flexible cables (long)	7 (12)	7	7	7
Connector on padplane		0.5		0.5
Traces on padplane [range]	5 [0.5–14]	6 [1–15]	8 [0.5–20]	6
Pad to Ground	0.2	0.4	0.6	0.5
Sum [range]	17.2 [12–28]	18.4 [12.5–29]	20.6 [12–33.5]	18.5

Table 6.4: Contributions and sum (mean value and range in square brackets) of capacitances for the current TPC readout (MW-PCs and PASA) for the three regions with different pad sizes [9, 10].

1328 **Noise contributions**

1329 The theoretical noise of the amplifier alone¹⁷ is about 300 e at zero capacitance. On top, also the ADC
 1330 contributes to the total noise with both input-referred noise¹⁸ and quantization noise, which is the dif-
 1331 ference between the actual analog value and the quantized digital value of an ideal ADC. The total
 1332 contribution of the ADC is ~ 300 e, which must be added quadratically, yielding 420 e. The measured
 1333 noise values of 550 to 670 e include all other effects like the finite input capacitance, contributions from
 1334 board design, power and ground and pickup of different kinds.

1335 **Noise considerations for mixed analog and digital ASIC designs**

1336 The two major differences between the SAMPA architecture foreseen for the readout of the GEM TPC
 1337 (see Fig. 6.4) and the existing system based on the two ASICs PASA and ALTRO are:

- 1338 – The analog signals are being processed at the input of the chip while concurrently the previously
 1339 acquired data are processed and shipped off through the serial interfaces (continuous readout).
- 1340 – Low-noise analog components and complex digital functions are implemented on the same silicon
 1341 die.

1342 The feasibility of the second item was demonstrated by the Super-ALTRO (S-ALTRO) chip [11]. The S-
 1343 ALTRO is a 16 channel demonstrator ASIC that was designed with the readout of the ILC-TPC in mind.
 1344 On a small area (3.07 mm²/channel) sensitive analog components and massive digital functionalities are
 1345 integrated on the same chip. The S-ALTRO chip showed that by using careful design techniques the
 1346 effect of the integration on the noise performance is small.

1347 Each S-ALTRO channel contains a low noise PASA, a pipeline ADC and a DSP unit. The 10 bit ADC
 1348 samples the output of the PASA at a frequency of up to 40 MHz before providing the digitized signal to
 1349 the DSP which performs baseline subtraction, signal conditioning and zero suppression. The PASA used
 1350 in the S-ALTRO is based on the 16 channel Programmable Charge Amplifier (PCA16) prototype [12].
 1351 It is programmable in terms of gain and peaking time and can operate with both positive and negative
 1352 polarities of input charge.

1353 Table 6.5 gives an overview over simulated and measured ENC figures, comparing the performance of
 1354 the original TPC PASA to values from tests using the PCA16 and the S-ALTRO in different configu-
 1355 rations. System measurements with the PCA16 have resulted in ENC values on-detector¹⁹ of 0.52 LSB

¹⁷The main *amplifier noise* sources are the series thermal noise from the ESD protection circuit, the (flicker) noise from the input transistor and the parallel thermal noise from the feedback transistor.

¹⁸The ADC internal circuits produce a certain amount of *sampling noise* due to resistors and “ kT/C ” noise.

¹⁹The settings used were 120 ns peaking time and 12 mV/fC conversion gain.

1356 and 0.55 LSB, as measured by the ILC-TPC collaboration [13] and with the ALICE TPC GEM IROC
 1357 prototype in 2012, respectively²⁰. With the S-ALTRO demonstrator chip an ENC value of 547 e was
 1358 measured in a laboratory setup²¹ [11]. This value was achieved with a chip with the input pins unbonded.
 1359 It includes all other noise sources, in particular pickup from the DSP, but also random noise from PASA
 1360 and ADC and the quantization error.

		Current TPC (PASA)	PCA16	S-ALTRO	SAMPA
Simulated	(w/o ADC)	244e (@0 pF)	220e (@0 pF)	260e (@0 pF)	
		385e (@12 pF)	320e (@10 pF)		
		480e (@18 pF)			480e (@18 pF)
Measured	(w/o ADC) (Laboratory) (System)	385e (@12 pF)	270e (@10 pF)		
		570e (@12 pF)		547e (@0 pF)	
		670e (@18.5 pF)			

Table 6.5: Simulated and measured ENC values for the current readout (PASA) and for PCA16 and S-ALTRO²². A first simulation result for the SAMPA ASIC is also added²³. Note that often slightly different values of the input capacitance were used. Further relevant parameters influencing the ENC value are given in the footnotes.

1361 It can be concluded that the integration of low-noise analog components and complex digital functions
 1362 on the same silicon die is possible. The design experiences from the S-ALTRO demonstrator are carried
 1363 along to the design of the SAMPA. However, it remains to be seen if the data readout from the SAMPA
 1364 will introduce additional noise to what is acceptable from the digital activity in the ALTRO.

1365 6.4.5 Further requirements for the analog part

1366 Some further important requirements are given in the following.

- 1367 – The GEM readout provides signals with opposite polarity as compared to those common in MW-
 1368 PCs. Thus the signal polarity has to be programmable in order for the ASIC to work with both
 1369 GEMs and MWPCs.
- 1370 – The DC level of the PASAs differential output (baseline) should be kept at a value sufficiently close
 1371 to the bottom of the circuits dynamic range, in order to preserve the maximum dynamic range (see
 1372 Tab. 6.2).
- 1373 – The baseline values have to be very stable in time in order to guarantee that the zero suppression
 1374 can work efficiently.
- 1375 – The signals have to return to the signal baseline within < 500 ns without undershoot.
- 1376 – Synchronous pulsing of all 32 channels must be possible without loss of resolution.
- 1377 – Crosstalk between adjacent channels can deteriorate the energy and position resolution and, there-
 1378 fore, has to be kept below 0.2 %.

²⁰A conversion to ENC is difficult, since the exact conversion gain is unknown. At 12 mV/fC the measured values would correspond to 520 e and 550 e, respectively.

²¹The settings used were 120 ns peaking time, 12 mV/fC conversion gain and 1 V bias decay voltage. The CDM input pad was connected.

²²The used setting is 120 ns peaking time.

²³The used setting is 160 ns peaking time and 70 Ω resistance in the ESD network.

1379 **6.4.6 Electrostatic discharge protection**

1380 The input of the SAMPA may be exposed to ESD²⁴ events. Semiconductor devices usually offer device-
1381 level ESD protection based on the charge device model (CDM) or the human body model (HBM). How-
1382 ever, device-level ESD specifications may not be sufficient to protect the SAMPA when connected to a
1383 readout detector. Some experience with destructive discharges exists in the collaboration. The current
1384 TPC readout system was suffering from such events in the first two years of operation at the LHC. The
1385 destructive events could be traced to the energy stored in capacitors used in the HV network (4.7 nF). In
1386 case of a discharge inside the MWPC the charge stored in these capacitors ($6\ \mu\text{C}$) would be released and
1387 injected through the readout pad into a FE channel, making it insensitive to further signals. In certain
1388 cases, presumably for large discharge events, a low impedance path was produced between the power
1389 (Vdd) and ground planes of one amplifier. As a consequence, the voltage regulator on the corresponding
1390 FEC could not supply the nominal voltage any longer, making the whole FEC unusable. After removing
1391 the HV capacitors in 2011 the amount of stored energy was reduced by a factor 10. After this intervention
1392 no more destructive events have been observed.

1393 Models for discharges in gaseous detectors are not available. However, laboratory tests have been carried
1394 out using a capacitor connected to a needle with micrometric adjustment. The needle was lowered onto
1395 pads on a test board connected to the inputs of a PASA chip. The capacitor was charged to different
1396 voltages by a high voltage generator in order to simulate discharge events of different severity. Such
1397 discharges are probably different from those in a gaseous detector, but help to understand the limitations
1398 of the ESD protection. It was found that a charge of a few hundred nC is sufficient to destroy the ESD
1399 network at the input of a PASA channel. Larger charges of a few μC may create a short between Vdd
1400 and ground. By inserting resistors before the input to the PASA, the tolerated charge could be increased
1401 to the required level. However, quite large resistors had to be used (several hundred Ω).

1402 Problems with destructive discharges have appeared in a similar manner also during prototype GEM
1403 tests both in the ALICE test at the PS and with ILC-TPC prototype tests. In GEM detectors discharges
1404 generally begin with a sudden, radiation-induced breakdown of the gas rigidity in one GEM, normally
1405 the last in a cascade of multipliers. The capacitance of one GEM segment is slightly smaller than 5 nF
1406 and the charge stored is $1.5\ \mu\text{C}$. The discharge may propagate to other electrodes such that a fraction (up
1407 to all) of the stored charge can be delivered to the readout pad.

1408 Additional resistances and capacitances (protection diodes) at the input to the SAMPA will have a neg-
1409 ative impact on the noise performance. Therefore, the best strategy is to implement device-level ESD
1410 specifications based on the HBM and add system-level protection on the front-end card level after addi-
1411 tional testing to derive a realistic estimation of the expected ESD energy.

1412 **6.4.7 Analog-to-digital conversion**

1413 The analog signal output of the PASA is sampled, at a rate of 10 MHz, by an ADC with 10-bit dynamic
1414 range. The requirement on the power consumption (below 35 mW per front-end channel) calls for low
1415 power ADCs. This requirement can be met by SAR ADCs implemented with a low power switching
1416 technique. They allow implementations with a low power consumption around 2 mW per channel.

1417 *Sampling frequency*

1418 A shaper peaking time of 160 ns preserves partially the spatial characteristics of the drifting electron
1419 clusters (see Sec. 6.4.3). In RUN 1 it was found that this feature can be best taken advantage of in
1420 the clusterization process when a sampling frequency of 10 MHz is chosen. Consequently, also for the
1421 GEM TPC readout this sampling frequency represents the optimum. The maximum electron drift time

²⁴ElectroStatic Discharge (ESD)

of $\sim 100 \mu\text{s}$ is in this case divided into about 1000 time bins, each corresponding to a drift distance of about 2.8 mm.

For Ne-CF₄ (90-10) the reduced peaking time combined with the larger drift velocity make a faster sampling of 20 MHz plausible. The maximum electron drift time of $30 \mu\text{s}$ would in this case be divided into about 600 time bins, each time bin corresponding to a drift distance of 4.2 mm. The occupancy values presented in Sec. 6.2 will not change significantly. The shorter width of the charge clusters in time direction (factor ~ 2.5) will be almost completely compensated by the faster sampling rate.

6.4.8 Digital signal processor

After the ADC the TPC signal is processed by a set of digital circuits integrated into the DSP part of the SAMPA.

Pedestal subtraction

The DC level of the PASAs differential output (baseline or pedestal) has to be subtracted from the ADC output for each channel in order to perform efficient zero suppression. A fixed pedestal subtraction mode, where one value can be subtracted for each channel for all time bins, has shown to be sufficient for the current system. The baseline values are actually extremely stable over time, requiring only very rarely pedestal calibration runs; a feature that should be kept.

Digital filter

Since the GEM signals do not feature a tail, the necessity to minimize the pileup effect of subsequent signal tails by a tail cancellation filter is removed.

A calculation and subtraction of the moving average may help to correct possible perturbation of the baseline produced by non-systematic effects. The value to be subtracted from the current samples is the moving average of the signal itself and of some previous samples. Fast variations in the signal, like clusters, are excluded from the baseline calculation. Such a filter is implemented in the ALTRO ASIC but could not yet be successfully used during data taking. The reason lies in the fact that in rare cases the calculation of the value to be subtracted may fail, resulting in a pedestal shift and failure of the zero suppression.

Data compression using zero suppression

If no data compression were applied in the front-end electronics, the 552,960 readout channels of the GEM TPC would produce data at a rate of 7 TByte/s (100 Mbit/s per channel). To reduce this throughput, it is foreseen to compress the data via zero suppression (ZS). In this mode all data words are dropped inside the SAMPA if their value is so close to the reference level (baseline or pedestal) that they can be assumed to not contain any useful information. In practice, a fixed threshold is applied for the data in each channel, and only values above this threshold are kept. The resulting signal clusters are run-length encoded, which requires the addition of two extra words, describing the start time and length of the non-suppressed cluster.

To remove glitches, the minimum number of consecutive samples needed to define a valid signal can be configured²⁵. If needed, a number of pre- and post-samples that should be kept before and after a peak can be defined²⁶. In order to perform the zero suppression, the pedestal is subtracted. The zero suppression threshold is naturally determined as a multiple of the width of the baseline distribution (noise). Pedestal and noise values are measured in a dedicated pedestal run and the measured values for

²⁵A minimum of 2 consecutive time bins above threshold is required in the current readout system.

²⁶This feature is not used in the current readout system.

1462 each channel are then used to configure the filter. The threshold must be configurable for each individual
 1463 front-end channel.

1464 This technique achieves compression ratios which are roughly inversely proportional to the TPC occu-
 1465 pancy. For occupancies of 15 % and 42 % the data compression ratio is about 0.18 and 0.5, respectively.
 1466 Table 6.6 shows the compression ratios for two different running scenarios. The thresholding and hit-
 1467 finding operations are lossy techniques which could lead to a loss of small clusters or tails of clusters.

	minimum bias	central
Average occupancy	0.15	0.24
Compressed data size (ZS)	0.18	0.28
Compressed data size (Huffman)	0.21	0.25

Table 6.6: Expected average pad occupancies and approximate data compression ratios (compressed data size relative to raw data size) for two different data compression modes.

1468 ***Other compression scenarios***

1469 Instead of (or in addition to) zero suppression, lossless transformations like variable length codes (e.g.
 1470 Huffman coding) or lossy compression methods like vector quantization may be applied to compress the
 1471 data.

1472 Small ADC values occur very often in the data stream of a gaseous detector like the TPC, but larger
 1473 ones are more rare. The distribution is approximately exponential. The expected size of the data can be
 1474 reduced if short words are used for frequent values and longer ones for rare values. The theoretical lower
 1475 bound on the average word size that can be achieved by this strategy is called the entropy of the data
 1476 source²⁷. Huffman coding [14] approaches this bound and is easy to implement. Only if the distribution
 1477 of input values is too extreme the method can run into problems. In such a case events can become larger
 1478 than uncompressed.

1479 A TPC is obviously not a stochastic data source, as the ADC values found in adjacent pads are highly
 1480 correlated. Therefore, it could be possible to compress the data to an even lower bit rate than the entropy
 1481 of the ADC values. In other words, there could be representations of the TPC data that have a lower
 1482 entropy than the formats described above. Various methods like differentiation, prediction, etc. have
 1483 been evaluated, but in the end none of these approaches yield results that are much better than plain
 1484 Huffman coding (see [1] and references therein).

1485 Huffman coding has been applied to TPC events before. The entropy analysis results in about 6 bits per
 1486 sample for cluster data, depending somewhat on the abundance of overlapping clusters due to high occu-
 1487 pancy. A noise of 0.7 ADC counts requires about 1.3 bits per sample for coding the baseline/pedestal.
 1488 Applying Huffman coding to non-zero-suppressed data will result in a compression ratio of about 0.3 for
 1489 an occupancy of 27 %, which is expected for the inner pad rows.

1490 Huffman coding can be implemented in the SAMPA for encoding and in an FPGA²⁸ on the online farm
 1491 side for decoding. It will give comparable or even better compression factors than ZS for occupancies
 1492 larger than 25 % (see Tab. 6.6), while ZS reduces the event size by a large margin at low occupancies.
 1493 Huffman coding is lossless, while ZS implies typically a loss of 15 % of the total charge of a MIP cluster.
 1494 Both methods require similar resources for implementation and suffer from the same drawbacks, i.e. that
 1495 the data volume might increase in case of noisy channels (by a larger factor in case of Huffman coding)

²⁷The entropy of the data source can be computed as the sum over the probability of the occurrence of an ADC value multiplied by the logarithm of the probability; the sum running over the set of all possible words that are output by the data source.

²⁸Field Programmable Gate Array (FPGA)

1496 and that the output format is more prone to errors induced e.g. by SEUs²⁹ than the raw ADC data. The
1497 first problem has to be taken care of by the output module in the SAMPA; the latter can be solved by
1498 applying error detection and correction techniques to the transmission protocol.

1499 *Event memory*

1500 The data read out from 32 channels is transferred into the SAMPA event memory. Before transferring
1501 the data from each channel off-chip, it is temporarily buffered here. Naturally occurring bursts with
1502 higher occupancy lead to temporarily increased data rates, which have to be smoothed properly by the
1503 event memory. The event memory in this case serves as a de-randomizing buffer, ensuring that the data
1504 throughput is always below the bandwidth of the serial output links from the SAMPA. The optimal size
1505 of this buffer has to be found in simulations. In the undesirable case where the data rate is too high for
1506 an extended period, the data will have to be truncated, which will be marked in the data stream.

1507 The event memory can also be used as a lookup table to generate patterns to be read out through the
1508 output links for test purposes.

1509 *Interfaces*

1510 The data are read from the event memory and transferred to four electrical links (*e-links*) with bandwidth
1511 320 Mbit/s each.

1512 For control and monitoring of the SAMPA the GBT-SCA³⁰, a dedicated ASIC implemented in CMOS
1513 130 nm using radiation tolerant techniques is used. It implements the I²C protocol³¹ towards the SAMPA
1514 chips and is controlled via a dedicated slow control e-link from a GBTx chip.

1515 **6.4.9 Testing**

1516 The ASICs have to be thoroughly tested before assembly on the front-end cards. Even minimal mechan-
1517 ical damage may lead to loss of assembly quality. Due to the large number of chips to be tested, an
1518 automatized testing bench is required in order to guarantee reliable sorting and book-keeping.

1519 In the manufacturing process for the original FECs for the ALICE TPC about 40,000 PASA and ALTRO
1520 chips each were tested at Lund University. A semi-automatic test system had been developed, with the
1521 test procedures described in [2] and on the web page [15]. A pick-and-place robot moved chips from the
1522 trays (see Fig. 6.7) and placed them in the test socket which opened and closed by compressed air control.
1523 The test boards with the socket carried buffer memories to allow the communication and operation of
1524 the chip under test to go on at nominal speed. Extensive testing takes quite long time per chip. It was
1525 not judged meaningful to automatize the exchange of chip trays as the robot could be loaded for about 4
1526 hours of testing.

1527 Each chip was tested for about 1 minute (the ALTRO slightly longer, the PASA slightly shorter). All
1528 supply currents were measured, all DC levels checked. The ALTRO channels were excited by a sinus
1529 waveform which was digitized and verified, thus checking all bits of the analog-to-digital conversion. All
1530 memory cells were checked by downloading test patterns and reading back. The PASA channels were
1531 excited by a step-voltage, feeding charge into the preamp input over a small capacitor. The waveform,
1532 sampled with a 12 bit ADC at 40 MHz was compared to the expectation and the amplifier gain was
1533 recorded. Chips were sorted in three categories depending on the test result: accepted, slightly outside
1534 the acceptance limits and failure. A test protocol for each chip was stored and a summary of the test
1535 results was published [9].

²⁹Singe Event Upset (SEU)

³⁰Slow Control Architecture (SCA)

³¹Inter-Integrated Circuit (I²C)



Figure 6.7: Image of the PASA and ALTRO testing robot at Lund University.

1536 All equipment and software for testing is still available and can be used for the new SAMPA by modifying
1537 the test card with a different socket, different output buffering and some other minor changes. The analog
1538 test pulsing feature can remain unchanged, but the procedures for ALTRO and PASA testing will have to
1539 be merged.

1540 6.5 Front-end card

1541 The front-end card (FEC) contains the complete readout chain for amplifying, shaping, digitizing, pro-
1542 cessing, and buffering the TPC signals. The FEC must be designed as an integral part of the detector to
1543 obtain the best performance for the experiment.

1544 6.5.1 Partitioning

1545 The FEC plays a crucial role in the optimization of the detector performance. Some boundary conditions
1546 are given in the following:

- 1547 1. **Available space:** the number of pads on the IROCs of the current TPC is as high as can be read
1548 out with the present channel density of the electronics (16 channels per ASIC). In order to manage
1549 this, the mechanical mounting of the FECs, as well as their cooling, is the result of a large engi-
1550 neering and construction effort. The resulting density of hardware has led to many difficulties in
1551 maintenance operations. However, for the OROCs the space situation is much more relaxed.
- 1552 2. **Reuse of mechanical structures:** with a new FEC with equal size one may take advantage of
1553 reusing the mechanical support and cooling structures.
- 1554 3. **Pad plane segmentation:** due to the size of the OROC, the pad plane PCB will have to be seg-
1555 mented. Since traces can not cross PCB segments, not all configurations for the traces are possible.

- 1556 4. **Trace lengths:** higher intergration of the readout system (more channels per FEC) could lead to
 1557 longer trace lengths on the pad plane PCB with a negative impact on the noise performance.
- 1558 5. **Flexible signal cables:** the trace density on the Kapton signal cables connecting to the readout
 1559 chambers also directly relates to the noise behavior.
- 1560 6. **Readout link:** the GBTx ASIC [3] can multiplex 10 (14) e-links with (without) forward error
 1561 correction enabled. This number together with the number of output e-links per SAMPA (4) makes
 1562 only certain combinations attractive. Not using all inputs to the GBTx ASIC effectively means a
 1563 waste of useful bandwidth.
- 1564 7. **Readout scheme:** when the data are shipped off-detector, they are ordered in such a way that the
 1565 information from all pads with hits are sent in consecutive order following the pad row structure
 1566 and directed to the same cluster finder instance (see Sec. 8.1.2).

1567 The 6th requirement basically defined the number of SAMPA chips per FEC to be 5 (or 7). Such a scheme
 1568 with 5 readout partitions per TPC sector is summarized in Tab. 6.1. The last requirement (data ordering)
 1569 can always be achieved in the CRU, which gathers the data from many FECs.

1570 6.5.2 PCB design and layout

1571 A simplified layout of the FEC is shown in Fig. 6.8. The FEC receives the analog signals from the
 1572 readout chamber through a set of flexible cables. To minimize the trace lengths and thus noise (but
 1573 also crosstalk), the SAMPAs have to be positioned very close to the input connectors. The signals are
 1574 processed by 5 SAMPAs, with an estimated maximum power consumption of less than about 1 W per
 1575 SAMPA. The FEC also contains additional protection for the input to all SAMPA channels (see next
 1576 section).

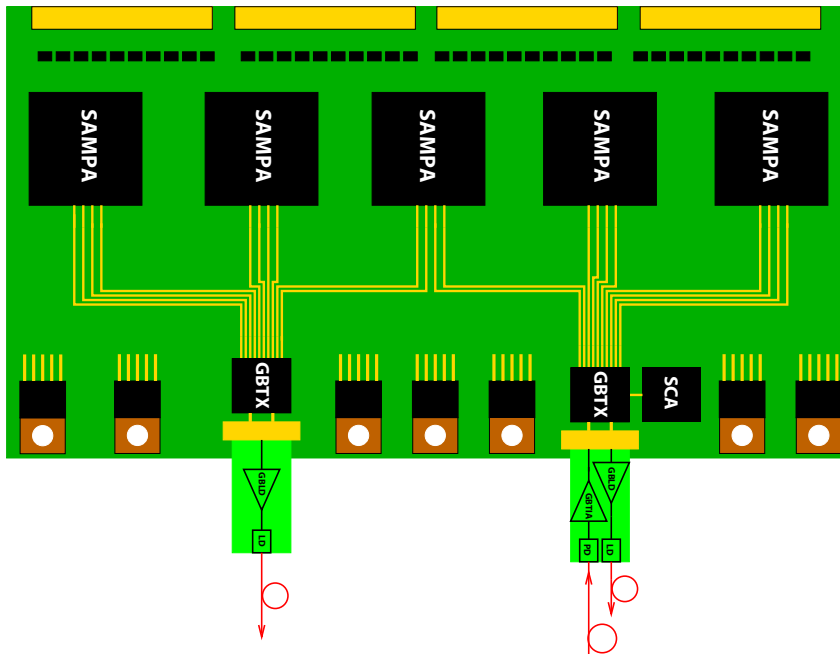


Figure 6.8: Schematic of the front-end card (FEC) with SAMPA. The connectivity is realized through the GBT system via optical links.

1577 Control and monitoring of the SAMPA is implemented via the GBT-SCA ASIC. Physics and monitoring
 1578 data are multiplexed on the FEC by up to two GBTx ASICs. The uni-directional versatile links [4] for the

1579 data to be sent to the CRU and online farm are driven by bi-directional optical transceivers (VTRx) or uni-
1580 directional twin transmitters (VTTx). Since the bandwidth needs in the up- and downstream directions
1581 are asymmetric, less VTRx are needed to receive trigger and timing information via the ALICE TTS³²
1582 system. We aim at installing one TTS link on every second FEC. Also configuration data and control
1583 commands to the FECs are sent via the TTS links. A possible distribution of optical components and
1584 links on the 36 TPC sectors is shown in Tab. 6.1, where we consider that less bandwidth is needed for
1585 the outermost readout partitions due to lower occupancies in this region.

1586 **6.5.3 System level input protection**

1587 The protection strategy foresees the implementation of system-level protection on the front-end card in
1588 the form of diode pairs, on top of the device-level protection in the SAMPA. Within the SRS project
1589 and the RD 51 collaboration a hybrid readout board for MPGD detectors has been developed. The
1590 module (RD51 APV25 HYBRID) is based on the APV25 chip and successfully uses an IC³³ with diode
1591 protection for 4 channels.

1592 Broken channels quite often lead to a short to ground which in fact makes the whole FEC inoperable.
1593 This could be avoided by separate voltage regulation for the analog power of each SAMPA (or possibly
1594 for each pair of SAMPAs).

1595 **6.5.4 Testing**

1596 The assembled FECs for the current TPC readout system were tested on the bench at Frankfurt University.
1597 This test step benefits from a final readout system being operational, which allows parallel testing of
1598 many FECs as well as long term testing (stress tests). The purpose of the test is to find assembly errors,
1599 chips which have broken during the mounting and handling, as well as any other malfunctioning of any
1600 component. The test procedures have been described in [2] and on the web page [15] and are a good
1601 starting point for the testing of the future FECs.

1602 **6.5.5 Irradiation campaign**

1603 The radiation levels expected for the high luminosity phase (50 kHz Pb–Pb collision rate) impose re-
1604 quirements on the radiation hardness/tolerance of the innermost FECs of the ALICE TPC. Fast hadrons
1605 can lead to a Single Event Upset (SEU) in digital structures, or to a Single Event Latch-up (SEL), a
1606 type of short circuit that triggers parasitic effects which can disrupt proper functioning of the element, or
1607 possibly even lead to its destruction.

1608 The flux of fast hadrons (> 20 MeV) at the TPC inner (outer) layer is expected to reach 3.4 kHz/cm²
1609 (0.7 kHz/cm²), including a safety factor of 2 [5]. The TPC electronics located at the inner radius of the
1610 service support wheel has to stand a dose of 2.1 krad.

1611 The SAMPA has to be designed carefully in order to avoid SELs and to protect critical logic against
1612 SEUs. FEC prototypes and all components will be irradiated in test beams of fast protons or neutrons,
1613 either individually in dedicated campaigns for critical components (e.g. FE ASIC) and/or finally after
1614 being mounted on FEC prototypes.

1615 **6.6 Common Readout Unit**

1616 The Common Readout Unit (CRU) is described in [5]. It provides the interface between the on-detector
1617 electronics and the trigger system, the online farm, and the DCS³⁴. The CRU units are located in the

³²Trigger and Timing distribution System (TTS)

³³NUP4114UPXV6T1G from ON semiconductor.

³⁴Detector Control System (DCS)

1618 control room outside the radiation area and will receive data from the detectors through optical fibers via
 1619 the GBT link. A schematic is shown in Fig. 6.9.

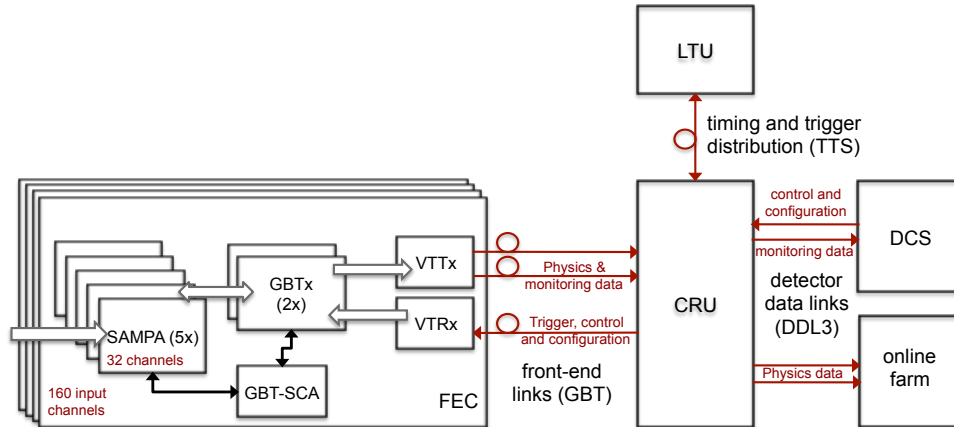


Figure 6.9: Schematic of the TPC readout system with the CRU as central part interfacing the front-end electronics to the trigger system, the DCS and the online farm.

1620 The CRU steers and controls the configuration, readout and monitoring of the FEE and the trigger handling.
 1621 When the TPC data are forwarded from the CRU to the online system, the individual data fragments
 1622 are ordered by the geometrical position of the pad rows and pads on which the charge cluster
 1623 signals were read such that the data are sent consecutively pad-by-pad, pad-row-by-pad-row. Also a
 1624 cluster finder algorithm could be implemented on the CRU.

1625 On each FEC the data from 5 SAMPAs are multiplexed by 2 GBTx ASICs [3] (only 1 for the outermost
 1626 readout partitions due to lower occupancies in this region) and sent to the CRU and online farm through
 1627 a double optical transmitter. The effective bandwidth for data readout is 2×3.2 Gbit/s using a special,
 1628 SEU robust transport protocol with forward error correction. The trigger, timing and clock distribution
 1629 and control and configuration data are transferred to the FEE on each TPC sector using fewer (e.g. one
 1630 per 2 FECs) uni-directional GBT links (TTS [5]).

1631 The CRU is the physical and logical interface to the ALICE online farm, to the DCS and to the trigger
 1632 system. Different firmware modules are required, that implement these interfaces:

- 1633 – The trigger module receives trigger and timing information, forwards a clock and a synchronisation
 1634 (or a trigger) signal to the FECs and prepares a timestamp header.
- 1635 – The data acquisition module receives the data from the FECs and checks its integrity. This module
 1636 will need to be a TPC specific implementation due to special requirements for the continuous
 1637 readout of data.
- 1638 – The TPC specific data formatter re-orders the channel data, adds header information into the data
 1639 stream and sends the data to the firmware module servicing the optical uplink.
- 1640 – A TPC specific DCS module may perform monitoring (voltages, currents and temperatures) and
 1641 time critical operations like switching off FECs in case of overheating.

1642 The configuration, control and monitoring of the TPC FEE (SAMPAs chips, FECs and CRUs) is integrated
 1643 into the existing hierarchical control structure of the ALICE DCS. A software FeeServer³⁵ at the CRU
 1644 configures the front-end electronics and monitors its status (see Sec. 10.2).

³⁵Front-End Server (FeeServer)

1645

Chapter 7

1646

Simulation and detector performance

1647

1648

1649

1650

1651

1652

1653

The expected performance of the upgraded GEM TPC during RUN 3 is described in this chapter. It starts with an overview on the performance of the current TPC, followed by a discussion of the intrinsic resolution of the GEM TPC (Sec. 7.2) and of the performance with track pileup from different interactions (Sec. 7.3). In Sec. 7.4 distortions due to space charge are discussed. In particular, the importance of space-charge fluctuations is pointed out. Finally, in Sec. 7.5 the performance including also space-charge distortions of the expected magnitude, and corrected with the online calibration tools discussed in Chap. 8, is presented.

1654

7.1 Current performance

1655

1656

1657

The current ALICE TPC was installed in the ALICE experimental cavern in 2007 and successfully operated since the LHC start-up in 2009. The observed performance is in agreement with or better than the design specifications reported in [1].

1658

7.1.1 Tracking performance

1659

1660

1661

In pp collisions the particle tracking efficiency within the TPC is better than 98 % for findable tracks¹. In Pb–Pb collisions it decreases by about 1–3 % due to the higher occupancy [2] ($dN_{\text{ch}}/d\eta \approx 1600$ in 0–5 % central collisions at $\sqrt{s_{\text{NN}}} = 2.76$ TeV).

1662

1663

1664

The achievable momentum resolution is driven by multiple scattering at low p_{T} , and by the space-point resolution and residual mis-calibration after all distortion corrections at high p_{T} . Both contributions are discussed in the following.

1665

1666

1667

1668

1669

1670

1671

1672

1673

1674

Space-point resolution The parameters dominating the space-point resolution of the TPC are diffusion (which depends on drift length z_{d}), track inclination angle and total cluster charge on a given pad row. For tracks with large transverse momentum p_{T} , and thus vanishing deflection angle, the space-point resolution in local- y ($r\phi$) direction² is around $400 \mu\text{m}$ ($800 \mu\text{m}$) for short (long) drift length [3]. The current results are at the level of the intrinsic (statistical) limit. From the covariance matrix of the tracks, the track resolution at different reference points can be obtained. For high- p_{T} tracks the intrinsic track resolution is approximately $\sigma_{\text{intr}} = 200 \mu\text{m}$ at the entrance of the TPC inner field cage and 2 mm extrapolated to the interaction point. This intrinsic track resolution determines the precision that is required for all calibrations and drift field distortion corrections, e.g. the drift velocity, alignment, $E \times B$ and space-charge distortion corrections.

¹Findable tracks are defined by a minimum track length in the active zones of the TPC.

²The space-point resolution in $r\phi$ determines the transverse momentum (p_{T}) resolution. For the coordinate system see Apx. A.

1675 **Drift field distortion corrections** For RUN 1 the largest systematic correction applied to the space-
 1676 point coordinates is due to the $E \times B$ effect, which reaches 1 cm (in very localized regions). The precision
 1677 of this correction is limited by the residual misalignment of the electric and magnetic fields.

1678 So far, space-charge effects due to ions in the TPC drift volume have been small. In the 2011 Pb–Pb data
 1679 a space-charge induced track distortion of $\sim 200 \mu\text{m}$ (when extrapolated to the interaction point) was
 1680 observed.

1681 **Momentum resolution** Figure 7.1 shows the resolution σ_{1/p_T} for the current status of the calibration
 1682 and for a data set from p–Pb collisions at $\sqrt{s_{NN}} = 5.02 \text{ TeV}$. Expressing the momentum resolution using
 1683 σ_{1/p_T} has the advantage that the distributions based on this variable are approximately Gaussian, even
 1684 at large p_T . The performance shown in Fig. 7.1 translates into a p_T resolution of $\sigma_{p_T}/p_T \lesssim 3.5\%$ at
 1685 $p_T = 50 \text{ GeV}/c$ and below 1% at $p_T = 1 \text{ GeV}/c$.

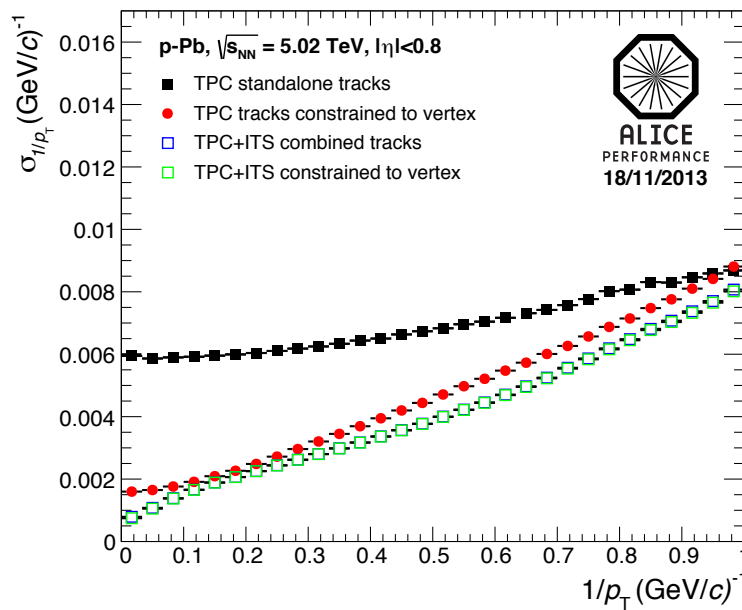


Figure 7.1: Resolution in $1/p_T$ as a function of $1/p_T$ for the ALICE central barrel (current system). The plot shows the $1/p_T$ resolution for TPC standalone tracks and for global tracks combining tracking in ITS and TPC with and without vertex constraint. The data is from p–Pb collisions collected in 2013.

1686 7.1.2 Particle identification performance

1687 The specific energy loss dE/dx is obtained for each track by calculating the truncated mean of the cluster
 1688 charges on currently up to 159 pad rows³, which adds significant PID⁴ capabilities to the ALICE central
 1689 barrel. Identification of pions, kaons, and protons is possible also in the relativistic rise region of the
 1690 Bethe-Bloch energy-loss curve [4] at high p_T . The p_T reach is currently limited to $20 \text{ GeV}/c$ by statistics.
 1691 With the event sample anticipated in RUN 2 and further improved understanding of the characteristics of
 1692 the energy-loss curve in the relativistic rise region, the identification of pions, kaons and protons up to
 1693 $50 \text{ GeV}/c$ is within reach. The usage of high-momentum cosmic muons to improve the understanding of
 1694 the energy loss in this p_T region is under study.

1695 In pp and central Pb–Pb collisions a dE/dx resolution of about 5.5% and 7% is achieved, respectively.
 1696 The resolution in pp is consistent with the intrinsic dE/dx resolution dominated by the ionization fluc-
 1697 tuations (Landau tail), folded with gas gain fluctuations, the detector readout granularity and threshold

³In the GEM TPC the number of pad rows is reduced to 158, see Sec. 4.5.

⁴Particle IDentification (PID)

1698 effects. In Pb–Pb collisions the performance deteriorates at large multiplicities mainly due to an increas-
 1699 ing overlap of clusters.

1700 **7.2 Intrinsic performance of the upgraded TPC**

1701 The expected performance of the TPC after upgrade with GEM-based readout is quantified using micro-
 1702 scopic simulations. For these studies, the current ITS design is used. Since the performance will improve
 1703 with the upgraded ITS [5, 6], the results on the global tracking performance reported in this chapter can
 1704 be considered as conservative.

1705 **7.2.1 Microscopic GEM simulations**

1706 The most important parameters for the microscopic simulation of the intrinsic performance are:

- 1707 – **Gas choice:** The baseline gas mixture is Ne-CO₂-N₂ (90-10-5), see Chap. 3.
- 1708 – **Pad geometry:** The baseline pad geometry of the upgraded TPC is very close to that of the current
 1709 system, see Sec. 4.5.
- 1710 – **Pad response function:** The shape of the induced charge distribution on the readout plane of a
 1711 GEM detector is very narrow, due to the parallel plate geometry of the induction gap. A purely
 1712 projective pad response function is used in the simulation, i.e. electrons create signals only on the
 1713 pad directly below their arrival point on the first GEM plane.

1714 Table 7.1 shows the parameters used for the simulations. The microscopic simulation algorithm is de-
 1715 scribed in [1] and has been validated with test beam data [7]. Here, only a short summary of the simula-
 1716 tion steps is given.

Item		Value
Mean number of primary electrons for MIP		14.0
First ionization potential I_0	(eV)	20.77
Effective energy for e-ion pair creation W_i	(eV)	37.3
Drift velocity at 400 V/cm	(cm/ μ s)	2.58
Longitudinal diffusion constant (D_L)	(μ m/ \sqrt cm)	221
Transverse diffusion constant (D_T)	(μ m/ \sqrt cm)	209
$\omega\tau$ (for magnetic field $B = 0.5$ T)		0.32
Oxygen content	(ppm)	5
Effective GEM gain		2000
System noise (RMS)	(e)	600
Dynamic range		2 V; 10 bits
Conversion gain	(mV/fC)	20
Shaping time (FWHM)	(ns)	190
Sampling frequency	(MHz)	10
Zero suppression settings		3 LSB ⁵ threshold; glitch filter

Table 7.1: Parameters used in the simulation: Gas properties, GEM effective gain (which includes the signal coupling to the readout plane) and electronics parameters.

1717 The simulation is based on a modified version of GEANT3 [1]. The ionization by charged particles
 1718 entering the active gas volume is simulated using a TPC-specific energy-loss method. Based on the
 1719 average number of primary electrons per cm of track length, the interaction length is calculated and a step

⁵Least Significant Bit (LSB)

length is randomly generated. A random energy-loss value is assigned to this step according to $1/E^{2.2}$ ($I_0 \leq E \leq 10\text{keV}$, where I_0 is the first ionization potential). The total number of ionization electrons including secondaries is calculated. Each of these electrons is drifted to the readout chambers, taking into account diffusion and residual distortions. Space-charge distortions are not taken into account at this point; they are discussed separately in Secs. 7.4 and 7.5. At the GEM readout stack an exponential gain variation is assumed for each electron. The charge is projected onto the pad plane using the described pad response function in space and a semi-Gaussian shaping function in time. The reconstruction of events simulated in this way does not differ from that of real data.

The described simulation algorithm is routinely used in the ALICE simulation and reconstruction framework and was thoroughly validated in the past years.

7.2.2 Tracking performance

The GEM-based readout chambers show slightly worse position resolution than the present MWPCs. This is due to the narrower pad response function, as discussed in Sec. 4.5. Figure 4.16 shows that the space-point resolution achieved with GEM readout is about 10 % worse than for the MWPC-based readout, except for very short drift lengths. Here, the difference gets larger due to the frequent occurrence of one-pad clusters. However, in most of the acceptance region $|\eta| < 0.9$ clusters with signals on more than one pad dominate, as shown in Fig. 4.17. Consequently, the momentum resolution in the acceptance of the central barrel detectors of ALICE will be maintained for the TPC with GEM-based readout, as shown in Fig. 7.2. The plot indicates a slight deterioration of the resolution in $1/p_T$ for tracks using only TPC information, consistent with the deterioration of the space-point resolution. This deterioration is however fully recovered for global tracks combining tracking in ITS and TPC.

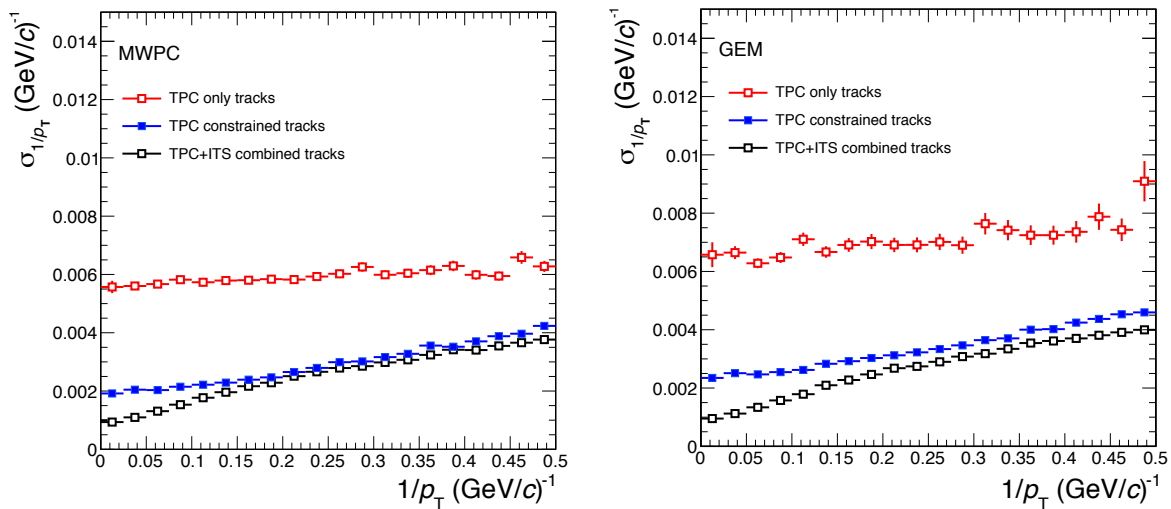


Figure 7.2: Resolution in $1/p_T$ as a function of $1/p_T$ for MWPC (left panel) and GEM readout (right panel). The open red squares are for tracks based on TPC information only, while the closed blue squares show TPC track fits including the vertex point. The open black squares show the result for combined fits to TPC and ITS track points.

The extraction of the p_T resolution from p–Pb data as shown in Fig. 7.1 relies on a thorough understanding of material budget and detector response. This achievement is reflected in the good agreement with the simulated data displayed in Fig. 7.2 (left panel).

7.2.3 Particle identification performance

The relative dE/dx resolution $\sigma_{dE/dx}/\langle dE/dx \rangle$ for isolated electron and pion tracks ($1 < p < 6\text{GeV}/c$) was measured with a triple-GEM IROC prototype at the CERN PS test beam. The results reported in Sec. 5.2.6 show that the dE/dx resolution observed with the GEM IROC is compatible with that of the

1748 MWPC IROCs. This behavior is confirmed in the simulation: Figure 7.3 shows the dE/dx resolution
 1749 as a function of the momentum for MWPC and GEM readout at low track multiplicity. No difference
 1750 between MWPC and GEM is observed.

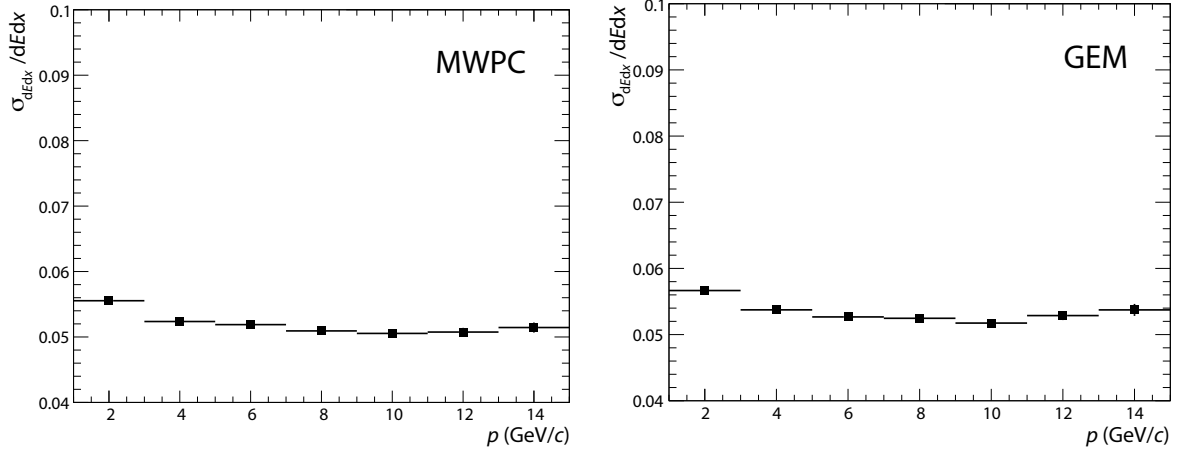


Figure 7.3: dE/dx resolution as a function of track momentum in the current TPC (left) and GEM TPC (right). The simulation is carried out at low multiplicity (pp). The performance at high multiplicities and with event pileup is discussed in Sec. 7.3.

1751 The simulations presented in this chapter assume a transmission efficiency of the readout system of
 1752 100 % for primary electrons. While this is a good assumption for an MWPC, the transmission efficiency
 1753 may be reduced in a GEM readout system due to the finite electron collection efficiency at the first
 1754 GEM stage. This effect is enhanced for settings which minimize ion backflow and manifests itself in
 1755 a degradation of the energy resolution, measured with an ^{55}Fe source, relative to an optimal value of
 1756 about 8.5 % at 5.9 keV, see Fig. 5.8. As shown in Fig. 7.4, the dE/dx resolution, which depends on the
 1757 energy resolution, degrades significantly only for values of the electron transmission efficiency below
 1758 0.5, both for pp and Pb–Pb collisions. If we consider the first GEM foil the main contributor to the
 1759 energy resolution, a transmission efficiency of 0.5 corresponds to a degradation of the energy resolution
 1760 at 5.9 keV to $8.5\%/\sqrt{0.5} \approx 12\%$. In the simulations presented here we assume that the energy resolution
 1761 of the GEM system is better than 12 %, and the dE/dx resolution is not affected by a finite transmission
 1762 efficiency.

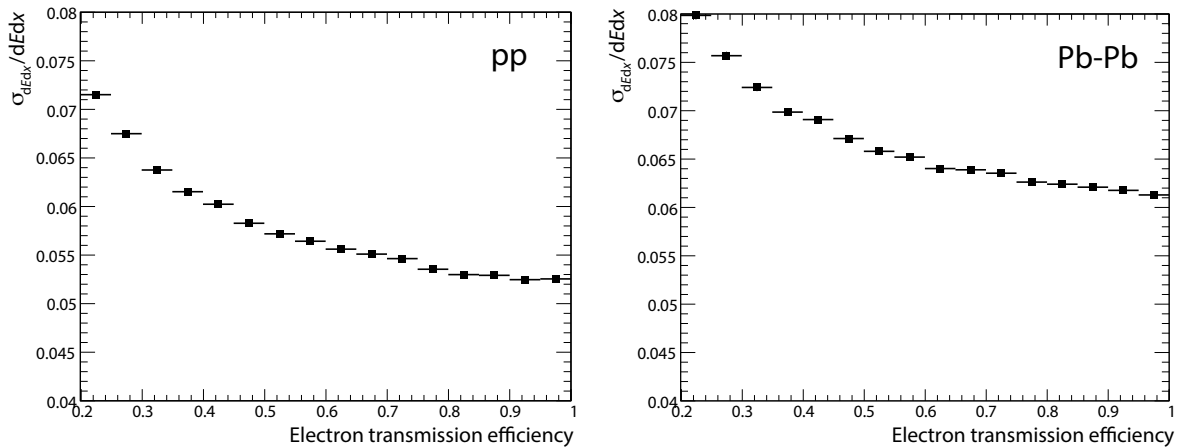


Figure 7.4: Simulated dE/dx resolution for MIP tracks crossing 158 pad rows as a function of the electron transmission efficiency in the GEM stack for pp (left) and Pb–Pb collisions (right).

1763 7.3 Performance with event pileup

1764 The GEM TPC will operate at a Pb–Pb interaction rate of 50 kHz, where particle tracks from $N_{\text{pileup}} = 5$
 1765 events on average are superimposed in the drift volume of the TPC. The resulting pad occupancies lead
 1766 to an increased probability for clusters to overlap and thus to be wrongly assigned during the tracking
 1767 step. In this section we study the impact of event pileup on the tracking performance. For more details
 1768 on the LHC running conditions see Sec. 8.1.1.

1769 The current TPC was designed for a charged particle multiplicity of $dN_{\text{ch}}/d\eta = 8000$ in central Pb–Pb
 1770 collisions. Comprehensive studies showed that the required performance can be achieved at such extreme
 1771 conditions [1]. For the anticipated data taking scenario at $R_{\text{int}} = 50$ kHz, corresponding to an equivalent
 1772 charged-particle multiplicity (see Sec. 6.2) of $dN_{\text{ch}}/d\eta|_{\text{equiv}} \approx 2500$, the effect of event pileup is thus
 1773 expected to be minor. However, the track topology in overlapping events is different from a single high-
 1774 multiplicity collision due to the displacement of the vertex positions. The performance of the TPC under
 1775 such conditions was verified in simulated central (0–5%) Pb–Pb events ($\langle dN_{\text{ch}}/d\eta \rangle$ scaled to 2000)
 1776 embedded in different pileup scenarios. A varying number of minimum bias events ($\langle dN_{\text{ch}}/d\eta \rangle$ scaled
 1777 to 500) are added at random distances within a time window of $\pm 80 \mu\text{s}$. Several jets are added to the
 1778 central event (simulated with Pythia) in order to enhance the fraction of high- p_T particles. Naturally, in
 1779 this simulation the actual tracks seen from the pileup events are constrained by the readout time window
 1780 defined by the central event.

1781 Figure 7.5 shows that the TPC standalone tracking efficiency at the different interaction rates is essen-
 1782 tially the same for the current TPC and for the GEM TPC. In these data, the lower bound scenario (central
 1783 event at $R_{\text{int}} = 20$ kHz) corresponds to an equivalent multiplicity $dN_{\text{ch}}/d\eta|_{\text{equiv}} = 2500$, while the most
 1784 extreme scenario (central event at $R_{\text{int}} = 70$ kHz) corresponds to $dN_{\text{ch}}/d\eta|_{\text{equiv}} = 5000$. Figure 7.6 shows
 1785 the resolution in $1/p_T$ for the GEM TPC for these different scenarios. The tracking performance is
 1786 essentially unaffected by the additional track load.

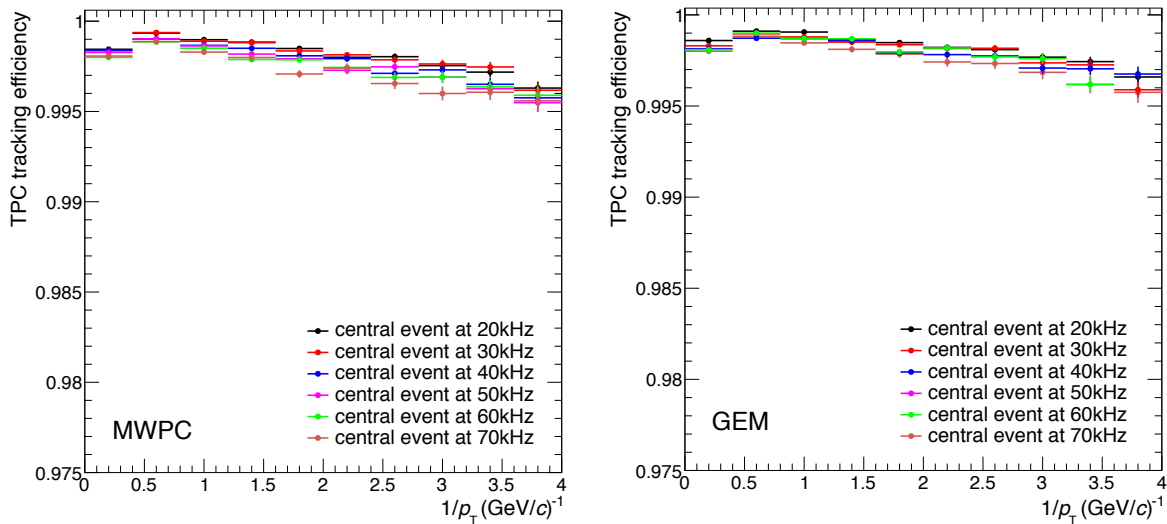


Figure 7.5: TPC standalone tracking efficiency for MWPC (left panel) and GEM (right panel) readout. In the simulated data central events ($\langle dN_{\text{ch}}/d\eta \rangle$ scaled to 2000) are embedded in the average background given by minimum bias events ($\langle dN_{\text{ch}}/d\eta \rangle$ scaled to 500) at different interaction rates.

1787 Figure 7.7 compares the dE/dx resolution for MWPC and GEM readout at different interaction rates. For
 1788 the MWPC readout the simulated performance is slightly better than the measured resolution of around
 1789 7%, since in the current framework the deterioration due to the ion tail is not part of the simulation.
 1790 This does however not affect the results obtained for the GEM readout. We can conclude that the dE/dx
 1791 resolution is not compromised by the upgrade with GEM readout.

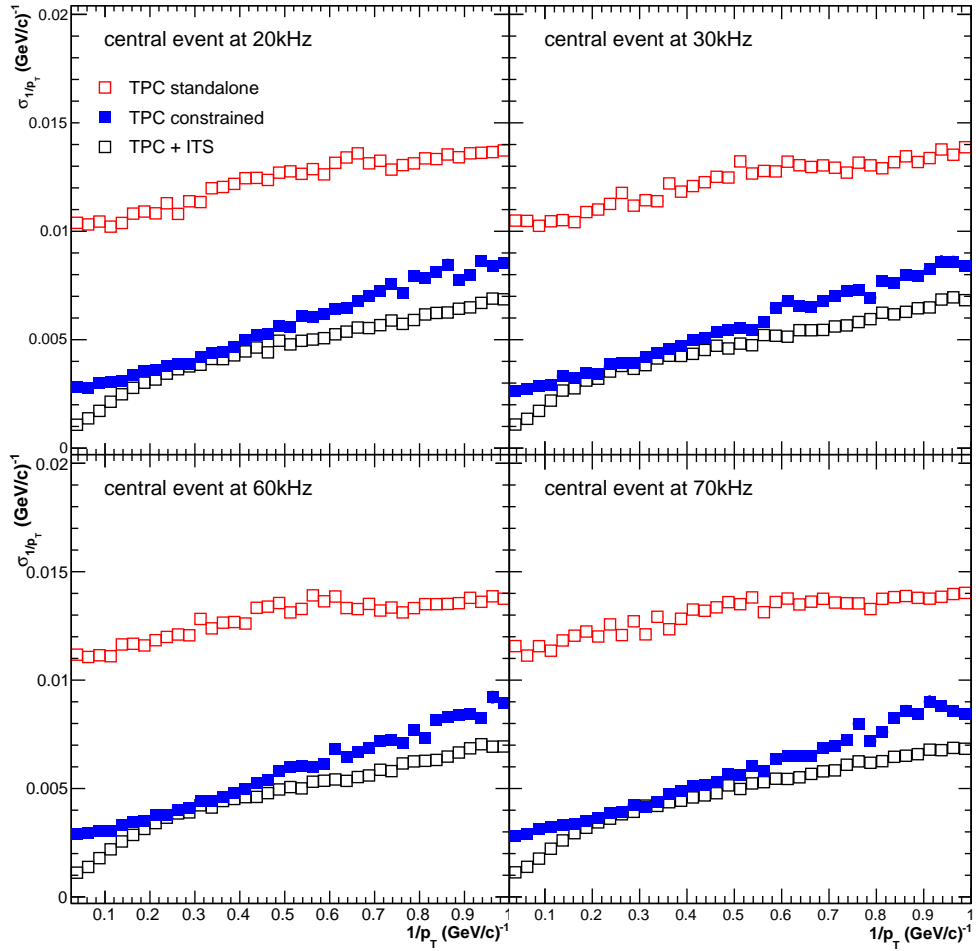


Figure 7.6: Resolution of $1/p_T$ as a function of $1/p_T$ for GEM readout. In the simulated data central events ($\langle dN_{ch}/d\eta \rangle$ scaled to 2000) are embedded in a background of minimum bias events ($\langle dN_{ch}/d\eta \rangle$ scaled to 500) at different interaction rates.

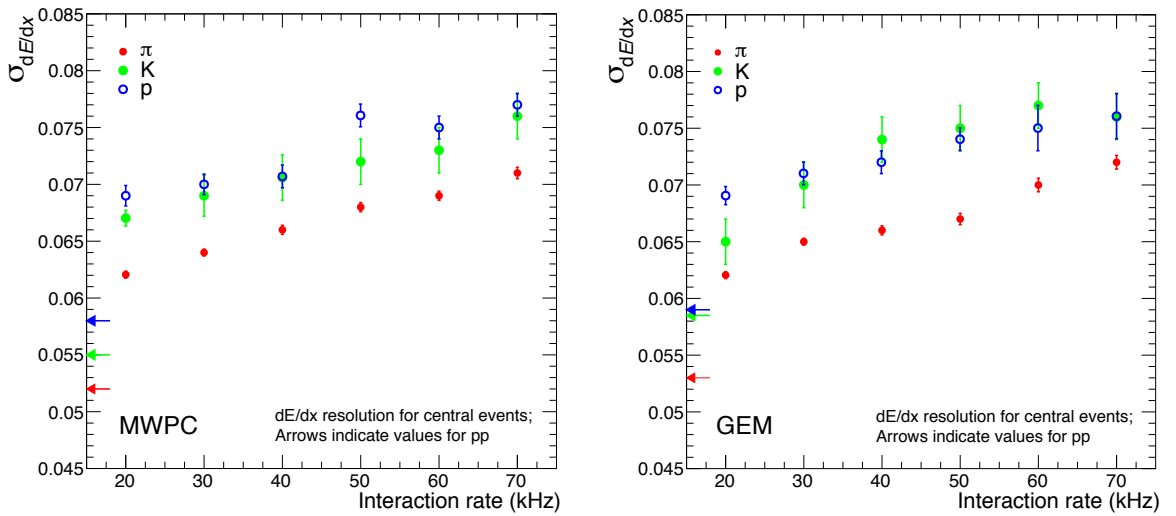


Figure 7.7: dE/dx resolution for central events as a function of the interaction rate for MWPC (left panel) and GEM (right panel) readout. In the simulated data central events ($\langle dN_{ch}/d\eta \rangle$ scaled to 2000) are embedded in a background of minimum bias events ($\langle dN_{ch}/d\eta \rangle$ scaled to 500). Only tracks in the momentum range from 4 to 5 GeV/c are used.

1792 7.4 Space-charge distortions and corrections

1793 At high collisions rates and large charged-particle multiplicities, the TPC drift volume contains a large
 1794 number of positive ions that pile up due to the slow ion drift velocity. The ion pileup effect can lead to a
 1795 significant accumulation of space charge. The resulting field distortions modify the electron drift lines,
 1796 introducing drift field distortions that have to be corrected. The correction of space-charge distortions
 1797 with sufficient precision is one of the major challenges within the TPC upgrade scheme. The goal is
 1798 to keep the residual distortions (after calibration) at a level not significantly larger than the intrinsic
 1799 resolution, i.e. a few hundred μm , as is achieved for the current TPC.

1800 7.4.1 Space-charge sources

1801 The ion pileup consists of the prompt contribution of the gas ionization by charged particles in the TPC
 1802 drift volume and the delayed contribution due to ion backflow from the GEM readout system. In case of
 1803 the upgraded TPC, the latter contribution is larger by a factor of 2ε on average, where ε is the number of
 1804 ions drifting back into the TPC drift volume for each electron entering the multiplication region⁶. For a
 1805 residual ion backflow of 1 % and an effective gain of 2000 the value of the ε parameter is 20.

1806 The average space-charge density is proportional to ε , to the interaction rate R_{int} and to the ion drift time
 1807 $t_{\text{d}}^{\text{ion}}$. For $R_{\text{int}} = 50\text{kHz}$ and $t_{\text{d}}^{\text{ion}} = 0.16\text{s}$ the tracks of ~ 8000 interactions contribute to the ion pileup at
 1808 any given moment.

1809 The magnitude of the space-charge distortions can be calculated using parametrized charged particle
 1810 density distributions under the assumption of certain symmetries:

$$\rho_{\text{sc}}(r, z) = \frac{a - bz + c\varepsilon}{r^d}. \quad (7.1)$$

1811 The resulting space-charge density map for $R_{\text{int}} = 50\text{kHz}$ and $\varepsilon = 20$ is shown in Fig. 7.8. The distri-
 1812 bution is symmetric in φ and linear in z (due to the constant ion drift velocity⁷). From data we extract a
 1813 radial dependence with a value of d between 1.5 and 2 (see Sec. 7.4.4). The small step at $z \approx 0$ is due to
 1814 additional background from the muon absorber on the C side.

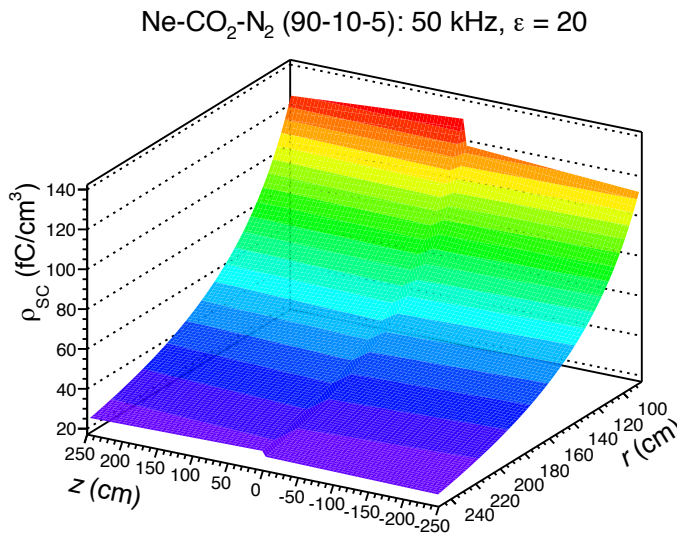


Figure 7.8: Average space charge density for Ne-CO₂-N₂ (90-10-5), $R_{\text{int}} = 50\text{kHz}$ and $\varepsilon = 20$.

⁶The factor of 2 describes the average drift length difference for ions from primary ionization and ions from ion backflow.

⁷The average interaction rate is also constant on the short timescales considered here.

1815 7.4.2 Magnitude of the distortions

1816 The magnitude of the space-charge distortions (without fluctuations) is calculated using parametrized
 1817 space-charge density distributions as in Eq. (7.1). The resulting average distortions in r , $r\phi$ and z direc-
 1818 tions are shown in Fig. 7.9.

1819 The space charge has a focusing effect, forcing the drifting electrons to divert from the ideal drift path
 1820 towards larger (smaller) radii at the inner (outer) field cage of the TPC. Moreover, the emerging radial
 1821 electric field component in the presence of the magnetic field leads to distortions in $r\phi$ due to the $E \times B$
 1822 effect. In general, the effect is strongest close to the central electrode ($|z| \approx 0$) and at the inner and outer
 1823 field cage.

1824 The magnitude of the distortions at the central electrode of the TPC (at $z \approx 0$ cm) is shown in Fig. 7.10. At
 1825 the inner field cage the space-point distortions reach up to 19 cm in r direction and 7 cm in $r\phi$ direction.
 1826 However, in the largest part of the volume, the distortions are well below 10 cm. Distortions of similar
 1827 magnitude are encountered or expected in the near future in the TPC of the STAR experiment at RHIC [8,
 1828 9]. The distortions expected for the TPC considered for the PANDA experiment at FAIR [10] are smaller
 1829 by an order of magnitude.

1830 The space-charge distortions do not increase linearly with ε . A drifting electron will be deflected by the
 1831 space-charge field towards regions with lower field gradients. The resulting saturation effect is shown in
 1832 Fig. 7.11.

1833 7.4.3 Simulation of the space-charge distortions

1834 Equation (7.1) provides a straightforward solution to calculate the magnitude of the space-charge distor-
 1835 tions. However, fluctuations in the space-charge density distribution are not taken into account. Conse-
 1836 quently, it describes well a situation with the main contribution to the space-charge distribution coming
 1837 from primary ionization ($\varepsilon \rightarrow 0$). In case of the upgraded ALICE TPC, however, the main contribution
 1838 to the space-charge distribution arises from ion backflow. Here, the non-active regions along the sector
 1839 boundaries together with local variations of gain and ε break the azimuthal symmetry. As we will see,
 1840 also the fluctuations in the number of interactions per unit time, and in the charged track multiplicity
 1841 per event have to be considered, as they give rise to space-charge fluctuations along z . Each interaction
 1842 actually creates a disc of slowly moving ions within the TPC volume, and the space charge density dis-
 1843 tribution at 50 kHz interaction rate consists of the superposition of ~ 8000 such disks with fluctuating
 1844 density.

1845 In the following, an detailed simulation procedure for space-charge distortions is described, that deals
 1846 with these features. It consists of the following steps:

1847 1. **Calculation of the space-charge density maps:** Detailed 3-dimensional average space-charge
 1848 maps can be calculated without any symmetry assumptions utilizing real raw data from minimum
 1849 bias Pb–Pb collisions from RUN 1. Approximately 130,000 events were used for this purpose. The
 1850 individual events are compressed along the z direction by a factor t_d/t_d^{ion} and superimposed with
 1851 random positions along z . Moreover, space-charge maps for randomly selected groups of events are
 1852 used to mimic the fluctuations of the space-charge distribution in space and time. A subset of 8000
 1853 events is needed to simulate an interaction rate of 50 kHz. The individual events are superimposed
 1854 with random positions along the z direction with a spacing defined by the interaction rate and the
 1855 ion drift velocity.

1856 2. **Calculation of the space-charge field:** Based on the space-charge maps obtained in the previous
 1857 step, the resulting electric field components are calculated. Taking into account the precision
 1858 requirement and the granularity of the space charge, it is clear that the electric field has to be

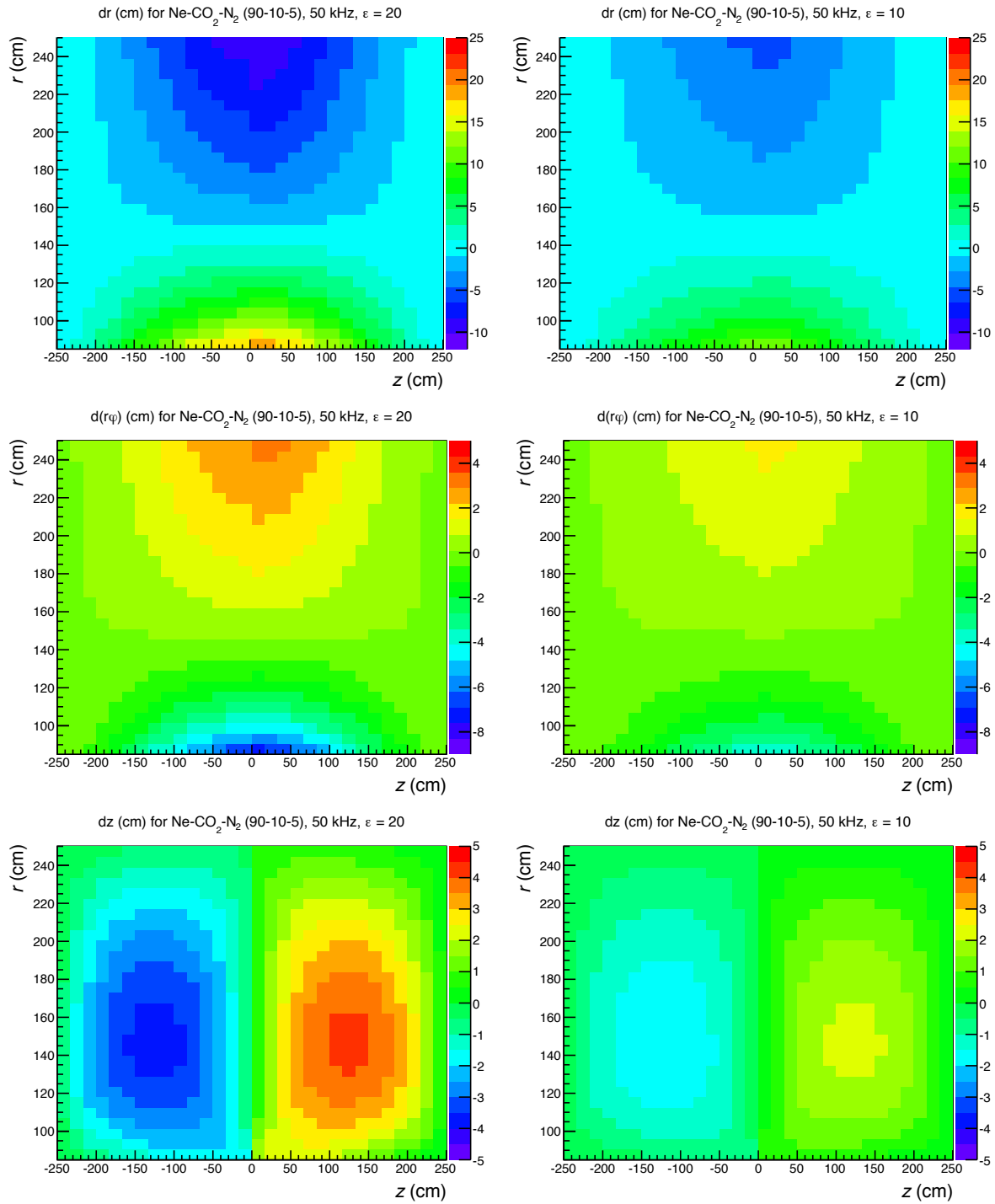


Figure 7.9: Space-point distortions in r (top panels), $r\phi$ (center panels) and z (bottom panels) for Ne-CO₂-N₂ (90-10-5), $R_{\text{int}} = 50$ kHz and $\epsilon = 20$ (left panels) and 10 (right panels). The data shows the integrated distortions for an electron originating at z, r as it drifts to the GEM readout at $z = \pm 250$ cm.

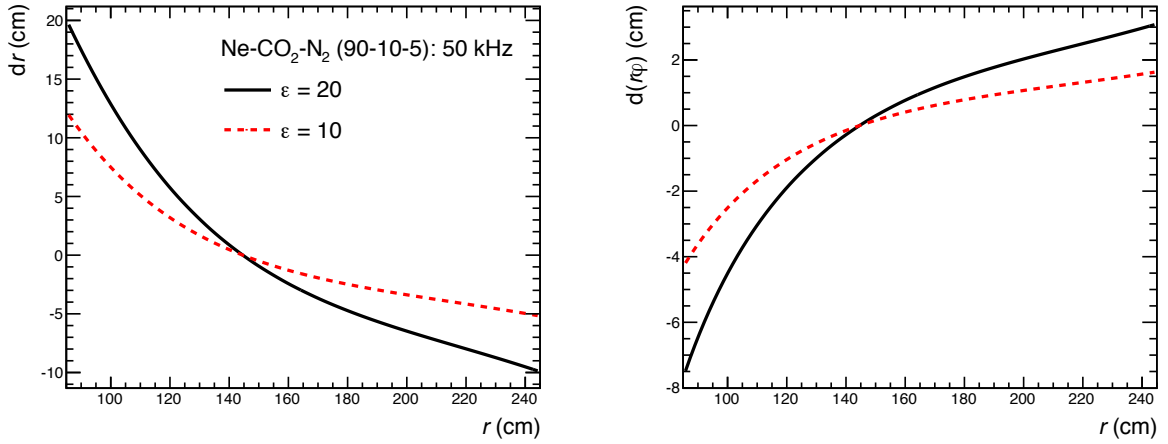


Figure 7.10: Space-point distortions in r (left panel) and $r\phi$ (right panel) as a function of the radial position r close to the central electrode ($z \approx 0$ cm) for Ne-CO₂-N₂ (90-10-5), $R_{\text{int}} = 50$ kHz, $\epsilon = 10$ and 20.

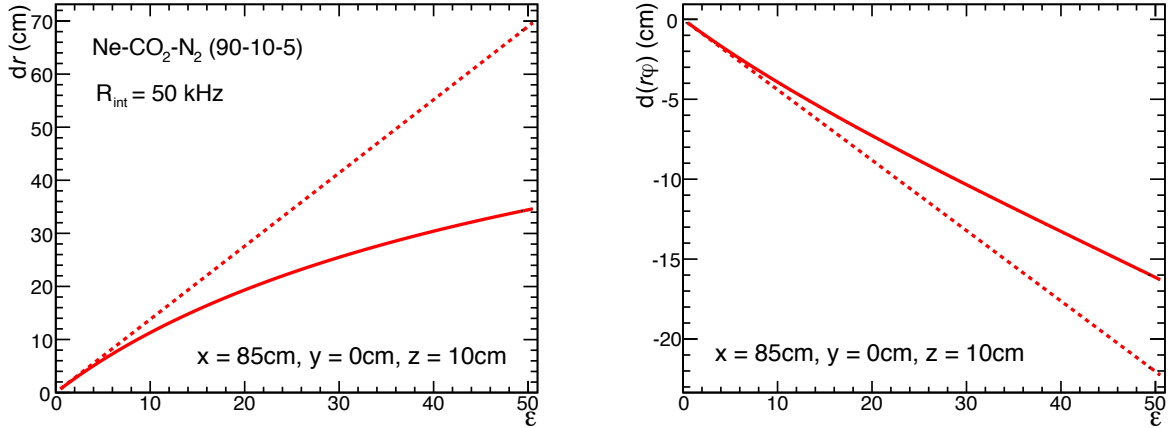


Figure 7.11: Space-point distortions in r (left panel) and $r\phi$ (right panel) close to the central electrode ($z \approx 10$ cm) and in the center of a readout chamber ($y = 0$) as a function of ϵ . The broken line is an eye guide representing linear increase with ϵ .

1859 calculated in 3 dimensions and with high spatial granularity. In the following studies a granularity
 1860 of 360 bins in $r\phi$, 125 bins in z , and 158 bins in r is used. A 3D electric field calculation is done
 1861 using a customized implementation of the Poisson relaxation method [11]. The originally proposed
 1862 analytical approach does not provide a 3D solution with sufficient spatial granularity.

1863 **3. Calculation of the distortion maps:** The electric field deviations $\Delta\vec{E}$ based on ρ_{sc} can be com-
 1864 puted by solving the inhomogeneous Laplace equation. This task is usually performed by solving
 1865 the Poisson equation with the help of discrete numerical methods like Finite Elements as applied
 1866 in STAR [8] and PANDA [10] or by using an analytical approach based on the Green's function
 1867 as proposed for ALICE [12]. However, these approaches turn out to be not able to cope with the
 1868 granularity requirements and instead the Poisson relaxation method is used.

1869 To compute the distortion maps as a function of the starting position of the drifting primary elec-
 1870 tron, the Langevin equation of motion for electrons in electric and magnetic fields is integrated
 1871 along the drift line with a fourth-order Runge Kutta algorithm [13].

1872 Repulsive electrostatic forces between the ions are not yet considered in this calculation. They will cause
 1873 distortions of the ion drift path as well, which will lead to smoother space-charge distributions than those

1874 discussed in this TDR.

1875 7.4.4 Space-charge density fluctuations

1876 In this section we investigate the fluctuations of the space-charge density distribution using data obtained
1877 with the simulation method described in Sec. 7.4.3 and with an analytical formula for the expected
1878 fluctuations.

1879 *Features of the space-charge map distributions*

1880 Figure 7.12 shows the xy and rz projections of 2 example space-charge density maps and of the full
1881 analysed event sample of 130,000 events.

1882 An almost regular sector modulation of the space charge due to the dead zones between the readout
1883 chambers is observed. Moreover, there is a step in the density distribution between the IROC and OROC
1884 regions, caused by the systematically different gas gain applied in order to keep the same signal-to-noise
1885 ratio in these two regions with different pad and wire geometry. An $r^{-1.5}$ -scaling is found for the radial
1886 dependence in the full analysed event sample (130,000 events), in contrast to the r^{-2} scaling used by
1887 STAR [14].

1888 Strong local variations of the space-charge density are observed. The effect is most pronounced in the z
1889 direction, where regions of high ion density corresponding to central events are clearly visible.

1890 In Fig. 7.13 the expected $r\phi$ distortion maps are shown without (left) and with (right) magnetic field.
1891 In these studies, the maps have been normalized to $\varepsilon = 5$ in order to avoid complications due to non-
1892 linearities. The figure illustrates the effect of a sector modulation that can be explained by the lower
1893 space-charge density close to the dead zones in between readout chambers. The positive ion charge
1894 attracts the drifting electrons towards the center of the readout chamber. In the setup with magnetic field
1895 the symmetry is broken due to the $E \times B$ effect. Consequently, the mean value of the distortion is shifted.

1896 *Contributions to the space-charge fluctuations*

1897 The average number of interactions contributing to the ion pileup in the TPC drift volume is $N_{\text{pileup}}^{\text{ion}} \approx$
1898 8000. The actual number of interactions is described by a Poissonian distribution around this mean
1899 value. The relative fluctuation of the space-charge density $\sigma_{\text{sc}}/\mu_{\text{sc}}$, where $\mu_{\text{sc}} = \langle \rho_{\text{sc}} \rangle$ is the average
1900 space-charge density, can then be written as:

$$\frac{\sigma_{\text{sc}}}{\mu_{\text{sc}}} = \frac{1}{\sqrt{N_{\text{pileup}}^{\text{ion}}}} \sqrt{1 + \left(\frac{\sigma_{N_{\text{mult}}}}{\mu_{N_{\text{mult}}}}\right)^2 + \frac{1}{F \mu_{N_{\text{mult}}}} \left(1 + \left(\frac{\sigma_{Q_{\text{track}}}}{\mu_{Q_{\text{track}}}}\right)^2\right)}. \quad (7.2)$$

1901 The relative fluctuation of the space-charge density depends on three contributions:

- 1902 1. $1/\sqrt{N_{\text{pileup}}^{\text{ion}}} \approx 1.1\%$ is the relative fluctuation of the number of ion pileup events. Already this
1903 contribution is larger than the required precision of a few %.
- 1904 2. $\frac{\sigma_{N_{\text{mult}}}}{\mu_{N_{\text{mult}}}} \approx 1.4\%$ is the relative RMS of the multiplicity distribution.
- 1905 3. $\frac{\sigma_{Q_{\text{track}}}}{\mu_{Q_{\text{track}}}} \approx 1.7\%$ is the relative variation of the ionization of a single track.

1906 F is a geometrical factor describing the spatial range over which the space-charge fluctuations are rel-
1907 evant for the distortions. To describe the fluctuation in the space-point distortions, the relevant scale is
1908 determined by the range of the Coulomb interaction.

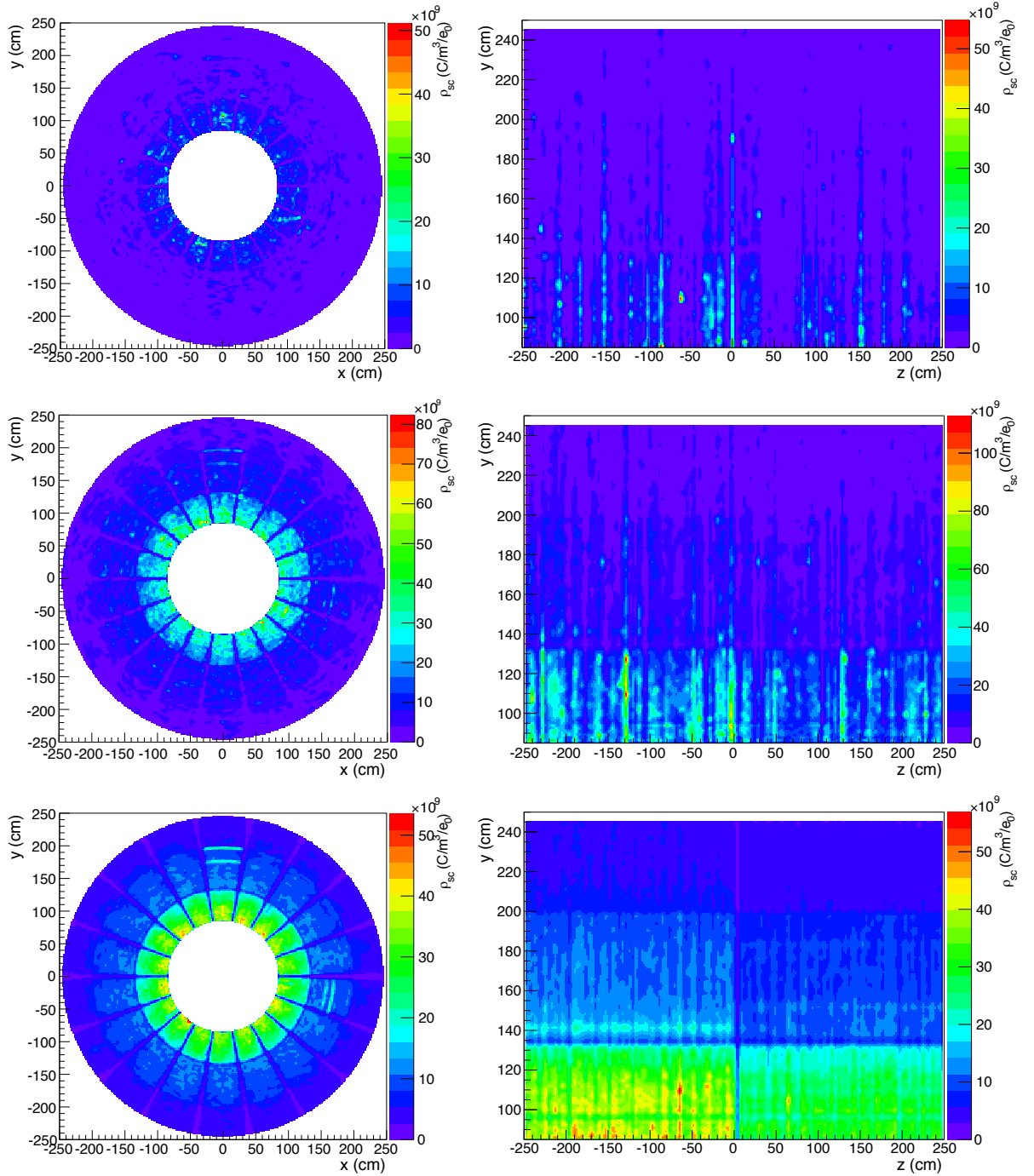


Figure 7.12: Calculated space-charge density maps based on raw data from minimum bias Pb–Pb collisions, simulating an ion pileup from 2000 (top row), 8000, and 130,000 interactions (bottom row). The histograms are normalized to 10,000 ion pileup events. Left column: xy projection at $z = 10$ cm. Right column: rz projection at $\varphi = 0.05$. In these plots on the horizontal axis the full drift length $|z| = z_{\text{ROC}} = 250$ cm corresponds to the ion drift time $t_d^{\text{ion}} = 0.16$ s. The data displayed is based on minimum bias Pb–Pb collisions recorded in RUN 1. The increased charge density in a few sectors at at certain radial positions is explained by a few faulty wires, which increase the local gas gain.

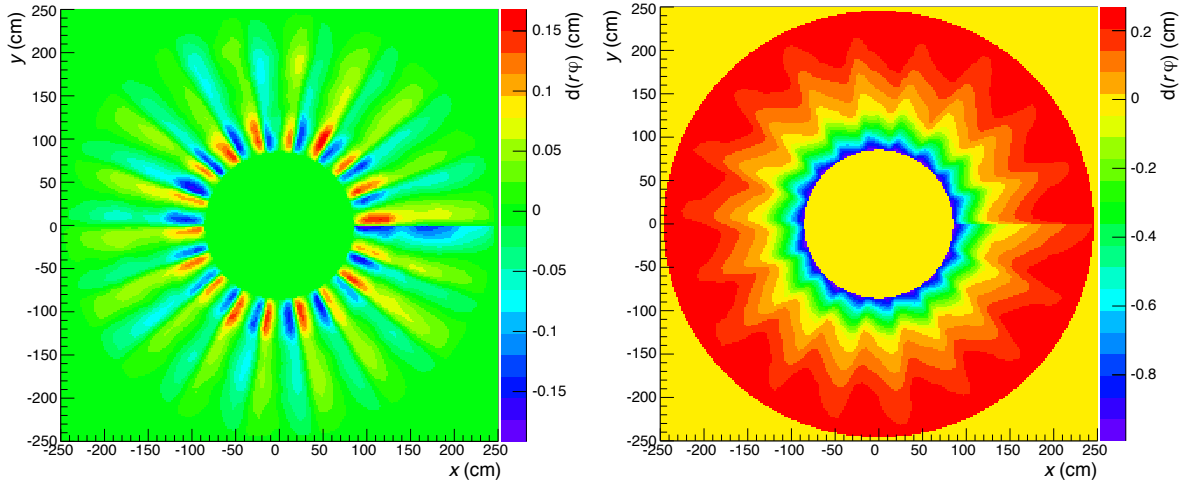


Figure 7.13: xy projection of the $r\phi$ distortion map close to the TPC central electrode (at $z = 10$ cm). The data are based on a detailed 3-dimensional space charge map for $\varepsilon \approx 5$ without magnetic field (left) and with $B = 0.5$ T (right).

1909 A fast Monte Carlo (MC) simulation has been developed in order to estimate the contributions to the
 1910 space-charge fluctuations (events, tracks and charge). The result is shown in Fig. 7.14. Here, sub-
 1911 volumes of 10 % of the size of a TPC sector are considered.

1912 The RMS of the space-charge fluctuations as obtained from the fast MC algorithm agrees well with the
 1913 expectations from the analytical formula, Eq. (7.2), for fluctuations of the number of events, number
 1914 of tracks (a Poissonian convoluted with the multiplicity distribution) and energy deposit. The relative
 1915 fluctuation scales with $1/\sqrt{N_{\text{pileup}}^{\text{ion}}}$. Depending on the spatial granularity, the relative fluctuation is around
 1916 2–3 % for $N_{\text{pileup}}^{\text{ion}} = 8000$. This result agrees well with the observations for the fluctuations of the charge
 1917 density reported in Sec. 7.4.3 and the fluctuations on the track level (see Sec. 7.4.5).

1918 7.4.5 Impact of the fluctuations on the distortion corrections

1919 To estimate the effect of fluctuations on the space-charge distortion corrections, 50 different space-charge
 1920 configurations are created. By random superposition of real Pb–Pb events, the number of ion pileup

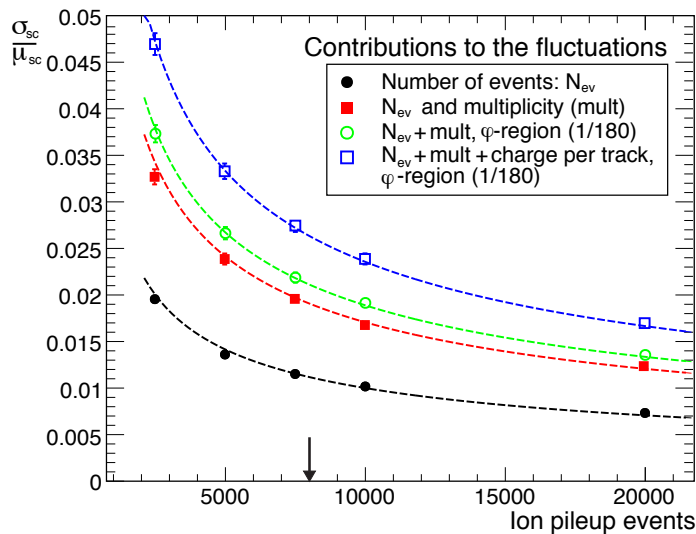


Figure 7.14: Relative fluctuation of the number of events, tracks and energy deposit (charge) from a MC simulation compared to expectations based on Eq. (7.2) as a function of $N_{\text{pileup}}^{\text{ion}}$.

1921 events $N_{\text{pileup}}^{\text{ion}}$ is varied between 2000 and 8000 in order to study different magnitudes of the ion pileup.
 1922 For each space-charge configuration, the distortion maps are calculated. The distorted tracks are cor-
 1923 rected using an *average map* based on the full sample of 130,000 interactions, that is normalized to the
 1924 corresponding $N_{\text{pileup}}^{\text{ion}}$. The $r\phi$ position of the tracks after correction is compared to that of undistorted
 1925 tracks. While the correction works well on average, there is a considerable spread. The RMS of this
 1926 spread as shown in Fig. 7.15 is characteristic for the expected space-charge fluctuations. For tracks with
 1927 $p_T > 1 \text{ GeV}/c$ the residual distortions yield up to $\sim 2.8 \text{ mm}$, which is significantly larger than the intrinsic
 1928 resolution limit σ_{intr} .

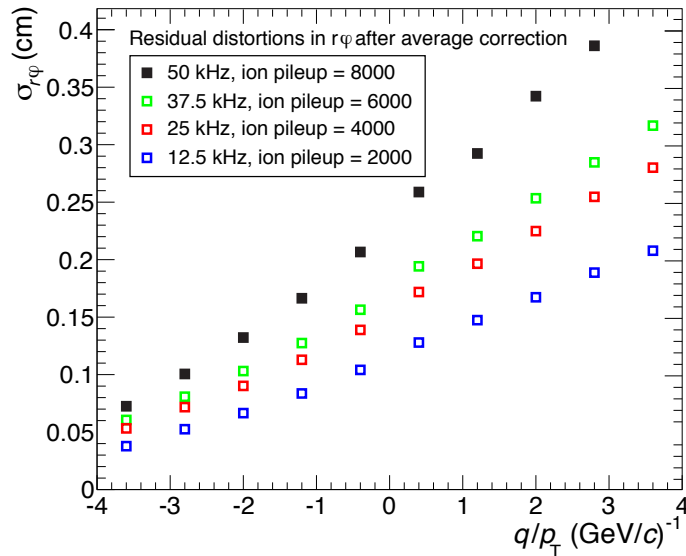


Figure 7.15: Residual $r\phi$ distortions as function of rigidity q/p_T after correction using an average space-charge distortion map (full sample of 130,000 interactions to the corresponding multiplicity). The asymmetry between positive and negative rigidity is related to the sector modulation effect, caused by the lower space-charge density close to the dead zones between readout chambers, as shown in Fig. 7.13 (right).

1929 Finally, we demonstrate the importance of the knowledge of the z distribution of the space charge and
 1930 estimate the frequency by which the space-charge distortion map needs to be updated. To this end, the
 1931 following procedure is carried out:

- 1932 1. The space-points of the TPC tracks are modified using a given distortion map.
- 1933 2. A second distortion map using the same space-charge density distribution, but shifted in z direction,
 1934 is used for correction: $\rho_2(x, y, z') = \rho_1(x, y, z + \Delta_z)$.

1935 The result of the correction is compared to the undistorted track position. The RMS of the observed
 1936 residual distributions is shown in Fig. 7.16 as a function of $1/p_T$. The residuals are increasing with Δ_z
 1937 and saturate at the random limit which is comparable with Fig. 7.15. The results shown in Fig. 7.15 reach
 1938 the intrinsic resolution limit of a few hundred μm already at effective displacements of $\Delta_z = 16 \text{ cm}$,
 1939 corresponding to an ion drift time of 10 ms. This defines the requirement to update the space-charge
 1940 correction maps during the online calibration procedure after about 5 ms, as described in Chap. 8.

1941 7.5 Performance with space-charge distortions

1942 The large space-charge densities expected during the high luminosity running in RUN 3 create distortions
 1943 which can locally exceed 10 cm, while being below that value in the largest part of the drift volume. In

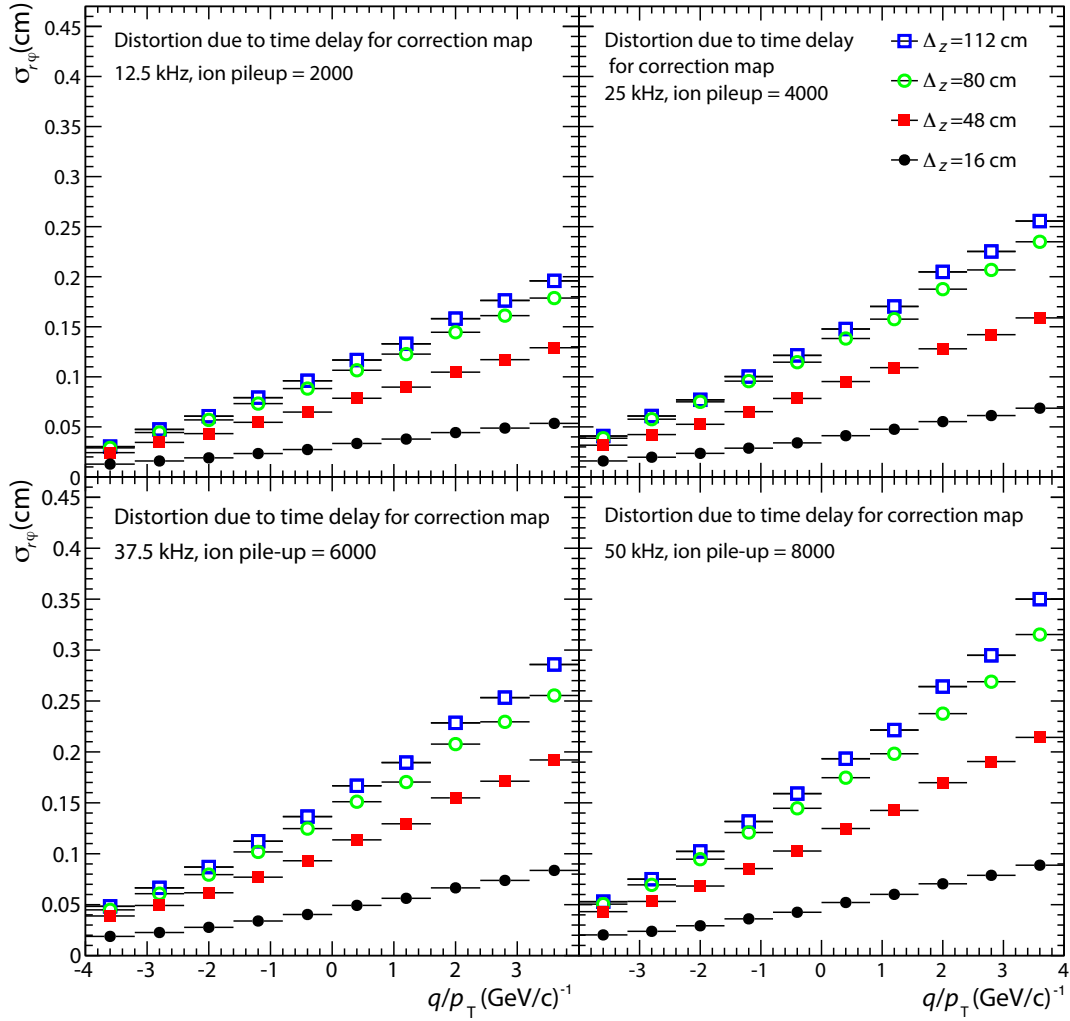


Figure 7.16: Residual $r\phi$ distortions of the tracks. The space points are distorted using randomly selected raw data with ion pileup numbers of 2000, 4000, 6000 and 8000 and corrected using the same space-charge map but shifted by an offset Δ_z .

1944 order to preserve the performance of the detector, the space-charge distortions have to be corrected with
 1945 a precision comparable to the intrinsic track resolution, which is of the order of a few hundred μm . The
 1946 implementation of a correction framework in the general calibration scheme is discussed in detail in the
 1947 following Chap. 8.

1948 Figure 7.17 shows the ITS-TPC matching efficiency (left) as well as the transverse momentum resolution
 1949 (right) obtained from a full MC, implementing the remaining residual space charge distortions after
 1950 applying the calibration procedure described in Sec. 8.4.

1951 The matching efficiency is above 95% for all momenta. For standalone TPC tracks (red), the p_T resolu-
 1952 tion is slightly worse than the one obtained without distortions (see also Fig. 7.6), while for TPC tracks
 1953 constrained to the interaction vertex (blue) and tracks matched to the ITS (black) the performance is
 1954 practically the same as for the ideal case without space-charge distortions.

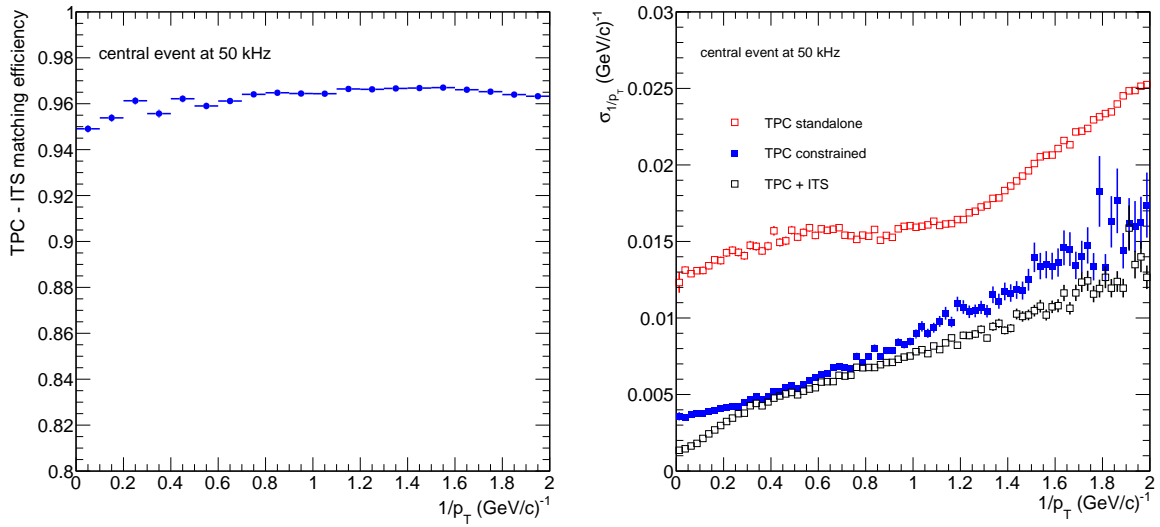


Figure 7.17: ITS-TPC track matching efficiency (right) after the second reconstruction stage.

1955 Chapter 8

1956 Online reconstruction, calibration, and 1957 monitoring

1958 Operation of the TPC in a continuous readout mode in the high-luminosity environment at the LHC in
1959 RUN 3 will produce a vast amount of data. This necessitates a change of the ALICE computing model
1960 towards massive online reconstruction, because only in this way it is possible to achieve sufficient data
1961 reduction such that the data can be stored.

1962 Efficient online cluster and track reconstruction implies that also a number of calibration steps need to
1963 be performed online. In particular, an online correction scheme for the space-point distortions induced
1964 by back-drifting ions must be applied to ensure efficient cluster-to-track association. Moreover, the
1965 online corrections have to be sufficiently precise to match TPC tracks efficiently to the external detectors
1966 ITS and TRD. If this can be achieved, a final calibration based on global tracks can be performed in a
1967 subsequent processing step.

1968 8.1 Continuous TPC operation at high luminosities

1969 The online reconstruction and calibration strategy is determined by the expected running conditions,
1970 defined by the LHC, as well as by the constraints given by the detector (continuous readout) and the
1971 online systems (need for data compression). In this section, the relevant operational conditions in RUN 3
1972 are summarized and an overview of the general online reconstruction and calibration scheme is given.

1973 8.1.1 LHC conditions in RUN 3

1974 The expected running conditions in RUN 3 are defined by beam energy, luminosity and interaction rates,
1975 and interaction spacing.

1976 *Average interaction rates*

1977 During the first Pb–Pb run in November 2010 a peak luminosity of $\mathcal{L}_{\text{peak}} = 2.5 \cdot 10^{25} \text{ cm}^{-2} \text{ s}^{-1}$ and
1978 a hadronic interaction rate of $\sim 200 \text{ Hz}$ was reached [1]. In the second Pb–Pb run in 2011 the peak
1979 luminosity reached $\mathcal{L}_{\text{peak}} = 4 \cdot 10^{26} \text{ cm}^{-2} \text{ s}^{-1}$ with a hadronic interaction rate of $\sim 3.5 \text{ kHz}$ [2]. At the
1980 same time the readout rate was limited to a few hundred Hz by the readout speed of the current TPC
1981 electronics [3].

1982 In RUN 3 the LHC will reach minimum bias hadronic interaction rates of $R_{\text{int}} = 50 \text{ kHz}$ in Pb–Pb
1983 collisions at the design center-of-mass energy of $\sqrt{s_{\text{NN}}} = 5.5 \text{ TeV}$, corresponding to a luminosity of
1984 $\mathcal{L} = 6 \cdot 10^{27} \text{ cm}^{-2} \text{ s}^{-1}$. For this TDR we assume a constant interaction rate of 50 kHz throughout a fill

of the LHC. An effective data-taking time of 10^6 s per year is assumed. This allows to collect a total integrated luminosity of at least $\mathcal{L}_{\text{int}} = 10 \text{ nb}^{-1}$ during RUN 3.

Beam structure and interaction spacing

A possible (simplified) LHC filling scheme for Pb-ions in RUN 3 consists of 12 equally-spaced bunch trains with 48 bunches each, leading to 576 bunches in each ring. The filling scheme and corresponding bunch train structure are depicted in Fig. 8.1.

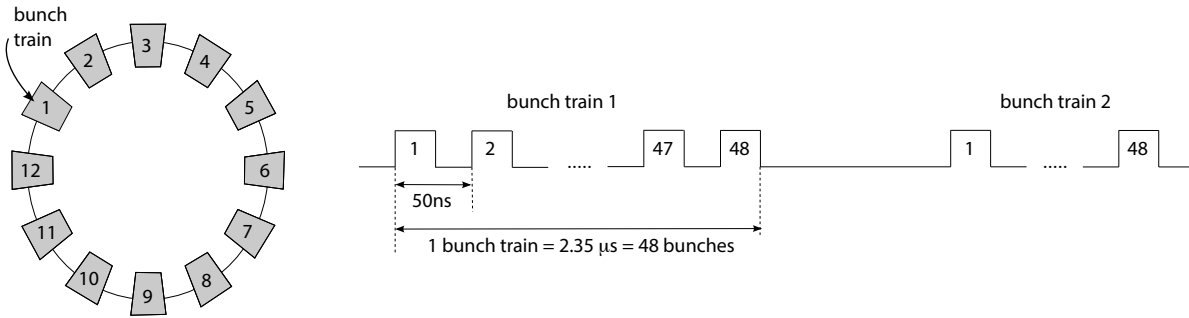


Figure 8.1: Schematic LHC filling scheme and bunch train structure.

When two bunch trains are passing, the instantaneous bunch-crossing rate is 20 MHz, while the average bunch-crossing rate is 6.3 MHz. The interaction rate of 50 kHz translates into a probability $\mu = 0.0079$ for a collision to occur in a single bunch crossing¹. Therefore, the probability for at least one hadronic interaction (for more than one interaction) within one bunch train crossing ($2.35 \mu\text{s}$) is $\sim 32\%$ (resp. $\sim 5.5\%$).

Event pileup

Event pileup in the TPC arises if more than one collision occurs within a time interval that corresponds to the maximum electron drift time, i.e. within $t_d \approx 100 \mu\text{s}$. Even though the effect increases the detector occupancy, it does not complicate the pattern recognition significantly, as demonstrated in Sec. 7.3.

Not only the average number of pileup events is of importance, but also their spacing in time. At an interaction rate of 50 kHz on average $N_{\text{pileup}} = 5$ interactions are contained in a time interval t_d . The average spacing between two collisions is $20 \mu\text{s}$ or 52 cm of drift length. The distribution of time differences between two collisions is Poissonian with the bunch train structure of the LHC beam superimposed, as illustrated in Fig. 8.2. Following the argumentation of the previous section, in $\sim 17\%$ of the cases a second collision occurs within the same bunch train crossing, i.e. within $2.35 \mu\text{s}$, corresponding to the first peak in Fig. 8.2. Separation of the tracks from two such collisions will be possible using external detector information, i.e. from the ITS.

Beam induced background

For colliding Pb beams in RUN 3 it is not expected that machine background contributes significantly to the charged track rates in the TPC. The beam currents ($\sim 85 \text{ mA}$) will not be large enough to trigger electron-cloud effects, which need at least 310 mA [4]. In the case of pp collisions, the beam currents will exceed the ones achieved in RUN 1, which were large enough to produce a background rate comparable to the interaction rate. However, several improvements are foreseen that should result in an improved background situation. These improvements include the replacement of the existing collimator at the end of the transfer line (TDI), which is now a major source of electron-cloud effects, the removal of bulky vacuum equipment near the ALICE interaction region, and the improvement of the vacuum at and near Interaction Point 2 (IP 2).

¹ $\mu = 50 \text{ kHz} / 11 \text{ kHz} / 576 = 0.0079$, with the LHC orbit frequency 11 kHz.

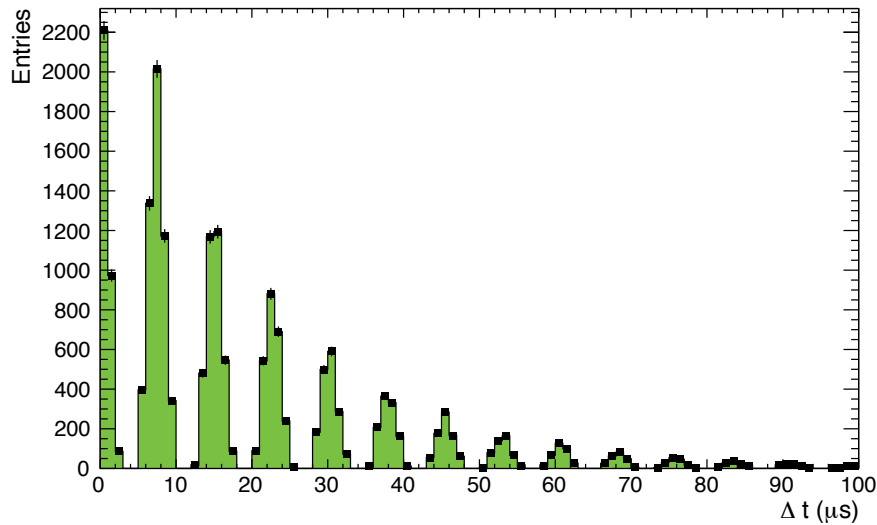


Figure 8.2: Distribution of time differences between two collisions at $R_{\text{int}} = 50$ kHz. A Poissonian distribution is superimposed by the bunch train structure of the LHC beam.

2018 8.1.2 TPC reconstruction, calibration, and data compression in RUN 3

2019 The ALICE upgrade requires a major change of the computing concept in order to be able to process and
 2020 store the large amount of data produced in Pb–Pb collisions. The main contributor to the data volume will
 2021 be the TPC operated in continuous readout mode. Most of the data processing and reconstruction will be
 2022 performed on the computing cluster of the new online systems [5]. New requirements to calibration and
 2023 reconstruction algorithms emerge in terms of running stability, processing time, memory consumption,
 2024 as well as parallelizability on different levels. These requirements build strict constraints on the data
 2025 reconstruction and calibration, as well as on data compression. A massive use of hardware co-processors,
 2026 such as FPGAs for the early processing steps, as well GPGPUs² for the later processing is foreseen.

2027 *Overview of the TPC reconstruction scheme*

2028 The choice of the reconstruction algorithms is strongly driven by the constraints of the online processing.
 2029 However, in the discussion below we will focus on demonstrating the overall strategy and the general
 2030 feasibility of online reconstruction under the operational conditions described above.

2031 A two-stage process, as depicted in Fig. 8.3, is foreseen for the online data processing. The first stage
 2032 (see below) will focus on cluster finding and the association of clusters to tracks, which are needed in
 2033 order to perform the necessary data size reduction (see Sec. 8.3). The compressed data will be written to
 2034 permanent storage. The reconstructed tracks have sufficient precision to allow matching to the external
 2035 detectors, mainly ITS and TRD. This is needed to improve the quality of the subsequent calibration step
 2036 during the next reconstruction stage.

2037 The second reconstruction stage (see Sec. 8.4) will also be performed on the online computing cluster, but
 2038 in an asynchronous mode, and can thus be repeated at any time. It aims at a further improvement of the
 2039 data quality, in particular in terms of the space-charge distortion calibrations, and employs information
 2040 from external detectors as well as more refined calibration data.

²General-Purpose Graphics Processing Units (GPGPUs)

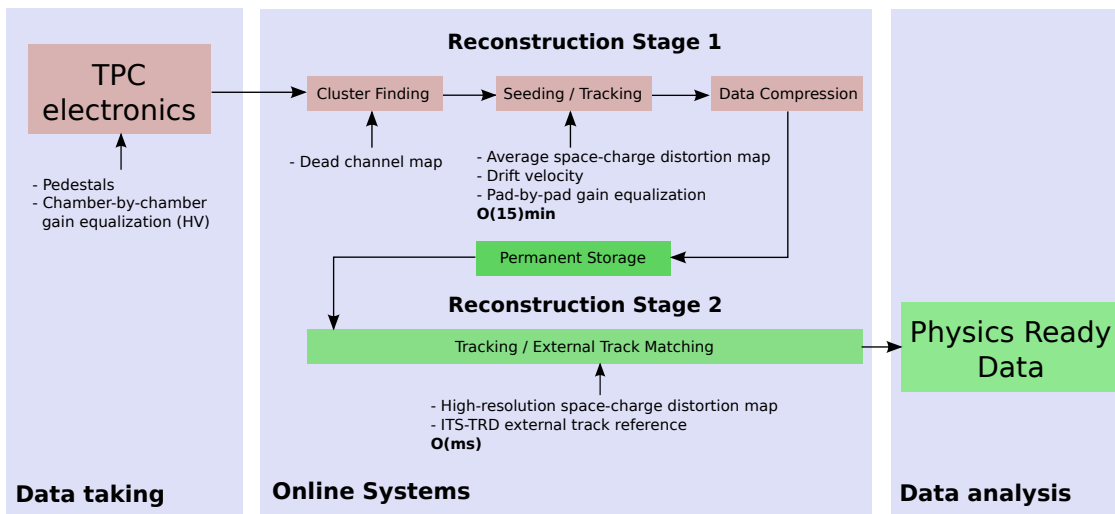


Figure 8.3: Schematic outline of the calibration flow during the data-taking and reconstruction process.

2041 *Data size and data compression*

2042 After zero suppression on the level of the front-end electronics, the average TPC raw data size in mini-
 2043 mum bias Pb–Pb interactions is $\sim 20\text{MByte}$ (see Sec. 6.3). At an interaction rate of 50kHz , this would
 2044 result in an input rate of about 1TByte/s to the online systems, and a total amount of 3EByte (10^{18}Byte)
 2045 of TPC data in RUN 3. Such numbers exceed the predicted available bandwidth and storage space by
 2046 a large factor. Thus, in order to permit permanent data storage, additional compression on top of zero
 2047 suppression to below 1MByte per interaction is required. This can be achieved by two levels of pattern
 2048 recognition that are performed in the online systems.

2049 The zero-suppressed raw data are decoded at the input to the online farm, where the raw data digits
 2050 (which consist of arrival time at the front-end electronics and signal amplitude) are associated with the
 2051 corresponding geometrical position (pad row and pad coordinates). Cluster finding is performed on the
 2052 digits, which produces three-dimensional charge clusters³.

2053 As the x_{TO} coordinate is fixed by the well-separated pad rows, cluster finding is reduced to a two-
 2054 dimensional problem in the pad–time plane⁴. A two-dimensional algorithm, as used in the current TPC
 2055 offline cluster finder, scans the pad–time plane for charge maxima using a sliding window. It allows a
 2056 good separation of close-by clusters. A different method is based on a one-dimensional algorithm, as
 2057 used in the current HLT system. It processes the pads sequentially, which allows to find the maxima
 2058 within neighboring pads on the same pad row. In this case the separation of close-by clusters is done
 2059 separately in both dimensions. The algorithm allows massive parallelization and, therefore, an easy im-
 2060 plementation into an FPGA⁵. It is the baseline solution for RUN 3, as it fits the necessity of an early data
 2061 reduction already at the input to the online systems.

2062 The cluster finding is accompanied by a further compression step based on intelligent Huffmann Cod-
 2063 ing [6] of selected parameters.

2064 Such a compression scheme has already been applied to TPC data during the 2011 Pb–Pb data taking
 2065 in RUN 1, resulting in a data compression factor of ~ 4 as compared to zero-suppressed raw data (see
 2066 Fig. 8.4). Further optimizations of the cluster data format and of the compression algorithm for RUN 3

³Alternatively the cluster finding could also be performed on the Common Readout Unit (CRU) modules for the TPC.

⁴Details on the local and global coordinate system can be found in Apx. A.

⁵Field Programmable Gate Array (FPGA)

2067 will allow a total data reduction by a factor five to seven during the cluster finding step [5].

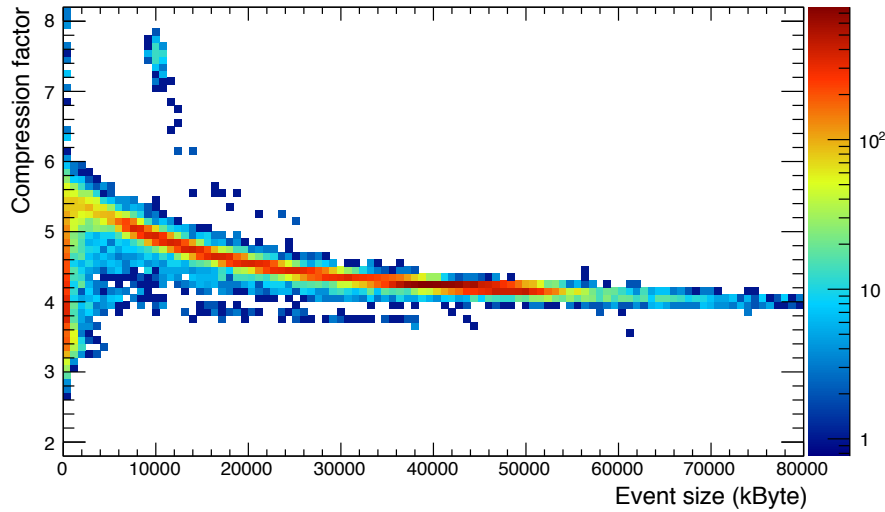


Figure 8.4: Data compression factor versus raw data size achieved using cluster finding and data-format optimizations in the High-Level Trigger during the Pb–Pb data taking in RUN 1. Adopted from [7].

2068 A further reduction in data size can be performed by tracking, where clusters are assigned to particle
 2069 tracks. This step, which is discussed in Sec. 8.3, allows to remove clusters that are not associated to
 2070 physics tracks (e.g. from delta electrons or noise) from the data stream. The possible reduction factor,
 2071 based on the experience from the past data taking in RUN 1, is of the order of two. The tracking step
 2072 also enables more advanced transformation schemes to optimize the parameter distributions for entropy
 2073 encoding, as well as the possible replacement of some of the individual cluster parameters by track-based
 2074 properties. We estimate the further reduction potential to be on the order of two to three.

2075 In total, the envisaged compression factor in the online system is of the order of 20, resulting in an
 2076 average data size per interaction of < 1 MByte. This will lead to a storage rate of ~ 50 GByte/s and a
 2077 total amount of ~ 150 PByte of stored data during RUN 3. To store the cluster information associated
 2078 to the reconstructed tracks is an advantage, allowing a possible re-calibration of individual clusters at a
 2079 later stage and, therefore, an improvement of the TPC performance. A summary of the consecutive data
 2080 compression factors is presented in Tab. 8.1.

Data Format	Data Compression Factor	Event Size (MByte)
Zero Suppression (FEE)		20
Clusterization	5-7	3
Remove clusters not associated to relevant tracks	2	1.5
Data format optimization	2-3	< 1

Table 8.1: The TPC event size and data compression factors for the different data compression steps performed in the front-end electronics and the online systems. Table adopted from [5].

2081 **Online calibration**

2082 Online reconstruction implies that also calibration information must be available at running time. Since
 2083 some of the calibration parameters change with time, a novel online calibration scheme must be im-
 2084 plemented, that allows to retrieve and update calibration information synchronous to the data collection
 2085 process.

2086 The calibration flow during the data taking and reconstruction process is schematically outlined in
 2087 Fig. 8.3 and described in the following. In the first reconstruction stage, the calibration needs to be
 2088 precise enough to associate clusters to tracks in order to allow the data compression (see Sec. 8.1.2). In
 2089 the second reconstruction stage the calibration aims at providing the detector performance required for
 2090 physics analysis⁶.

- 2091 1. Before the start of data taking, the front-end electronics need to be configured with the correct
 2092 pedestal values and zero suppression thresholds for each readout channel (see also Sec. 6.4.8) and
 2093 with the current map of active channels. These values are extracted from data recorded in special
 2094 pedestal runs between LHC fills. The high voltage of the readout chambers is set such that the
 2095 average gain of the chambers is equalized throughout the TPC. The settings are based on data
 2096 obtained using the Krypton calibration method (see Sec. 8.6.1).
- 2097 2. During data taking the cluster finder accesses the map of active channels in order to account for
 2098 broken or malfunctioning readout equipment.
- 2099 3. For the **first reconstruction stage** the relevant calibrations include drift velocity, effective gain,
 2100 and space-charge distortions. The corresponding calibration parameters change with time and have
 2101 to be updated in intervals of $\mathcal{O}(15\text{min})$, but also the static pad-by-pad equalization of the gain
 2102 extracted using the Krypton calibration method is also applied at this stage. An average space-
 2103 charge map, updated in intervals $\mathcal{O}(15\text{min})$ as well, is used for a coarse space-charge distortion
 2104 correction. It accounts for slow variations of the luminosity, pressure and temperature and for
 2105 malfunctioning sectors. To improve the precision for use during the first reconstruction stage,
 2106 the average space-charge map is scaled by the actual charged-particle multiplicity integrated over
 2107 the preceding 160ms, i.e. the maximum ion drift time in the TPC. This scaling procedure is
 2108 based on a running integral of TPC current and amplitude information over the corresponding
 2109 time window and reduces significantly the error due to temporal ion density fluctuations in the
 2110 TPC. The resulting *scaled* space-charge map ρ_{scaled} is used in the first reconstruction step.
- 2111 4. During the **second reconstruction stage** a high-resolution distortion correction map is derived to
 2112 achieve the required momentum resolution. The final distortion correction is based on external
 2113 reference track information from ITS and TRD and employs space-charge information from TPC
 2114 clusters with high granularity in space and time. According to the typical time scales of space-
 2115 charge fluctuations (see Sec. 7.4.5) the final distortion correction map must be determined in time
 2116 intervals of a few ms.

2117 8.2 Space-charge distortion corrections

2118 The largest contribution to drift distortions in the GEM TPC are due to the accumulation of space charge
 2119 in the drift volume. The magnitude and implications of such distortions are described in detail in Sec. 7.4.
 2120 For an ion backflow of $\varepsilon = 20$ the distortions reach up to 20cm in radial direction and 8 cm in $r\phi$.

2121 Below we describe how distortions due to space charge are treated when the TPC is operated in contin-
 2122 uous readout, discuss how distortion corrections are obtained, and describe different levels of precision
 2123 that can be reached depending on the available calibration input.

2124 8.2.1 TPC coordinate transformation

2125 Each TPC raw data digit consists of a geometrical position at the readout plane (pad row and pad co-
 2126 ordinates), the arrival time at the front-end electronics (t_{digit}) and the corresponding signal amplitude.

⁶The achievable TPC performance is discussed in detail in Chap. 7.

2127 Charge clusters usually spread over a few pads and time bins. The center-of-mass of a charge cluster
 2128 corresponds to a three-dimensional space point $\vec{r}_{\text{cls}} = (x, y, z)$. The proper assignment of \vec{r}_{cls} requires a
 2129 precise knowledge of the drift time t_d of the cluster:

$$\vec{r}_{\text{cls}} = \vec{r}_{\text{ro}} + \int_0^{-t_d} \vec{v}_d(x, y, z) dt, \quad (8.1)$$

2130 where \vec{v}_d is the drift velocity vector of electrons in the TPC and $\vec{r}_{\text{ro}} = (x_{\text{ro}}, y_{\text{ro}}, z_{\text{roc}})$ is the position of the
 2131 center-of-mass of the charge cluster at the readout plane (z_{roc} is the z -position of the read-out chamber).
 2132 Neglecting distortions, i.e. for $\vec{v}_d = (0, 0, v_d)$, Eq. (8.1) translates into

$$\vec{r}_{\text{cls}} = (x_{\text{ro}}, y_{\text{ro}}, z_{\text{roc}} - v_d t_d) \quad (8.2)$$

2133 In a triggered readout mode there is a strict relation between t_{digit} and t_d ,

$$t_d = t_{\text{digit}} - t_0, \quad (8.3)$$

2134 where t_0 is the time of the interaction that triggers the readout. In data acquired with a TPC in continuous
 2135 readout mode the important parameter t_0 is a priori unknown, but can be derived using the information
 2136 from external detectors. However, even in a TPC standalone tracking scheme without external detec-
 2137 tor information, t_0 can be estimated by extrapolation of track segments to $x = y = 0$, as discussed in
 2138 Sec. 8.5.1.

2139 8.2.2 Space point corrections

2140 In practice, the drift velocity vector is approximated by $\vec{v}_d = (0, 0, v_d)$ and drift-field distortions, i.e. the
 2141 effect of non-vanishing v_x and v_y are treated by effective corrections:

$$\vec{r}_{\text{cls}} = (x_{\text{ro}}, y_{\text{ro}}, z_{\text{ro}}) + \vec{\Delta}(x_{\text{ro}}, y_{\text{ro}}, z_{\text{ro}}), \quad (8.4)$$

2142 with $z_{\text{ro}} = z_{\text{roc}} - t_d \cdot v_d$ and the drift time $t_d = t_{\text{digit}} - t_0$ (see Eq. (8.3)).

2143 Numerical as well as analytical calculations of $\vec{\Delta}$ are based on the knowledge of the density distribution
 2144 of the space charge (ρ_{sc}), as described in 7.4.3. Such maps are available with different levels of precision
 2145 as described below.

2146 8.2.3 Space-charge density maps

2147 During the two reconstruction stages, estimates of the current space charge distributions have to be
 2148 available for distortion correction with different precision and granularity. For the first reconstruction
 2149 stage, at the level of the single cluster resolution ($\mathcal{O}(\text{mm})$) is sufficient in order to perform the cluster-
 2150 to-track association. The second reconstruction stage aims at reaching the intrinsic performance of the
 2151 detector, therefore requiring effective residual space-charge distortions at the level of the intrinsic track
 2152 resolution of a few $100 \mu\text{m}$ in $r\phi$.

2153 Space-charge density maps on different levels of precision are considered:

- 2154 – The **reference map** ρ_{ref} can be obtained from simulations. It is based on the geometric acceptance
 2155 of the readout chambers (incorporating non-active regions at the sector boundaries), dead regions
 2156 of the GEM system and the known gain and ϵ variations. This map can serve as an input at the
 2157 startup of the data taking.

2158 – The **average map** ρ_{av} , updated several times per fill, accounts for slow variations of the luminosity,
 2159 ambient conditions and readout chamber status. It can for example be derived from an external,
 2160 high- p_T track sample ($\mathcal{O}(1 \text{ min})$ statistics).

2161 Space-charge maps with better precision include also the effect of fluctuations.

2162 – The **scaled map** ρ_{scaled} is based on ρ_{av} , but scaled by the instantaneous ion current during the
 2163 last $t_{\text{d}}^{\text{ion}} = 160 \text{ ms}$. This covers the largest part ($\sim 2\%$) of the space-charge fluctuations (see also
 2164 Fig. 7.15), which are the contributions due to fluctuations in the number of ion pileup events⁷
 2165 and the fluctuations in the track multiplicity (centrality). These parameters are accessible online
 2166 through external detectors (collision counter, centrality measure) or from the TPC (r and $r\phi$ aver-
 2167 aged signal charges or GEM currents).

2168 – The **high-resolution map** $\rho_{\text{high-res}}$ also contains topological fluctuations in r and $r\phi$, which are
 2169 responsible for the remaining fluctuations of the space charge of $\sim 1\%$. It can be obtained by the
 2170 calibration of TPC cluster residuals with respect to a track interpolation from the ITS and TRD
 2171 detectors, as described in Sec. 8.4.1

2172 We aim at using ρ_{scaled} and $\rho_{\text{high-res}}$ for distortion corrections in the first and second reconstruction stage,
 2173 respectively.

2174 8.3 First reconstruction stage

2175 Online reconstruction is necessary in order to achieve data compression by a factor of 20 as compared
 2176 to the raw data size, and to allow for permanent storage of the data. Such compression factors can be
 2177 achieved if the association of clusters to tracks can be performed online, which implies also the necessity
 2178 for sufficient online correction of the space-charge distortions. In order to correct for these distortions
 2179 using Eq. (8.4), an estimate for the time of the interaction t_0 is needed, such that the cluster arrival time
 2180 t_{digit} can be related to the drift time t_{d} (see Sec. 8.2.1). The standard TPC offline tracking approach
 2181 employs t_0 information from external trigger detectors and was used to study the expected performance
 2182 of the first reconstruction stage, as described below.

2183 8.3.1 Standard tracking approach

2184 In this section we discuss the application of the standard TPC tracking algorithm in the first online re-
 2185 construction stage, where t_0 information from external trigger detectors is used. In this tracking scheme,
 2186 distortion corrections are applied to all clusters found within a time interval $(t_{0,i}, t_{0,i} + t_{\text{d}})$, where $t_{0,i}$ is the
 2187 time of the interaction i , which is recorded in a trigger detector. Here, we assume that all clusters found
 2188 within this time interval emerge from the interaction with collision time $t_{0,i}$. The distortion correction
 2189 is performed by employing the scaled average space-charge map ρ_{scaled} . This implies that residual dis-
 2190 tortions due to fluctuations on the level of a few percent of the initial distortions will remain. For those
 2191 clusters which belong to tracks from the interaction at time $t_{0,i}$, such residual distortions yield up to a few
 2192 mm. Clusters from interactions which occurred not at $t_{0,i}$ are not properly corrected due to the improper
 2193 drift time assumption and form background to this interaction. After tracking of interaction i is finished,
 2194 the procedure is repeated for interaction $i + 1$ at time $t_{0,i+1}$.

⁷The number of ion pileup events during $t_{\text{d}}^{\text{ion}}$ is described by a Poissonian with mean $N_{\text{pileup}}^{\text{ion}} = R_{\text{int}} t_{\text{d}}^{\text{ion}} \approx 8000$ at $R_{\text{int}} = 50 \text{ kHz}$.

2195 **8.3.2 Performance using corrections from the scaled average map**

 2196 The performance of the tracking algorithm in this approach is studied using the full microscopic simulation
 2197 chain described in Sec. 7.3. Residual distortions as expected after correction with ρ_{scaled} are imposed
 2198 to the clusters following the data-driven description given in Sec. 7.4, and assuming $\varepsilon = 20$.

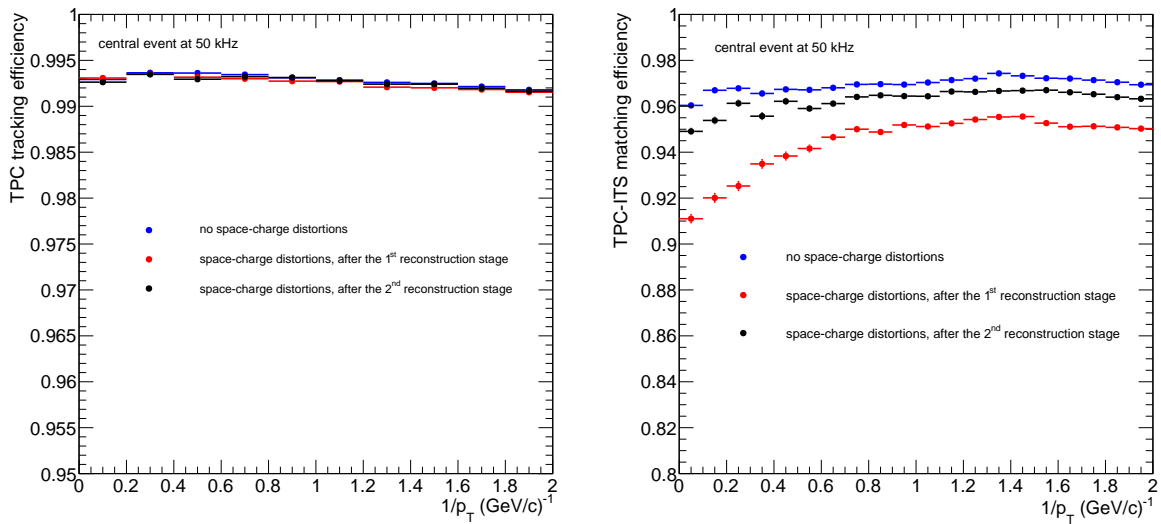
 2199 Figure 8.5 shows a comparison of the TPC tracking efficiency (left) and the TPC-ITS matching efficiency
 2200 (right) without and with space charge distortions. Even with residual distortions applying corrections
 2201 from the scaled average map (red points), i.e. in the first reconstruction stage, the efficiency of the TPC
 2202 tracking is not affected compared to the ideal case without distortions (blue points). The TPC-ITS
 2203 matching efficiency is lower by about 5% at high p_T and 2% at low p_T (0.5 GeV). This slightly lower
 2204 efficiency does not affect the requirements of the calibration though, and is recovered in the second
 2205 reconstruction stage (black points) described in Sec. 8.4.


Figure 8.5: TPC track reconstruction efficiency (left) and TPC-ITS track matching efficiency (right) in Pb–Pb collisions at 50kHz without distortion and with residual distortions after the first and second reconstruction stage.

 2206 The fraction of assigned clusters, defined as the number of associated clusters divided by the maximum
 2207 number of assignable clusters in the active region, is shown in Fig. 8.6. It is compared for the ideal case
 2208 without distortions (blue points) and with residual distortions using the scaled average space charge map
 2209 (red points) or a high-granularity map (black points). There is no significant modification in the cluster
 2210 association when residual distortions are present.

 2211 This clearly demonstrates that space-charge corrections using time-averaged maps, scaled by the instan-
 2212 taneous ion density, yield sufficient precision for efficient online tracking and cluster-to-track associ-
 2213 ation. This allows for powerful data compression and matching to the external detectors to perform
 2214 high-granularity distortion corrections for the second reconstruction stage.

 2215 It should be noted that the procedure described above is not optimized in terms of computing speed.
 2216 It implies multiple corrections of each cluster in the case of event pile-up, i.e. on average five times at
 2217 50 kHz. As a possible improvement, an alternative TPC standalone approach was developed, where an
 2218 initial estimate of the collision time, t_0^{seed} , is derived from TPC track seeds. This procedure is described
 2219 in Sec. 8.5.1.

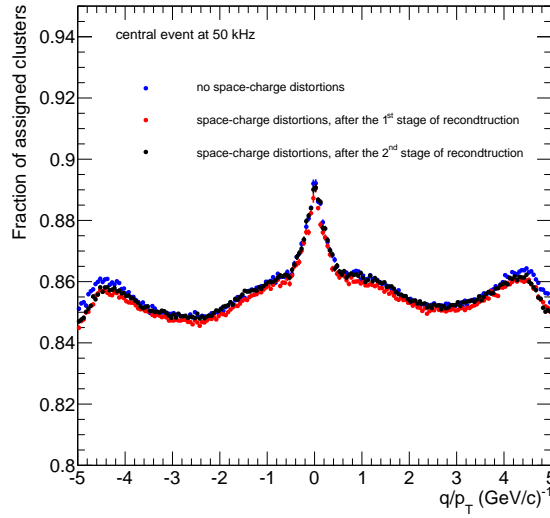


Figure 8.6: Cluster-to-track association efficiency in Pb–Pb collisions at 50 kHz without and with residual distortions using the scaled average map (first stage) and a high-granularity distortion correction (second stage).

2220 8.4 Second reconstruction stage

2221 The second reconstruction stage aims to restore the intrinsic detector resolution. Therefore, the main
 2222 objective is to reduce the effective residual space-charge distortions to the level of the intrinsic track
 2223 resolution of a few $100\mu\text{m}$ in $r\phi$. Essentially this implies a correction of the remaining local space-
 2224 charge fluctuations, which were not accounted for by the usage of the scaled map ρ_{scaled} during the first
 2225 reconstruction stage.

2226 Such a residual mis-calibration can be directly determined by measuring the TPC cluster residuals with
 2227 respect to an external track reference obtained from interpolation between ITS and TRD track segments.
 2228 This straight-forward calibration procedure relies on the availability and proper calibration of those de-
 2229 tectors. It is eventually limited by the available track statistics in a typical calibration interval. The
 2230 procedure is described below.

2231 8.4.1 ITS-TRD track interpolation approach

2232 In this approach the TPC volume is subdivided into a number of volume elements (‘voxels’). Each voxel
 2233 is aligned by minimizing the mean residual of the TPC clusters within this voxel with respect to external
 2234 reference tracks. The number of voxels must be sufficiently large to account for the local variations
 2235 of the residual distortions with sufficient granularity. On the other hand, the voxel size determines the
 2236 statistical precision that can be achieved within a typical calibration interval. For the present study a total
 2237 number of 72k voxels in the TPC is assumed, corresponding to a voxel size of 10cm, 16cm and $1/72\pi$
 2238 in z , r , and ϕ direction, respectively. The optimization of the granularity is based on a detailed study of
 2239 the residual distortion pattern after the first reconstruction stage. The required precision sets demands on
 2240 the cluster statistics within a voxel in combination with the precision of the external track reference. The
 2241 resolution achieved from a single track within a voxel, σ_{vx1} , is given by

$$\sigma_{\text{vx1}} = \sqrt{\sigma_{\text{tr}}^2 + \left(\frac{\sigma_{\text{cl}}}{\sqrt{N_{\text{cl}}}}\right)^2}, \quad (8.5)$$

2242 where σ_{tr} is the external track precision, σ_{cl} the local single cluster resolution, and N_{cl} the number of
 2243 clusters of the track in the voxel.

2244 Figure 8.7 shows the precision of external reference tracks in $r\phi$ inside the TPC for momenta above
 2245 1 GeV/ c as a function of r , assuming perfectly aligned detectors. Extrapolation from the ITS and in-
 2246 terpolation between ITS and TRD are shown on the upper and middle panel, respectively. The ITS
 2247 extrapolation uncertainty ranges from < 1 mm at the inner radius to ~ 1.5 cm at the outer radius of the
 2248 TPC. For high momentum tracks the extrapolation uncertainty is ≤ 1 mm for all radii. Using the ITS-
 2249 TRD interpolation the precision is always better than ~ 0.8 mm for momenta above 1 GeV/ c and falls
 2250 below $100 \mu\text{m}$ for high momentum tracks.

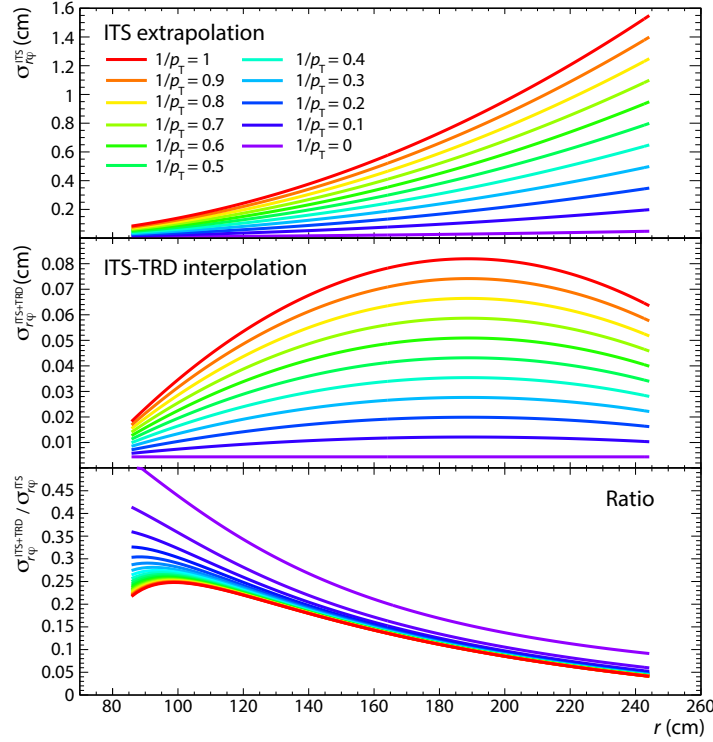


Figure 8.7: Precision of external tracks as a function of the radius inside the TPC. The color scale represents different values of $1/p_T$. Top: Extrapolation error of ITS tracks; center: Interpolation error for ITS-TRD tracks; bottom: Ratio.

2251 The track interpolation approach was studied using a fast MC, assuming perfectly aligned detectors. In
 2252 this MC, tracks from interactions at different t_0 are propagated through the detector, creating track points
 2253 along their trajectory. Those track points are distorted according to the expected space-charge distortions
 2254 for $\varepsilon = 20$ (see Sec. 7.4) and smeared with the intrinsic cluster resolution (~ 1 mm in local- y and z).
 2255 Typical space-charge density fluctuations are considered. In the reconstruction step, the distorted space
 2256 points were corrected using the scaled average map, ρ_{scaled} . A realistic parametrization of the charged-
 2257 particle momentum distribution based on measurements was used to generate the tracks. The simulated
 2258 track statistics corresponds to 5 ms of data taking at 50 kHz, i.e. tracks from 250 minimum bias Pb-Pb
 2259 events. This corresponds to a typical calibration interval over which the space-charge density can be
 2260 considered as static (see Sec. 7.4.5). For the analysis only tracks reaching the TRD detector were used.

2261 The measured local distortion $dr\phi'$ is correlated with the radial distortion dr , if the track crosses the
 2262 padrow under an inclination angle, see Fig. 8.8 (left). In this case, the true distortion $dr\phi$ and the
 2263 radial distortion can be extracted employing a linear relation:

$$dr\phi' = dr\phi + dr \cdot \tan \alpha \quad (8.6)$$

2264 where α is the local track inclination angle. An example of such a fit is shown in Fig. 8.8 (right).

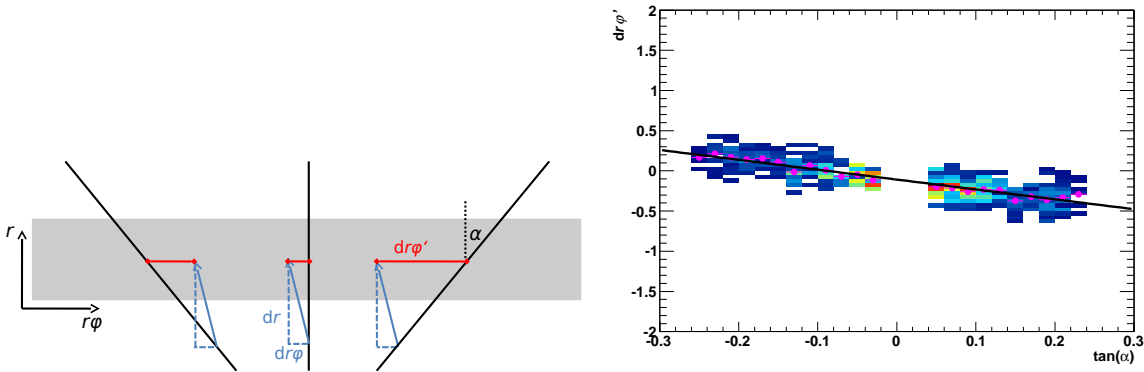


Figure 8.8: Left: Illustration of the measured $r\phi$ distortions as a combination of the real $r\phi$ distortions and the radial distortions. Right: Measured correlation between $dr\phi'$ and $\tan(\alpha)$ (see text).

2265 Figure 8.9 shows an example of the comparison between the measured residual distortions as determined
 2266 by the ITS-TRD interpolation method (points) and the real residual distortions from MC (line). The
 2267 comparison is shown in the region of smallest radius and largest drift length, i.e. $86 < r < 102$ cm and
 2268 $0 < z < 10$ cm, where the residual distortions are largest. Each data point corresponds to the fit result
 2269 in a single voxel and is used as a local correction to all space points within this voxel. The pattern of
 2270 the residual distortions is well described by the interpolation method. The momentum resolution after
 2271 application of this correction will be presented in Sec. 8.4.2.

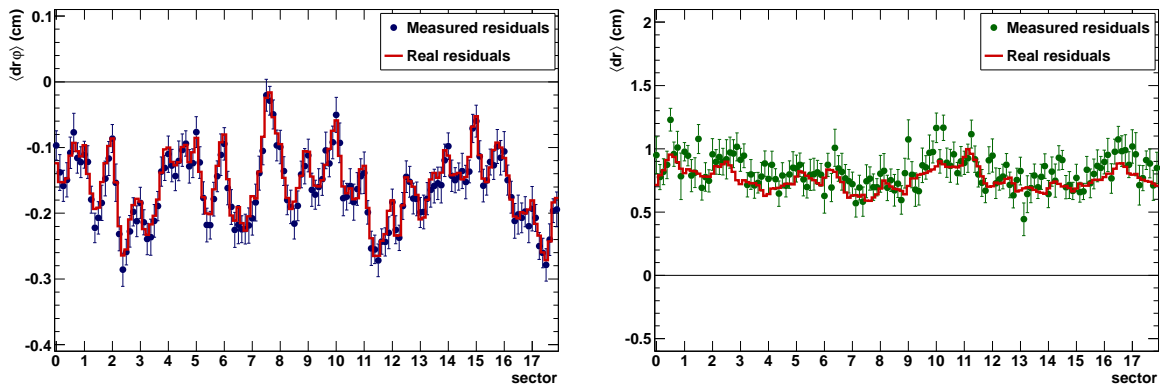


Figure 8.9: Comparison of measured and real residual distortions in $r\phi$ (left) and r (right) for $86 < r < 102$ cm and $0 < z < 10$ cm.

2272 In Fig. 8.10, the resolution of the interpolation method is shown as the difference between the measured
 2273 and the real residual distortions. The results are integrated over the full TPC acceptance.

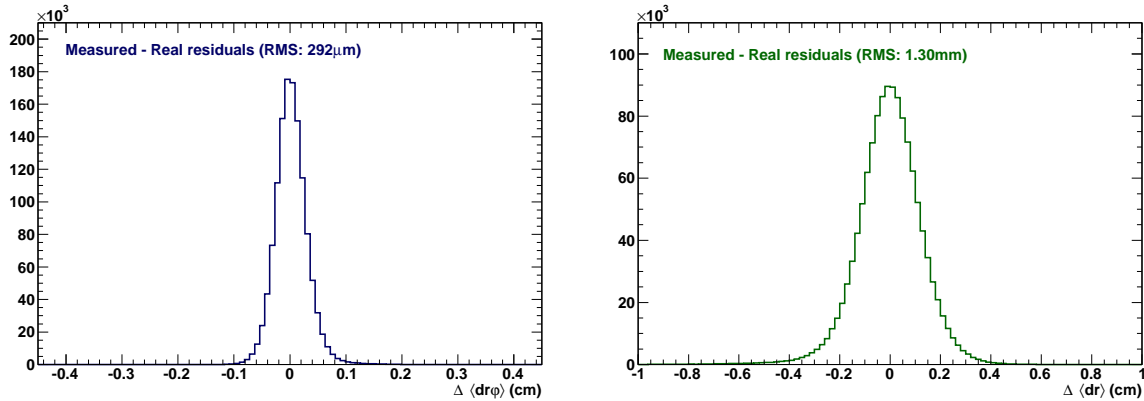


Figure 8.10: Distribution of measured minus real residual distortions for all fluctuation scenarios integrated over full acceptance of the TPC. (Left) $r\phi$ -distortions. (Right) r -distortions.

2274 In $r\phi$ the remaining residual distortions are $\sim 300 \mu\text{m}$, i.e. compatible with the intrinsic track resolution.
 2275 The remaining distortions in radial direction are $\sim 1.3 \text{ mm}$.

2276 It should be noted that the distortion vectors in nearby voxels are correlated. Exploiting the knowledge of
 2277 the functional dependence of the residual distortions on variations of the space-charge density will allow
 2278 to constrain the extracted distortion correction, and thus further improve the precision of the method and
 2279 relax the required statistics per voxel.

2280 In addition, the statistics at low radii can be enhanced adding tracks that do not reach the TRD by using
 2281 the ITS extrapolation only. This will help increasing the statistics in the region where the distortions are
 2282 largest and improve the precision of the measurement.

2283 8.4.2 Momentum resolution after residual correction

2284 In order to verify the final tracking performance after application of the high-granularity corrections
 2285 derived from the ITS-TRD interpolation method, the remaining residual distortions were mapped and
 2286 used as input for the microscopic MC. The results presented in the following are for central Pb–Pb
 2287 collisions at a minimum bias collision rate of 50 kHz.

2288 Figure 8.5 (Sec. 8.3.2) shows a comparison of the TPC tracking efficiency (left) and the TPC-ITS match-
 2289 ing efficiency (right). The results are shown for the ideal scenario without space-charge distortions (blue
 2290 points) and including the expected residual distortions after the first reconstruction stage (red points)
 2291 and after the second reconstruction stage (black points), i.e. after application of the high-granularity
 2292 corrections derived from the ITS-TRD interpolation method as described above.

2293 The TPC tracking efficiency is not affected by the residual space-charge distortions, even when only
 2294 the scaled average correction map is applied (first reconstruction stage). After application of the high-
 2295 granularity space-charge corrections using the interpolation method, the TPC-ITS matching efficiency
 2296 is about 1% lower compared to undistorted tracks. A better tuning of matching, taking into account
 2297 the measured residual distortion will further improve the matching. For residual distortions as expected
 2298 during the first reconstruction stage, the matching efficiency is slightly reduced, however this does not
 2299 significantly affect the requirements for the subsequent calibration step in the second reconstruction
 2300 stage.

2301 Figure 8.11 shows a comparison of the transverse momentum resolution for undistorted tracks (left panel)
 2302 as well as for tracks with residual distortions expected after the first (middle panel) and second recon-
 2303 struction stage (right panel). After the first reconstruction stage, the residual distortions lead to a de-
 2304 terioration of the p_T resolution by about a factor ~ 1.5 -2 as compared to the ideal case. A significant
 2305 improvement is achieved after application of the corrections derived in the second reconstruction stage.

2306 While the TPC standalone resolution after stage two is still somewhat worse than in the ideal case, the
 2307 detector resolution of the undistorted case is practically fully restored if combined TPC-ITS tracks are
 2308 considered.

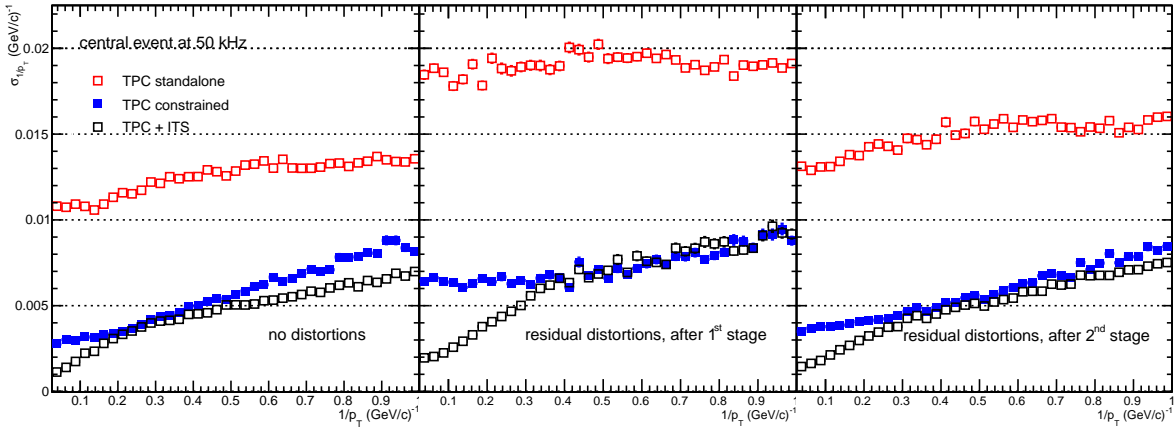


Figure 8.11: Comparison of the momentum resolution without distortions (left) and with residual distortions after the first (middle) and second (right) reconstruction stage in Pb–Pb collisions at 50 kHz.

2309 In summary, the voxel alignment approach employing interpolation of track segments from the ITS and
 2310 TRD detector provides a method to minimize the remaining residual distortions and to restore the detector
 2311 performance without distortions. It is expected that further optimizations of the described method will
 2312 even improve the results. This includes further optimization of the voxel size to account for the radial
 2313 dependence of the reference track resolution, of the hit density and of the residual distortion magnitude
 2314 and variation. Further improvement is also expected by considering the correlations of the distortions in
 2315 consecutive calibration time intervals. The current measurement approach described in Sec. 8.5.2 will
 2316 lead to an improved description of the local space-charge density fluctuations. Application of such an
 2317 improved space-charge map before the ITS-TRD interpolation method will considerably reduce the local
 2318 variations of the distortions. This will allow for a larger voxel size and thus for an improved statistical
 2319 precision of the correction.

2320 8.5 Further optimizations

2321 In addition to the studies presented above, further improvements of the online pattern recognition as well
 2322 as the space-charge distortion correction can be achieved following the concepts described below.

2323 8.5.1 TPC standalone tracking approach

2324 In order to improve computational aspects of the online reconstruction, an alternative tracking approach
 2325 which does not rely on t_0 information from external detectors was studied. To this end, a “fast” Monte
 2326 Carlo (MC) simulation was developed, that allows to vary the essential parameters and to develop and
 2327 validate the reconstruction strategy. In this MC, tracks from interactions at different t_0 are propagated
 2328 through the detector, creating track points along their trajectory. Those track points are distorted accord-
 2329 ing to the expected space-charge distributions (see Sec. 7.4) and are smeared with the expected intrinsic
 2330 cluster resolution (~ 1 mm in local- y and z).

2331 The results from the fast MC discussed below were obtained by distorting the clusters including real-
 2332 istic space-charge density fluctuations and assuming $\varepsilon = 20$. The cluster corrections in the subsequent
 2333 reconstructions step employ the scaled average map ρ_{scaled} .

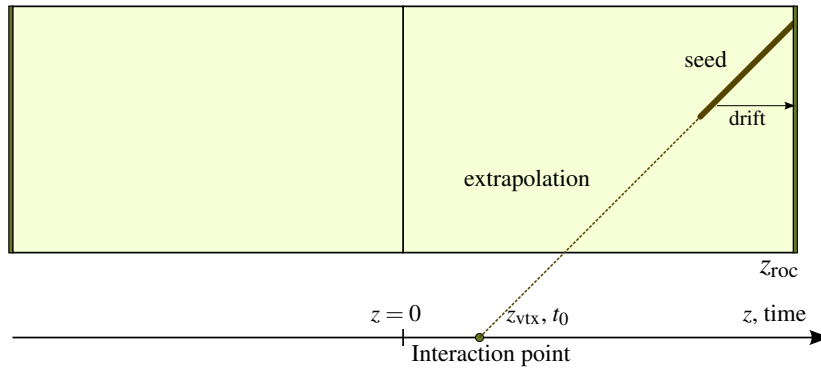
2334 **Seeding**

2335 In this approach, seeding is the first online tracking step after the cluster finding. A track seed is defined
 2336 as a set of several clusters being close in space. The seeding procedure developed for the current TPC,
 2337 described in detail in [8], is used for these studies. It starts with a pair of points in pad rows (k) and
 2338 ($k - n$). Clusters that are found within a search road between the starting points are associated to the
 2339 seed. The seed is rejected if less than $n/2$ clusters are found.

2340 In order to maximize the efficiency of the seeding step, a coarse space-charge distortion correction is
 2341 applied to each cluster. It is based on the scaled average space-charge map, ρ_{scaled} , not taking into
 2342 account topological fluctuations. Moreover, the t_0 of the corresponding interaction is not known at this
 2343 stage. It is thus assumed, that all clusters belong to a track that has about half of the maximum drift
 2344 length, i.e. $|\eta| = 0.45$. Under this assumption, a hypothetical z_{ro} -position can be assigned to each cluster
 2345 and allows an ad-hoc distortion correction following Eq. (8.4). In this way, the maximal distortions are
 2346 reduced to about one half which improves the seeding efficiency. It should be noted that seeding is
 2347 performed in regions where the distortions are not largest, and that distortions vary only slowly over the
 2348 length of the seed.

 2349 **Initial t_0 estimate**

2350 An initial estimate of the time of the interaction can be derived from a track seed by extrapolating it in the
 2351 x, y, t space to the interaction region ($x = y = 0$). This procedure is schematically depicted in Fig. 8.12.
 The calculated time from the extrapolation, t_{extrapol} , can be associated with the time of the interaction,


 Figure 8.12: Schematic drawing of the seeding procedure and the t_0 estimation.

2352 t_0^{seed} , using the relation $z = z_{\text{roc}} - v_d t_d$ (from Eq. (8.2)):

$$t_0^{\text{seed}} = t_{\text{extrapol}} - \frac{z_{\text{roc}} - z_{\text{vtx}}}{v_d} . \quad (8.7)$$

2354 Here, z_{vtx} is the z -position of the interaction vertex which can be approximated by $z_{\text{vtx}} \approx 0$. In this case
 2355 the extrapolated time at the interaction region t_{extrapol} is one full drift time ($t_d = z_{\text{roc}}/v_d$) after the t_0 of the
 2356 interaction:

$$t_0^{\text{seed}} \approx t_{\text{extrapol}} - \frac{z_{\text{roc}}}{v_d} . \quad (8.8)$$

2357 This assumption leads to an irreducible uncertainty in t_0^{seed} due to the spread of the collision vertices
 2358 around the nominal interaction point ($\sigma_z = 7$ cm corresponding to a drift time of $2.7 \mu\text{s}$), to which the
 2359 finite precision of the distortion correction adds.

2360 Figure 8.13 shows the track-by-track distribution of the difference between the estimated t_0^{seed} and the
 2361 true interaction time t_0 , multiplied by the drift velocity. The distribution has a width of about 5.2 cm. In
 2362 the simulation only events with vertices within 10 cm of the nominal interaction point were kept. The
 2363 RMS of the simulated event vertices is 4.7 cm, which implies that the precision of t_0^{seed} is dominated by
 2364 the irreducible contribution from the vertex spread.

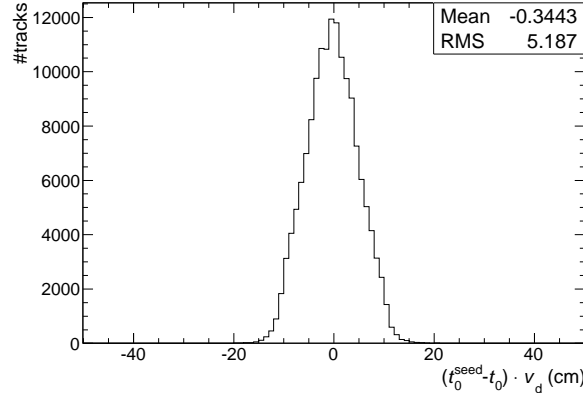


Figure 8.13: Deviation of t_0^{seed} from the real t_0 multiplied by v_d . Space-point distortions for $\varepsilon = 20$ were used in the MC.

2365 *Cluster-to-track association*

2366 The cluster-to-track association is an integral part of the first stage of the reconstruction. Starting from
 2367 track seeds, the track parameters are extrapolated inwards (smaller radii) and outwards (larger radii).
 2368 Then, within a road in the z and local- y directions, clusters are searched that are close to the track
 2369 extrapolation.

2370 The efficiency of this procedure suffers from the coarse distortion corrections in the first step, in particular
 2371 in regions where the distortions are large, i.e. at small r and z . Therefore, the search road of the tracking is
 2372 modified according to the local distortions estimated from t_0^{seed} . The t_0^{seed} resolution presented in Fig. 8.13
 2373 implies that the uncertainty on the cluster drift time can be reduced from the maximum of $\sim \pm 50 \mu\text{s}$ to
 2374 only a few microseconds (corresponding to the width of Fig. 8.13). Consequently, the distortions can be
 2375 corrected to the level of a few percent using t_0^{seed} , assuming that the distortions scale approximately linear
 2376 with the drift time. On this level, $\mathcal{O}(1 \text{ mm})$, the remaining distortions do not affect the cluster-to-track
 2377 association.

2378 It should be mentioned that the remaining distortions can be improved at this point of the reconstruction
 2379 by matching the track t_0^{seed} to the closest t_0 from the list of collision times from an external trigger
 2380 detector. Given the t_0^{seed} resolution of $\sim 2.7 \mu\text{s}$ quoted above, unambiguous matching to the proper
 2381 interaction t_0 is possible if no other collision occurred in the same bunch train crossing. This is the case
 2382 for $\sim 83\%$ of the collisions, see Fig. 8.2. In the remaining cases, the achievable precision will be limited
 2383 to that of t_0^{seed} , as long as no external tracking information from ITS is included.

2384 *Matching with external detectors*

2385 A key issue for the calibration and reconstruction is the matching of TPC tracks to external detectors,
 2386 mainly ITS and TRD. Here, we focus on the implications for ITS matching since the occupancies and
 2387 distortions at smaller radii are much larger, and therefore, more demanding for the internal track calibra-
 2388 tion.

2389 For the matching with the ITS we assume that a standalone ITS tracking will be performed based on
 2390 the ITS hits. This will allow a matching on the track level, in terms of the following track parameters:
 2391 the local- y and z position, the sine of the inclination angle in the bending plane, the tangent of the dip

2392 angle of the track, and the curvature expressed as $1/p_T$. In addition, by propagating the ITS track, a
 2393 comparison of the track parameters at the inner wall of the TPC rather than at the ITS can be performed.
 2394 This allows a better matching precision since the uncertainties on the track points of the ITS are much
 2395 smaller than for the TPC. Therefore, an extrapolation of the ITS track towards the TPC is more precise
 2396 than vice versa.

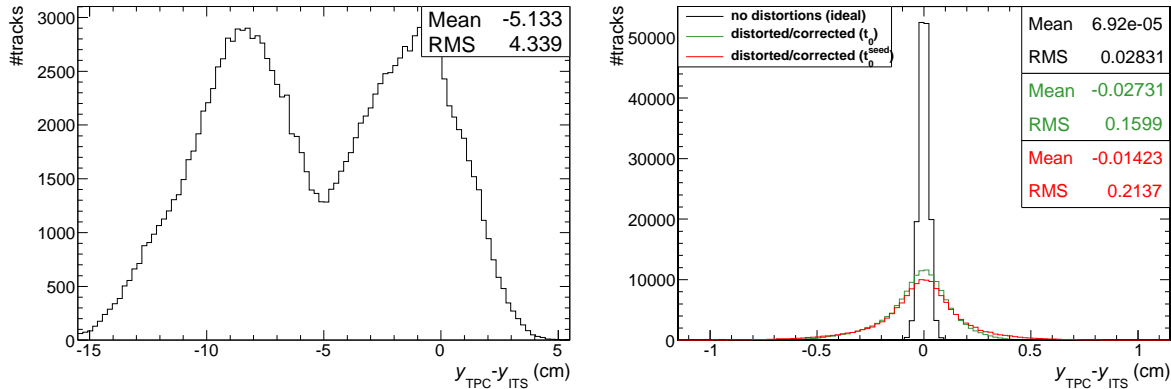


Figure 8.14: Matching of the local- y coordinate of ITS and TPC tracks. (Left) For tracks from undistorted clusters at the outermost ITS layer (red) and the inner wall of the TPC (black). (Right) For tracks from fully distorted clusters without correction (at the inner wall of the TPC).

2397 The challenge of matching TPC tracks, distorted due to space-charge, with ITS information is manifest
 2398 in Fig. 8.14 (left panel). It shows the local- y matching of ITS and TPC tracks built from distorted clusters
 2399 without performing any correction on the distortions. The shift and asymmetry of the distribution arises
 2400 from an interplay between charge and curvature of the track and the $E \times B$ effect. The deviations are
 2401 large which makes unambiguous track matching at high occupancies impossible.

2402 Figure 8.14 (right panel) shows the local- y matching of ITS and TPC tracks built from distorted clusters
 2403 and correcting them with the z -position estimate obtained from t_0^{seed} (red histogram). The RMS of this
 2404 distribution is about 2.1 mm, being half the width of the readout pads of the inner readout chamber. In
 2405 comparison to Fig. 8.14 (left panel) a strong improvement of the matching precision is observed, leading
 2406 to a large reduction of the combinatorial background in the TPC-ITS matching procedure. Note that this
 2407 resolution is a result of the first online reconstruction stage based entirely on TPC information.

2408 Matching with the proper ITS track will provide t_0 information and thus further improvement of the
 2409 space-point distortion corrections, as shown in the same figure (green histogram). In addition, the match-
 2410 ing is compared with the intrinsic resolution (black histogram). For performing the final matching, all
 2411 possible TPC-ITS track combinations within a matching window are formed, each time refitting the TPC
 2412 track parameters using the correct t_0 information delivered by the ITS for the z -position estimate. By
 2413 using all five track parameters for the matching, the number of candidates can be reduced further.

2414 After this step, the residual distortions of the TPC clusters are dominated by the space-charge fluctua-
 2415 tions, which are not accounted for by using the scaled space-charge map ρ_{scaled} for distortion correction.
 2416 As discussed in Sec. 8.5.2, the quality of the employed space-charge distortion maps can be further im-
 2417 proved by making use of the measured currents with high temporal and spacial granularity. Consequently,
 2418 also a large improvement on the matching precision is expected.

2419 8.5.2 Space-charge calibration by current measurements

2420 For the first reconstruction stage it is foreseen to base the space-charge distortion correction on the scaled
 2421 average space-charge density map, where the total space charge integrated over the ion drift time, t_d^{ion} ,
 2422 of 160 ms is used for scaling (see Sec. 8.3). This method can, however, be refined by using the detailed
 2423 ion density distributions in time and space. Using such a procedure would yield a much more precise

2424 description of the space-charge distortions. The idea is described in the following.

2425 The space-charge density is proportional to the ‘signal current’ I_{roc} at the readout chambers multiplied
2426 by ε , the number of back drifting ions per incoming electron:

$$\rho_{\text{sc}} \sim I_{\text{roc}} \cdot \varepsilon . \quad (8.9)$$

2427 Two methods are considered to measure I_{roc} :

2428 – **Hardware-based method:** The currents on the GEM HV sectors are proportional to the charge
2429 locally produced by gas amplification. They can be measured with high temporal granularity (see
2430 Secs. 4.4, 10.3, and 11.4.1). A similar current measurement is currently being prepared for RUN 2
2431 for a subset of the HV channels, albeit for data taking with the TPC in gated mode.

2432 – **Software-based method:** The cluster charges in the raw data are proportional to the current, I_{roc} .
2433 They can be measured with the granularity in space and time required to derive a high-resolution
2434 space-charge map. The data are available at the input to the online farm on the FPGAs which
2435 perform the cluster finding.

2436 From either, or a combination of these methods, it will be possible to follow the amount of ions created in
2437 space and time with high granularity. An integration over the full drift of the ions allows the calculation
2438 of the present space-charge density maps ρ_{scaled} and $\rho_{\text{high-res}}$.

2439 From any space-charge density map ρ_{sc} , obtained e.g. from the current measurement approach, the distortions
2440 can be derived analytically. However, with the methods currently available this will not be possible
2441 on the required time scale of a few ms. To overcome this limitation, the following method is foreseen:

2442 The actual space-charge distortion map, $\vec{\Delta}$, is estimated by performing a Taylor expansion of a reference
2443 distortion map, $\vec{\Delta}_{\text{ref}}$, obtained for a reference space-charge distribution⁸, ρ_{ref} , over volume cells i :

$$\vec{\Delta} = \vec{\Delta}_{\text{ref}} + \sum_i \frac{\partial \vec{\Delta}_{\text{ref}}}{\partial \rho_{\text{sc}}^i} \delta \rho_{\text{sc}}^i , \quad (8.10)$$

2444 where $\partial/\partial \rho_{\text{sc}}^i$ is the partial derivative with respect to a change of the space-charge density in a volume
2445 cell i and $\delta \rho_{\text{sc}}^i = \rho_{\text{ref}}^i - \rho_{\text{sc}}^i$ the variation of the space-charge density in cell i . The local derivatives can be
2446 pre-calculated analytically and stored in lookup tables for fast access. Together with the measured actual
2447 space charge density ρ_{sc} , this will allow a fast calculation of the present space-charge distortion map $\vec{\Delta}$.

2448 For the expected space-charge densities, the distortions do not scale linearly with the average space-
2449 charge density. Therefore, if the deviation of $\langle \rho_{\text{sc}} \rangle$ is large, $\mathcal{O}(10\%)$, compared to $\langle \rho_{\text{ref}} \rangle$, $\vec{\Delta}_{\text{ref}}$ needs to be
2450 updated. This can happen e.g. due to a change in luminosity. Such updates are expected at most on the
2451 level of $\mathcal{O}(1 - 10 \text{ min})$, making feasible the analytic recalculation of $\vec{\Delta}_{\text{ref}}$.

2452 8.6 Additional calibration requirements, monitoring, and quality control

2453 This section summarizes the additional calibration steps that have to be applied to the TPC data and
2454 discusses the requirements for online monitoring and quality control.

⁸This could be e.g. be the long term average map, ρ_{av} , see Sec. 8.2.3

2455 **8.6.1 Further calibration requirements**

2456 As most of the TPC calibration methods have been already developed for RUN 1, they are only briefly
 2457 mentioned in this section and references to them are given. According to their characteristic dependence
 2458 on ambient conditions over time, they are divided in time-independent and time-dependent calibrations.

2459 *Time-independent calibrations*

2460 Time-independent calibrations are characterized by a stable behavior over long periods. The pedestal
 2461 values and zero suppression thresholds for the individual front-end electronics channels, as well as the
 2462 map of dead channels, only change on time scales of the order of weeks or longer.

2463 A proper calibration of the effective gain of the GEM readout system is mandatory for providing particle
 2464 identification with best quality. The gain needs to be corrected for time-independent pad-by-pad and
 2465 chamber-by-chamber variations. The retrieval of these calibration parameters is done typically once
 2466 per year based on the Krypton calibration method, originally developed by the ALEPH [9, 10] and
 2467 DELPHI [11] collaborations. The decay clusters of radioactive ^{83}Kr , which is released into the TPC gas,
 2468 are analyzed and allow the extraction of the mean gain per readout chamber, but also the relative gain of
 2469 each readout pad with respect to the mean value. The method was already successfully used for the gain
 2470 calibration of a GEM based TPC [12, 13].

2471 An additional method for pad-by-pad gain calibration is based on charged-particle tracks. The relative
 2472 pad gain factors can be retrieved from large statistics samples of clusters from a selected sample of
 2473 tracks with well-defined mean energy loss, e.g. MIPs. This method allows a higher granularity in time,
 2474 but needs additional attention when running in an environment of high space-charge distortions, due to
 2475 the compression of tracks in radial direction and the merging of ionization clusters.

2476 *Time-dependent calibrations*

2477 The calibration of the drift velocity v_d and the gas gain have a time-dependent component that is con-
 2478 nected to changes of the ambient conditions and of the gas composition. Moreover, the average space-
 2479 charge map has to be updated periodically in order to account for slow variations of luminosity, ambient
 2480 conditions, and for malfunctioning sectors.

2481 Different methods for determining the drift velocity and gain are described below. An update of the
 2482 corresponding calibration parameters every 15 min has proven sufficient in the calibration scheme for
 2483 RUN 1. Between updates, a simple scaling based on pressure and temperature changes is performed.
 2484 Such a scaling can be used also for RUN 3, but also other possibilities are investigated.

2485 **Drift velocity** The variations of the drift velocity v_d in time are mainly induced by changes of the
 2486 ambient conditions (pressure and temperature) and of the gas composition. Two methods for determining
 2487 v_d have been routinely used in RUN 1.

2488 Laser measurements yield a very robust estimate for the drift velocity, which is independent of reference
 2489 detectors. Laser events are triggered and, therefore, the t_0 of the laser event is known. The arrival time
 2490 of photo-electrons emitted from the central electrode (CE), which are created by scattered laser light
 2491 inside the TPC, determines the drift time for the full drift length. The method allows to extract local drift
 2492 velocity gradients and thus to monitor local temperature variations in the gas [14].

2493 Track matching with external detectors (in particular the matching with ITS tracks) allows the determi-
 2494 nation of the drift velocity with high granularity in time⁹. The drift velocity can be determined using a
 2495 Kalman-filter approach, fitting the differences in the z -positions of the TPC and ITS track. The method

⁹In the RUN 1 calibration scheme laser measurements were used as an initial estimate for the reconstruction. However, track matching was the main source of the drift velocity calibration.

2496 is also used for the other track parameters and allows to simultaneously fit the distortions in addition (see
2497 also Sec. 7.4.5).

2498 **Readout chamber gain** Like the drift velocity, the gas amplification is influenced by the ambient
2499 conditions. The variations of the effective gain in the readout chambers can be followed using tracks
2500 with a constant dE/dx . Minimum ionizing (MIP) pions or electrons are used for this purpose. Pions
2501 are abundant, the MIP region is easy to identify, and the signal is clean from contamination. Electrons
2502 can be extracted using topological reconstruction of conversion photons in the detector material. The
2503 advantage of electrons is that their energy-loss is about 50% higher than that of MIPs, and therefore,
2504 usually less prone to threshold effects. However, it requires the reconstruction of secondary vertices and
2505 thus they need either longer integration times or yield lower precision. Methods using both particles will
2506 be applied for gain calibration of the upgraded TPC on the readout chamber level, allowing to follow the
2507 gain variations.

2508 8.6.2 Monitoring and quality control

2509 The concept of online Quality Control (QC) combines aspects of continuous monitoring and control of
2510 the data in order to ensure the required prompt reaction on appearing issues already during the data tak-
2511 ing. The specific monitoring tasks are based on the solutions developed already in RUN 1. Additionally,
2512 the monitoring of the space-charge distortions and their correction will be an integral part of this strategy.

2513 In case of spotted incidents during the offline reconstruction process, the basic strategy has been to restart
2514 the reconstruction process (ie. another reconstruction pass). This procedure is very successful in order to
2515 utilize a maximum of recorded data for physics analysis, but can not be transferred to RUN 3, due to the
2516 online reconstruction paradigm. Therefore, an optimized concept for data quality monitoring is needed
2517 for RUN 3, which is discussed below.

2518 *Monitoring*

2519 Different kinds of input data will be used for the QC in RUN 3. These data comprise not only different
2520 levels of reconstructed data and global, environmental observables, but also the calibration parameters
2521 produced online. The key feature of QC will be the time-wise trending of those observables. This has
2522 been demonstrated to be very successful during RUN 1 in the offline QA, as well as HLT online QA on a
2523 run-by-run basis.

2524 The observables, which have been already defined, will be used also for RUN 3, as they have been proven
2525 to allow a good and comprehensive judgment of the performance of the TPC. A list of observables to be
2526 monitored is given here:

- 2527 – **External Parameters** such as as instantaneous and integrated luminosity, beam-background, am-
2528 – bient pressure, and temperature, which slowly change in time.
- 2529 – **Global Event Properties** such as data sizes per interaction or per time frame, track multiplicities,
2530 – and compression factors.
- 2531 – **Calibration Objects** such as alignment stability, drift velocity, gain stability, and space-charge
2532 – distortions.
- 2533 – **Cluster Parameters** such as cluster charge and width, as well as fraction of clusters associated to
2534 – tracks from interactions.
- 2535 – **Track Parameters** such as number of clusters associated to tracks, pseudo-rapidity, angular, and
2536 – momentum distributions, as well as $\langle dE/dx \rangle$ signal and $\langle dE/dx \rangle$ resolution of minimum-ionizing

2537 particles. Furthermore, also distances-of-closest-approach to the primary vertex, as well as the
 2538 track matching efficiency to the external detectors, such as ITS, TRD, and TOF.

2539 – **Advanced Physics Observables** such as fits to the invariant mass distributions of V0 particles (K_s^0
 2540 and Λ), fits to the transverse momentum distributions, as well as parameters of tracks from cosmic
 2541 particles within normal collisions events. Finally, also the particle identification performance can
 2542 immediately be verified.

2543 *Space-charge calibration monitoring*

2544 The TPC laser system is an ideal tool to monitor the quality of the space-charge calibration because it
 2545 provides reproducible straight ionization tracks at known positions. In the TPC laser system the laser
 2546 light is split in several beams through an optical system of semitransparent beam splitters, micro mirrors
 2547 and bending prisms, and guided into the TPC at different entry points through quartz windows (see
 2548 Sec. 11.4.4 and [15]). The individual position, as well as the inclination angle of each micro mirror, has
 2549 been measured and is available in a database. Laser tracks can thus be easily associated to a micro mirror
 2550 from the different angles and z -positions of the reconstructed track parameters. Figure 8.15 shows the
 2551 result for simulated laser tracks with the space-charge distortions expected for $\epsilon = 20$. Together with
 2552 the different layers along the z -axis such data allow to verify the quality of the extracted correction maps
 2553 with sufficient precision. Therefore, laser data are ideally suited for quality assurance purposes.

2554 *Quality control*

2555 The calibration parameters applied in the online reconstruction process have to be closely monitored and
 2556 validated. This will allow to identify wrongly calculated values or even outliers in a trend, in cases where
 2557 a fit to data might have failed. A similar validation step has been already applied during RUN 1 before
 2558 the created calibration objects have been uploaded to the Offline Conditions DataBase (OCDB).

2559 In order to establish these monitoring and control layers, a high level of automation is required not only
 2560 to allow fast reaction, but also to minimize manual interventions by shift personnel. Automatic alarms on
 2561 basis of smaller subsets of key trending histograms will be constantly available, in order to inform about
 2562 potential problems. A more detailed set of observables has to be collected at the same time in order to
 2563 allow the experts to react quickly in case of issues with the quality of the data and the performance of
 2564 the online reconstruction of the TPC. Predefined procedures for fast detection of those error conditions
 2565 are crucial to ensure a prompt reaction. Actually, error conditions could be anticipated using predictions
 2566 based on trending information on changing detector behaviour and/or conditions.

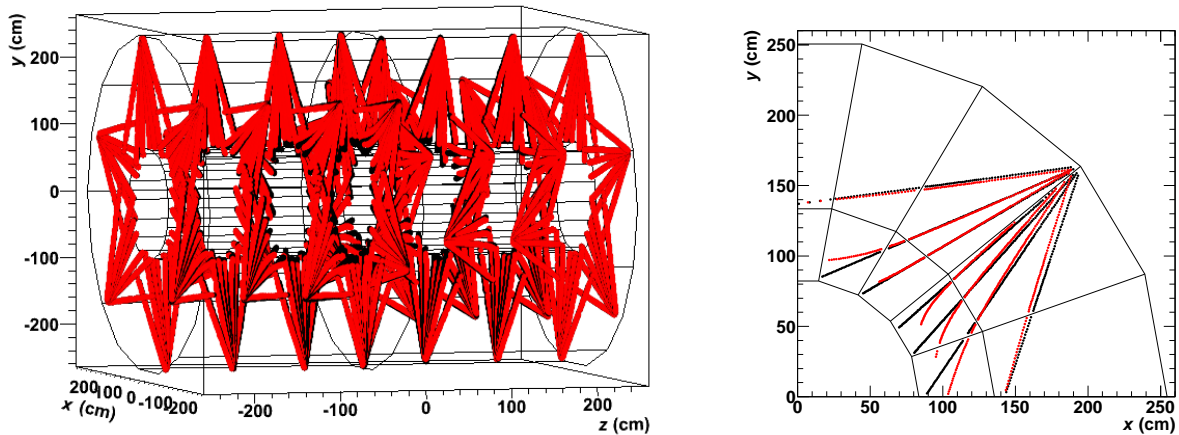


Figure 8.15: Simulated laser event. Black points indicate undistorted clusters, red points show distorted clusters, assuming $\epsilon = 20$. Left panel: all laser tracks. Right panel: laser tracks from one micro-mirror bundle.

2567

Chapter 9

2568

Alternative R&D options

2569

This chapter describes the R&D status of alternative options for the upgrade of the TPC readout.

2570

2571

2572

2573

2574

The baseline proposal for the design of the readout chambers of the upgraded TPC foresees a quadruple GEM stack with asymmetric field configurations, as described in Chap. 4. This baseline approach fulfills the requirements listed in Chap. 1. In parallel, alternative R&D efforts have been made to study and develop options to further improve the detector performance. The following key issues have been addressed:

2575

- minimize ion backflow,

2576

- minimize pileup of tracks from different events and

2577

- preserve or improve the space-point, momentum, and dE/dx resolutions.

2578

2579

2580

In particular, COBRA GEMs, perspectives of using a different gas mixture containing CF_4 in combination with chevron-shaped readout pads, and a gas amplification option based on 2 GEMs and one MMG¹ were studied in detail.

2581

9.1 R&D with COBRA GEMs

2582

2583

2584

A COBRA GEM is a GEM with a patterned electrode on the surface, which helps to trap back-flowing ions very efficiently [1, 2]. To characterize the properties of COBRA GEMs in a TPC application, a comprehensive R&D study was performed.

2585

2586

2587

Three kinds of COBRA GEMs have been developed in collaboration with SciEnergy Co. Ltd [3]. Table 9.1 summarizes their specifications. In addition, two types of standard GEMs were used for the present measurements, which are listed in Tab. 9.1 as well. Figure 9.1 shows a photograph of COBRA 1.

notation	thickness (μm)	hole size (ϕ) (μm)	pitch (μm)	rim size (μm)	insulator
COBRA 1	400	300	1000	100	FR5
COBRA 2	200	150	500	50	FR5
COBRA 3	100	100	400	0	LCP
GEM 50	50	70	140	0	LCP
GEM 100	100	70	140	0	LCP

Table 9.1: Geometries of COBRA GEMs and standard GEMs used for the measurements.

¹MicroMegas: Micro-Mesh Gaseous Structure (MMG)

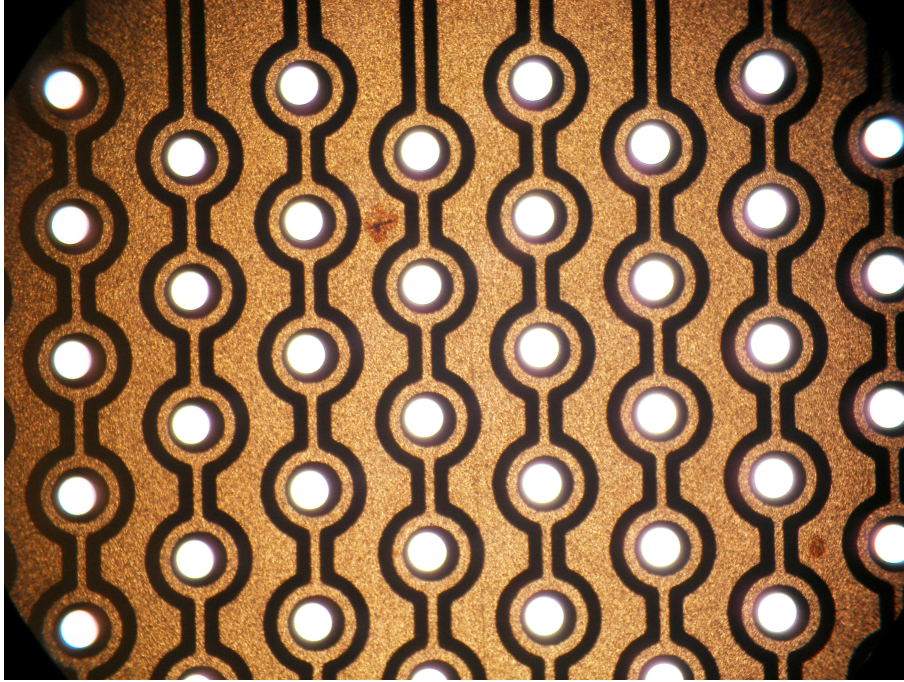
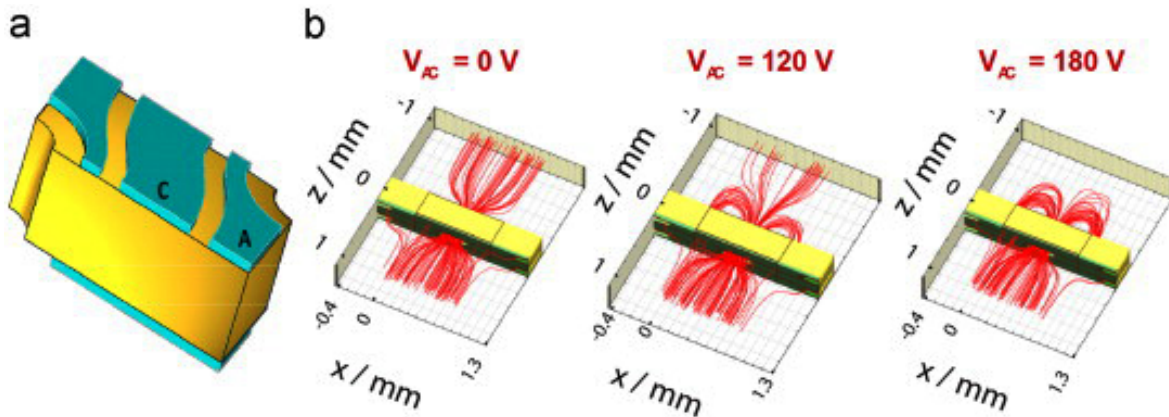


Figure 9.1: Photograph of COBRA 1.

Figure 9.2: (a) COBRA GEM unit cell built in the simulation program ANSYS (b) ion drift lines in a COBRA GEM with a potential difference ΔU_{AC} between GEM electrode (A) and COBRA electrode (C). Image is taken from [1].

2588 COBRA 1 and COBRA 2 are based on glass epoxy laminate (FR5) as insulator and $6 \mu\text{m}$ Cu layers,
 2589 covering an active area of $3 \times 3 \text{ cm}^2$. The holes are pierced by a mechanical drilling technique. The
 2590 additional pattern on the top and bottom surface of the GEMs are produced by wet etching. Clearances
 2591 from the edge of the hole (rim) of $100 \mu\text{m}$ and $50 \mu\text{m}$, respectively, are introduced to protect from
 2592 discharges. However, the possibility of charge-up at the rim of the FR5 insulator occurs, which affects
 2593 the gas gain and long term stability. To avoid this effect, a new production method for a COBRA GEM
 2594 with standard thickness ($100 \mu\text{m}$) and standard insulator (LCP²) without rim was started³ (COBRA3).

2595 Figure 9.2 is taken from [1]. It shows a COBRA unit cell built in the simulation software ANSYS and drift
 2596 lines of ions at different potential differences ($\Delta U_{AC} = U_{\text{GEM}} - U_{\text{COBRA}} = 0, 120, \text{ and } 180 \text{ V}$) between
 2597 GEM electrode (A) and COBRA electrode (C). The reduction of the ion backflow as the potential ΔU_{AC}
 2598 increases is evident.

²Liquid Crystal Polymer (LCP)

³Unfortunately, the production of COBRA3 is still underway such that at the time of writing this TDR it is not yet ready for testing.

2599 **9.1.1 Characterization of single COBRA GEMs**

2600 Measurements of gas gain and ion backflow with a single COBRA 1 and COBRA 2 have been performed
 2601 at different voltages U_{GEM} and ΔU_{AC} . All measurements have been performed in Ne-CO₂ (90-10). Fig-
 2602 ure 9.3 shows the schematics of the measurement setup. The length of the drift volume is 3 mm. X-rays
 2603 are injected into the detector from the top of the chamber. Primary electrons created between shield
 2604 and mesh (cathode) do not contribute to the multiplication of electrons, whereas the electrons created
 2605 between the mesh and the GEM (drift region) enter the multiplication region. The currents on the mesh
 2606 and on the pad anode are read out by picoammeters (ADC R8240 x2 or KEITHLEY 6487), while the
 2607 currents on the GEM electrodes are read out by high voltage power supply modules (CAEN N1471)
 2608 with 0.5 nA resolution. The tube current of the X-ray generator is varied between 0.03 and 3 mA, which
 2609 results in a current on the readout pad anode of between around 1 and 100 nA at a gas gain of ~ 2000
 2610 in Ne-CO₂ (90-10). Since the expected current density in 50 kHz Pb-Pb collisions is of the order of
 2611 1 nA/cm^2 , a tube current $\leq 0.3 \text{ mA}$ was found to be best suited for the measurements.

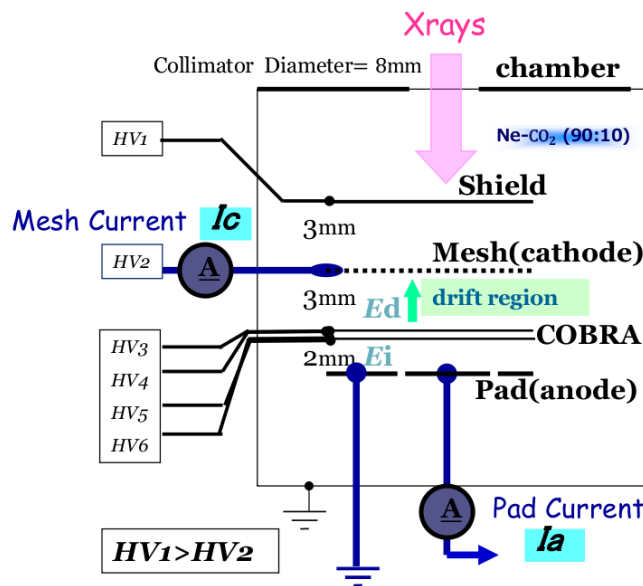


Figure 9.3: Schematic setup for the measurement of gas gain and ion backflow with an X-ray source.

2612 The ion backflow is measured by $IB = (I_{\text{cathode}} - I_{\text{cathode}}^0) / I_{\text{anode}}$, where I_{cathode} is the current measured at
 2613 the mesh, I_{cathode}^0 is the current from primary ions and I_{anode} is the current read on the readout pad
 2614 plane. The current from primary ions is measured at a drift field $E_{\text{drift}} = 0.4 \text{ kV/cm}$ applied both between
 2615 shield and mesh, and between mesh and the top of the GEM electrode. No voltage difference is applied
 2616 across the GEM for the measurement of I_{cathode}^0 . Note that the sign of the electric field flips at the mesh.
 2617 This means that ions from both sides of the mesh contribute to the primary current, but not electrons.

2618 The effective gain is estimated by the ratio $I_{\text{anode}} / (I_{\text{cathode}}^0 / 2)$: the primary electron current contributing
 2619 to the gas amplification is half the primary current I_{cathode}^0 measured at the mesh. The electric fields in
 2620 the drift and induction regions have been kept at 0.4 kV/cm and 3 kV/cm , respectively.

 2621 **Dependence on ΔU_{GEM}**

2622 Figure 9.4 shows the effective gas gain and ion backflow of GEM 50, GEM 100 and COBRA 2 with
 2623 $\Delta U_{\text{AC}} = 0 \text{ V}$. The electric fields in the drift and induction regions are kept at 0.4 kV/cm and 3 kV/cm ,
 2624 respectively. The observed ion backflow for GEM 50 and GEM 100 is about 20–30%. The ion backflow
 2625 with COBRA 2 is $\sim 40\text{--}50\%$ and gradually decreases for gas gains larger than 200.

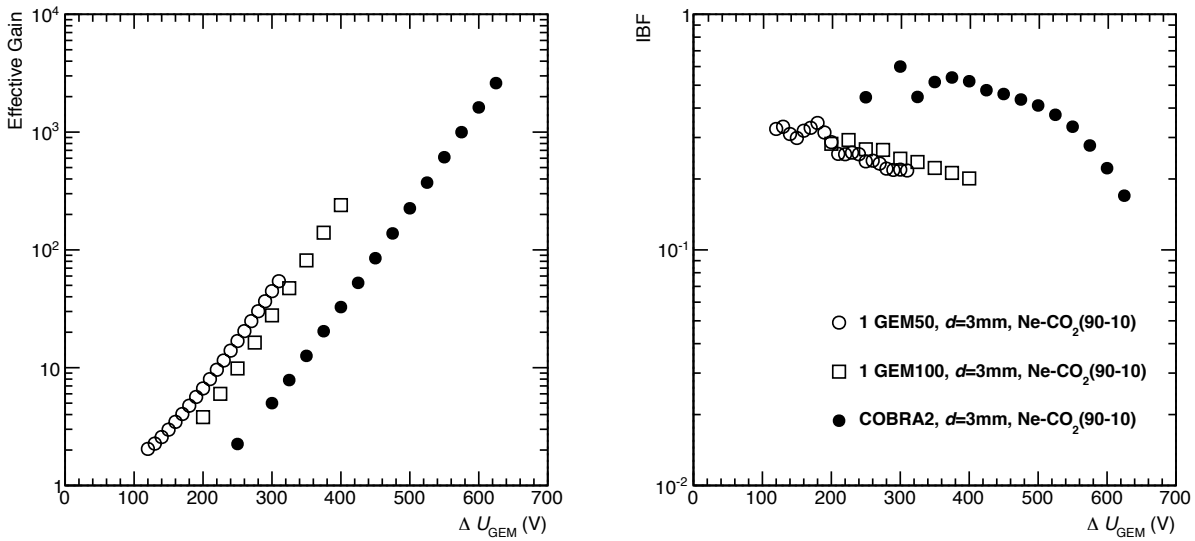


Figure 9.4: Effective gain (left panel) and ion backflow (right panel) in Ne-CO₂ (90-10) as a function of the voltage across the GEM for GEM 50 (open circles), GEM 100 (open squares) and COBRA 2 (closed circles). The voltage across the GEM and COBRA electrodes ΔU_{AC} is kept at 0 V.

2626 *Dependence on ΔU_{AC}*

2627 The effective gain and ion backflow of COBRA 2 as a function of ΔU_{AC} were measured in Ne-CO₂
 2628 (90-10) for $\Delta U_{GEM} = 575$ V and 390 V. Figure 9.5 shows that positive ΔU_{AC}^{up} and negative ΔU_{AC}^{bot} tend
 2629 to increase the effective gain, which may be related to an improved efficiency for the collection of the
 2630 primary electrons into the GEM holes and for the extraction of avalanche electrons into the induction
 2631 region. The ion backflow depends both on ΔU_{GEM} and ΔU_{AC} and is thus correlated with the effective
 2632 gain. While the dependence of the ion backflow on ΔU_{GEM} is rather weak, a factor of 2–3 within the
 2633 range of this study, the ion backflow drops by more than an order of magnitude if ΔU_{AC}^{up}
 2634 is increased to 200 V. It should be noted that an ion backflow of 1 % or less can be achieved with a single COBRA
 2635 GEM, albeit at rather large gas gains.

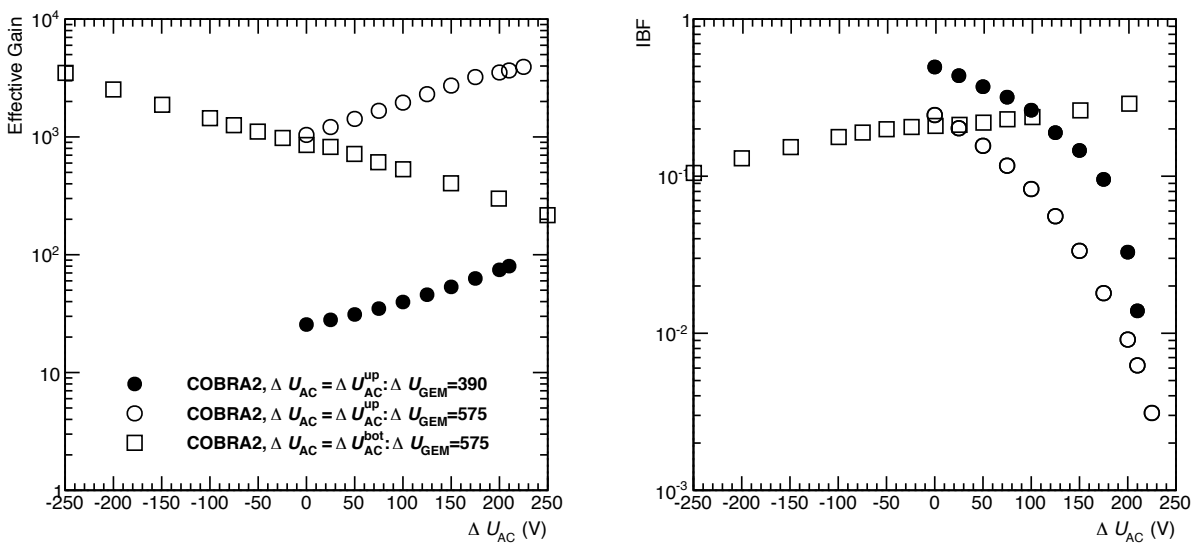


Figure 9.5: Effective gas gain (left panel) and ion backflow (right panel) of COBRA 2 in Ne-CO₂ (90-10) as a function of ΔU_{AC}^{up} (circles) with $\Delta U_{GEM} = 575$ V (open circles), $\Delta U_{GEM} = 390$ V (closed circles) and ΔU_{AC}^{bot} with $\Delta U_{GEM} = 575$ V (open squares). The drift length is 3 mm, E_{drift} is 0.4 kV/cm in all measurements.

2636 **9.1.2 Triple structures with COBRA and standard GEMs**

2637 Studies of triple GEM systems including one or two COBRA GEMs were performed. It was found that
 2638 a COBRA GEM placed as the first GEM layer is not effective for ion backflow suppression. This result
 2639 was confirmed in electrostatic simulations and is the consequence of the large distance between the GEM
 2640 surface and the drift electrode. Therefore, only configurations with COBRA GEMs in the second or third
 2641 layer are considered in the following.

2642 The effective gain and ion backflow are studied for the triple GEM configurations (GEM 1 – GEM 2 –
 2643 GEM 3): GEM 50 – COBRA 2 – GEM 50 and GEM 50 – COBRA 2 – COBRA 2. In these measurements,
 2644 the dependence on ΔU_{AC}^{up} , on the second transfer field E_{T2} , and on the X-ray tube current were studied.
 2645 The drift length and the transfer gaps all measure 3 mm. The electric fields E_{drift} and E_{T1} are set to
 2646 0.4 kV/cm, while E_{ind} is 3 kV/cm. The voltage across GEM 1 is set to 200 V. The X-ray tube current is
 2647 varied from 0.03 mA to 3 mA.

2648 *Standard GEM – COBRA GEM – Standard GEM*

2649 Figure 9.6 shows the gas gain and the ion backflow measured with the GEM 50 – COBRA 2 – GEM 50
 2650 setup as a function of ΔU_{AC}^{up} on COBRA 2. The measurement is performed with $\Delta U_{COBRA2} = 400$ V,
 2651 $\Delta U_{GEM3} = 300$ V and $E_{T2} = 0.75$ kV/cm. The results were obtained with X-ray tube currents of 3 mA,
 2652 0.3 mA, and 0.03 mA. The dependence of the gas gain on ΔU_{AC} and on the X-ray tube current is weak.
 2653 The ion backflow depends strongly on ΔU_{AC} , as already observed in the single GEM setup. A signifi-
 2654 cant dependence on the X-ray tube current is also observed, indicating the importance of space-charge
 2655 effects for tube currents above 0.3 mA. At small tube currents, values of the ion backflow below 1 %
 2656 can be achieved. Note that the COBRA GEM in the triple GEM setup is operated at rather low gain
 2657 ($\Delta U_{COBRA2} = 400$ V, see also Fig. 9.5).

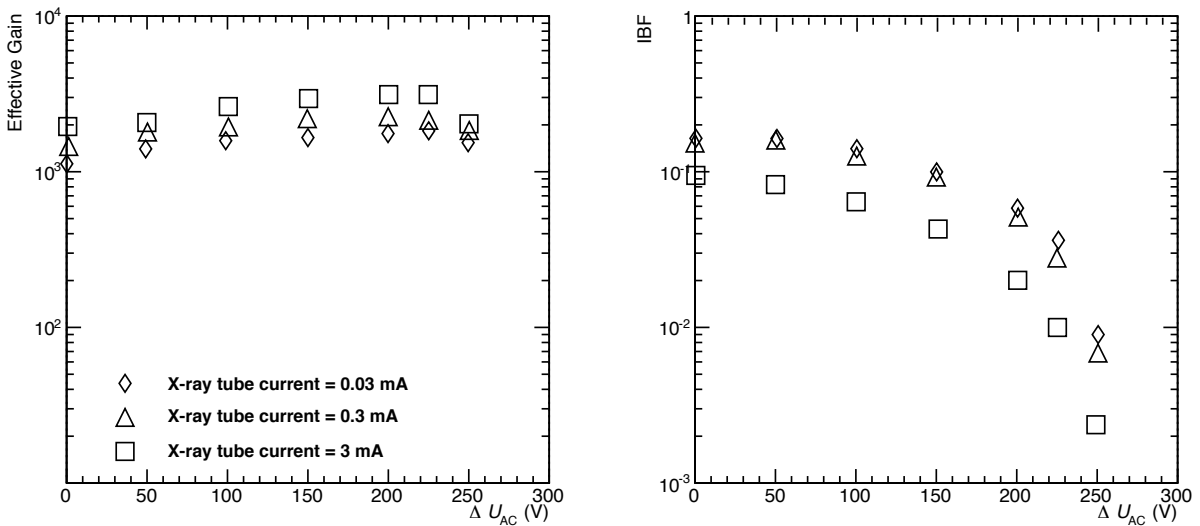


Figure 9.6: Gas gain (left panel) and ion backflow (right panel) measured with the GEM 50 – COBRA 2 – GEM 50 configuration as a function of ΔU_{AC}^{up} on COBRA 2 for different X-ray tube currents. The second transfer field is $E_{T2} = 0.75$ kV/cm.

2658 For the same setup, the gas gain and ion backflow as a function of ΔU_{AC}^{up} on COBRA 2 is shown in
 2659 Fig. 9.7 for different transfer fields E_{T2} in the range 0.25 – 1 kV/cm. The voltage on GEM 3 (ΔU_{GEM3}) is
 2660 adjusted for each E_{T2} setup to provide an effective gas gain in the range 1000 – 2000. The tube current of
 2661 the X-ray generator used in these measurements is 0.03 mA. A significant reduction of the ion backflow
 2662 can be achieved by lowering E_{T2} , which matches the observations in a standard triple GEM system (see
 2663 Sec. 5.1). For the triple GEM system with one COBRA GEM, an ion backflow of 0.5 % can be achieved.

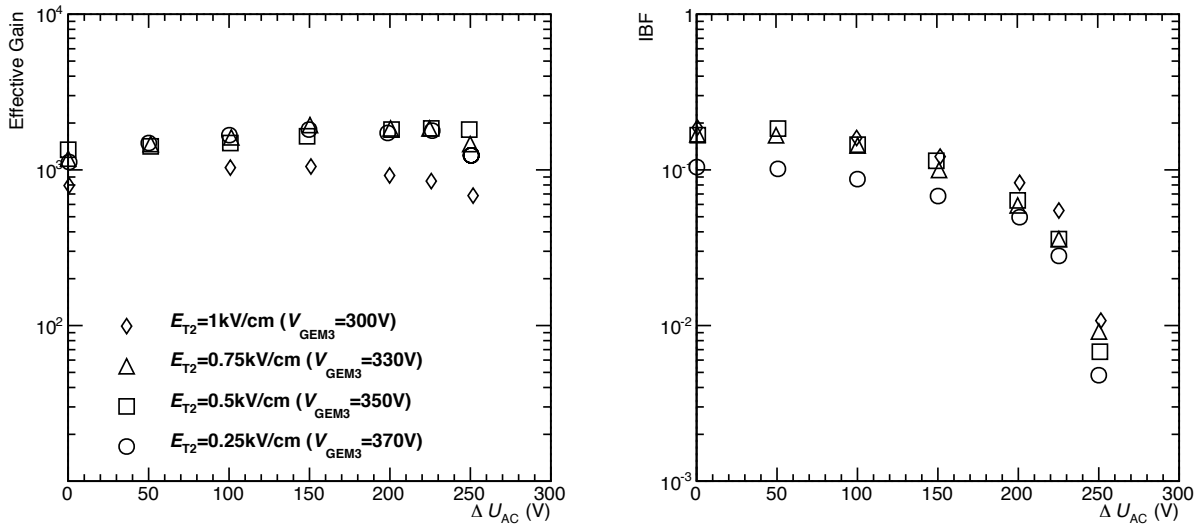


Figure 9.7: Effective gas gain (left panel) and ion backflow (right panel) measured as a function of ΔU_{AC}^{up} on COBRA 2 with the GEM 50 – COBRA 2 – GEM 50 configuration. The X-ray tube current is 0.03 mA.

2664 *Standard GEM – COBRA GEM – COBRA GEM*

2665 In the following, we present measurements with a standard GEM in the first layer, and COBRA GEMs
 2666 in the second and third layer (GEM 50 – COBRA 2 – COBRA 2). Figure 9.8 shows the gas gain and the
 2667 ion backflow as a function of ΔU_{AC}^{up} on the COBRA GEMs at different X-ray tube currents. Open sym-
 2668 bols correspond to measurements where $\Delta U_{AC}^{up}(\text{GEM2}) = \Delta U_{AC}^{up}(\text{GEM3})$, i.e. both voltages are varied
 2669 simultaneously, while the closed symbols correspond to results where one of the ΔU_{AC}^{up} voltages are fixed.
 2670 The GEM voltage and the field configurations are $\Delta U_{GEM1} = 200$ V, $\Delta U_{GEM2} = 430$ V, $\Delta U_{GEM3} = 430$ V,
 2671 $E_{drift} = 0.4$ kV/cm, $E_{T1} = 0.4$ kV/cm, $E_{T2} = 0.4$ kV/cm and $E_{ind} = 3$ kV/cm. For $\Delta U_{AC} \sim 250$ V, an ion
 2672 backflow of $\sim 0.5\%$ is achieved at the lowest X-ray tube currents.

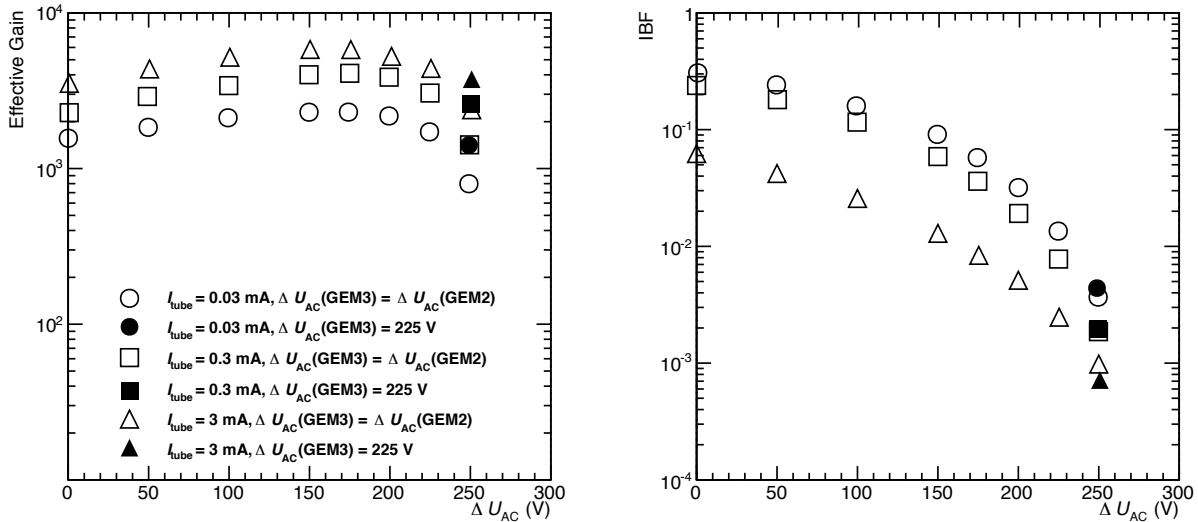


Figure 9.8: Effective gas gain (left panel) and ion backflow (right panel) measured with the GEM 50 – COBRA 2 – COBRA 2 configuration as a function of ΔU_{AC}^{up} on the COBRA GEMs for different X-ray tube currents. Open symbols correspond to the settings with $\Delta U_{AC}^{up}(\text{GEM2}) = \Delta U_{AC}^{up}(\text{GEM3})$, while the closed symbols are for $\Delta U_{AC}^{up}(\text{GEM2}) = 250$ V and $\Delta U_{AC}^{up}(\text{GEM3}) = 225$ V.

2673 Further reduction of the ion backflow is possible by tuning the values of ΔU_{GEM2} and ΔU_{GEM3} . Figure 9.9
 2674 shows the gas gain and the ion backflow as a function of ΔU_{AC}^{up} changed simultaneously on GEM 2 and
 2675 GEM 3 (so that $\Delta U_{AC}^{up}(\text{GEM2}) = \Delta U_{AC}^{up}(\text{GEM3})$) at different values of ΔU_{GEM2} and ΔU_{GEM3} . An ion

2676 backflow of less than 0.25% is achieved with $\Delta U_{\text{GEM2}} \leq 390$ V and $\Delta U_{\text{GEM3}} \geq 470$ V.

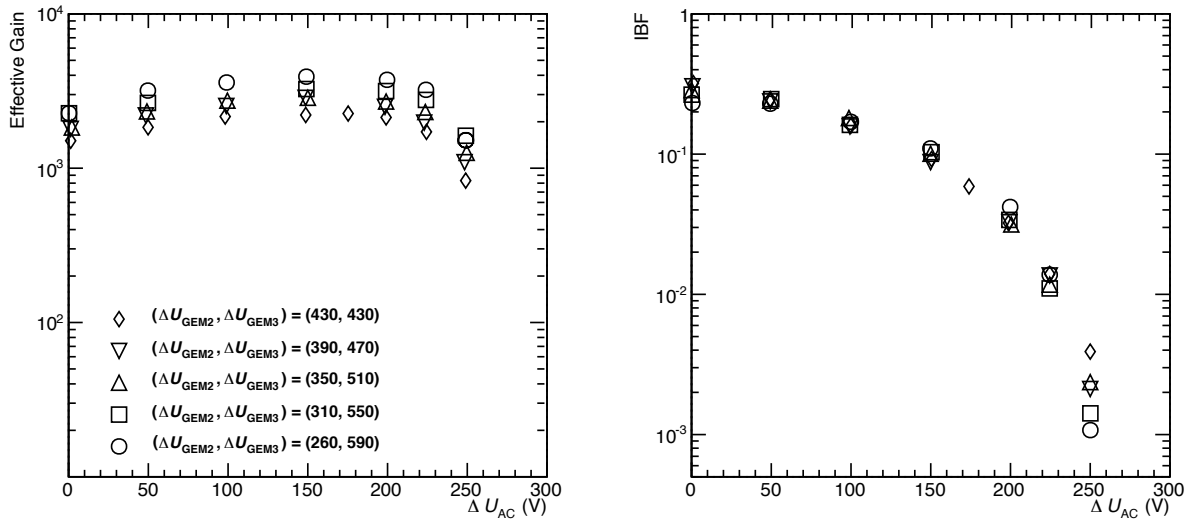


Figure 9.9: Effective gas gain (left panel) and ion backflow (right panel) as a function of $\Delta U_{\text{AC}}^{\text{up}}$ of the COBRA GEMs (with the condition $\Delta U_{\text{AC}}^{\text{up}}(\text{GEM2}) = \Delta U_{\text{AC}}^{\text{up}}(\text{GEM3})$) measured with the GEM 50–COBRA 2–COBRA 2 configuration at different ΔU_{GEM2} and ΔU_{GEM3} .

2677 **9.1.3 Energy resolution**

2678 The energy resolution as a function of $\Delta U_{\text{AC}}^{\text{up}}$ has been measured in a GEM 50–COBRA 2–COBRA 2
 2679 configuration. Like all other measurements reported here we used the gas mixture Ne-CO₂ (90-10).
 2680 The drift length is 30 mm and a ⁵⁵Fe X-ray source radiates from the top of the drift field. Induced
 2681 signals on the anode pad (3×3 cm²) are amplified by a pre-amplifier and shaper and read out by an MCA
 2682 (KromeK K102). In these measurements, ΔU_{GEM1} , ΔU_{GEM2} , and ΔU_{GEM3} are fixed to 200 V, 430 V, and
 2683 430 V, respectively, while $\Delta U_{\text{AC}}^{\text{up}}$ is varied between 0 and 200 V. ΔU_{GEM2} and ΔU_{GEM3} are increased to
 2684 445 V at $\Delta U_{\text{AC}}^{\text{up}} = 200$ V in order to keep the gain constant. Further settings are: $E_{\text{drift}} = 0.4$ kV/cm,
 2685 $E_{\text{T1}} = 0.4$ kV/cm, $E_{\text{T2}} = 0.4$ kV/cm, and $E_{\text{ind}} = 3$ kV/cm. Figure 9.10 shows the energy spectra obtained
 2686 at the different settings of $\Delta U_{\text{AC}}^{\text{up}}$ V. An energy resolution (σ) of 17%, 16%, 18%, and 21% is achieved
 2687 with $\Delta U_{\text{AC}}^{\text{up}} = 0$ V, 100 V, 150 V, and 200 V, respectively.

2688 The resolution is worse by a factor ~ 2 compared to the resolution achieved with a prototype IROC (see
 2689 Fig. 5.20). Possible reasons could be a decreased electron collection efficiency at GEM 1 due to the large
 2690 pitch between the holes of the COBRA GEM or the non-uniform multiplication inside the hole due to
 2691 the relatively small ratio of hole size to thickness.

2692 **9.1.4 Conclusion and outlook**

2693 Measurements with triple GEM systems including one or two COBRA GEMs show that an ion backflow
 2694 of 0.25–0.5% can be achieved by tuning the potentials on the COBRA electrodes and the fields between
 2695 the GEMs. However, the energy resolution obtained is not on the level required for the GEM TPC.
 2696 The characterization of COBRA GEM systems will be continued in the future. In particular, the perfor-
 2697 mance of COBRA3 (see Tab. 9.1) will be studied. Further plans include the characterisation of large-size
 2698 COBRA GEMs (50×50 cm²) in terms of uniformity of gas gain, ion backflow, energy resolution, and
 2699 long-term stability.

2700 **9.2 R&D with hybrid gain structures: 2GEMs + MicroMegas**

2701 MicroMegas (MMG) intrinsically have very low ion backflow due to the very high ratio of the values of
 2702 the electric fields in the small amplification gap to the drift field above the MMG. Ion backflow values of

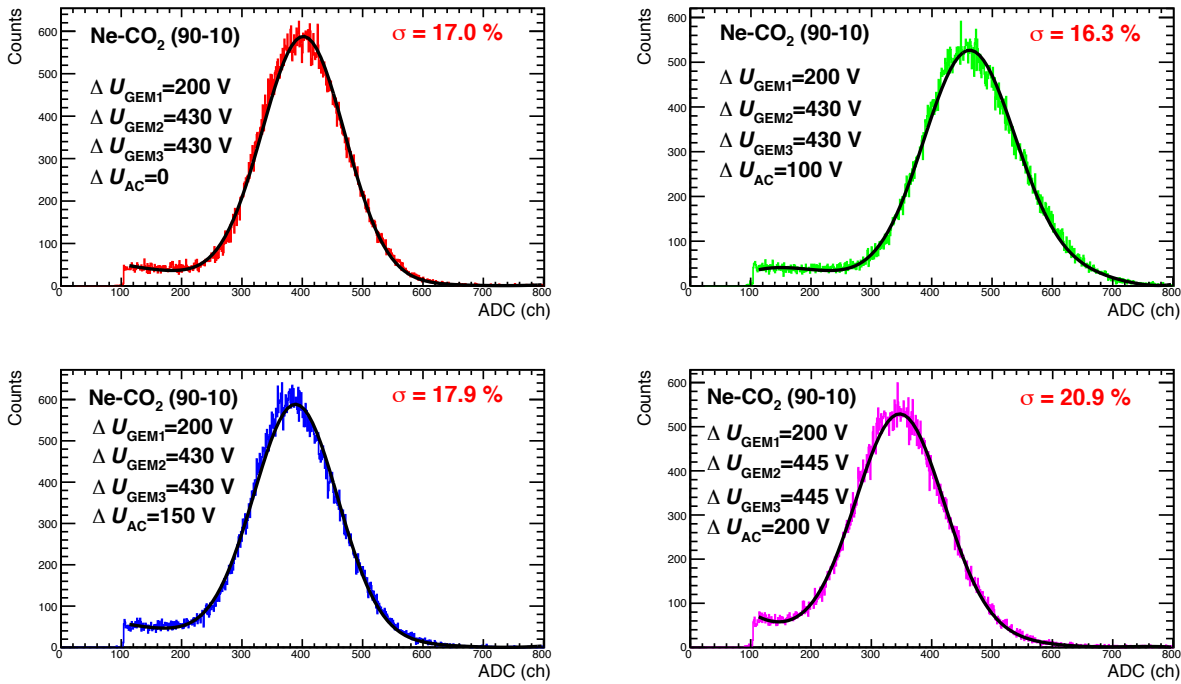


Figure 9.10: ^{55}Fe energy spectra measured in Ne- CO_2 (90-10) with a GEM 50 – COBRA 2 – COBRA 2 configuration for different values of $\Delta U_{\text{AC}}^{\text{up}}$.

2703 less than 1 % was measured in [4] and [5].

2704 It is difficult to maintain stable operation in an MMG detector at the gain $(1 - 10 \times 10^3)$ necessary to
 2705 measure single-charged MIPs. To overcome this limitation, studies have been carried out on a hybrid
 2706 GEM + MMG detector with the primary goal of achieving stable operation [6–8]. The addition of a
 2707 GEM to the gain structure has the advantage of ”preamplifying” the signal such that the MMG can be
 2708 operated at a lower gain. Furthermore, the GEM spreads the electron cloud in space transverse to the
 2709 drift direction, distributing the signal over a larger spot on the MMG. Both effects lead to an increased
 2710 stability of the MMG. Discharge rates of $< 10^{-5}$ at gains of 10^4 were measured in [9] for such hybrid
 2711 structures. It was also established that the MMG has very good energy resolution. Finally, the technology
 2712 for large-scale production of MMG detectors is in hand [10].

2713 Based on existing measurements and experience, a hybrid gain structure using two GEM foils above
 2714 an MMG appears to be a promising candidate to be able to achieve very low IBF and stable operation
 2715 while maintaining good spatial and energy resolution. A detailed response simulation was carried out
 2716 using 2 GEM + MMG with a chevron pad readout plane. The resulting resolution in $r\phi$ and momentum
 2717 are shown in Figs. ?? (green points), which are presented and discussed in Sec. 9.3. The addition of a
 2718 second GEM should reduce further the ion backflow and allow operation of all elements at modest gains,
 2719 and thus lead to completely stable operation. We have started a program to investigate the operation of
 2720 a 2 GEM + MMG chamber while varying all parameters. A newly constructed hybrid 2 GEM + MMG
 2721 chamber using standard $10 \times 10 \text{ cm}^2$ GEM foils and an MMG with 400 lines-per-inch of the same size
 2722 has been operating to perform initial ion backflow and energy resolution measurements. Figure 9.11
 2723 shows the setup.

2724 Measurements were performed using the two mixtures Ar- CO_2 (70-30) and Ar- CO_2 (90-10) with GEM
 2725 foil voltages set to fix the total GEM + MMG gain and constant drift, transfer and induction fields. Results
 2726 are shown in Fig. 9.12. The voltage on the MMG mesh was varied to change the ratio of the fields above
 2727 and below the MMG mesh (see Fig. 9.11). The ratio of the currents at the cathode and the anode have
 2728 been measured using a radioactive source. The dependence on the MMG voltage is shown in the left

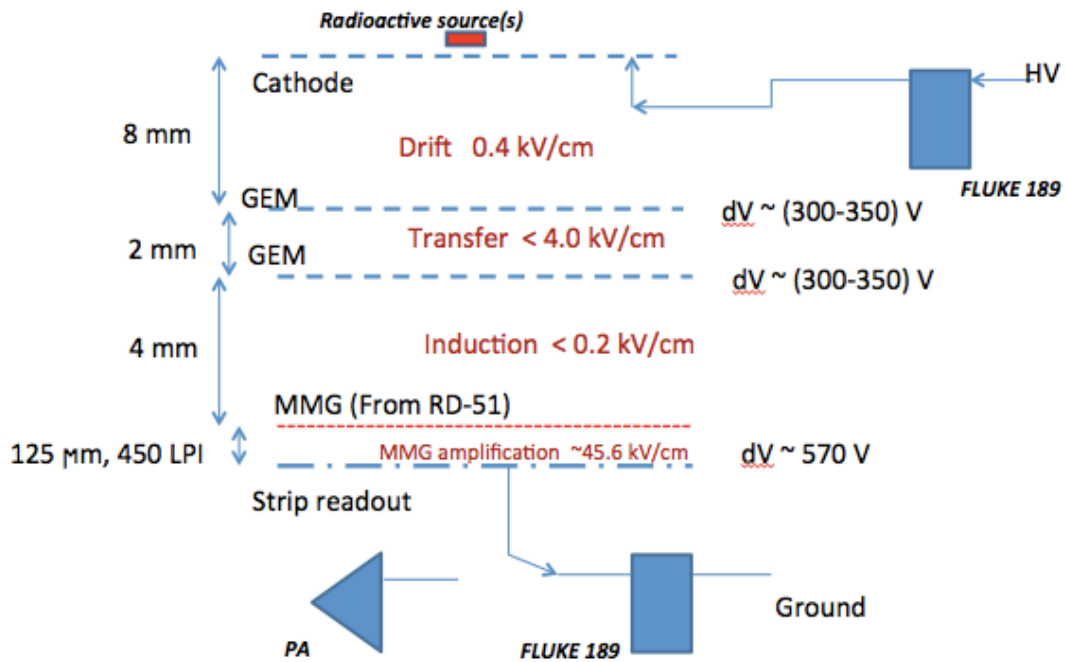


Figure 9.11: Setup used for preliminary ion backflow measurement for the hybrid 2 GEM + MMG system.

2729 panel of Fig. 9.12 (red) along with the FWHM for the peak from ^{55}Fe x-rays (blue).

2730 The following settings were used for these measurements: $E_{\text{drift}} = 0.4 \text{ kV/cm}$, $E_{T1} = 3.5 \text{ kV/cm}$, $E_{\text{ind}} =$
 2731 0.125 kV/cm , total gain = $3.5 (\pm 0.5) \times 10^3$. For the 620 V mesh setting four measurements were made
 2732 over a range of source intensities varying by a factor of 10. All 4 ion backflow measurements are in the
 2733 range 0.15–0.16 %, consistent with the measurement error. At each MMG voltage setting the total gain
 2734 was adjusted and the resolution checked by measuring the PH spectrum at the anode (read-out plane)
 2735 with a standard CSP and shaper and an ADC with the chamber illuminated by a ^{55}Fe source (right panel
 2736 in Fig. 9.12).

2737 Encouraged by these measurements, a new MMG is being procured for further studies. Since also the

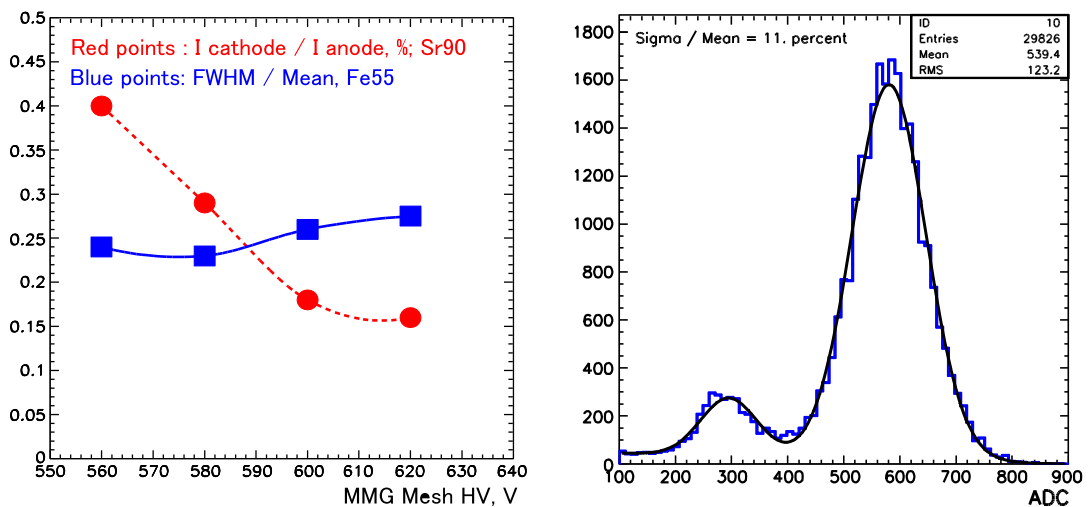


Figure 9.12: (Left) Preliminary ion backflow measurement for hybrid 2 GEM + MMG system. The horizontal scale is the voltage on the MMG mesh. The vertical scale is the ratio of cathode to anode currents in % (red points) and the FWHM of the ^{55}Fe peak (blue boxes). (Right) Typical PH spectrum from the hybrid 2 GEM + MMG system irradiated with an ^{55}Fe source.

2738 mesh pitch influences the ion backflow performance of an MMG system [5], it is expected that the ion
 2739 backflow can be suppressed further by a factor of about 1.5–2 by using a finer mesh with ≥ 600 lines-
 2740 per-inch. Such an MMG is currently being sought for the continuation of the tests, which will include
 2741 also the use of Ne-CO₂ and Ne-CF₄ gas mixtures.

2742 9.3 Studies with fast gas mixtures

2743 In Ne-CO₂ (90-10) and Ne-CO₂-N₂ (90-10-5) the maximum electron drift time is $\sim 100 \mu\text{s}$, resulting
 2744 in an average overlap of $N_{\text{pileup}} = 5$ minimum bias events. This motivates the search for alternative gas
 2745 mixtures with significantly larger drift velocities at similar electric fields.

2746 One of these options implies the use of CF₄ as a quencher gas. As shown in Tab. 3.1, drift velocities of
 2747 about $8 \text{ cm}/\mu\text{s}$ can be achieved in Ne-CF₄ (90-10), which exceeds the drift velocity in Ne-CO₂ (90-10)
 2748 by a factor of ~ 3 at the same drift field. As a result, the event pileup can be reduced by a similar factor.

2749 The high electron mobility in Ne-CF₄ (90-10) implies also a large $\omega\tau$ factor and small diffusion at the
 2750 nominal magnetic field $B = 0.5 \text{ T}$ (see also Tab. 3.1). The latter may potentially lead to a significant
 2751 improvement of the position resolution, if the readout pads are accordingly adjusted to smaller cluster
 2752 sizes.

2753 In the following, results from detailed simulations of the TPC response in Ne-CO₂ (90-10) and Ne-CF₄
 2754 (90-10) including a microscopic description of a triple-GEM readout system are presented.

2755 As discussed in Sec. 4.5, the present pad geometry of the TPC readout chambers leads to limitations of
 2756 the space-point resolution. The narrower pad response function in GEMs, which is approximately equal
 2757 to the width of the charge cloud emerging from the last GEM, implies that charge sharing among adjacent
 2758 pads is insufficient for small drift lengths. This is illustrated in Fig. 9.13 (left panel) where the fraction of
 2759 clusters with $n = 1, 2$ and 3 pads is shown as a function of the drift distance. The calculation is performed
 2760 for Ne-CF₄ (90-10) assuming rectangular readout pads of size $6 \times 15 \text{ mm}^2$. The large occurrence of one-
 2761 pad clusters at small drift distance leads to a deterioration of the space-point resolution in this region.

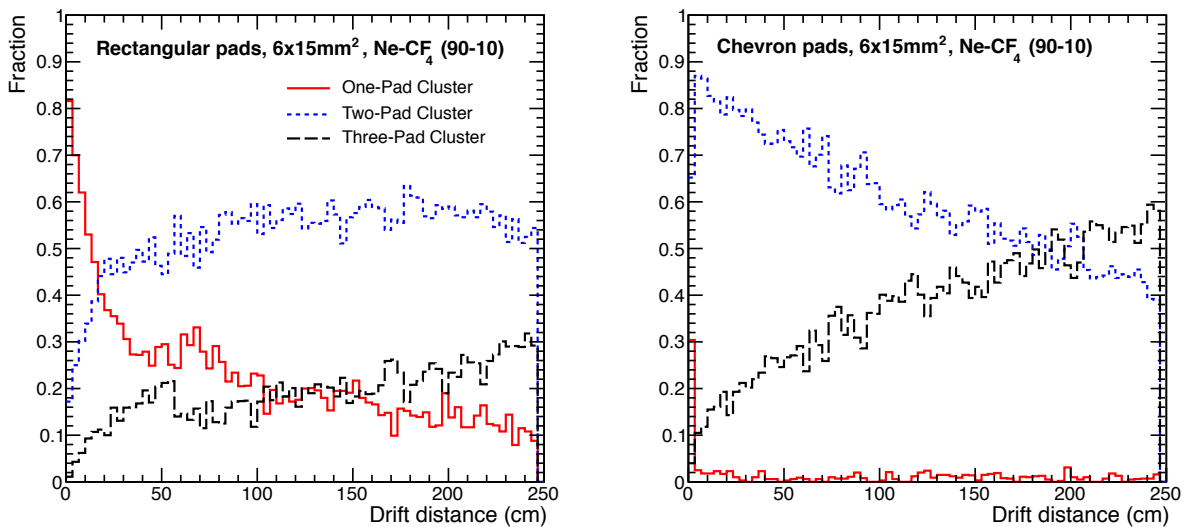


Figure 9.13: Fraction of one-, two-, and three-pad clusters for rectangular (left) and chevron-shaped (right) pads ($6 \times 15 \text{ mm}^2$) in a triple GEM readout system with Ne-CF₄ (90-10).

2762 This can be overcome by choosing chevron-shaped pads [11] instead of rectangular ones. The frequency
 2763 of n -pad clusters for $6 \times 15 \text{ mm}^2$ pads with an n -fold chevron structure is shown on the right panel of
 2764 Fig. 9.13. The majority of clusters have a signal on two or three adjacent pads, while the probability for
 2765 one-pad clusters is negligible.

2766 The space-point resolution in $r\phi$ direction as a function of the drift length is shown in Fig. 9.14. For the
 2767 gas mixture Ne-CO₂ (90-10) and with rectangular pads ($6 \times 15 \text{ mm}^2$) a deterioration of the space-point
 2768 resolution is seen at small drift length, which is due to the increasing fraction of one-pad clusters. In
 2769 Ne-CF₄ (90-10) with rectangular pads this effect is even more pronounced, due to the smaller transverse
 2770 diffusion. The space-point resolution can be improved by a factor ~ 3 in Ne-CF₄ (90-10) if chevron pads
 2771 are used.

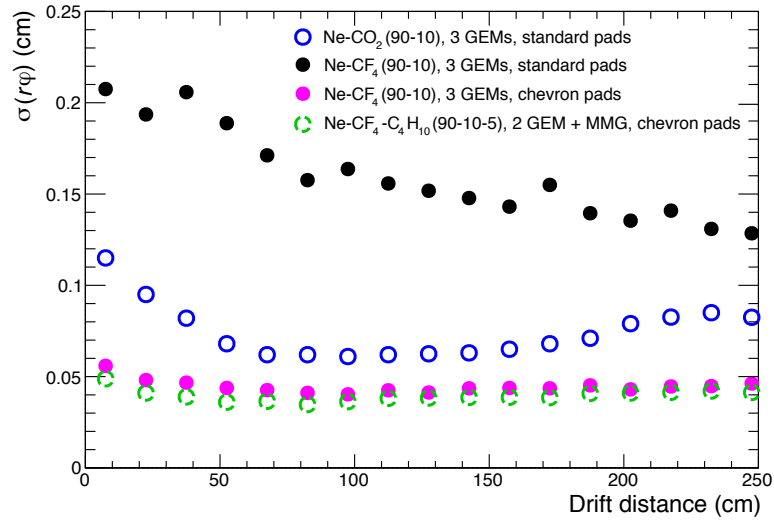


Figure 9.14: Space-point resolution in $r\phi$ obtained with rectangular and chevron pads in different gas mixtures.

2772 The combined ITS-TPC momentum resolution as a function of p_T is shown in Fig. 9.15. In a triple GEM
 2773 system using Ne-CO₂ (90-10) and the present rectangular pad shape the resolution is worse by 5–10 %
 2774 as compared with the present MWPC readout. In Ne-CF₄ (90-10) with chevron pads the resolution of
 2775 the present MWPC readout is restored or even slightly improved.

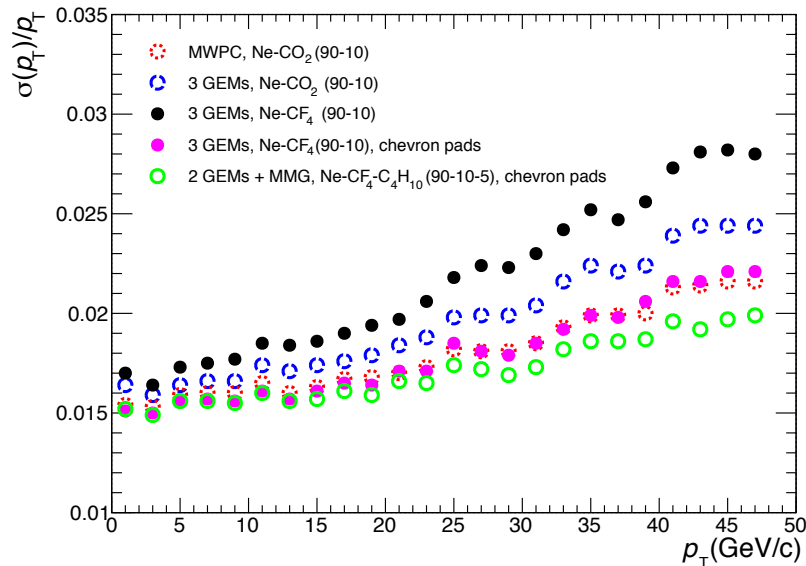


Figure 9.15: Combined ITS-TPC momentum resolution for MWPC (red open circles) and triple GEM system obtained with rectangular and chevron pads in different gas mixtures.

2776 It should be noted that the full charged particle tracking scheme includes also the Transition Radiation
 2777 Detector (TRD) which improves the overall resolution by about a factor two, making the differences

2778 between the different design choices in the TPC smaller. Still, a slight improvement using Ne-CF₄
2779 (90-10) can be achieved if chevron pads are employed. The strongest argument in favor of Ne-CF₄
2780 (90-10) is the larger drift velocity that will lead to a significant decrease of the event pileup. However,
2781 comprehensive studies are necessary to investigate the chemical properties of CF₄ in combination with
2782 the materials used in the TPC. A detailed R&D study is presently being performed.

2783 Chapter 10

2784 Detector control system

2785 The TPC detector control system (DCS) is part of the global ALICE DCS and will follow its evolu-
2786 tion accordingly. Since a large part of the TPC hardware will not be replaced after RUN 2, also the
2787 corresponding DCS subsystems will not be redesigned. The implementation of the control of new TPC
2788 components will be adapted to the current one. This concerns the high voltage control for the new readout
2789 chambers (GEM HV control) as well as the front-end electronics configuration and monitoring.

2790 10.1 Overview

2791 The upgrade of the DCS system and its interface with the online farm will be described in detail in the
2792 Online Systems Technical Design Report, which will be available in the year 2014.

2793 10.1.1 Hardware architecture

2794 The hardware architecture of the TPC DCS can be divided into three functional layers. The *field layer*
2795 contains the actual hardware to be controlled (power supplies, front-end electronics...). The *control layer*
2796 consists of devices for collecting and processing information from the field layer and making it available
2797 to the *supervisory layer*. At the same time the devices of the control layer receive commands from the
2798 supervisory layer to be processed and distributed to the field layer. The equipment in the supervisory
2799 layer consists of computers and servers, providing the user interfaces and connecting to central DCS
2800 infrastructure consisting of file servers, database servers managing the configuration and archival data,
2801 etc. The three layers interface mainly through a local area network (LAN).

2802 10.1.2 Software architecture

2803 The software architecture is a tree structure that represents the structure of the TPC, its subsystems and
2804 devices. The structure, as shown in Fig. 10.1, is composed of control and device units with a single top
2805 node (TPC DCS). The control unit steers the sub-tree below it and the device unit drives a device. The
2806 behavior and functionality of each control unit is implemented as a finite state machine.

2807 The control system is built using a control framework that includes drivers for the different types of
2808 hardware, communication protocols, and configurable components for commonly used applications such
2809 as high or low voltage power supplies [1, 2].

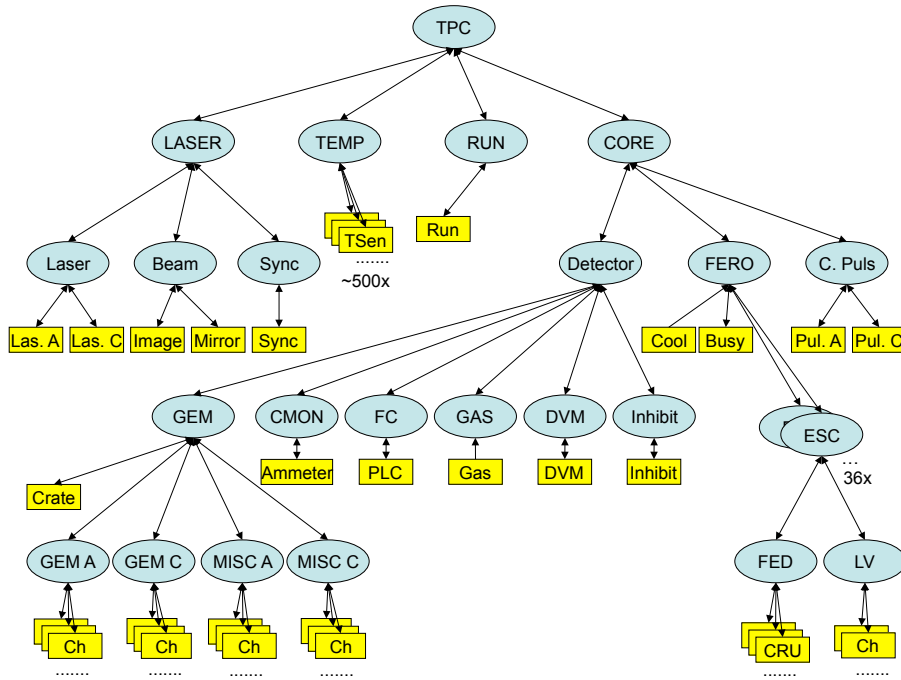


Figure 10.1: Overview of the software architecture of the DCS. The tree structure is built out of Device Units (boxes) and Control Units (ellipses).

2810 10.1.3 System implementation

2811 The core software of the control system is the commercial SCADA¹ system SIMATIC WinCC Open
 2812 Architecture (OA), formerly known as PVSS II, from the company ETM [3]. WinCC OA is an object-
 2813 oriented process visualization and control system that is used in industry as well as by the four LHC
 2814 experiments. It is event-driven and has a highly distributed architecture. The SCADA System for the
 2815 TPC is currently distributed over 12 computers.

2816 10.1.4 Interfaces to devices

2817 Where possible, commercial servers using the OPC² standard of process control are used to interface the
 2818 SCADA system to devices. OPC servers interface the field cage high voltage, the front-end electronics
 2819 low voltage and the temperature monitoring system. For the readout chamber HV control the usage of the
 2820 OPC standard is envisaged as well. For non-commercial hardware the communication can be based on
 2821 the communication framework Distributed Information Management (DIM [4]). In a similar approach
 2822 DIM is currently used in the laser system, in the drift velocity monitor and the calibration pulser control
 2823 and will be used for the front-end electronics control and monitoring.

2824 10.1.5 Interlocks

2825 The safety of the detector is based on three layers of interlocks:

- 2826 – **Internal interlock:** The internal mechanism of devices (e.g. power supply trip) are used wherever
 2827 applicable. The threshold and status of these interlocks are controlled by the SCADA system, but
 2828 their function is independent of the communication between hardware and software.
- 2829 – **External interlock:** The interlocks between different subsystems are realized using Programmable
 2830 Logical Controller (PLC) systems with the possibility to enable or disable them.

¹Supervisory Controls And Data Acquisition (SCADA)

²Open Platform Communications (OPC)

2831 – **Software interlock.** Software interlocks are realized in the supervisory layer. They rely on the
 2832 communication between the hardware and the SCADA system and are thus only used to prevent
 2833 the system from unwanted but not harmful events like switching off the power supplies under full
 2834 load. The safety of the equipment does not rely on the software interlocks.

2835 Internal interlocks are used for the readout chamber high voltage, the field cage high voltage, the front-
 2836 end electronics low voltage, the cooling and the gas system. External interlocks are implemented for the
 2837 field cage high voltage, the front-end electronics low voltage and the cooling system. Software interlocks
 2838 are used for the readout chamber high voltage, the front-end electronics low voltage and the front-end
 2839 electronics. In addition to the interlocks, the alert system of the SCADA system is set up to inform the
 2840 shift crew of unusual or potentially dangerous situations.

2841 **10.2 Front-end electronics control**

2842 The new front-end electronics (see Chap. 6) requires an updated DCS subsystem. It should provide
 2843 monitoring of temperatures, voltages, currents and status information and the ability to configure the
 2844 front-end electronics for data taking with different run types.

2845 **10.2.1 Overview**

2846 A schematic of the front-end electronics control is shown in Fig. 10.2. Between the common readout
 2847 unit (CRU) system in the control room and the on-detector electronics (front-end cards), the readout
 2848 architecture foresees 6336 GBT unidirectional links for the readout of the physics data. Interleaved with
 2849 the physics data about 1 % or less of DCS monitoring data will be transmitted on the same links to the
 2850 CRU where it is extracted and sent through a dedicated DCS output link to a DCS front-end processor.
 2851 The DCS front-end processor is a computer that hosts a dedicated front-end server application, which
 2852 pre-processes and filters the monitoring data and forwards it to the SCADA system for further processing
 2853 (alarm handling) and display. It also handles configuration requests from the supervisory layer. The
 2854 configuration data from the configuration data base and other control data (commands) are sent from
 2855 the CRU to the FECs via 1584 unidirectional links for the timing, trigger and clock distribution system
 2856 (TTS).

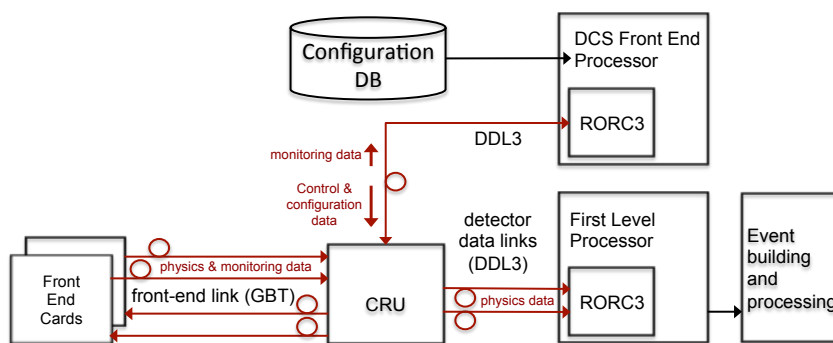


Figure 10.2: Schematic of the front-end electronics control and monitoring.

2857 **10.2.2 Monitoring**

2858 The SCADA system implements archiving and automatic checking of the monitoring data that it receives
 2859 from the front-end server, mainly consisting of temperatures, voltages, currents and status information.
 2860 Graphical user interfaces allow to display the data. Experience has shown that such functionality is very
 2861 useful as it allows to identify problems such as voltage drops or locally reduced cooling performance.

2862 10.2.3 Configuration and control

2863 Each configuration of the TPC front-end electronics includes about 5 million configurable parameters.
 2864 The parameters for the FE chips, FECs and CRUs are stored in a configuration database hosted on central
 2865 DCS ORACLE servers. Configurations may change over time due to disfunctional or replaced hardware
 2866 or due to changing hardware behavior.

2867 Only simple configuration commands are passed from the supervisory layer to the FE server, which
 2868 handles the actual configuration process. The command contains only a parameter which describes the
 2869 configuration type. Based on this the FE server assembles queries to the configuration database which
 2870 retrieve the configuration data for each CRU and its associated equipment.

2871 10.3 Parameter export for online calibration and reconstruction

2872 Many parameters that are gathered by the DCS system are of relevance for the online calibration and
 2873 reconstruction in the online systems.

2874 – **Environmental conditions data:** The temperature and pressure trends are of special importance
 2875 for the drift velocity and gain calibration of the TPC data. They have to be made available to the
 2876 online calibration and reconstruction algorithms with a time granularity of a few Hz.

2877 – **GEM currents and detector status:** The currents measured in the different GEM HV segments
 2878 are directly related to the amount of space charge produced in the corresponding section of the
 2879 drift volume. In order to correct online for space-charge effects (see Sec. 7.4.3), the currents must
 2880 be measured with a precision of nA and must be included in the TPC data stream in order to
 2881 be immediately available (see Sec. 11.4.1). Moreover, the status of the HV channels has to be
 2882 available in order to identify tripped GEM sectors where the voltage is below nominal or ramping.
 2883 This can be achieved by reading the currents from digital current meters through ethernet into a
 2884 computer that is included in the online processing farm. In this way the GEM currents and HV
 2885 states can be continuously injected into the data stream. The same computer runs a server software
 2886 making the currents available also to the DCS system (see Fig. 10.3).

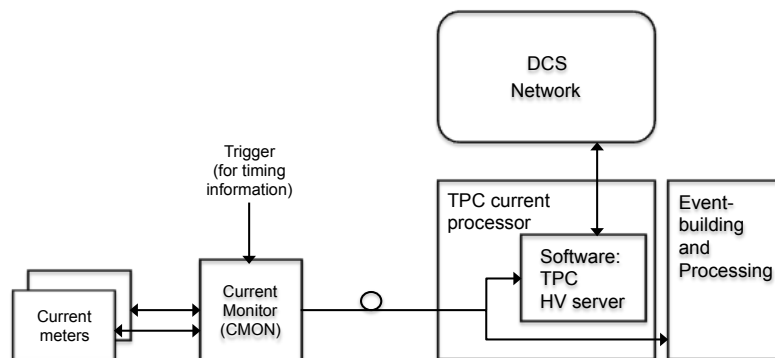


Figure 10.3: Schematic showing how the GEM current values can be read out for online calibration and DCS.

2887 – **Front-end configuration:** The latest FE configuration parameters (e.g. inactive regions and analog and DSP parameters) are also of importance to the online calibration and reconstruction algorithms and are thus exported for each data taking session in a suitable format.

2890 – **Further parameters** of relevance for the online calibration and reconstruction algorithms include
 2891 the status of the laser system to identify periods with laser activity during a data taking session.
 2892 The list of needed parameters will probably be extended.

2893 Chapter 11

2894 Installation, commissioning and services

2895 11.1 General

2896 In this chapter the installation of the GEM readout chambers into the TPC, the subsequent commissioning
2897 of the new front-end electronics and readout system, and the re-installation of the upgraded TPC in the
2898 ALICE cavern are described. In addition, all the required services to operate the TPC are discussed and
2899 necessary upgrades and modifications are introduced. The total time estimated for the exchange of the
2900 readout chambers and electronics, various upgrade activities and pre-commissioning on the surface is
2901 estimated to be at minimum 40 weeks.

2902 11.2 Installation

2903 For the installation of the GEM readout chambers, the TPC is removed from its position in the ALICE
2904 cavern and moved into the so-called Delphi frame to give it the proper mechanical support. Then it can
2905 be moved by crane and truck to the clean room in building SXL2. Due to the sensitivity of the GEM foils
2906 to dust a class 10 clean room is required (see also Sec. 4.7). This requirement is more stringent than the
2907 one applied during the installation of the original MWPC (class 100 - 1000).

2908 **Installation tool** For the dismantling of the MWPCs and the installation of the GEM readout chambers
2909 (see Sec. 2.3) a special tool has been developed and successfully used in the past (photos see [1]). For the
2910 proper positioning of this tool, it is attached to a hydraulically controlled platform (the so-called Yellow
2911 Platform) and allows access to one side of the TPC at a time (Fig. 11.1). Safe operation of the installation
2912 tool requires two trained persons.

2913 11.3 Commissioning

2914 After the installation of the GEM readout chambers they have to be aligned to ensure the planarity of the
2915 readout plane. This procedure is described in [1]. After the two SSWs are mounted in front of the end
2916 plates the front-end electronics can be mounted together with the connections to LV, HV, and the cooling
2917 distribution system. To ensure the proper working of the new chambers a pre-commissioning phase in
2918 the clean room follows. This includes pedestal and noise measurements as well as calibration pulser tests
2919 to validate the full functionality of the readout. For this purpose, a cooling system for at least two sectors
2920 at a time and the corresponding readout chain has to be available in the clean room. In the next step, the
2921 TPC is connected to a gas system and measurements of cosmic rays, using a dedicated trigger system,
2922 will be performed. In addition, a laser system generates tracks at well-defined positions for alignment
2923 purposes.

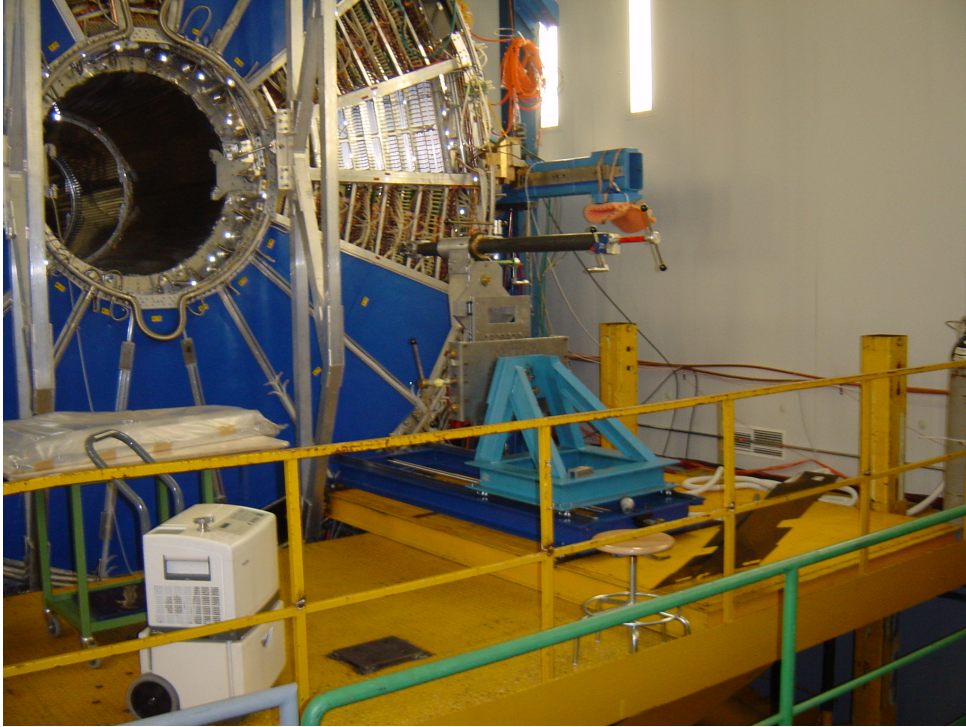


Figure 11.1: TPC with the Yellow Platform and the mounting tool.

2924 In Tab. 11.1 an overview of the main installation steps is given together with the corresponding time
 2925 estimates. These are partly based on past experience.

Activity	duration (weeks)
Dismantling of FEE and FEC frames	2
Replacement of ROCs	12
Resistor Rod modifications	1
Chamber alignment	2
Mounting of temperature sensors etc.	2
Mounting of FEC frames	2
Various upgrades: cooling pipes, cables	2
FEE installation	5
Pulser, cosmics and laser tests	12
Total	40

Table 11.1: Time required for the most relevant activities of the GEM readout installation and commissioning in the clean room (SXL2), partly based on past pre-commissioning experience, partly estimated.

2926 **Installation in the ALICE cavern** After all pre-commissioning measurements in the clean room are
 2927 performed, the TPC can be moved from the clean room into the ALICE cavern. To protect against
 2928 influences from ambient conditions i.e., rain and or large temperature gradients, the TPC will be properly
 2929 packed before being placed on a truck and transported to the ALICE building where it is lowered into the
 2930 pit by crane. Once installed, the final commissioning of the GEM TPC will be performed. Essentially all
 2931 measurements from the clean room will be repeated in the cavern, now involving the full detector.

2932 11.4 Services

2933 In this section the various services necessary to operate the TPC are described and necessary modifica-
 2934 tions and upgrades are discussed.

2935 **11.4.1 High voltage**

2936 **Readout chamber high voltage**

2937 For the operation of the GEM stacks new high voltage power supplies with negative output voltage
 2938 are required. Due to the use of voltage dividers (see Sec. 4.4) the required current is much larger than
 2939 before. We estimate 2 mA to achieve the necessary voltage stability. The use of actively regulated voltage
 2940 dividers are an attractive option. They are presently under development [2] and would possibly allow to
 2941 operate the divider chains at lower currents while still keeping voltage variations (relevant for the dE/dx
 2942 resolution) sufficiently small under changing loads.

2943 A new fast high-precision current monitoring system for the GEM currents is foreseen to allow the
 2944 estimation of space charge due to the positive ion backflow with high time granularity. It will monitor
 2945 the currents to the individual GEM foils, i.e. after the voltage divider. The precision should allow to
 2946 measure the GEM currents down to 100 pA and up to 10 μ A at a sampling rate of 1 kHz. In total 8 x 72
 2947 channels are needed. A schematic drawing of the input stage of such a device is shown in Fig. 11.2. In
 2948 Sec. 10.3 the overall setup with emphasis on the connection to DCS and DAQ is described.

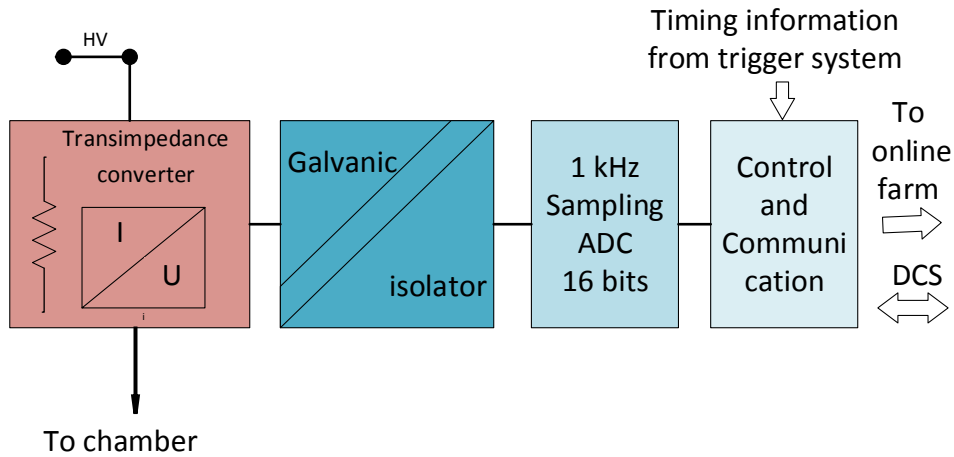


Figure 11.2: Schematic diagram illustrating the working principle of the current monitoring system.

2949 The chamber high-voltage setup mapping the 32 channels of a set of HV modules to the 18 sectors per
 2950 side of the TPC is schematically shown in Fig. 11.3. A similar scheme is used for the OROCs.

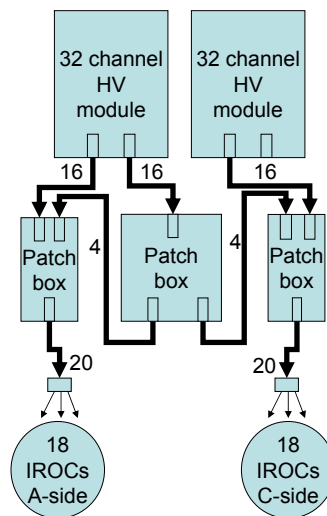


Figure 11.3: Mapping scheme of the high voltage power supplies to the IROCs.

2951 **Field cage high voltage**

2952 The present system providing the drift high voltage of 100kV for the field cage (Heinzinger power
 2953 supply) has proven to work well and will remain unmodified. Since the upper side of the first GEM layer
 2954 is on a potential of about -3 kV (see Sec. 2.4), depending on the gain settings, additional high voltage
 2955 supplies are needed to allow the adjustment of the voltage at the ground end of the four voltage dividers
 2956 (voltage of the last strip of the field cage) to different GEM gain settings. They are connected to the
 2957 bottom of the voltage divider replacing the static last resistor in the present setup. This is illustrated in
 2958 Fig. 11.4.

2959 The total current across the four voltage dividers of the TPC is about $374\ \mu\text{A}$. Therefore, each of the four
 2960 power supplies has to be able to work as a current sink and accommodate up to $100\ \mu\text{A}$ current.

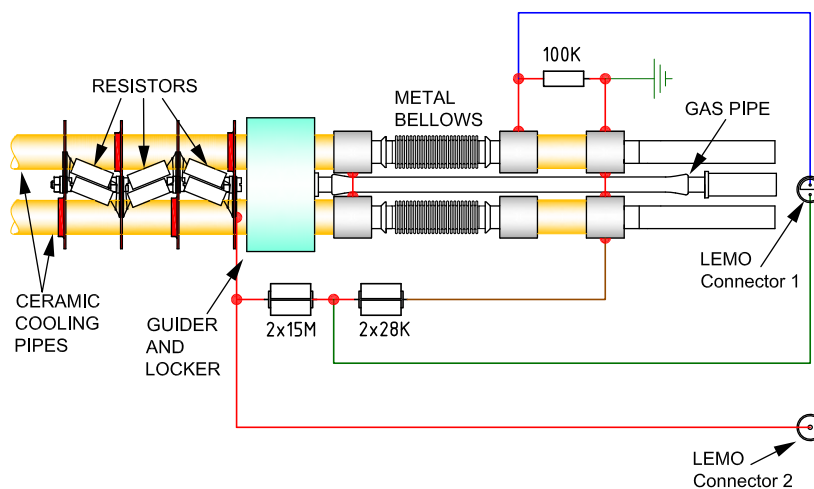


Figure 11.4: Schematic diagram of the ground sides of the four resistor rods indicating the connections to the current measuring system (connector 1) and to the new HV power supply (connector 2).

2961 **11.4.2 Low voltage**

2962 The present setup of the low voltage system supplying the voltages to the front-end electronics has
 2963 worked well in the past and can be reused without modifications [1]. It provides separate voltages for the
 2964 analog and digital parts of the front-end electronics. The presently foreseen new readout electronics for
 2965 the GEM based chambers will most likely need less voltage and less overall power (see Tab. 6.2).

2966 Also the LV cables connecting the power supply to the local distribution boards via bus bars running
 2967 along the spokes of the SSW within the sectors can be reused. The low voltage setup is schematically
 2968 shown in Fig. 11.5 indicating the supply of two sectors by one power supply module.

2969 In Tab. 11.2 the parameters of the LV power supplies are listed.

Supply	channels/crate	nom. power (W)	voltage (V)	max. current (V)	continuous current (A)
Analog	2	600	2 - 7	115	100
Digital	2	1200	2 - 7	230	200

Table 11.2: Specifications of the existing LV power supply system.

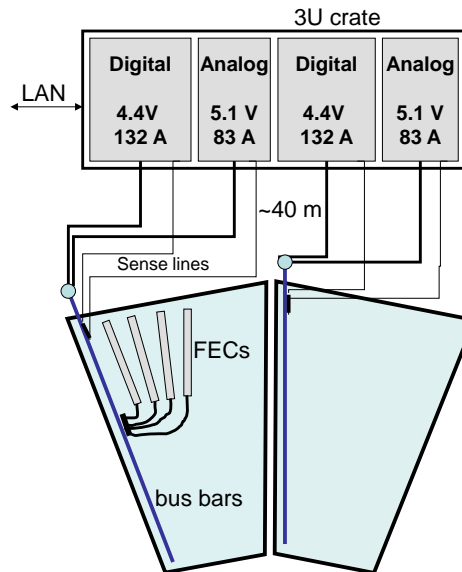


Figure 11.5: Schematic of the low voltage setup for two sectors indicating typical voltages and currents for the present system.

2970 11.4.3 Cooling

2971 *FEE cooling*

2972 The cooling system for the front-end electronics is an under-pressure leak-less water cooled system. It
 2973 has gone through several upgrades in the past and is considered to be well suited for the cooling of the
 2974 new front-end electronics. Due to the lower power consumption foreseen, also the presently available
 2975 cooling power (25kW) will be sufficient. Nevertheless, some minor modifications mainly regarding the
 2976 leak tightness are envisaged.

2977 *Resistor rod cooling*

2978 For the cooling of the resistor rods a separate cooling plant is used. It is also an under-pressure leak-less
 2979 water cooled system, however, with well controlled conductivity, since the water is exposed to the very
 2980 high voltage (100kV) of the field cage. For the future activities, only minor modifications are foreseen.
 2981 These include better control of the flow through the resistor rods and better heat exchangers close to the
 2982 TPC for better temperature control and stability.

2983 *Heat screens*

2984 To thermally separate the TPC from neighboring detectors two different heat screens are used. The outer
 2985 heat screen isolates the TPC from the TRD and is supplied by the cooling plant of the TRD due to the
 2986 use of aluminum cooling panels (unlike the FEE cooling system which uses copper based pipes and
 2987 components). No changes are foreseen here. For the shielding against thermal effects from the ITS the
 2988 inner heat screen is used. Due to the use of stainless steel cooling panels it can be supplied by the TPC
 2989 cooling plant. No major changes are foreseen at this time.

2990 11.4.4 Calibration

2991 *Calibration pulser*

2992 For the monitoring and gain calibration of the readout electronics a calibration pulser system will be
 2993 installed. It is connected to the output side of the last GEM and injects charge into the pre-amplifiers
 2994 by sending a voltage step to the bottom side of GEM 4. Its working principle is schematically shown in
 2995 Fig. 11.6. The potential of the bottom side of GEM 4 is determined by the induction field and is typically

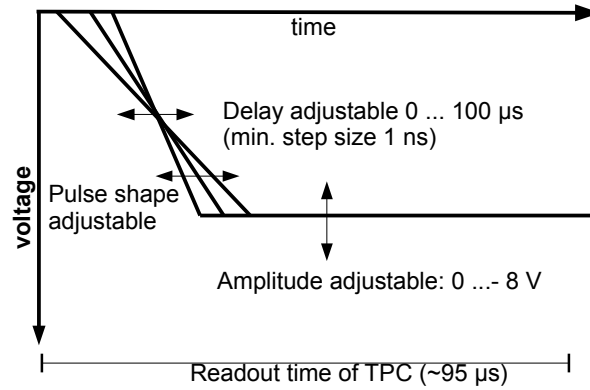


Figure 11.6: Working principle of the calibration pulser system.

2996 around 1 kV. Therefore, a decoupling HV capacitor is needed. Its capacity should be as small as possible
 2997 in order not to store charge that could lead to damages of the front-end electronics in case of a discharge.
 2998 Depending on the necessary signal amplitudes it may be possible to reuse the existing calibration pulser
 2999 setup shown schematically in Fig. 11.7. The present design provides amplitudes of up to -3.5 V. Since it
 3000 is foreseen to modify the ALICE trigger hardware, a new connection to the trigger and clock distribution
 3001 needs to be developed. The remote control of the system by DCS will be modified to allow direct access
 3002 via network.

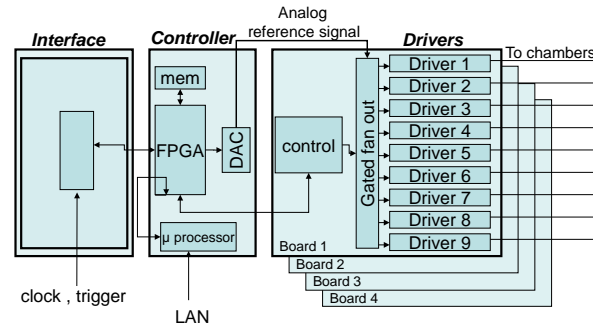


Figure 11.7: Schematic setup of the calibration pulser system.

3003 *Laser*

3004 The laser system provides tracks at well defined locations in the TPC and represents an important calibra-
 3005 tion tool [1]. The hardware may need some upgrades over time like the exchange of the frame grabbers
 3006 of the cameras due to obsolete components of the system. To accommodate new requirements we may
 3007 change to diode pumped lasers since it improves our capability to generate laser events at a higher rate
 3008 compared to the present flashlight pumped laser system. This would facilitate the monitoring of space-
 3009 charge distortion corrections (see Sec. 8.5.2). Like for the calibration pulser system, the connection to
 3010 the trigger system and the control via network has to be upgraded when changing to continuous readout.

3011 *Krypton calibration*

3012 Another important calibration tool is the Krypton calibration, described in Sec. 8.6.1. The container
 3013 with the Rubidium source decaying into the radioactive Krypton is connected to a bypass line in the gas
 3014 system and there is no change foreseen in the way it is used [1].

3015 Chapter 12

3016 Project organization, cost estimate and 3017 time line

3018 12.1 Participating institutions

3019 The list of institutions participating in the TPC upgrade is shown in Tab. 12.1. About half of the groups
3020 were involved in the construction and operation of the present TPC. New institutes have recently joined
3021 the TPC collaboration, among them a large number of US groups, that bring in significant expertise in
3022 GEM technology, detector construction, engineering, electronics, and computing. The full TPC upgrade
3023 collaboration list is shown in Apx. B.

3024 The TPC upgrade project is represented and coordinated by a project leader, two deputy project leaders
3025 and a technical coordinator, as shown in Fig. 12.1. The TPC upgrade project is split into a number of
3026 sub-projects, covering all relevant aspects of detector development, installation, software development,
3027 simulation, online computing and calibration. The TPC upgrade project emerges from the existing TPC
3028 project structure and partially overlaps with it. Items or components where only minor modifications to
3029 the present system are involved (e.g. laser system, gas system, detector control system) are not shown in
3030 Fig. 12.1.

3031 The sharing of responsibilities for the TPC upgrade among the participating institutions is shown in
3032 Tab. 12.2.

3033 12.2 Cost estimate

3034 The CORE cost estimate for the TPC upgrade is summarized in Tab. 12.3. CORE costs include detector
3035 components and production cost as well as external manpower for production and installation. They do
3036 not include cost for internal manpower, basic infrastructure, and R&D.

3037 A provisional funding scheme includes the following major contributions: The possibility of funds of
3038 the order of 50 % of the total cost is indicated by the German BMBF and HGF. A substantial contri-
3039 bution to the TPC upgrade is foreseen by the groups from the US, where the construction, assembly
3040 and test of the IROCs will be conducted. This will be part of a wider involvement of US-DOE into the
3041 upgrade of the ALICE central barrel detectors. A provisional funding scheme is consistent with a US-
3042 DOE CORE contribution to the TPC that corresponds to the IROC fraction of the total cost ($\sim 36\%$).
3043 The development of the SAMPA ASIC within a common ALICE project is conducted by the Electrical
3044 Engineering-Polytechnical School, University of Sao Paulo. Funds from Brazil for the development,
3045 production, and test of the TPC SAMPA chips are envisaged. The Common Readout Unit CRU is being
3046 developed by groups from the Wigner Research Center for Physics, Budapest, and from VECC, Kolkata,

Country Funding Agency	City	Institute
Croatia	Zagreb	Department of Physics, University of Zagreb
Denmark	Copenhagen	Niels Bohr Institute, University of Copenhagen
Finland	Helsinki	Helsinki Institute of Physics
Germany BMBF	Bonn	Helmholtz-Institut für Kern- und Strahlenphysik, Rheinische Friedrich-Wilhelms-Universität Bonn
Germany BMBF	Frankfurt	Institut für Kernphysik, Johann Wolfgang Goethe-Universität Frankfurt
Germany BMBF	Heidelberg	Physikalisches Institut, Ruprecht-Karls Universität Heidelberg
Germany BMBF	Munich	Physik Department, Technische Universität München
Germany BMBF	Tübingen	Physikalisches Institut, Eberhard Karls Universität Tübingen
Germany BMBF	Worms	FH Worms, Worms
Germany GSI	Darmstadt	Research Division and ExtreMe Matter Institute EMMI, GSI Helmholtzzentrum für Schwerionenforschung
Hungary	Budapest	Wigner Research Center for Physics, Budapest
India	Kolkata	Bose Institute
India	Bhubaneswar	Institute of Physics
India	Bhubaneswar	National Institute of Science Education and Research
India	Indore	Indian Institute of Technology
India	Mumbai	Indian Institute of Technology
India	Kolkata	Variable Energy Cyclotron Centre
Japan	Tokyo	University of Tokyo
Mexico	Mexico City	Instituto de Ciencias Nucleares, Universidad Nacional Autónoma de México
Norway	Bergen / Tonsberg	Department of Physics, University of Bergen, Vestfold University College, Tonsberg
Norway	Bergen	Faculty of Engineering, Bergen University College
Pakistan	Islamabad	Department of Physics, COMSATS Institute of Information Technology Islamabad
Poland	Cracow	The Henryk Niewodniczanski Institute of Nuclear Physics, Polish Academy of Science
Romania	Bucharest	National Institute for Physics and Nuclear Engineering
Slovakia	Bratislava	Faculty of Mathematics, Physics and Informatics, Comenius University
Sweden	Lund	Division of Experimental High Energy Physics, University of Lund
USA DOE	Omaha	Creighton University, Omaha, Nebraska
USA DOE	Houston	University of Houston, Houston, Texas
USA DOE	Berkeley	Lawrence Berkeley National Laboratory, Berkeley, California
USA DOE	Livermore	Lawrence Livermore National Laboratory, Livermore, California
USA DOE	Oak Ridge	Oak Ridge National Laboratory, Oak Ridge, Tennessee
USA DOE	West Lafayette	Purdue University, West Lafayette, Indiana
USA DOE	Knoxville	University of Tennessee, Knoxville, Tennessee
USA DOE	Austin	The University of Texas at Austin, Austin, Texas
USA DOE	Detroit	Wayne State University, Detroit, Michigan
USA DOE	New Haven	Yale University, New Haven, Connecticut
USA NSF	San Luis Obispo	California Polytechnic State University, San Luis Obispo, California
USA NSF	Chicago	Chicago State University, Chicago, Illinois

Table 12.1: List of institutions participating in the TPC upgrade.

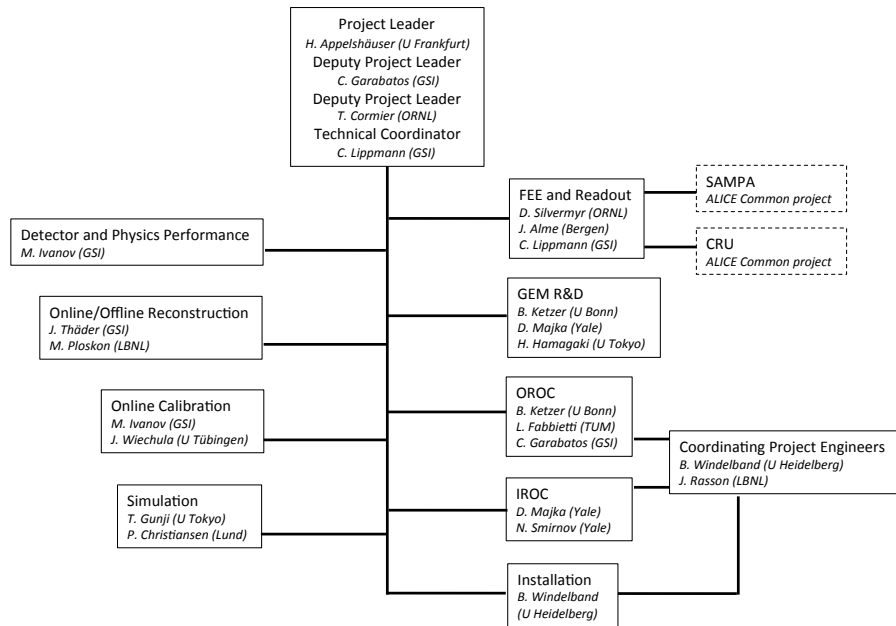


Figure 12.1: Structure of the TPC upgrade project.

Item	Institution
IROC	Yale, Detroit, Oak Ridge, Knoxville, Austin
OROC	Munich, Frankfurt, GSI, Heidelberg, Budapest, Bucharest
GEM R&D and QA	Helsinki, Munich, Tokyo, Yale, Zagreb, GSI
Frontend Card	Lund, Oak Ridge
FEE integration and test	Oak Ridge, Lund, Houston, Tokyo, Bergen, Oslo, GSI
HV, LV, cooling	Mexico-City, GSI, Munich
Detector Control	GSI, Worms
Installation and engineering	Heidelberg, Berkeley
Gas system and field cage	GSI
SAMPA ASIC	Sao Paulo, Bergen, Oslo, CERN
CRU	Budapest, Kolkata, Bergen, CERN

Table 12.2: Sharing of responsibilities for construction and installation of the TPC upgrade. Note that SAMPA ASIC and CRU are parts of common ALICE projects.

3047 in close collaboration with CERN. India and Hungary have indicated the possibility of funding for the
 3048 production cost of the TPC CRU. Further requests for funding are presently being prepared by the groups
 3049 from Finland, Japan, Mexico, Norway, and Sweden.

3050 **12.3 Schedule**

3051 The current LHC schedule foresees LS2 to start in summer 2018. This defines the time schedule for
 3052 the TPC upgrade, see Fig. 12.2. Major technological choices will have to be made by the end of 2014
 3053 to allow finalization of the design, a timely procurement of detector materials and preparation of the
 3054 series production. Such decisions involve a definition of the GEM configuration, geometry, and their
 3055 operational point, as well as the final gas mixture. Besides proceeding studies with small prototypes,
 3056 a further test campaign of a full size IROC prototypes equipped with a quadruple GEM stack will be

Readout chambers	Quantity	Cost (MCHF)
GEM foils	700	0.5
Frames and components	700	0.1
Pad planes	160	0.4
Chamber bodies	80	0.3
HV divider	80	0.1
Assembly and installation tooling		0.4
Total Readout Chambers		1.8
Services		Cost (MCHF)
GEM HV system		0.2
Fast current monitoring		0.2
HV supply for last FC resistor		0.1
Other services		0.2
Total Services		0.7
FEE and Readout	Quantity (incl. spares)	Cost (MCHF)
SAMPA ASIC	19,500	0.78
Front-end card	3900	0.35
GBTx ASIC	7000	0.38
Optical transmitters/receivers	5500	0.79
CRU (control room, AMC40)		2.00
Optical fibers	9000	1.32
TPC Event Processing Nodes (TPC-EPN)		1.0
Other		0.02
Total Electronics		6.64
Total IROC	40	3.3
Total OROC	40	5.84
Total		9.14

Table 12.3: CORE cost estimate for the TPC upgrade.

3057 performed. This includes a test beam time at PS with mixed electron and pion beams in autumn 2014
3058 to validate the dE/dx performance of this configuration, and a stability test with hadron beams in 2015.
3059 Moreover, the availability of GEM foils from different suppliers needs to be investigated. At present,
3060 three possible suppliers exist: TechEtch (USA), SciEnergy (Japan) and CERN TS-DEM. Foils from all
3061 three suppliers are being studied.

3062 The assembly and test of the readout chambers will be distributed among various collaborating institu-
3063 tions in Europe (OROCs) and the US (IROCs), making optimum use of their experience, resources and
3064 facilities (see Tab. 12.2). Delivery of the tested readout chambers to CERN will happen in 2017. A
3065 similar timeline for R&D, production and test is imposed to the frontend electronics.

3066 Since the GEM readout chamber installation will have to be carried out in a clean environment, the TPC
3067 must be removed from the cavern and moved into the SXL2 cleanroom on the P2 surface. In order to
3068 maximize the available time for the readout chamber and electronics installation, the TPC removal will
3069 take place at the beginning of LS2 (Scenario 1). The total duration of LS2 is 18 months. This will leave 40
3070 weeks for replacing of the readout chambers, installation of the new electronics and pre-commissioning
3071 on the surface before reinstallation towards the end of the shutdown period (see also Sec. 11.3).

3072 In an alternative scenario the TPC will be removed already during an extended "End-of-the-Year" Tech-
3073 nical Stop 2016/2017 to leave sufficient time for readout chamber and electronics installation on the
3074 surface. In Scenario 2, ALICE will not operate in 2017, the TPC will be in the clean room for more than
3075 two years, and reinstallation of the TPC will happen during LS2.

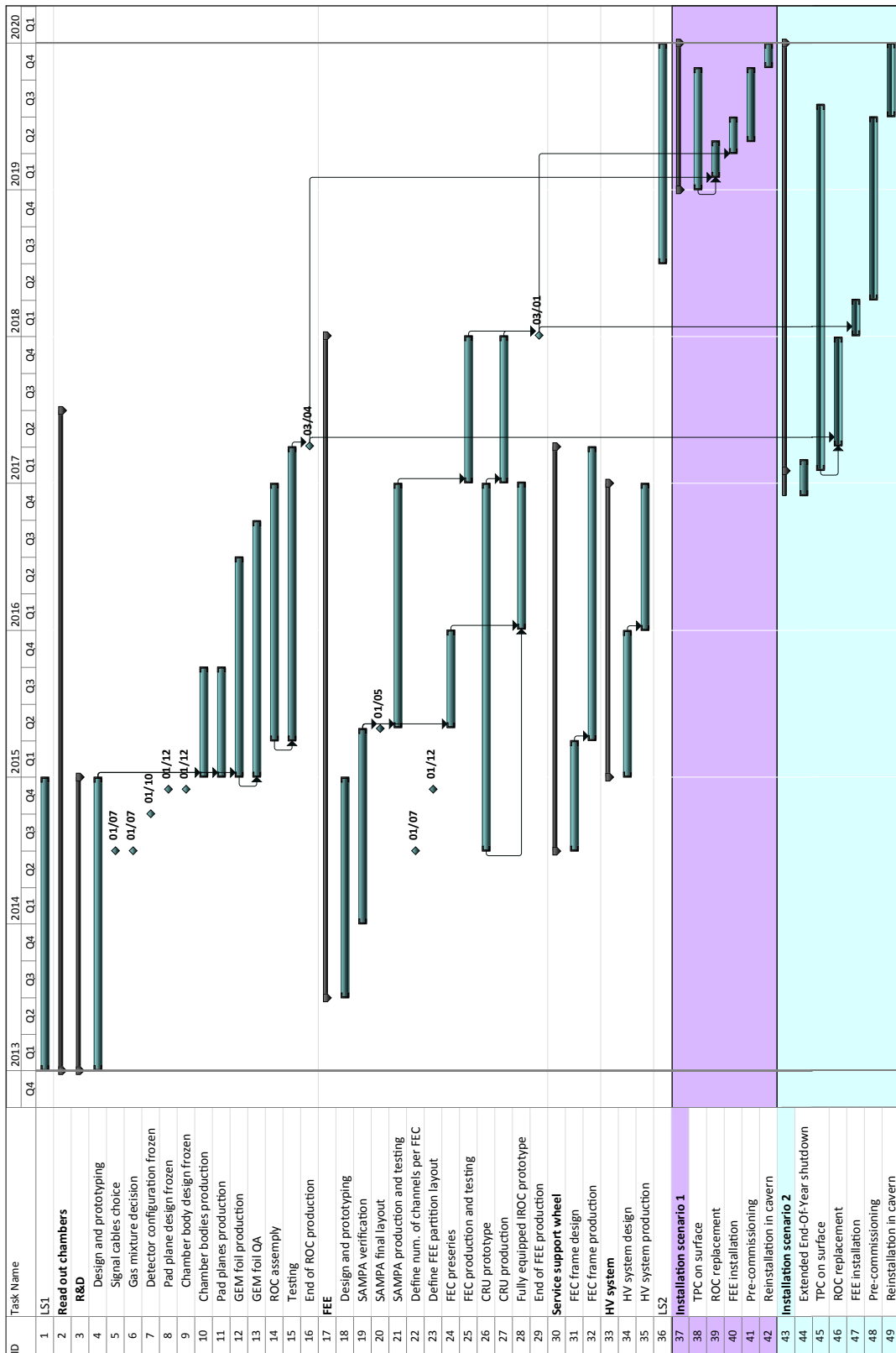


Figure 12.2: Time line for the TPC upgrade. The two installation scenarios are indicated with different colors.

3076 **12.4 TPC upgrade TDR editorial committee**

3077 The editorial committee of this TDR was formed by the following persons:

3078 H. Appelshäuser, M. Ball, P. Christiansen, C. Garabatos, P. Gasik, T. Gunji, J. Harris, M. Ivanov, B. Ket-
3079 zer, C. Lippmann, A. Oskarsson, N. Smirnov, R. Renfordt, D. Röhrich, J. Thäder, J. Wiechula.

3080 **12.5 TPC upgrade TDR task force**

3081 The following persons have contributed to the work presented in this TDR:

3082 H. Appelshäuser, M. Ball, G. Barnaföldi, E. Bartsch, J. Bloemer, P. Christiansen, T. Cormier, K. Eckstein,
3083 L. Fabbietti, C. Garabatos, F. Garcia, P. Gasik, T. Gunji, H. Hamagaki, J. Harris, E. Hellbär, D. Heuchel,
3084 A. Hönle, M. Ivanov, B. Ketzer, M. Kowalski, C. Lippmann, M. Ljunggren, J. Margutti, S. Masciocchi,
3085 A. Mathis, A. Oskarsson, V. Peskov, R. Renfordt, D. Röhrich, R. Shahoyan, D. Silvermyr, N. Smirnov,
3086 K. Terasaki, J. Thäder, D. Vranic, M. Weber, J. Wiechula, Y. Yamaguchi.

Appendices

3088 Appendix A

3089 Coordinate systems

3090 Below we describe the coordinate systems used in ALICE.

3091 A.1 Global coordinate system

3092 The global ALICE coordinate system [1] is a right-handed orthogonal cartesian system, which has its
3093 origin at the beam interaction point. A sketch of the global coordinate system is given in Fig. A.1.

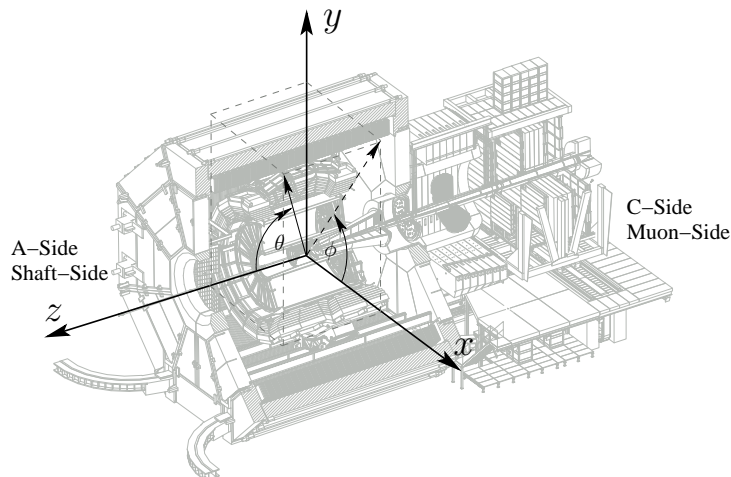


Figure A.1: ALICE global coordinate system.

3094 Its z -axis is parallel to the mean beam direction, pointing towards the ‘A-side’, away from the muon arm.
3095 This side is also called shaft- or RB24-side. The opposite side (negative z values) is called C-side, or
3096 also Muon- or RB26-side. The x -axis is lying in the local horizontal accelerator plane, pointing towards
3097 the centre of the LHC ring. The side with positive x values is also called I-side (inner), the opposite
3098 side correspondingly O-side (outer). The y -axis is chosen to define a right-handed system, thus pointing
3099 upwards. The azimuthal angle φ is increasing counterclockwise, starting from the x -axis ($\varphi = 0$) and
3100 looking from the A-side towards the C-side. The polar angle θ is increasing from the z -axis towards the
3101 xy -plane.

3102 A.2 Local coordinate system

3103 To account for the azimuthal segmentation of the central barrel detectors the reconstruction software uses
3104 a local coordinate system [2] related to a given sub-detector (TPC sector, ITS module etc.). The local

3105 coordinate system is also a right-handed cartesian system. It has the same origin and z -axis as the global
3106 coordinate system, which is perpendicular to the sensitive planes of the TPC sectors. The local x -axis lies
3107 in the sensitive plane and is parallel to the pad rows. Therefore, the pads in each row are in the direction
3108 of the y -axis. Small variations in the direction of the pads can be expressed as variations in $r \cdot \varphi$ and are
3109 often quoted as $r\varphi$. A sketch of the local coordinate system is given in Fig. A.2.

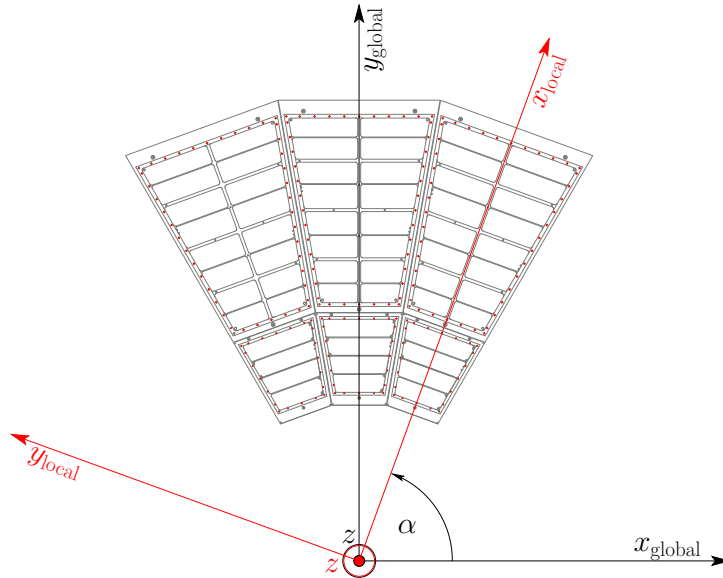


Figure A.2: ALICE local coordinate systems.

3110 **Appendix B**

3111 **TPC upgrade collaboration**

3112 **Department of Physics, University of Zagreb, Zagreb, Croatia**

3113 M. Planicic, N. Poljak, G. Simatovic, A. Utrobicic

3114

3115 **Niels Bohr Institute, University of Copenhagen, Copenhagen, Denmark**

3116 J.J. Gaardhøje, B. Nielsen

3117

3118 **Helsinki Institute of Physics, Helsinki, Finland**

3119 E. Brucken, F. Garcia, T. Hilden, J. Rak

3120

3121 **Helmholtz-Institut für Kern- und Strahlenphysik, Rheinische Friedrich-Wilhelms-Universität, Bonn, Germany**

3122 F. Boehmer, B. Ketzer

3123

3124 **Institut für Kernphysik, Johann Wolfgang Goethe-Universität, Frankfurt, Germany**

3125 W. Amend, H. Appelshäuser, M. Arslandok, E. Bartsch, T. Bröker, S. Heckel, E. Hellbär, D. Just,

3126 P. Lüttig, V. Peskov, F. Pliquett, P. Reichelt, R. Renfordt, A. Tarantola Peloni

3127

3128 **Physikalisches Institut, Ruprecht-Karls Universität, Heidelberg, Germany**

3129 P. Glässel, J. Stachel, D. Vranic, B. Windelband

3130

3131 **Physik Department, Technische Universität München, Germany**

3132 M. Ball, J. Bloemer, K. Eckstein, P. Gasik, D. Heuchel, A. Hönle, L. Fabbietti, J. Margutti, A. Mathis,

3133 S. Weber

3134

3135 **Physikalisches Institut, Eberhard Karls Universität, Tübingen, Germany**

3136 H. Schmidt, J. Wiechula

3137

3138 **FH Worms, Worms, Germany**

3139 R. Keidel

3140

3141 **Research Division and ExtreMe Matter Institute EMMI, GSI Helmholtzzentrum für Schwerio-**
3142 **nenforschung, Darmstadt, Germany**

3143 A. Andronic, R. Averbeck, P. Braun-Munzinger, U. Frankenfild, C. Garabatos, M. Ivanov, M. Köhler,

3144 M. Krzewicki, C. Lippmann, A. Marin, N. Martin, S. Masciocchi, D. Miskowiec, M. Nicassio, J. Otwinowski,

3145 C. Schmidt, K. Schweda, I. Selyuzhenkov, J. Thäder, J. Wagner

- 3147
3148 **Wigner Research Center for Physics, Budapest, Hungary**
3149 G. Barnaföldi, G. Bencedi, G. Hamar, D. Varga
3150
3151 **Bose Institute, Kolkata, India**
3152 S. Das, S.K. Ghosh, S.K. Prasad, S. Raha
3153
3154 **Institute of Physics, Bhubaneswar, India**
3155 P. Sahu, N. Sharma
3156
3157 **National Institute of Science Education and Research, Bhubaneswar, India**
3158 S. Biswas, L. Kumar, B. Mohanty
3159
3160 **Indian Institute of Technology, Indore, India**
3161 A. Roy, R. Sahoo
3162
3163 **Indian Institute of Technology, Mumbai, India**
3164 S. Dash, B.K. Nandi, R. Varma
3165
3166 **Variable Energy Cyclotron Centre, Kolkata, India**
3167 Z. Ahammed, S. Chattopadhyay, A.K. Dubey, P. Ghosh, S.A. Khan, T.K. Nayak, S.K. Pal, J. Saini,
3168 R.N. Singaraju, Y.P. Viyogi
3169
3170 **University of Tokyo, Tokyo, Japan**
3171 H. Hamagaki, T. Gunji, K. Terasaki, Y. Yamaguchi, K. Yukawa
3172
3173 **Instituto de Ciencias Nucleares, Universidad Nacional Autónoma de México, Mexico-City, Mex-**
3174 **ico**
3175 G. Paic
3176
3177 **Department of Physics and Technology, University of Bergen, Bergen, Norway**
3178 D. Röhrich, K. Ullaland, A. Velure
3179
3180 **Faculty of Engineering, Bergen University College, Bergen, Norway**
3181 J. Alme, H. Helstrup
3182
3183 **Department of Physics, University of Oslo, Oslo, Norway**
3184 K. Røed, S. Mahmood, C. Zhao
3185
3186 **Department of Technology, Vestfold University College, Tonsberg, Norway**
3187 J. Lien, R. Langoey
3188
3189 **Department of Physics, COMSATS Institute of Information Technology Islamabad, Islamabad,**
3190 **Pakistan**
3191 A. Bhatti, A. Rehman
3192
3193 **The Henryk Niewodniczanski Institute of Nuclear Physics, Polish Academy of Science, Cracow,**
3194 **Poland**
3195 M. Kowalski, A. Matyja
3196

- 3197 **National Institute for Physics and Nuclear Engineering, Bucharest, Romania**
3198 M. Petris, M. Petrovici
3199
- 3200 **Faculty of Mathematics, Physics and Informatics, Comenius University, Bratislava, Slovakia**
3201 M. Pikna, B. Sitár, P. Strmeň, I. Szarka
3202
- 3203 **Division of Particle Physics, University of Lund, Lund, Sweden**
3204 P. Christiansen, M. Ljunggren, L. Österman, E. Stenlund, A. Oskarsson, T. Richert
3205
- 3206 **Creighton University, Omaha, Nebraska, USA**
3207 M. Cherney, M. Poghosyan, J. Seger
3208
- 3209 **University of Houston, Houston, Texas, USA**
3210 R. Bellwied, S. Jena, D. McDonald, L. Pinsky, A. Timmins, M. Weber
3211
- 3212 **Lawrence Berkeley National Laboratory, Berkeley, California, USA**
3213 D. Gangadharan, P.M. Jacobs, C. Loizides, M. Ploskon, J. Porter, J. Rasson, X. Zhang
3214
- 3215 **Lawrence Livermore National Laboratory, Livermore, California, USA**
3216 R. Soltz
3217
- 3218 **Oak Ridge National Laboratory, Oak Ridge, Tennessee, USA**
3219 T.M. Cormier, D.J. Dean, M. Middlebrook, K.F. Read, D. Silvermyr
3220
- 3221 **Purdue University, West Lafayette, Indiana, USA**
3222 R.P. Scharenberg, B.K. Srivastava
3223
- 3224 **University of Tennessee, Knoxville, Tennessee, USA**
3225 C. Nattrass, N. Sharma, S.P. Sorensen
3226
- 3227 **The University of Texas at Austin, Austin, Texas, USA**
3228 A.G. Knospe, C. Markert, J. Schambach
3229
- 3230 **Wayne State University, Detroit, Michigan, USA**
3231 R. Belmont, C.A. Pruneau, P. Pujahari, J. Putschke, M. Verweij, S. Voloshin
3232
- 3233 **Yale University, New Haven, Connecticut, USA**
3234 H. Caines, M.E. Connors, J.W. Harris, R. Majka, R.J. Reed, T. Schuster, N. Smirnov
3235
- 3236 **California Polytechnic State University, San Luis Obispo, California, USA**
3237 J. L. Klay
3238
- 3239 **Chicago State University, Chicago, Illinois, USA**
3240 E. Garcia-Solis, A. Harton
3241
3242

The ALICE Collaboration

- 3245 B. Abelev⁷², J. Adam³⁷, D. Adamová⁸⁰, M.M. Aggarwal⁸⁴, M. Agnello^{91,108}, A. Agostinelli²⁶,
 3246 N. Agrawal⁴⁴, Z. Ahammed¹²⁶, N. Ahmad¹⁸, A. Ahmad Masoodi¹⁸, I. Ahmed¹⁵, S.U. Ahn⁶⁵,
 3247 S.A. Ahn⁶⁵, I. Aimo^{91,108}, S. Aiola¹³¹, M. Ajaz¹⁵, A. Akindinov⁵⁵, D. Aleksandrov⁹⁷, B. Alessandro¹⁰⁸,
 3248 D. Alexandre⁹⁹, A. Alici^{102,12}, A. Alkin³, J. Alme³⁵, T. Alt³⁹, V. Altini³¹, S. Altinpinar¹⁷,
 3249 I. Altsybeev¹²⁵, C. Alves Garcia Prado¹¹⁵, C. Andrei⁷⁵, A. Andronic⁹⁴, V. Anguelov⁹⁰, J. Anielski⁵⁰,
 3250 T. Antičić⁹⁵, F. Antinori¹⁰⁵, P. Antonioli¹⁰², L. Aphecetche¹⁰⁹, H. Appelshäuser⁴⁹, N. Arbor⁶⁸,
 3251 S. Arcelli²⁶, N. Armesto¹⁶, R. Arnaldi¹⁰⁸, T. Aronsson¹³¹, I.C. Arsene^{21,94}, M. Arslanok⁴⁹,
 3252 A. Augustinus³⁴, R. Averbeck⁹⁴, T.C. Awes⁸¹, M.D. Azmi^{18,86}, M. Bach³⁹, A. Badalà¹⁰⁴,
 3253 Y.W. Baek^{40,67}, S. Bagnasco¹⁰⁸, R. Bailhache⁴⁹, R. Bala⁸⁷, A. Baldisseri¹⁴, M. Ball⁸⁹,
 3254 F. Baltasar Dos Santos Pedrosa³⁴, R.C. Baral⁵⁸, R. Barbera²⁷, F. Barile³¹, G.G. Barnaföldi¹³⁰,
 3255 L.S. Barnby⁹⁹, V. Barret⁶⁷, J. Bartke¹¹², M. Basile²⁶, N. Bastid⁶⁷, S. Basu¹²⁶, B. Bathen⁵⁰,
 3256 G. Batigne¹⁰⁹, B. Batyunya⁶³, P.C. Batzing²¹, C. Baumann⁴⁹, I.G. Bearden⁷⁷, H. Beck⁴⁹, C. Bedda⁹¹,
 3257 N.K. Behera⁴⁴, I. Belikov⁵¹, R. Bellwied¹¹⁷, E. Belmont-Moreno⁶¹, G. Bencedi¹³⁰, S. Beole²⁵,
 3258 I. Berceau⁷⁵, A. Bercuci⁷⁵, Y. Berdnikov^{II,82}, D. Berenyi¹³⁰, M.E. Berger⁸⁹, R.A. Bertens⁵⁴,
 3259 D. Berzano²⁵, L. Betev³⁴, A. Bhasin⁸⁷, A.K. Bhati⁸⁴, B. Bhattacharjee⁴¹, J. Bhom¹²², L. Bianchi²⁵,
 3260 N. Bianchi⁶⁹, C. Bianchin⁵⁴, J. Bielčák³⁷, J. Bielčíková⁸⁰, A. Bilandzic⁷⁷, S. Bjelogrić⁵⁴, F. Blanco¹⁰,
 3261 D. Blau⁹⁷, C. Blume⁴⁹, F. Bock^{90,71}, A. Bogdanov⁷³, H. Bøggild^{III,77}, M. Bogolyubsky⁵²,
 3262 F.V. Böhmer⁸⁹, L. Boldizsár¹³⁰, M. Bombara³⁸, J. Book⁴⁹, H. Borel¹⁴, A. Borissov^{93,129}, F. Bossú⁶²,
 3263 M. Botje⁷⁸, E. Botta²⁵, S. Böttger⁴⁸, P. Braun-Munzinger⁹⁴, T. Breitner⁴⁸, T.A. Broker⁴⁹,
 3264 T.A. Browning⁹², M. Broz³⁶, E. Bruna¹⁰⁸, G.E. Bruno³¹, D. Budnikov⁹⁶, H. Buesching⁴⁹,
 3265 S. Bufalino¹⁰⁸, P. Buncic³⁴, O. Busch⁹⁰, Z. Buthelezi⁶², D. Caffarri²⁸, X. Cai⁷, H. Caines¹³¹,
 3266 A. Caliva⁵⁴, E. Calvo Villar¹⁰⁰, P. Camerini²⁴, F. Carena³⁴, W. Carena³⁴, J. Castillo Castellanos¹⁴,
 3267 E.A.R. Casula²³, V. Catanescu⁷⁵, C. Cavicchioli³⁴, C. Ceballos Sanchez⁹, J. Cepila³⁷, P. Cerello¹⁰⁸,
 3268 B. Chang¹¹⁸, S. Chapeland³⁴, J.L. Charvet¹⁴, S. Chattopadhyay¹²⁶, S. Chattopadhyay⁹⁸, M. Cherney⁸³,
 3269 C. Cheshkov¹²⁴, B. Cheynis¹²⁴, V. Chibante Barroso³⁴, D.D. Chinellato^{117,116}, P. Chochula³⁴,
 3270 M. Chojnacki⁷⁷, S. Choudhury¹²⁶, P. Christakoglou⁷⁸, C.H. Christensen⁷⁷, P. Christiansen³²,
 3271 T. Chujo¹²², S.U. Chung⁹³, C. Cicalo¹⁰³, L. Cifarelli^{26,12}, F. Cindolo¹⁰², J. Cleymans⁸⁶, F. Colamaria³¹,
 3272 D. Colella³¹, A. Collu²³, M. Colocci²⁶, G. Conesa Balbastre⁶⁸, Z. Conesa del Valle⁴⁷, M.E. Connors¹³¹,
 3273 J.G. Contreras¹¹, T.M. Cormier^{81,129}, Y. Corrales Morales²⁵, P. Cortese³⁰, I. Cortés Maldonado²,
 3274 M.R. Cosentino¹¹⁵, F. Costa³⁴, P. Crochet⁶⁷, R. Cruz Albino¹¹, E. Cuautle⁶⁰, L. Cunqueiro^{69,34},
 3275 A. Dainese¹⁰⁵, R. Dang⁷, D. Das⁹⁸, I. Das⁴⁷, K. Das⁹⁸, S. Das⁴, A. Dash¹¹⁶, S. Dash⁴⁴, S. De¹²⁶,
 3276 H. Delagrangé^{I,109}, A. Deloff⁷⁴, E. Dénes¹³⁰, G. D'Erasmus³¹, A. De Caro^{29,12}, G. de Cataldo¹⁰¹,
 3277 J. de Cuveland³⁹, A. De Falco²³, D. De Gruttola^{12,29}, N. De Marco¹⁰⁸, S. De Pasquale²⁹, R. de Rooij⁵⁴,
 3278 M.A. Diaz Corchero¹⁰, T. Dietel^{50,86}, R. Divià³⁴, D. Di Bari³¹, S. Di Liberto¹⁰⁶, A. Di Mauro³⁴,
 3279 P. Di Nezza⁶⁹, Ø. Djuvsland¹⁷, A. Dobrin⁵⁴, T. Dobrowolski⁷⁴, D. Domenicis Gimenez¹¹⁵, O. Dordic²¹,

3280 S. Dørheim⁸⁹, A.K. Dubey¹²⁶, A. Dubla⁵⁴, L. Ducroux¹²⁴, P. Dupieux⁶⁷, A.K. Dutta Majumdar⁹⁸,
 3281 R.J. Ehlers¹³¹, D. Elia¹⁰¹, H. Engel⁴⁸, B. Erazmus^{34,109}, H.A. Erdal³⁵, D. Eschweiler³⁹, B. Espagnon⁴⁷,
 3282 M. Esposito³⁴, M. Estienne¹⁰⁹, S. Esumi¹²², D. Evans⁹⁹, S. Evdokimov⁵², D. Fabris¹⁰⁵, J. Faivre⁶⁸,
 3283 D. Falchieri²⁶, A. Fantoni⁶⁹, M. Fasel⁹⁰, D. Fehlker¹⁷, L. Feldkamp⁵⁰, D. Felea⁵⁹, A. Feliciello¹⁰⁸,
 3284 G. Feofilov¹²⁵, J. Ferencei⁸⁰, A. Fernández Téllez², E.G. Ferreira¹⁶, A. Ferretti²⁵, A. Festanti²⁸,
 3285 J. Figiel¹¹², S. Filchagin⁹⁶, D. Finogeev⁵³, F.M. Fionda^{31,101}, E.M. Fiore³¹, E. Floratos⁸⁵, M. Floris³⁴,
 3286 S. Foertsch⁶², P. Foka⁹⁴, S. Fokin⁹⁷, E. Fragiaco¹⁰⁷, A. Francescon^{28,34}, U. Frankenfeld⁹⁴,
 3287 U. Fuchs³⁴, C. Furget⁶⁸, M. Fusco Girard²⁹, J.J. Gaardhøje⁷⁷, M. Gagliardi²⁵, A.M. Gago¹⁰⁰,
 3288 M. Gallio²⁵, D.R. Gangadharan^{19,71}, P. Ganoti^{81,85}, C. Garabatos⁹⁴, E. Garcia-Solis¹³, C. Gargiulo³⁴,
 3289 I. Garishvili⁷², J. Gerhard³⁹, M. Germain¹⁰⁹, A. Gheata³⁴, M. Gheata^{34,59}, B. Ghidini³¹, P. Ghosh¹²⁶,
 3290 S.K. Ghosh⁴, P. Gianotti⁶⁹, P. Giubellino³⁴, E. Gladysz-Dziadus¹¹², P. Glässel⁹⁰, A. Gomez Ramirez⁴⁸,
 3291 P. González-Zamora¹⁰, S. Gorbunov³⁹, L. Görlich¹¹², S. Gotovac¹¹¹, L.K. Graczykowski¹²⁸,
 3292 A. Grelli⁵⁴, A. Grigoras³⁴, C. Grigoras³⁴, V. Grigoriev⁷³, A. Grigoryan¹, S. Grigoryan⁶³, B. Grinyov³,
 3293 N. Grion¹⁰⁷, J.F. Grosse-Oetringhaus³⁴, J.-Y. Grossiord¹²⁴, R. Grosso³⁴, F. Guber⁵³, R. Guernane⁶⁸,
 3294 B. Guerzoni²⁶, M. Guilbaud¹²⁴, K. Gulbrandsen⁷⁷, H. Gulkanyan¹, T. Gunji¹²¹, A. Gupta⁸⁷, R. Gupta⁸⁷,
 3295 K. H. Khan¹⁵, R. Haake⁵⁰, Ø. Haaland¹⁷, C. Hadjidakis⁴⁷, M. Haiduc⁵⁹, H. Hamagaki¹²¹, G. Hamar¹³⁰,
 3296 L.D. Hanratty⁹⁹, A. Hansen⁷⁷, J.W. Harris¹³¹, H. Hartmann³⁹, A. Harton¹³, D. Hatzifotiadou¹⁰²,
 3297 S. Hayashi¹²¹, S.T. Heckel⁴⁹, M. Heide⁵⁰, H. Helstrup³⁵, A. Herghelegiu⁷⁵, G. Herrera Corral¹¹,
 3298 B.A. Hess³³, K.F. Hetland³⁵, B. Hicks¹³¹, B. Hippolyte⁵¹, J. Hladky⁵⁷, P. Hristov³⁴, M. Huang¹⁷,
 3299 T.J. Humanic¹⁹, D. Hutter³⁹, D.S. Hwang²⁰, R. Ilkaev⁹⁶, I. Ilkiv⁷⁴, M. Inaba¹²², G.M. Innocenti²⁵,
 3300 C. Ionita³⁴, M. Ippolitov⁹⁷, M. Irfan¹⁸, M. Ivanov⁹⁴, V. Ivanov⁸², O. Ivanytskyi³, A. Jachołkowski²⁷,
 3301 P.M. Jacobs⁷¹, C. Jahnke¹¹⁵, H.J. Jang⁶⁵, M.A. Janik¹²⁸, P.H.S.Y. Jayarathna¹¹⁷,
 3302 R.T. Jimenez Bustamante⁶⁰, P.G. Jones⁹⁹, H. Jung⁴⁰, A. Jusko⁹⁹, S. Kalcher³⁹, P. Kalinak⁵⁶,
 3303 A. Kalweit³⁴, J. Kamin⁴⁹, J.H. Kang¹³², V. Kaplin⁷³, S. Kar¹²⁶, A. Karasu Uysal⁶⁶, O. Karavichev⁵³,
 3304 T. Karavicheva⁵³, E. Karpechev⁵³, U. Kebschull⁴⁸, R. Keidel¹³³, B. Ketzer⁸⁹, M.M. Khan^{IV,18},
 3305 P. Khan⁹⁸, S.A. Khan¹²⁶, A. Khanzadeev⁸², Y. Kharlov⁵², B. Kileng³⁵, B. Kim¹³², D.W. Kim^{65,40},
 3306 D.J. Kim¹¹⁸, J.S. Kim⁴⁰, M. Kim⁴⁰, M. Kim¹³², S. Kim²⁰, T. Kim¹³², S. Kirsch³⁹, I. Kisel³⁹,
 3307 S. Kiselev⁵⁵, A. Kisiel¹²⁸, G. Kiss¹³⁰, J.L. Klay⁶, J. Klein⁹⁰, C. Klein-Bösing⁵⁰, A. Kluge³⁴,
 3308 M.L. Knichel^{94,90}, A.G. Knospe¹¹³, C. Kobdaj^{34,110}, M. Kofarago³⁴, M.K. Köhler⁹⁴, T. Kollegger³⁹,
 3309 A. Kolojvari¹²⁵, V. Kondratiev¹²⁵, N. Kondratyeva⁷³, A. Konevskikh⁵³, V. Kovalenko¹²⁵,
 3310 M. Kowalski^{34,112}, S. Kox⁶⁸, G. Koyithatta Meethaleveedu⁴⁴, J. Kral¹¹⁸, I. Králik⁵⁶, F. Kramer⁴⁹,
 3311 A. Kravčáková³⁸, M. Kreliina³⁷, M. Kretz³⁹, M. Krivda^{99,56}, F. Krizek⁸⁰, M. Krus³⁷, E. Kryshen⁸²,
 3312 M. Krzewicki⁹⁴, V. Kučera⁸⁰, Y. Kucheriaev^{I,97}, T. Kugathasan³⁴, C. Kuhn⁵¹, P.G. Kuijter⁷⁸,
 3313 I. Kulakov⁴⁹, J. Kumar⁴⁴, P. Kurashvili⁷⁴, A. Kurepin⁵³, A.B. Kurepin⁵³, A. Kuryakin⁹⁶, S. Kushpil⁸⁰,
 3314 M.J. Kweon^{90,46}, Y. Kwon¹³², P. Ladron de Guevara⁶⁰, C. Lagana Fernandes¹¹⁵, I. Lakomov⁴⁷,
 3315 R. Langoy¹²⁷, C. Lara⁴⁸, A. Lardeux¹⁰⁹, A. Lattuca²⁵, S.L. La Pointe^{54,108}, P. La Rocca²⁷, R. Lea²⁴,
 3316 G.R. Lee⁹⁹, I. Legrand³⁴, J. Lehnert⁴⁹, R.C. Lemmon⁷⁹, V. Lenti¹⁰¹, E. Leogrande⁵⁴, M. Leoncino²⁵,
 3317 I. León Monzón¹¹⁴, P. Lévai¹³⁰, S. Li^{7,67}, J. Lien¹²⁷, R. Lietava⁹⁹, S. Lindal²¹, V. Lindenstruth³⁹,
 3318 C. Lippmann⁹⁴, M.A. Lisa¹⁹, H.M. Ljunggren³², D.F. Lodato⁵⁴, P.I. Loenne¹⁷, V.R. Loggins¹²⁹,
 3319 V. Loginov⁷³, D. Lohner⁹⁰, C. Loizides⁷¹, X. Lopez⁶⁷, E. López Torres⁹, X.-G. Lu⁹⁰, P. Luettig⁴⁹,
 3320 M. Lunardon²⁸, J. Luo⁷, G. Luparello⁵⁴, C. Luzzi³⁴, R. Ma¹³¹, A. Maevskaya⁵³, M. Mager³⁴,
 3321 D.P. Mahapatra⁵⁸, A. Maire^{90,51}, R.D. Majka¹³¹, M. Malaev⁸², I. Maldonado Cervantes⁶⁰,
 3322 L. Malinina^{V,63}, D. Mal'Kevich⁵⁵, P. Malzacher⁹⁴, A. Mamonov⁹⁶, L. Manceau¹⁰⁸, V. Manko⁹⁷,
 3323 F. Manso⁶⁷, V. Manzari^{101,34}, M. Marchisone^{67,25}, J. Mareš⁵⁷, G.V. Margagliotti²⁴, A. Margotti¹⁰²,
 3324 A. Marín⁹⁴, C. Markert^{113,34}, M. Marquard⁴⁹, I. Martashvili¹²⁰, N.A. Martin⁹⁴, P. Martinengo³⁴,
 3325 M.I. Martínez², G. Martínez García¹⁰⁹, J. Martin Blanco¹⁰⁹, Y. Martynov³, A. Mas¹⁰⁹, S. Masciocchi⁹⁴,
 3326 M. Masera²⁵, A. Masoni¹⁰³, L. Massacrier¹⁰⁹, A. Mastroserio³¹, A. Matyja¹¹², C. Mayer¹¹²,
 3327 J. Mazer¹²⁰, M.A. Mazzoni¹⁰⁶, F. Meddi²², A. Menchaca-Rocha⁶¹, E. Meninno²⁹, J. Mercado Pérez⁹⁰,
 3328 M. Meres³⁶, Y. Miake¹²², K. Mikhaylov^{55,63}, L. Milano³⁴, J. Milosevic^{VI,21}, A. Mischke⁵⁴,
 3329 A.N. Mishra⁴⁵, D. Miśkowiec⁹⁴, C.M. Mitu⁵⁹, J. Mlynarz¹²⁹, B. Mohanty^{126,76}, L. Molnar⁵¹,

- 3330 L. Montaña Zetina¹¹, E. Montes¹⁰, M. Morando²⁸, D.A. Moreira De Godoy¹¹⁵, S. Moretto²⁸,
3331 A. Morreale^{118,109}, A. Morsch³⁴, V. Muccifora⁶⁹, E. Mudnic¹¹¹, S. Muhuri¹²⁶, M. Mukherjee¹²⁶,
3332 H. Müller³⁴, M.G. Munhoz¹¹⁵, S. Murray⁸⁶, L. Musa³⁴, J. Musinsky⁵⁶, B.K. Nandi⁴⁴, R. Nania¹⁰²,
3333 E. Nappi¹⁰¹, C. Nattrass¹²⁰, T.K. Nayak¹²⁶, S. Nazarenko⁹⁶, A. Nedosekin⁵⁵, M. Nicassio⁹⁴,
3334 M. Niculescu^{59,34}, B.S. Nielsen⁷⁷, S. Nikolaev⁹⁷, S. Nikulin⁹⁷, V. Nikulin⁸², B.S. Nilsen⁸³,
3335 F. Noferini^{12,102}, P. Nomokonov⁶³, G. Nooren⁵⁴, A. Nyanin⁹⁷, J. Nystrand¹⁷, H. Oeschler⁹⁰, S. Oh¹³¹,
3336 S.K. Oh^{VII,64,40}, A. Okatan⁶⁶, L. Olah¹³⁰, J. Oleniacz¹²⁸, A.C. Oliveira Da Silva¹¹⁵, J. Onderwaater⁹⁴,
3337 C. Oppedisano¹⁰⁸, A. Ortiz Velasquez^{60,32}, A. Oskarsson³², J. Otwinowski⁹⁴, K. Oyama⁹⁰, P. Sahoo⁴⁵,
3338 Y. Pachmayer⁹⁰, M. Pacher³⁷, P. Pagano²⁹, G. Paic⁶⁰, F. Painke³⁹, C. Pajares¹⁶, S.K. Pal¹²⁶,
3339 A. Palmeri¹⁰⁴, D. Pant⁴⁴, V. Papikyan¹, G.S. Pappalardo¹⁰⁴, P. Pareek⁴⁵, W.J. Park⁹⁴, S. Parmar⁸⁴,
3340 A. Passfeld⁵⁰, D.I. Patalakha⁵², V. Patichio¹⁰¹, B. Paul⁹⁸, T. Pawlak¹²⁸, T. Peitzmann⁵⁴,
3341 H. Pereira Da Costa¹⁴, E. Pereira De Oliveira Filho¹¹⁵, D. Peresunko⁹⁷, C.E. Pérez Lara⁷⁸, A. Pesci¹⁰²,
3342 Y. Pestov⁵, V. Petráček³⁷, M. Petran³⁷, M. Petris⁷⁵, M. Petrovici⁷⁵, C. Petta²⁷, S. Piano¹⁰⁷, M. Pikna³⁶,
3343 P. Pillot¹⁰⁹, O. Pinazza^{102,34}, L. Pinsky¹¹⁷, D.B. Piyarathna¹¹⁷, M. Płoskoń⁷¹, M. Planinic^{123,95},
3344 J. Pluta¹²⁸, S. Pochybova¹³⁰, P.L.M. Podesta-Lerma¹¹⁴, M.G. Poghosyan^{83,34}, E.H.O. Pohjoisahö⁴²,
3345 B. Polichtchouk⁵², N. Poljak^{123,95}, A. Pop⁷⁵, S. Porteboeuf-Houssais⁶⁷, J. Porter⁷¹, V. Pospisil³⁷,
3346 B. Potukuchi⁸⁷, S.K. Prasad^{129,4}, R. Preghenella^{12,102}, F. Prino¹⁰⁸, C.A. Pruneau¹²⁹, I. Pshenichnov⁵³,
3347 M. Puccio¹⁰⁸, G. Puddu²³, P. Pujahari¹²⁹, V. Punin⁹⁶, J. Putschke¹²⁹, H. Qvigstad²¹, A. Rachevski¹⁰⁷,
3348 S. Raha⁴, J. Rak¹¹⁸, A. Rakotozafindrabe¹⁴, L. Ramello³⁰, R. Raniwala⁸⁸, S. Raniwala⁸⁸,
3349 S.S. Räsänen⁴², B.T. Rascanu⁴⁹, D. Rathee⁸⁴, A.W. Rauf¹⁵, V. Razazi²³, K.F. Read¹²⁰, J.S. Real⁶⁸,
3350 K. Redlich^{VIII,74}, R.J. Reed^{131,129}, A. Rehman¹⁷, P. Reichelt⁴⁹, M. Reicher⁵⁴, F. Reidt^{34,90},
3351 R. Renfordt⁴⁹, A.R. Reolon⁶⁹, A. Reshetin⁵³, F. Rettig³⁹, J.-P. Revol³⁴, K. Reygers⁹⁰, V. Riabov⁸²,
3352 R.A. Ricci⁷⁰, T. Richert³², M. Richter²¹, P. Riedler³⁴, W. Riegler³⁴, F. Riggi²⁷, A. Rivetti¹⁰⁸,
3353 E. Rocco⁵⁴, M. Rodríguez Cahuantzi², A. Rodríguez Manso⁷⁸, K. Røed²¹, E. Rogochaya⁶³, S. Rohni⁸⁷,
3354 D. Rohr³⁹, D. Röhrich¹⁷, R. Romita^{79,119}, F. Ronchetti⁶⁹, L. Ronflette¹⁰⁹, P. Rosnet⁶⁷, S. Rossegger³⁴,
3355 A. Rossi³⁴, F. Roukoutakis⁸⁵, A. Roy⁴⁵, C. Roy⁵¹, P. Roy⁹⁸, A.J. Rubio Montero¹⁰, R. Rui²⁴,
3356 R. Russo²⁵, E. Ryabinkin⁹⁷, Y. Ryabov⁸², A. Rybicki¹¹², S. Sadovsky⁵², K. Šafařík³⁴, B. Sahlmuller⁴⁹,
3357 R. Sahoo⁴⁵, P.K. Sahu⁵⁸, J. Saini¹²⁶, C.A. Salgado¹⁶, J. Salzwedel¹⁹, S. Sambyal⁸⁷, V. Samsonov⁸²,
3358 X. Sanchez Castro⁵¹, F.J. Sánchez Rodríguez¹¹⁴, L. Šándor⁵⁶, A. Sandoval⁶¹, M. Sano¹²²,
3359 G. Santagati²⁷, D. Sarkar¹²⁶, E. Scapparone¹⁰², F. Scarlassara²⁸, R.P. Scharenberg⁹², C. Schiaua⁷⁵,
3360 R. Schicker⁹⁰, C. Schmidt⁹⁴, H.R. Schmidt³³, S. Schuchmann⁴⁹, J. Schukraft³⁴, M. Schulc³⁷,
3361 T. Schuster¹³¹, Y. Schutz^{109,34}, K. Schwarz⁹⁴, K. Schweda⁹⁴, G. Scioli²⁶, E. Scomparin¹⁰⁸, R. Scott¹²⁰,
3362 G. Segato²⁸, J.E. Seger⁸³, I. Selyuzhenkov⁹⁴, J. Seo⁹³, E. Serradilla^{10,61}, A. Sevcenco⁵⁹, A. Shabetai¹⁰⁹,
3363 G. Shabratova⁶³, R. Shahoyan³⁴, A. Shangaraev⁵², N. Sharma^{120,58}, S. Sharma⁸⁷, K. Shigaki⁴³,
3364 K. Shtejer²⁵, Y. Sibiriak⁹⁷, S. Siddhanta¹⁰³, T. Siemiarczuk⁷⁴, D. Silvermyr⁸¹, C. Silvestre⁶⁸,
3365 G. Simatovic¹²³, R. Singaraju¹²⁶, R. Singh⁸⁷, S. Singha^{76,126}, V. Singhal¹²⁶, B.C. Sinha¹²⁶, T. Sinha⁹⁸,
3366 B. Sitar³⁶, M. Sitta³⁰, T.B. Skaali²¹, K. Skjerdal¹⁷, R. Smakal³⁷, N. Smirnov¹³¹, R.J.M. Snellings⁵⁴,
3367 C. Sjøgaard³², R. Soltz⁷², J. Song⁹³, M. Song¹³², F. Soramel²⁸, S. Sorensen¹²⁰, M. Spacek³⁷,
3368 I. Sputowska¹¹², M. Spyropoulou-Stassinaki⁸⁵, B.K. Srivastava⁹², J. Stachel⁹⁰, I. Stan⁵⁹, G. Stefanek⁷⁴,
3369 M. Steinpreis¹⁹, E. Stenlund³², G. Steyn⁶², J.H. Stiller⁹⁰, D. Stocco¹⁰⁹, M. Stolpovskiy⁵², P. Strmen³⁶,
3370 A.A.P. Suaide¹¹⁵, T. Sugitate⁴³, C. Suire⁴⁷, M. Suleymanov¹⁵, R. Sultanov⁵⁵, M. Šumbera⁸⁰, T. Susa⁹⁵,
3371 T.J.M. Symons⁷¹, A. Szanto de Toledo¹¹⁵, I. Szarka³⁶, A. Szczepankiewicz³⁴, M. Szymanski¹²⁸,
3372 J. Takahashi¹¹⁶, M.A. Tangaro³¹, J.D. Tapia Takaki^{IX,47}, A. Tarantola Peloni⁴⁹, A. Tarazona Martinez³⁴,
3373 M.G. Tarzila⁷⁵, A. Tauro³⁴, G. Tejada Muñoz², A. Telesca³⁴, C. Terrevoli³¹, J. Thäder⁹⁴, D. Thomas⁵⁴,
3374 R. Tieulent¹²⁴, A.R. Timmins¹¹⁷, A. Toia^{105,49}, H. Torii¹²¹, V. Trubnikov³, W.H. Trzaska¹¹⁸, T. Tsuji¹²¹,
3375 A. Tumkin⁹⁶, R. Turrisi¹⁰⁵, T.S. Tveter²¹, J. Ulery⁴⁹, K. Ullaland¹⁷, A. Uras¹²⁴, G.L. Usai²³,
3376 M. Vajzer⁸⁰, M. Vala^{56,63}, L. Valencia Palomo⁴⁷, S. Vallero^{25,90}, P. Vande Vyvre³⁴, L. Vannucci⁷⁰,
3377 J.W. Van Hoorne³⁴, M. van Leeuwen⁵⁴, A. Vargas², R. Varma⁴⁴, M. Vasileiou⁸⁵, A. Vasiliev⁹⁷,
3378 V. Vechernin¹²⁵, M. Veldhoen⁵⁴, A. Velure¹⁷, M. Venaruzzo²⁴, E. Vercellin²⁵, S. Vergara Limón²,
3379 R. Vernet⁸, L. Vickovic¹¹¹, G. Viesti²⁸, J. Viinikainen¹¹⁸, Z. Vilakazi⁶², O. Villalobos Baillie⁹⁹,

3380 A. Vinogradov⁹⁷, L. Vinogradov¹²⁵, Y. Vinogradov⁹⁶, T. Virgili²⁹, V. Viskavicius³², Y.P. Viyogi¹²⁶,
 3381 A. Vodopyanov⁶³, M.A. Völkl⁹⁰, K. Voloshin⁵⁵, S.A. Voloshin¹²⁹, G. Volpe³⁴, B. von Haller³⁴,
 3382 I. Vorobyev¹²⁵, D. Vranic^{94,34}, J. Vrláková³⁸, B. Vulpescu⁶⁷, A. Vyushin⁹⁶, B. Wagner¹⁷, J. Wagner⁹⁴,
 3383 V. Wagner³⁷, M. Wang^{7,109}, Y. Wang⁹⁰, D. Watanabe¹²², M. Weber^{34,117}, S.G. Weber⁹⁴, J.P. Wessels⁵⁰,
 3384 U. Westerhoff⁵⁰, J. Wiechula³³, J. Wikne²¹, M. Wilde⁵⁰, G. Wilk⁷⁴, J. Wilkinson⁹⁰, M.C.S. Williams¹⁰²,
 3385 B. Windelband⁹⁰, M. Winn⁹⁰, C. Xiang⁷, C.G. Yaldo¹²⁹, Y. Yamaguchi¹²¹, H. Yang⁵⁴, P. Yang⁷,
 3386 S. Yang¹⁷, S. Yano⁴³, S. Yasnopolskiy⁹⁷, J. Yi⁹³, Z. Yin⁷, I.-K. Yoo⁹³, I. Yushmanov⁹⁷, V. Zaccolo⁷⁷,
 3387 C. Zach³⁷, A. Zaman¹⁵, C. Zampolli¹⁰², S. Zaporozhets⁶³, A. Zarochentsev¹²⁵, P. Závada⁵⁷,
 3388 N. Zaviyalov⁹⁶, H. Zbroszczyk¹²⁸, I.S. Zgura⁵⁹, M. Zhalov⁸², H. Zhang⁷, X. Zhang^{71,7}, Y. Zhang⁷,
 3389 C. Zhao²¹, N. Zhigareva⁵⁵, D. Zhou⁷, F. Zhou⁷, Y. Zhou⁵⁴, H. Zhu⁷, J. Zhu^{109,7}, X. Zhu⁷,
 3390 A. Zichichi^{12,26}, A. Zimmermann⁹⁰, M.B. Zimmermann^{50,34}, G. Zinovjev³, Y. Zoccarato¹²⁴,
 3391 M. Zynovyev³, M. Zyzak⁴⁹

3392 Affiliation Notes

3393 ^I Deceased
 3394 ^{II} Also at: St. Petersburg State Polytechnical University
 3395 ^{III} emeritus
 3396 ^{IV} Also at: Department of Applied Physics, Aligarh Muslim University, Aligarh, India
 3397 ^V Also at: M.V. Lomonosov Moscow State University, D.V. Skobeltsyn Institute of Nuclear Physics,
 3398 Moscow, Russia
 3399 ^{VI} Also at: University of Belgrade, Faculty of Physics and "Vinča" Institute of Nuclear Sciences,
 3400 Belgrade, Serbia
 3401 ^{VII} Permanent Address: Konkuk University, Seoul, Korea
 3402 ^{VIII} Also at: Institute of Theoretical Physics, University of Wrocław, Wrocław, Poland
 3403 ^{IX} Also at: University of Kansas, Lawrence, KS, United States

3404 Collaboration Institutes

3405 ¹ A.I. Alikhanyan National Science Laboratory (Yerevan Physics Institute) Foundation, Yerevan,
 3406 Armenia
 3407 ² Benemérita Universidad Autónoma de Puebla, Puebla, Mexico
 3408 ³ Bogolyubov Institute for Theoretical Physics, Kiev, Ukraine
 3409 ⁴ Bose Institute, Department of Physics and Centre for Astroparticle Physics and Space Science
 3410 (CAPSS), Kolkata, India
 3411 ⁵ Budker Institute for Nuclear Physics, Novosibirsk, Russia
 3412 ⁶ California Polytechnic State University, San Luis Obispo, CA, United States
 3413 ⁷ Central China Normal University, Wuhan, China
 3414 ⁸ Centre de Calcul de l'IN2P3, Villeurbanne, France
 3415 ⁹ Centro de Aplicaciones Tecnológicas y Desarrollo Nuclear (CEADEN), Havana, Cuba
 3416 ¹⁰ Centro de Investigaciones Energéticas Medioambientales y Tecnológicas (CIEMAT), Madrid, Spain
 3417 ¹¹ Centro de Investigación y de Estudios Avanzados (CINVESTAV), Mexico City and Mérida, Mexico
 3418 ¹² Centro Fermi - Museo Storico della Fisica e Centro Studi e Ricerche "Enrico Fermi", Rome, Italy
 3419 ¹³ Chicago State University, Chicago, USA
 3420 ¹⁴ Commissariat à l'Energie Atomique, IRFU, Saclay, France
 3421 ¹⁵ COMSATS Institute of Information Technology (CIIT), Islamabad, Pakistan
 3422 ¹⁶ Departamento de Física de Partículas and IGFAE, Universidad de Santiago de Compostela, Santiago
 3423 de Compostela, Spain

- 3424 ¹⁷ Department of Physics and Technology, University of Bergen, Bergen, Norway
- 3425 ¹⁸ Department of Physics, Aligarh Muslim University, Aligarh, India
- 3426 ¹⁹ Department of Physics, Ohio State University, Columbus, OH, United States
- 3427 ²⁰ Department of Physics, Sejong University, Seoul, South Korea
- 3428 ²¹ Department of Physics, University of Oslo, Oslo, Norway
- 3429 ²² Dipartimento di Fisica dell'Università 'La Sapienza' and Sezione INFN Rome, Italy
- 3430 ²³ Dipartimento di Fisica dell'Università and Sezione INFN, Cagliari, Italy
- 3431 ²⁴ Dipartimento di Fisica dell'Università and Sezione INFN, Trieste, Italy
- 3432 ²⁵ Dipartimento di Fisica dell'Università and Sezione INFN, Turin, Italy
- 3433 ²⁶ Dipartimento di Fisica e Astronomia dell'Università and Sezione INFN, Bologna, Italy
- 3434 ²⁷ Dipartimento di Fisica e Astronomia dell'Università and Sezione INFN, Catania, Italy
- 3435 ²⁸ Dipartimento di Fisica e Astronomia dell'Università and Sezione INFN, Padova, Italy
- 3436 ²⁹ Dipartimento di Fisica 'E.R. Caianiello' dell'Università and Gruppo Collegato INFN, Salerno, Italy
- 3437 ³⁰ Dipartimento di Scienze e Innovazione Tecnologica dell'Università del Piemonte Orientale and Gruppo Collegato INFN, Alessandria, Italy
- 3438 ³¹ Dipartimento Interateneo di Fisica 'M. Merlin' and Sezione INFN, Bari, Italy
- 3439 ³² Division of Experimental High Energy Physics, University of Lund, Lund, Sweden
- 3440 ³³ Eberhard Karls Universität Tübingen, Tübingen, Germany
- 3441 ³⁴ European Organization for Nuclear Research (CERN), Geneva, Switzerland
- 3442 ³⁵ Faculty of Engineering, Bergen University College, Bergen, Norway
- 3443 ³⁶ Faculty of Mathematics, Physics and Informatics, Comenius University, Bratislava, Slovakia
- 3444 ³⁷ Faculty of Nuclear Sciences and Physical Engineering, Czech Technical University in Prague, Prague, Czech Republic
- 3445 ³⁸ Faculty of Science, P.J. Šafárik University, Košice, Slovakia
- 3446 ³⁹ Frankfurt Institute for Advanced Studies, Johann Wolfgang Goethe-Universität Frankfurt, Frankfurt, Germany
- 3447 ⁴⁰ Gangneung-Wonju National University, Gangneung, South Korea
- 3448 ⁴¹ Gauhati University, Department of Physics, Guwahati, India
- 3449 ⁴² Helsinki Institute of Physics (HIP), Helsinki, Finland
- 3450 ⁴³ Hiroshima University, Hiroshima, Japan
- 3451 ⁴⁴ Indian Institute of Technology Bombay (IIT), Mumbai, India
- 3452 ⁴⁵ Indian Institute of Technology Indore, Indore (IITI), India
- 3453 ⁴⁶ Inha University, Incheon, South Korea
- 3454 ⁴⁷ Institut de Physique Nucléaire d'Orsay (IPNO), Université Paris-Sud, CNRS-IN2P3, Orsay, France
- 3455 ⁴⁸ Institut für Informatik, Johann Wolfgang Goethe-Universität Frankfurt, Frankfurt, Germany
- 3456 ⁴⁹ Institut für Kernphysik, Johann Wolfgang Goethe-Universität Frankfurt, Frankfurt, Germany
- 3457 ⁵⁰ Institut für Kernphysik, Westfälische Wilhelms-Universität Münster, Münster, Germany
- 3458 ⁵¹ Institut Pluridisciplinaire Hubert Curien (IPHC), Université de Strasbourg, CNRS-IN2P3, Strasbourg, France
- 3459 ⁵² Institute for High Energy Physics, Protvino, Russia
- 3460 ⁵³ Institute for Nuclear Research, Academy of Sciences, Moscow, Russia
- 3461 ⁵⁴ Institute for Subatomic Physics of Utrecht University, Utrecht, Netherlands
- 3462 ⁵⁵ Institute for Theoretical and Experimental Physics, Moscow, Russia
- 3463 ⁵⁶ Institute of Experimental Physics, Slovak Academy of Sciences, Košice, Slovakia
- 3464 ⁵⁷ Institute of Physics, Academy of Sciences of the Czech Republic, Prague, Czech Republic
- 3465 ⁵⁸ Institute of Physics, Bhubaneswar, India
- 3466 ⁵⁹ Institute of Space Science (ISS), Bucharest, Romania
- 3467 ⁶⁰ Instituto de Ciencias Nucleares, Universidad Nacional Autónoma de México, Mexico City, Mexico
- 3468 ⁶¹ Instituto de Física, Universidad Nacional Autónoma de México, Mexico City, Mexico
- 3469 ⁶² iThemba LABS, National Research Foundation, Somerset West, South Africa

- 3474 ⁶³ Joint Institute for Nuclear Research (JINR), Dubna, Russia
3475 ⁶⁴ Konkuk University, Seoul, South Korea
3476 ⁶⁵ Korea Institute of Science and Technology Information, Daejeon, South Korea
3477 ⁶⁶ KTO Karatay University, Konya, Turkey
3478 ⁶⁷ Laboratoire de Physique Corpusculaire (LPC), Clermont Université, Université Blaise Pascal,
3479 CNRS-IN2P3, Clermont-Ferrand, France
3480 ⁶⁸ Laboratoire de Physique Subatomique et de Cosmologie (LPSC), Université Joseph Fourier,
3481 CNRS-IN2P3, Institut Polytechnique de Grenoble, Grenoble, France
3482 ⁶⁹ Laboratori Nazionali di Frascati, INFN, Frascati, Italy
3483 ⁷⁰ Laboratori Nazionali di Legnaro, INFN, Legnaro, Italy
3484 ⁷¹ Lawrence Berkeley National Laboratory, Berkeley, CA, United States
3485 ⁷² Lawrence Livermore National Laboratory, Livermore, CA, United States
3486 ⁷³ Moscow Engineering Physics Institute, Moscow, Russia
3487 ⁷⁴ National Centre for Nuclear Studies, Warsaw, Poland
3488 ⁷⁵ National Institute for Physics and Nuclear Engineering, Bucharest, Romania
3489 ⁷⁶ National Institute of Science Education and Research, Bhubaneswar, India
3490 ⁷⁷ Niels Bohr Institute, University of Copenhagen, Copenhagen, Denmark
3491 ⁷⁸ Nikhef, National Institute for Subatomic Physics, Amsterdam, Netherlands
3492 ⁷⁹ Nuclear Physics Group, STFC Daresbury Laboratory, Daresbury, United Kingdom
3493 ⁸⁰ Nuclear Physics Institute, Academy of Sciences of the Czech Republic, Řež u Prahy, Czech Republic
3494 ⁸¹ Oak Ridge National Laboratory, Oak Ridge, TN, United States
3495 ⁸² Petersburg Nuclear Physics Institute, Gatchina, Russia
3496 ⁸³ Physics Department, Creighton University, Omaha, NE, United States
3497 ⁸⁴ Physics Department, Panjab University, Chandigarh, India
3498 ⁸⁵ Physics Department, University of Athens, Athens, Greece
3499 ⁸⁶ Physics Department, University of Cape Town, Cape Town, South Africa
3500 ⁸⁷ Physics Department, University of Jammu, Jammu, India
3501 ⁸⁸ Physics Department, University of Rajasthan, Jaipur, India
3502 ⁸⁹ Physik Department, Technische Universität München, Munich, Germany
3503 ⁹⁰ Physikalisches Institut, Ruprecht-Karls-Universität Heidelberg, Heidelberg, Germany
3504 ⁹¹ Politecnico di Torino, Turin, Italy
3505 ⁹² Purdue University, West Lafayette, IN, United States
3506 ⁹³ Pusan National University, Pusan, South Korea
3507 ⁹⁴ Research Division and ExtreMe Matter Institute EMMI, GSI Helmholtzzentrum für
3508 Schwerionenforschung, Darmstadt, Germany
3509 ⁹⁵ Rudjer Bošković Institute, Zagreb, Croatia
3510 ⁹⁶ Russian Federal Nuclear Center (VNIIEF), Sarov, Russia
3511 ⁹⁷ Russian Research Centre Kurchatov Institute, Moscow, Russia
3512 ⁹⁸ Saha Institute of Nuclear Physics, Kolkata, India
3513 ⁹⁹ School of Physics and Astronomy, University of Birmingham, Birmingham, United Kingdom
3514 ¹⁰⁰ Sección Física, Departamento de Ciencias, Pontificia Universidad Católica del Perú, Lima, Peru
3515 ¹⁰¹ Sezione INFN, Bari, Italy
3516 ¹⁰² Sezione INFN, Bologna, Italy
3517 ¹⁰³ Sezione INFN, Cagliari, Italy
3518 ¹⁰⁴ Sezione INFN, Catania, Italy
3519 ¹⁰⁵ Sezione INFN, Padova, Italy
3520 ¹⁰⁶ Sezione INFN, Rome, Italy
3521 ¹⁰⁷ Sezione INFN, Trieste, Italy
3522 ¹⁰⁸ Sezione INFN, Turin, Italy
3523 ¹⁰⁹ SUBATECH, Ecole des Mines de Nantes, Université de Nantes, CNRS-IN2P3, Nantes, France

- 3524 ¹¹⁰ Suranaree University of Technology, Nakhon Ratchasima, Thailand
3525 ¹¹¹ Technical University of Split FESB, Split, Croatia
3526 ¹¹² The Henryk Niewodniczanski Institute of Nuclear Physics, Polish Academy of Sciences, Cracow,
3527 Poland
3528 ¹¹³ The University of Texas at Austin, Physics Department, Austin, TX, USA
3529 ¹¹⁴ Universidad Autónoma de Sinaloa, Culiacán, Mexico
3530 ¹¹⁵ Universidade de São Paulo (USP), São Paulo, Brazil
3531 ¹¹⁶ Universidade Estadual de Campinas (UNICAMP), Campinas, Brazil
3532 ¹¹⁷ University of Houston, Houston, TX, United States
3533 ¹¹⁸ University of Jyväskylä, Jyväskylä, Finland
3534 ¹¹⁹ University of Liverpool, Liverpool, United Kingdom
3535 ¹²⁰ University of Tennessee, Knoxville, TN, United States
3536 ¹²¹ University of Tokyo, Tokyo, Japan
3537 ¹²² University of Tsukuba, Tsukuba, Japan
3538 ¹²³ University of Zagreb, Zagreb, Croatia
3539 ¹²⁴ Université de Lyon, Université Lyon 1, CNRS/IN2P3, IPN-Lyon, Villeurbanne, France
3540 ¹²⁵ V. Fock Institute for Physics, St. Petersburg State University, St. Petersburg, Russia
3541 ¹²⁶ Variable Energy Cyclotron Centre, Kolkata, India
3542 ¹²⁷ Vestfold University College, Tonsberg, Norway
3543 ¹²⁸ Warsaw University of Technology, Warsaw, Poland
3544 ¹²⁹ Wayne State University, Detroit, MI, United States
3545 ¹³⁰ Wigner Research Centre for Physics, Hungarian Academy of Sciences, Budapest, Hungary
3546 ¹³¹ Yale University, New Haven, CT, United States
3547 ¹³² Yonsei University, Seoul, South Korea
3548 ¹³³ Zentrum für Technologietransfer und Telekommunikation (ZTT), Fachhochschule Worms, Worms,
3549 Germany

3550 **Acknowledgements**

- 3551 The Collaboration wishes to thank the following persons for their contribution to the preparation of this
3552 TDR:
3553 A. Augustinus, M. Berger, F. Böhmer, F. Carena, F. Costa, S. Dørheim, J. Hehner, H. D. Hernández,
3554 A. Jusko, M. Krivda, P. Martinengo, A. Di Mauro, T. Morhardt, R. de Oliveira, E. Oliveri, F. Raviel,
3555 L. Ropelewski, G. Scioli, M. Van Stenis, A. Tauro and A. Wasem.

3556

References

3557

References for Chapter 1

3558

[1] ALICE Collaboration. “The ALICE experiment at the CERN LHC”. In: *JINST* 3.08 (2008), S08002. DOI: [10.1088/1748-0221/3/08/S08002](https://doi.org/10.1088/1748-0221/3/08/S08002).

3559

3560

[2] ALICE Collaboration. *Upgrade of the ALICE Experiment: Letter Of Intent*. CERN-LHCC-2012-012 / LHCC-I-022. 2012. URL: <http://cds.cern.ch/record/1475243/>.

3561

3562

[3] ALICE Collaboration. *Technical Design Report of the Time Projection Chamber*. CERN/LHCC 2000-001. 2000. URL: <https://edms.cern.ch/document/398930/1>.

3563

3564

[4] ALICE TPC Collaboration. “The ALICE TPC, a Large 3-Dimensional Tracking Device with Fast Read-out for Ultra-high Multiplicity Events”. In: *Nucl. Instr. Meth. A* 622.1 (2010), pp. 316–367. DOI: [10.1016/j.nima.2010.04.042](https://doi.org/10.1016/j.nima.2010.04.042).

3565

3566

3567

References for Chapter 2

3568

[1] ALICE Collaboration. *Technical Design Report of the Time Projection Chamber*. CERN/LHCC 2000-001. 2000. URL: <https://edms.cern.ch/document/398930/1>.

3569

3570

References for Chapter 3

3571

[1] ALICE TPC Collaboration. “The ALICE TPC, a Large 3-Dimensional Tracking Device with Fast Read-out for Ultra-high Multiplicity Events”. In: *Nucl. Instr. Meth. A* 622.1 (2010), pp. 316–367. DOI: [10.1016/j.nima.2010.04.042](https://doi.org/10.1016/j.nima.2010.04.042).

3572

3573

3574

References for Chapter 4

3575

[1] ALICE Collaboration. *Upgrade of the ALICE Experiment: Letter Of Intent*. CERN-LHCC-2012-012 / LHCC-I-022. 2012. URL: <http://cds.cern.ch/record/1475243/>.

3576

3577

[2] F. Sauli. “GEM: A new concept for electron amplification in gas detectors”. In: *Nucl. Instr. Meth. A* 386.2-3 (1997), pp. 531–534. DOI: [10.1016/S0168-9002\(96\)01172-2](https://doi.org/10.1016/S0168-9002(96)01172-2).

3578

3579

[3] R. Veenhof. *Garfield - simulation of gaseous detectors*. 1984 - 2010. URL: <http://garfield.web.cern.ch>.

3580

3581

[4] F. V. Böhmer et al. “Simulation of Space-Charge Effects in an Ungated GEM-based TPC”. In: *Nucl. Instr. Meth. A* 719.0 (2013), pp. 101–108. DOI: [10.1016/j.nima.2013.04.020](https://doi.org/10.1016/j.nima.2013.04.020).

3582

3583

[5] S. Bachmann et al. “Discharge studies and prevention in the gas electron multiplier (GEM)”. In: *Nucl. Instr. Meth. A* 479.2-3 (2002), pp. 294–308. DOI: [10.1016/S0168-9002\(01\)00931-7](https://doi.org/10.1016/S0168-9002(01)00931-7).

3584

3585

[6] S. Blatt et al. “Charge transfer of GEM structures in high magnetic fields”. In: *Nucl. Phys. B (Proc. Suppl.)* 150.0 (2006), pp. 155–158. DOI: [10.1016/j.nuclphysbps.2004.07.005](https://doi.org/10.1016/j.nuclphysbps.2004.07.005).

3586

- 3587 [7] C. Altunbas et al. “Construction, test and commissioning of the triple-GEM tracking detectors
3588 for COMPASS”. In: *Nucl. Instr. Meth. A* 490.1-2 (2002), pp. 177–203. DOI: [10.1016/S0168-
3589 9002\(02\)00910-5](https://doi.org/10.1016/S0168-9002(02)00910-5).
- 3590 [8] B. Ketzer et al. “Performance of triple GEM tracking detectors in the COMPASS experiment”. In:
3591 *Nucl. Instr. Meth. A* 535.1 (2004), pp. 314–318. DOI: [10.1016/j.nima.2011.06.028](https://doi.org/10.1016/j.nima.2011.06.028).
- 3592 [9] B. Ketzer et al. “A triple-GEM detector with pixel readout for high-rate beam tracking in COM-
3593 PASS”. In: *Nuclear Science Symposium Conference Record, 2007. NSS '07. IEEE*. Vol. 1. Piscat-
3594 away, NJ: IEEE, 2007, pp. 242–244. DOI: [10.1109/NSSMIC.2007.4436323](https://doi.org/10.1109/NSSMIC.2007.4436323).
- 3595 [10] P. Abbon et al. “The COMPASS Experiment at CERN”. In: *Nucl. Instr. Meth. A* 577.3 (2007),
3596 pp. 455–518. DOI: [10.1016/j.nima.2007.03.026](https://doi.org/10.1016/j.nima.2007.03.026).
- 3597 [11] G. Bencivenni et al. “A triple GEM detector with pad readout for high rate charged particle trig-
3598 gering”. In: *Nucl. Instr. Meth. A* 488.3 (2002), pp. 493–502. DOI: [10.1016/S0168-9002\(02\)
3599 00515-6](https://doi.org/10.1016/S0168-9002(02)00515-6).
- 3600 [12] Z. Fraenkel et al. “A hadron blind detector for the PHENIX experiment at RHIC”. In: *Nucl. Instr.*
3601 *Meth. A* 546.3 (2005), pp. 466–480. DOI: [10.1016/j.nima.2005.02.039](https://doi.org/10.1016/j.nima.2005.02.039).
- 3602 [13] M. G. Bagliesi et al. “The TOTEM T2 telescope based on triple-GEM chambers”. In: *Nucl. Instr.*
3603 *Meth. A* 617.1-3 (2010), pp. 134–137. DOI: [10.1016/j.nima.2009.07.006](https://doi.org/10.1016/j.nima.2009.07.006).
- 3604 [14] G. Bencivenni and D. Domenici. “An ultra-light cylindrical GEM detector as inner tracker at
3605 KLOE-2”. In: *Nucl. Instr. Meth. A* 581.1-2 (2007), pp. 221–224. DOI: [10.1016/j.nima.2007.
3606 07.082](https://doi.org/10.1016/j.nima.2007.07.082).
- 3607 [15] D. Abbaneo et al. “Characterization of GEM detectors for application in the CMS muon detec-
3608 tion system”. In: *Nuclear Science Symposium Conference Record (NSS/MIC), 2010 IEEE*. 2010,
3609 pp. 1416–1422. DOI: [10.1109/NSSMIC.2010.5874006](https://doi.org/10.1109/NSSMIC.2010.5874006).
- 3610 [16] M. Alfonsi et al. “High-rate particle triggering with triple-GEM detector”. In: *Nucl. Instr. Meth. A*
3611 518.1-2 (2004), pp. 106–112. DOI: [10.1016/j.nima.2003.10.035](https://doi.org/10.1016/j.nima.2003.10.035).
- 3612 [17] S. Duarte Pinto et al. “Progress on large area GEMs”. In: *JINST* 4.12 (2009), P12009. DOI: [10.
3613 1088/1748-0221/4/12/P12009](https://doi.org/10.1088/1748-0221/4/12/P12009).
- 3614 [18] M. Alfonsi et al. “Activity of CERN and LNF groups on large area GEM detectors”. In: *Nucl.*
3615 *Instr. Meth. A* 617.1-3 (2010), pp. 151–154. DOI: [DOI:10.1016/j.nima.2009.06.063](https://doi.org/10.1016/j.nima.2009.06.063).
- 3616 [19] A. Balla et al. “Construction and test of the cylindrical-GEM detectors for the KLOE-2 Inner
3617 Tracker”. In: *Nucl. Instr. Meth. A* (2013). DOI: [10.1016/j.nima.2013.08.021](https://doi.org/10.1016/j.nima.2013.08.021).
- 3618 [20] D. Abbaneo et al. “The status of the GEM project for CMS high- η muon system”. In: *Nucl. Instr.*
3619 *Meth. A* (2013). DOI: [10.1016/j.nima.2013.08.015](https://doi.org/10.1016/j.nima.2013.08.015).
- 3620 [21] B. Ketzer. “A Time Projection Chamber for High-Rate Experiments: Towards an Upgrade of the
3621 ALICE TPC”. In: (2013). arXiv:[1303.6694](https://arxiv.org/abs/1303.6694) [[physics.ins-det](https://arxiv.org/abs/1303.6694)].
- 3622 [22] M. Alfonsi et al. “The triple-GEM detector for the M1R1 muon station at LHCb”. In: *Nuclear*
3623 *Science Symposium Conference Record (NSS/MIC), 2005, IEEE*. 2005, pp. 811–815. DOI: [10.
3624 1109/NSSMIC.2005.1596379](https://doi.org/10.1109/NSSMIC.2005.1596379).
- 3625 [23] F. Garcia et al. “GEM-TPC Prototype for Beam Diagnostics of Super-FRS in NUSTAR Experi-
3626 ment - FAIR”. In: *Nuclear Science Symposium Conference Record (NSS/MIC), 2009, IEEE*. 2009,
3627 pp. 269–272. DOI: [10.1109/NSSMIC.2009.5401762](https://doi.org/10.1109/NSSMIC.2009.5401762).
- 3628 [24] F. Garcia et al. “Prototype development of a GEM-TPC for the Super-FRS of the FAIR facility”.
3629 In: *Nuclear Science Symposium Conference Record (NSS/MIC), 2011, IEEE*. 2011, pp. 1788–
3630 1792. DOI: [10.1109/NSSMIC.2011.6154683](https://doi.org/10.1109/NSSMIC.2011.6154683).

- 3631 [25] M. Kalliokoski et al. “Optical scanning system for quality control of GEM-foils”. In: *Nucl. Instr.*
3632 *Meth. A* 664.1 (2012), pp. 223–230. DOI: [10.1016/j.nima.2011.10.058](https://doi.org/10.1016/j.nima.2011.10.058).

3633 **References for Chapter 5**

- 3634 [1] M. Killenberg et al. “Charge transfer and charge broadening of GEM structures in high magnetic
3635 fields”. In: *Nucl. Instr. Meth. A* 530.3 (2004), pp. 251–257. DOI: [10.1016/j.nima.2004.04.](https://doi.org/10.1016/j.nima.2004.04.241)
3636 [241](https://doi.org/10.1016/j.nima.2004.04.241).
- 3637 [2] Leszek Ropelewski. *Private communication*.
- 3638 [3] S Bachmann et al. “Discharge studies and prevention in the gas electron multiplier (GEM)”. In:
3639 *Nucl. Instrum. Methods Phys. Res., A* 479.CERN-EP-2000-151. 2-3 (2000), 294–308. 25 p.
- 3640 [4] Alessandro Cardini, Giovanni Bencivenni, and Patrizia De Simone. “The Operational Experience
3641 of the Triple-GEM Detectors of the LHCb Muon System: Summary of 2 Years of Data Taking”.
3642 In: (2012).
- 3643 [5] M Alfonsi et al. “High-rate particle triggering with triple-GEM detector”. In: *Nucl. Instrum. Meth-*
3644 *ods Phys. Res., A* 518 (2004), pp. 106–112.
- 3645 [6] R. Veenhof. *Garfield - simulation of tracking detectors*. 2012. URL: [http://garfieldpp.web.](http://garfieldpp.web.cern.ch)
3646 [cern.ch](http://garfieldpp.web.cern.ch).
- 3647 [7] ANSYS®. Academic Research, Release 13.0. 2012.
- 3648 [8] I. Smirnov. *Interactions of particles with gases*. URL: [http://consult.cern.ch/writeup/](http://consult.cern.ch/writeup/heed/)
3649 [heed/](http://consult.cern.ch/writeup/heed/).
- 3650 [9] S.F. Biagi. “Monte Carlo simulation of electron drift and diffusion in counting gases under the
3651 influence of electric and magnetic fields”. In: *Nucl. Instr. Meth. A* 421 (1999), pp. 234–240.
- 3652 [10] H. W. Ellis et al. “Transport properties of gaseous ions over a wide energy range”. In: *Atomic Data*
3653 *and Nuclear Data Tables* 17 (1976), pp. 177–210. DOI: [10.1016/0092-640X\(76\)90001-2](https://doi.org/10.1016/0092-640X(76)90001-2).
- 3654 [11] H. W. Ellis et al. “Transport properties of gaseous ions over a wide energy range II”. In: *Atomic*
3655 *Data and Nuclear Data Tables* 22 (1978), pp. 179–217. DOI: [10.1016/0092-640X\(78\)90014-](https://doi.org/10.1016/0092-640X(78)90014-1)
3656 [1](https://doi.org/10.1016/0092-640X(78)90014-1).
- 3657 [12] H. W. Ellis et al. “Transport properties of gaseous ions over a wide energy range III”. In: *Atomic*
3658 *Data and Nuclear Data Tables* 31 (1984), pp. 113–151. DOI: [10.1016/0092-640X\(84\)90018-](https://doi.org/10.1016/0092-640X(84)90018-4)
3659 [4](https://doi.org/10.1016/0092-640X(84)90018-4).
- 3660 [13] ALICE TPC Collaboration. “The ALICE TPC, a Large 3-Dimensional Tracking Device with Fast
3661 Read-out for Ultra-high Multiplicity Events”. In: *Nucl. Instr. Meth. A* 622.1 (2010), pp. 316–367.
3662 DOI: [10.1016/j.nima.2010.04.042](https://doi.org/10.1016/j.nima.2010.04.042).
- 3663 [14] *Huntsman Advanced Materials (Schweiz) GmbH, Klybeckstrasse 200, 4057 Basel, Switzerland*.
3664 URL: http://www.huntsman.com/advanced_materials.
- 3665 [15] C. Altunbas et al. “Construction, test and commissioning of the triple-GEM tracking detectors
3666 for COMPASS”. In: *Nucl. Instr. Meth. A* 490.1-2 (2002), pp. 177–203. DOI: [10.1016/S0168-](https://doi.org/10.1016/S0168-9002(02)00910-5)
3667 [9002\(02\)00910-5](https://doi.org/10.1016/S0168-9002(02)00910-5).
- 3668 [16] S. Bachmann et al. “Discharge studies and prevention in the gas electron multiplier (GEM)”. In:
3669 *Nucl. Instr. Meth. A* 479.2-3 (2002), pp. 294–308. DOI: [10.1016/S0168-9002\(01\)00931-7](https://doi.org/10.1016/S0168-9002(01)00931-7).

3670 **References for Chapter 6**

- 3671 [1] ALICE Collaboration. *Technical Design Report of the Time Projection Chamber*. CERN/LHCC
3672 2000-001. 2000. URL: <https://edms.cern.ch/document/398930/1>.

- 3673 [2] ALICE TPC Collaboration. “The ALICE TPC, a Large 3-Dimensional Tracking Device with Fast
3674 Read-out for Ultra-high Multiplicity Events”. In: *Nucl. Instr. Meth. A* 622.1 (2010), pp. 316–367.
3675 DOI: [10.1016/j.nima.2010.04.042](https://doi.org/10.1016/j.nima.2010.04.042).
- 3676 [3] P. Moreira et al. “The GBT Project”. In: *Proceedings of the Topical workshop on electronics for
3677 particle physics in Paris, France, September 2125* (2009), pp. 342–346. DOI: [10.5170/CERN-
3678 2009-006](https://doi.org/10.5170/CERN-2009-006).
- 3679 [4] J. Troska et al. “The Versatile Transceiver Proof of Concept”. In: *Proceedings of the Topical
3680 workshop on electronics for particle physics in Paris, France, September 2125* (2009), pp. 347–
3681 349. DOI: [10.5170/CERN-2009-006](https://doi.org/10.5170/CERN-2009-006).
- 3682 [5] ALICE Collaboration. *Upgrade of the ALICE Read-Out and Trigger system, Technical Design
3683 Report*. To be published in Dec 2013.
- 3684 [6] ALICE Collaboration. “Centrality dependence of the charged-particle multiplicity density at mid-
3685 rapidity in Pb-Pb collisions at $\sqrt{s_{NN}} = 2.76$ TeV”. In: *Phys. Rev. Lett.* 106 (2011), p. 032301. DOI:
3686 [10.1103/PhysRevLett.106.032301](https://doi.org/10.1103/PhysRevLett.106.032301).
- 3687 [7] ALICE Collaboration. “Charged-particle multiplicity density at mid-rapidity in central PbPb colli-
3688 sions at $\sqrt{s_{NN}} = 2.76$ TeV”. In: *Phys. Rev. Lett.* 105 (2010), p. 252301. DOI: [10.1103/PhysRevLett.
3689 105.252301](https://doi.org/10.1103/PhysRevLett.105.252301).
- 3690 [8] J. Wiechula. “Commissioning and Calibration of the ALICE TPC”. PhD thesis. Goethe-Universität
3691 Frankfurt am Main, 2009.
- 3692 [9] H. K. Soltveit et al. “The preamplifier-shaper for the ALICE TPC-Detector”. In: *Nucl. Instr.
3693 Meth. A* 676.0 (2012), pp. 106–119. DOI: [10.1016/j.nima.2012.02.012](https://doi.org/10.1016/j.nima.2012.02.012).
- 3694 [10] H. Stelzer et al. *The ALICE TPC Readout Chamber: From Prototypes to Series Production*.
3695 ALICE-INT-2003-017. 2003. URL: <https://edms.cern.ch/document/384259>.
- 3696 [11] M. De Gaspari. “Systems-on-Chip (SoC) for applications in High-Energy Physics”. PhD thesis.
3697 Ruprecht-Karls-Universität Heidelberg, 2012.
- 3698 [12] G. Trampitsch. “Design and Characterization of an Analogue Amplifier for the Readout of Micro-
3699 Pattern Gaseous Detectors”. PhD thesis. Graz University of Technology, 2007.
- 3700 [13] L. Jönsson. *Front end electronics for a TPC at future linear colliders*. EUDET-Memo-2010-30.
3701 2010. URL: [http://www.eudet.org/e26/e28/e86887/e105928/EUDET-Memo-2010-
3702 30.pdf](http://www.eudet.org/e26/e28/e86887/e105928/EUDET-Memo-2010-30.pdf).
- 3703 [14] D. A. Huffman. “A Method for the Construction of Minimum-Redundancy Codes”. In: *Proc. IRE*
3704 40.9 (1952), pp. 1098–1101. DOI: [10.1109/JRPROC.1952.273898](https://doi.org/10.1109/JRPROC.1952.273898).
- 3705 [15] *Mass production Tests of the ALICE TPC Front End Electronics*. 2007. URL: [http://ep-ed-
3706 alice-tpc.web.cern.ch/ep-ed-alice-tpc/testing.htm](http://ep-ed-alice-tpc.web.cern.ch/ep-ed-alice-tpc/testing.htm).

3707 References for Chapter 7

- 3708 [1] ALICE Collaboration. *Technical Design Report of the Time Projection Chamber*. CERN/LHCC
3709 2000-001. 2000. URL: <https://edms.cern.ch/document/398930/1>.
- 3710 [2] ALICE Collaboration. “Centrality Dependence of Charged Particle Production at Large Trans-
3711 verse Momentum in Pb–Pb Collisions at $\sqrt{s_{NN}} = 2.76$ TeV”. In: *Phys. Lett. B* 720.1-3 (2013),
3712 pp. 52–62. DOI: [10.1016/j.physletb.2013.01.051](https://doi.org/10.1016/j.physletb.2013.01.051).
- 3713 [3] ALICE TPC Collaboration. “The ALICE TPC, a Large 3-Dimensional Tracking Device with Fast
3714 Read-out for Ultra-high Multiplicity Events”. In: *Nucl. Instr. Meth. A* 622.1 (2010), pp. 316–367.
3715 DOI: [10.1016/j.nima.2010.04.042](https://doi.org/10.1016/j.nima.2010.04.042).

- 3716 [4] A. Ortiz Velasquez. “Production of pions, kaons and protons at high p_T in $\sqrt{s_{NN}} = 2.76$ TeV Pb-Pb
3717 collisions”. In: *Nucl. Phys. A* 904-905.0 (2013), pp. 763c–766c. DOI: [10.1016/j.nuclphysa.
3718 2013.02.129](https://doi.org/10.1016/j.nuclphysa.2013.02.129).
- 3719 [5] ALICE Collaboration. *Upgrade of the ALICE Experiment: Letter Of Intent*. CERN-LHCC-2012-
3720 012 / LHCC-I-022. 2012. URL: <http://cds.cern.ch/record/1475243/>.
- 3721 [6] ALICE Collaboration. *Upgrade of the ALICE Inner Tracking System, Technical Design Report*.
3722 To be published in Dec 2013.
- 3723 [7] P. Christiansen et al. “The influence of detector effects on TPC performance”. In: *Nucl. Instr.
3724 Meth. A* 609.1 (2009), pp. 149–155. DOI: [10.1016/j.nima.2009.08.052](https://doi.org/10.1016/j.nima.2009.08.052).
- 3725 [8] G. Van Buren et al. “Correcting for distortions due to ionization in the STAR TPC”. In: *Nucl. Instr.
3726 Meth. A* 566.1 (2006), pp. 22–25. DOI: [10.1016/j.nima.2006.05.131](https://doi.org/10.1016/j.nima.2006.05.131).
- 3727 [9] G. Van Buren. *private communication*.
- 3728 [10] F. V. Böhmer et al. “Simulation of Space-Charge Effects in an Ungated GEM-based TPC”. In:
3729 *Nucl. Instr. Meth. A* 719.0 (2013), pp. 101–108. DOI: [10.1016/j.nima.2013.04.020](https://doi.org/10.1016/j.nima.2013.04.020).
- 3730 [11] M. Mager, S. Rossegger, and J. Thomas. *Composed correction framework for modeling the TPC
3731 field distortions in AliRoot*. ALICE-INT-2010-018, 2010. URL: [https://edms.cern.ch/
3732 document/1113105/1/](https://edms.cern.ch/document/1113105/1/).
- 3733 [12] S. Rossegger, B. Schnizer, and W. Riegler. “Analytical solutions for space charge fields in TPC
3734 drift volumes”. In: *Nucl. Instr. Meth. A* 632.1 (2011), pp. 52–58. DOI: [10.1016/j.nima.2010.
3735 12.213](https://doi.org/10.1016/j.nima.2010.12.213).
- 3736 [13] M. Mager, S. Rossegger, and J. Thomas. *The Langevin equation expanded to 2nd order and com-
3737 ments on using the equation to correct for space point distortions in a TPC*. ALICE-INT-2010-
3738 016, 2010. URL: <https://edms.cern.ch/document/1108138/1>.
- 3739 [14] M. Mager, S. Rossegger, and J. Thomas. *Space-charge effects in the ALICE TPC: a comparison
3740 between expected ALICE performance and current results from the STAR TPC*. ALICE-INT-2010-
3741 017, 2010. URL: <https://edms.cern.ch/document/1113087/1>.

3742 **References for Chapter 8**

- 3743 [1] LHC Programme Coordination. *LHC Luminosity Plots for the 2010 Heavy-Ion Run. Website*.
3744 2010. URL: http://lpc.web.cern.ch/lpc/lumiplots_ions_2010.htm.
- 3745 [2] LHC Programme Coordination. *LHC Luminosity Plots for the 2011 Heavy-Ion Run. Website*.
3746 2011. URL: http://lpc.web.cern.ch/lpc/lumiplots_ion.htm.
- 3747 [3] The ALICE DAQ group. *ALICE Electronic Logbook. Website*. 2012. URL: [https://alice-
3748 logbook.cern.ch/logbook](https://alice-logbook.cern.ch/logbook).
- 3749 [4] G. Bregliozzi. Private Communication. 2013.
- 3750 [5] ALICE Collaboration. *Upgrade of the ALICE Experiment: Letter Of Intent*. CERN-LHCC-2012-
3751 012 / LHCC-I-022. 2012. URL: <http://cds.cern.ch/record/1475243/>.
- 3752 [6] D. A. Huffman. “A Method for the Construction of Minimum-Redundancy Codes”. In: *Proc. IRE*
3753 40.9 (1952), pp. 1098–1101. DOI: [10.1109/JRPROC.1952.273898](https://doi.org/10.1109/JRPROC.1952.273898).
- 3754 [7] T. Kollegger. “The ALICE high level trigger: The 2011 run experience”. In: *Real Time Conference
3755 (RT), 2012 18th IEEE-NPSS*. 2012, pp. 1–4. DOI: [10.1109/RTC.2012.6418366](https://doi.org/10.1109/RTC.2012.6418366).
- 3756 [8] ALICE Collaboration. *Technical Design Report of the Time Projection Chamber*. CERN/LHCC
3757 2000-001. 2000. URL: <https://edms.cern.ch/document/398930/1>.

- 3758 [9] D. Decamp et al. “ALEPH: A detector for electron-positron annihilations at LEP”. In: *Nucl. Instr.*
3759 *Meth. A* 294.1-2 (1990), pp. 121–178. DOI: [10.1016/0168-9002\(90\)91831-U](https://doi.org/10.1016/0168-9002(90)91831-U).
- 3760 [10] Walter Blum. *The ALEPH handbook*. CERN-ALEPH-89-077. Geneva: CERN, 1989. URL: <http://cdsweb.cern.ch/record/227125>.
3761
- 3762 [11] A. De Min et al. “Performance of the HPC calorimeter in DELPHI”. In: *IEEE Trans. Nucl. Sci.* 42
3763 (1995), pp. 491–498. DOI: [10.1109/23.467923](https://doi.org/10.1109/23.467923).
- 3764 [12] M. Ball et al. “Technical Design Study for the PANDA Time Projection Chamber”. In: (2012).
3765 arXiv:1207.0013 [physics.ins-det].
- 3766 [13] B. Ketzer. “A Time Projection Chamber for High-Rate Experiments: Towards an Upgrade of the
3767 ALICE TPC”. In: (2013). arXiv:1303.6694 [physics.ins-det].
- 3768 [14] J. Wiechula. “Commissioning and Calibration of the ALICE TPC”. PhD thesis. Goethe-Universität
3769 Frankfurt am Main, 2009.
- 3770 [15] ALICE TPC Collaboration. “The ALICE TPC, a Large 3-Dimensional Tracking Device with Fast
3771 Read-out for Ultra-high Multiplicity Events”. In: *Nucl. Instr. Meth. A* 622.1 (2010), pp. 316–367.
3772 DOI: [10.1016/j.nima.2010.04.042](https://doi.org/10.1016/j.nima.2010.04.042).

3773 References for Chapter 9

- 3774 [1] J. F. C. A. Veloso et al. “THCOBRA: Ion back flow reduction in patterned THGEM cascades”. In:
3775 *Nucl. Instr. Meth. A* 639.1 (2011), pp. 134–136. DOI: [10.1016/j.nima.2010.10.083](https://doi.org/10.1016/j.nima.2010.10.083).
- 3776 [2] F. D. Amaro et al. “The Thick-COBRA: a new gaseous electron multiplier for radiation detectors”.
3777 In: *JINST* 5.10 (2010), P10002. DOI: [10.1088/1748-0221/5/10/P10002](https://doi.org/10.1088/1748-0221/5/10/P10002).
- 3778 [3] *SciEnergy Co. Ltd.* URL: <http://www.scienergy.jp/>.
- 3779 [4] Takayuki Sumiyoshi et al. “Development of a gaseous PMT with micro-pattern gas detectors”. In:
3780 *Nucl.Instrum.Meth.* A639 (2011), pp. 121–125. DOI: [10.1016/j.nima.2010.10.032](https://doi.org/10.1016/j.nima.2010.10.032).
- 3781 [5] P. Colas, I. Giomataris, and V. Lepeltier. “Ion backflow in the Micromegas TPC for the future
3782 linear collider”. In: *Nucl. Instr. Meth. A* 535.1-2 (2004), pp. 226–230. DOI: [10.1016/j.nima.2004.07.274](https://doi.org/10.1016/j.nima.2004.07.274).
3783
- 3784 [6] S. Kane et al. *A STUDY OF MICROMEGAS WITH PREAMPLIFICATION WITH A SINGLE*
3785 *GEM*. World Scientific. 2004.
- 3786 [7] M. Vandenbroucke et al. *Discharge reduction technologies for Micromegas detectors in high*
3787 *hadron flux environments*. 2nd International Conference on Micro Pattern Gaseous Detectors.
3788 2011.
- 3789 [8] G. Charles et al. “Discharge studies in Micromegas detectors in low energy hadron beams”. In:
3790 *Nucl.Instrum.Meth.* A648 (2011), pp. 174–179. DOI: [10.1016/j.nima.2011.05.056](https://doi.org/10.1016/j.nima.2011.05.056).
- 3791 [9] M. Vandenbroucke. *Development and Characterization of Micro-Pattern Gas Detectors for In-*
3792 *tense Beams of Hadrons*. Ph.D. Thesis, Universite Pierre et Marie Curie and Technische Universi-
3793 tat Munchen. 2012.
- 3794 [10] G. Sekhniadze. *Construction and experience with a 2.4 x 1. m2 MMG chamber*. RD51 meeting,
3795 Zaragoza, 2013. 2013.
- 3796 [11] B. Yu et al. “Investigation of Chevron Cathode Pads for Position Encoding in Very High Rate, Gas
3797 Proportional Chambers”. In: *IEEE Trans. Nucl. Sci.* 38.2 (1991), pp. 454–460. DOI: [10.1109/23.289339](https://doi.org/10.1109/23.289339).
3798

3799 **References for Chapter 10**

- 3800 [1] S. Schmeling. “Common tools for large experiment controls: A common approach for deployment,
3801 maintenance, and support”. In: *IEEE Trans. Nucl. Sci.* 53.3 (2006), pp. 970–973. DOI: [10.1109/
3802 TNS.2006.873706](https://doi.org/10.1109/TNS.2006.873706).
- 3803 [2] B. Franek and C. Gaspar. “SMI++: An Object Oriented Framework for Designing Distributed
3804 Control Systems”. In: *IEEE Trans. Nucl. Sci.* 45.4 (1998), pp. 1946–1950. DOI: [10.1109/23.
3805 710969](https://doi.org/10.1109/23.710969).
- 3806 [3] *ETM professional control GmbH, A Siemens Company, Marktstrae 3, A-7000 Eisenstadt, Austria.*
3807 URL: <http://www.etm.at>.
- 3808 [4] C. Gaspar, M. Dönszelmann, and Ph. Charpentier. “DIM, a portable, light-weight package for in-
3809 formation publishing, data transfer and inter-process communication”. In: *Computer Phys. Com-
3810 muni.* 140 (2001), pp. 102–109. URL: [http://dim.web.cern.ch/dim/papers/CHEP/DIM.
3811 PDF](http://dim.web.cern.ch/dim/papers/CHEP/DIM.PDF).

3812 **References for Chapter 11**

- 3813 [1] ALICE TPC Collaboration. “The ALICE TPC, a Large 3-Dimensional Tracking Device with Fast
3814 Read-out for Ultra-high Multiplicity Events”. In: *Nucl. Instr. Meth. A* 622.1 (2010), pp. 316–367.
3815 DOI: [10.1016/j.nima.2010.04.042](https://doi.org/10.1016/j.nima.2010.04.042).
- 3816 [2] H. Müller. *SRS commercial status 2013*. Talk at the RD51 Collaboration Meeting, Zaragosa,
3817 Spain, July 1 – 6. 2013. URL: [http://indico.cern.ch/contributionDisplay.py?
3818 contribId=129&sessionId=6&confId=258852](http://indico.cern.ch/contributionDisplay.py?contribId=129&sessionId=6&confId=258852).

3819 **References for Chapter A**

- 3820 [1] L. Betev and P. Chochula. *Definition of the ALICE Coordinate System and basic rules for Sub-
3821 Detector Components numbering*. ALICE-INT-2003-038. 2003. URL: [https://edms.cern.
3822 ch/document/406391/2](https://edms.cern.ch/document/406391/2).
- 3823 [2] ALICE Collaboration. “ALICE: Physics Performance Report, Volume II”. In: *J. Phys.* G32 (2006),
3824 pp. 1295–2040. DOI: [10.1088/0954-3899/32/10/001](https://doi.org/10.1088/0954-3899/32/10/001).

List of Figures

3826	1.1	Inclusive e^+e^- invariant mass spectrum for central Pb–Pb collisions	3
3827	2.1	Schematic view of the TPC	8
3828	2.2	View of TPC endplates and rods	8
3829	2.3	Clearance during IROC insertion	9
3830	2.4	Detail of OROC insertion	9
3831	2.5	Side view showing clearance during OROC insertion	10
3832	2.6	Detailed view of skirt electrode	10
3833	2.7	Overall view of TPC with Service Support Wheel	11
3834	2.8	Schematic diagram of the TPC gas system	12
3835	3.1	Drift velocity and diffusion gas mixtures based on Ne and CO_2	13
3836	3.2	Distortions at the central electrode for all gases	14
3837	3.3	Townsend and Attachment coefficients for three gas mixtures	14
3838	3.4	Drift velocity and diffusion for gas mixtures based on Ne and CF_4	15
3839	4.1	Photograph of standard GEM foil	18
3840	4.2	Photograph of large pitch GEM foil	18
3841	4.3	Simulated avalanche in GEM hole	19
3842	4.4	Dimensions of the ALICE TPC readout chambers	21
3843	4.5	Exploded view of a GEM IROC	22
3844	4.6	Exploded view of a GEM OROC	22
3845	4.7	Schematic exploded cross section of the GEM stack	23
3846	4.8	Photograph of an IROC GEM foil in the stretching frame	24
3847	4.9	Dimensions of an IROC GEM foil	25
3848	4.10	Photograph of an IROC GEM foil	26
3849	4.11	Detailed view of the HV distribution on an IROC GEM foil	27

3850	4.12 Bias resistors and HV supply of an IROC GEM foil	27
3851	4.13 Dimensions of OROC GEM foils	28
3852	4.14 Schematics of the HV distribution scheme	29
3853	4.15 Potentials on all GEM electrodes of a quadruple GEM stack	30
3854	4.16 Point resolution in the magnetic bending plane for MWPC and GEM	32
3855	4.17 Fraction of one-, two-, three-, and four-pad clusters for MWPC and GEM	33
3856	4.18 Cluster sizes for MWPC and GEM	33
3857	4.19 Pad layout of an ALICE OROC	35
3858	4.20 GEM foil transportation package	36
3859	4.21 Leakage current measurement setup	37
3860	4.22 Leakage current results from a good GEM foil	38
3861	4.23 Leakage current results from a recovered GEM foil	38
3862	4.24 Setup of the high resolution scanning system	39
3863	4.25 Distributions of geometrical parameters of GEM holes	39
3864	4.26 Example map of hole diameters	40
3865	4.27 Setup for gain mapping measurement	40
3866	4.28 Setup for gain mapping	41
3867	4.29 Pulse height distribution for a single pad	41
3868	4.30 Relative gain map of a single GEM foil	42
3869	5.1 GEM setup at TUM	44
3870	5.2 Signal and current vs. time	45
3871	5.3 Gain fluctuations in Ne-CO ₂ (90-10)	45
3872	5.4 Measured IB vs E_{T1} for different settings of E_{T2}	47
3873	5.5 2D IB scan in a quadrupole standard GEM	47
3874	5.6 2D IB scan for S-S-LP-S quadruple GEM setup	48
3875	5.7 IB and energy resolution for LP-S-LP-S configuration	48
3876	5.8 IB and energy resolution for S-LP-S-LP configuration	49
3877	5.9 Energy resolution in a quadruple S-LP-LP-S GEM vs $1/\sqrt{IBF}$	50
3878	5.10 Probability distribution of random alignment between two GEM layers	51
3879	5.11 IB vs E_{T1} and E_{T2} from measurements and simulations (Ne-CO ₂ -N ₂ (90-10-5))	51
3880	5.12 IB as a function of E_{T1} from measurements and simulations for quadruple GEM setup	52
3881	5.13 Layout of the GEM foil	53
3882	5.14 Support frame details	54

3883	5.15 Foil gluing procedure	55
3884	5.16 Assembly of the prototype	56
3885	5.17 Test box with field cage and IROC	57
3886	5.18 HV distribution of the prototype	57
3887	5.19 Effective gain of the chamber as a function of HV	59
3888	5.20 ^{55}Fe spectra obtained in Ar-CO ₂ (90-10) and Ne-CO ₂ (90-10)	60
3889	5.21 Detector equipped with front-end electronics	60
3890	5.22 Gain map	61
3891	5.23 dE/dx spectrum for electrons and pions	61
3892	5.24 dE/dx resolution	62
3893	5.25 Separation power between pions and electrons.	63
3894	5.26 Simulated dE/dx spectrum for 1 GeV/c pions	63
3895	6.1 Schematics of readout electronics	66
3896	6.2 Equivalent $dN_{\text{ch}}/d\eta$ fluctuations	67
3897	6.3 Expected signal occupancy (worst case)	68
3898	6.4 Schematic of SAMPA	69
3899	6.5 Time properties of clusters for two gases	71
3900	6.6 Noise distribution on current system	72
3901	6.7 SAMPA testing robot	79
3902	6.8 Schematic of FEC	80
3903	6.9 Schematic of readout system with FEC, CRU, trigger, DCS and online farm	82
3904	7.1 Current performance: $1/p_T$ resolution in p-Pb collisions	84
3905	7.2 $1/p_T$ resolution for central barrel with current and GEM TPC	86
3906	7.3 dE/dx resolution with current and GEM readout	87
3907	7.4 Energy resolution as function of electron transparency	87
3908	7.5 Tracking efficiency at different interaction rates	88
3909	7.6 Momentum resolution at different interaction rates	89
3910	7.7 dE/dx resolution at different interaction rates	89
3911	7.8 Average space-charge density map	90
3912	7.9 Space-charge distortions for Ne-CO ₂ -N ₂ (90-10-5)	92
3913	7.10 Space-charge distortions at inner field cage	93
3914	7.11 Space-charge distortions vs. epsilon	93

3915	7.12 Ion pileup simulation	95
3916	7.13 Influence of space-charge fluctuations on distortions	96
3917	7.14 Relative fluctuations of the space charge	96
3918	7.15 Residual space-charge distortions after mean correction	97
3919	7.16 Fluctuation of drift distortions; z scan	98
3920	7.17 TPC Performance after distortion corrections	99
3921	8.1 Schematic LHC filling scheme and bunch train structure	102
3922	8.2 Distribution of time differences between two collisions	103
3923	8.3 Schematic outline of the calibration flow	104
3924	8.4 Data compression factor via cluster finding in RUN 1	105
3925	8.5 Comparison of the tracking performance	109
3926	8.6 Cluster-to-track association efficiency	110
3927	8.7 ITS and ITS-TRD track precision inside the TPC.	111
3928	8.8 Space-charge calibration from track interpolation.	112
3929	8.9 Results from the ITS-TRD interpolation method.	112
3930	8.10 Resolution of the ITS-TRD interpolation method.	113
3931	8.11 Comparison of the momentum resolution with and without distortions	114
3932	8.12 Schematic drawing of the seeding procedure and the t_0 estimation.	115
3933	8.13 Deviation of t_0^{seed} from real t_0	116
3934	8.14 Matching of the local- y coordinate of ITS and TPC tracks.	117
3935	8.15 Simulated laser event	121
3936	9.1 Photograph of COBRA 1.	124
3937	9.2 Working principle of COBRA GEM for the suppression of the ion backflow	124
3938	9.3 Setup for the measurement of gas gain and ion backflow	125
3939	9.4 Effective gain and IB in Ne-CO ₂ (90-10) as a function of the voltage across the GEM	126
3940	9.5 Effective gain and IB as a function of $\Delta U_{AC}^{\text{up}}$	126
3941	9.6 Effective gain and IB scan vs. X-ray tube current for GEM 50–COBRA 2–GEM 50	127
3942	9.7 Effective gain and IB vs. $\Delta U_{AC}^{\text{up}}$ and E_{T2} for GEM 50–COBRA 2–GEM 50	128
3943	9.8 Effective gain and IB vs. X-ray tube current for GEM 50–COBRA 2–COBRA 2	128
3944	9.9 Effective gain and IB voltage scan for GEM 50–COBRA 2–COBRA 2	129
3945	9.10 ⁵⁵ Fe energy spectra with GEM 50–COBRA 2–COBRA 2	130
3946	9.11 Setup to measure hybrid 2 GEM + MMG system	131

3947	9.12 IB , energy resolution and energy spectrum for hybrid 2 GEM + MMG system	131
3948	9.13 One-, two-, and three-pad clusters for rectangular and chevron-shaped readout pads . . .	132
3949	9.14 Space-point resolution in $r\phi$ obtained with different pad geometries	133
3950	9.15 ITS-TPC momentum resolution with different pad geometries and gas mixtures	133
3951	10.1 DCS subsystems overview	136
3952	10.2 Schematic of the front-end electronics DCS	137
3953	10.3 Current readout for online calibration and DCS	138
3954	11.1 Yellow platform	140
3955	11.2 Schematic of current monitoring system	141
3956	11.3 Schematic of HV mapping scheme	141
3957	11.4 Schematic of RR system	142
3958	11.5 Schematic of LV setup	143
3959	11.6 Working principle of the calibration pulser system.	144
3960	11.7 Schematic setup of the calibration pulser system.	144
3961	12.1 TPC upgrade project structure.	147
3962	12.2 Timeline of TPC upgrade	149
3963	A.1 Global coordinate system used in this document	153
3964	A.2 Local coordinate system used in this document	154

3965

List of Tables

3966	1.1	Synopsis of parameters of the upgraded TPC.	6
3967	3.1	Properties of gas mixtures	15
3968	4.1	Parameters of GEM foils for the ALICE TPC	26
3969	4.2	Typical high voltage settings for minimal ion backflow	31
3970	4.3	Dimensions and parameters of readout planes and pads	34
3971	5.1	Geometry test detector	44
3972	5.2	Electric field configuration for the triple GEM	46
3973	5.3	Results of the HV test of a total of 72 HV sectors on 4 GEM foils.	55
3974	5.4	Standard and ion backflow high voltage settings	58
3975	6.1	Data rates and partitioning for 5 readout partitions	68
3976	6.2	SAMPA parameters	70
3977	6.3	System parameters and ENC values for the current TPC	72
3978	6.4	Contributions to the capacitances for the current TPC readout	73
3979	6.5	Simulated and measured ENC for PASA, PCA16, S-ALTRO and SAMPA	74
3980	6.6	Occupancies and data sizes in RUN 3	77
3981	7.1	Overview of simulation parameters	85
3982	8.1	Event size and data compression factors	105
3983	9.1	Geometries of COBRA GEMs and standard GEMs used for the measurements.	123
3984	11.1	Time required for the most relevant activities	140
3985	11.2	Specifications of the existing LV power supply system.	142
3986	12.1	List of institutions participating in the TPC upgrade.	146

3987	12.2 Sharing of responsibilities for construction and installation of the TPC upgrade	147
3988	12.3 CORE cost estimate for the TPC upgrade.	148